AD-A191 926 NONLINEAR OPTICAL PROPERTIES AND SUBPICOSECOND DYNAMICS 1/3
OF EXCITONS AND E..(U) ARMY LAB COMMAND WATERTOWN MA
MATERIAL TECHNOLOGY LAB T F BOGGESS ET AL. DEC 87
UNCLASSIFIED MAC-REF-F4767 AFOSR-TR-88-0012 F/G 20/12 NL

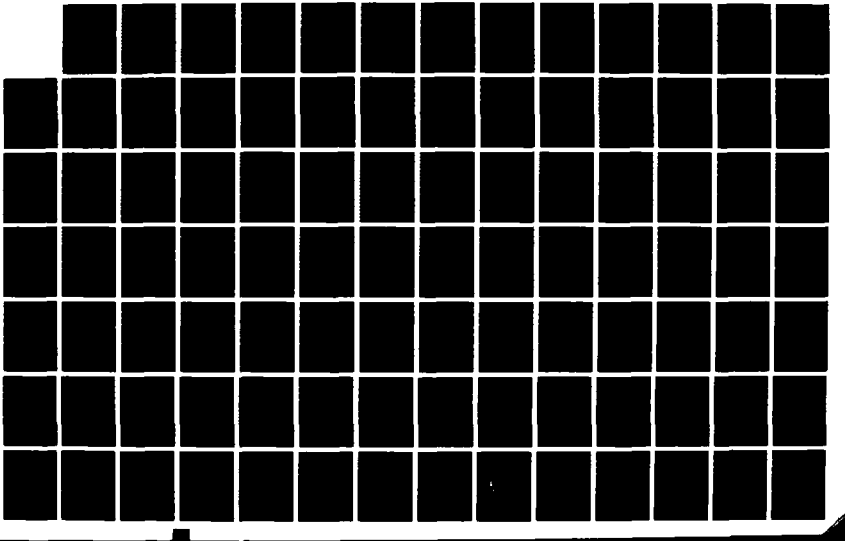

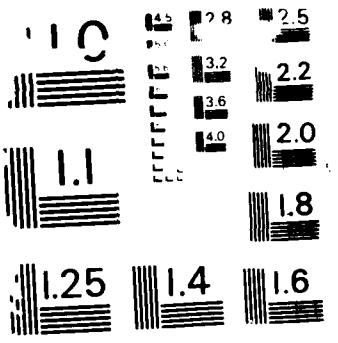

TEST CHART

HAC REF. F4767

(2)

DTIC FILE COPY

AFOSR-TR- 88-0012

AD-A191 926

NONLINEAR OPTICAL PROPERTIES AND SUBPICOSECOND DYNAMICS OF EXCITONS AND ELECTRON-HOLE PLASMAS IN MULTIPLE QUANTUM WELL STRUCTURES

T.F. Boggess, A.L. Smirl, R.A. McFarlane, and J.F. Lam

Hughes Research Laboratories
3011 Malibu Canyon Road
Malibu, California 90265

DECEMBER 1987

Final Report
Contract F49620-84-C-0083
July 1984 through October 1987

Approved for public release;
distribution unlimited.

AIR FORCE OFFICE OF SCIENTIFIC RESEARCH
Directorate of Electronic and Material Sciences AFOSR
Building 410
Bolling AFB, DC 20332-6448

88 2 21 098

UNCLASSIFIED
SECURITY CLASSIFICATION OF THIS PAGE

REPORT DOCUMENTATION PAGE

Form Approved
OMB No. 0704-0188

1a. REPORT SECURITY CLASSIFICATION: Unclassified	1b. RESTRICTIVE MARKINGS
2a. SECURITY CLASSIFICATION AUTHORITY	3. DISTRIBUTION/AVAILABILITY OF REPORT: Approved for public release, distribution unlimited
2b. DECLASSIFICATION/DOWNGRADING SCHEDULE	
4. PERFORMING ORGANIZATION REPORT NUMBER(S)	5. MONITORING ORGANIZATION REPORT NUMBER(S): AFOSR-TR- 88-0012
6a. NAME OF PERFORMING ORGANIZATION: Hughes Research Laboratories; 6b. OFFICE SYMBOL (If applicable)	7a. NAME OF MONITORING ORGANIZATION: Same as 8a
6c. ADDRESS (City, State, and ZIP Code): 3011 Malibu Canyon Road, Malibu, CA 90265	7b. ADDRESS (City, State, and ZIP Code): Same as 8b
8a. NAME OF FUNDING/SPONSORING ORGANIZATION: Air Force Office of Scientific Research; 8b. OFFICE SYMBOL (If applicable): NE	9. PROCUREMENT INSTRUMENT IDENTIFICATION NUMBER: F49620-84-C-0083
8c. ADDRESS (City, State, and ZIP Code): Building 410, Bolling AFB, DC 20332-6448	10. SOURCE OF FUNDING NUMBERS: PROGRAM ELEMENT NO. 61102F; PROJECT NO. 2305; TASK NO. B4; WORK UNIT ACCESSION NO.

11. TITLE (Include Security Classification)
Nonlinear Optical Properties and Subpicosecond Dynamics of Excitons and Electron-Hole Plasmas in Multiple Quantum Well Structures

12. PERSONAL AUTHOR(S)
T.F. Boggess, A.L. Smirl, R.A. McFarlane, and J.F. Lam

13a. TYPE OF REPORT	13b. TIME COVERED	14. DATE OF REPORT (Year, Month, Day)	15. PAGE COUNT
Final	FROM July 84' TO Oct 87'	1987, December, 14	219

16. SUPPLEMENTARY NOTATION
This manuscript is submitted for publication with the understanding that the United States Government is authorized to reproduce and distribute reprints for governmental purposes.

17. COSATI CODES		
FIELD	GROUP	SUB-GROUP

18. SUBJECT TERMS (Continue on reverse if necessary and identify by block number)
Nonlinear optics; ultrafast phenomena; multiple quantum wells; band-gap renormalization; alloy disorder; optical bistability.

19. ABSTRACT (Continue on reverse if necessary and identify by block number)

Here, we provide a final report describing our progress in measuring and modeling the nonlinear optical properties of and picosecond carrier dynamics in bulk ternary alloys and multiple quantum wells (MQWs). Studies of the bulk alloy $Al_xGa_{1-x}As$ have produced the first experimental isolation of the electron exchange energy in a dense electron-hole plasma, and the observation of enhanced band-gap renormalization as a consequence of alloy disorder, stimulated emission from the indirect gap for x-values as large as 0.52, and large optical nonlinearities from band filling, band-gap renormalization, and screening of the excitonic continuum states. The latter appear promising for room-temperature absorptive and dispersive optical bistability. An exact theory of the influence of an intense radiation field on the excitonic energy levels of a MQW has been developed and has led to the prediction of two-wave mixing gain.

20. DISTRIBUTION/AVAILABILITY OF ABSTRACT	21. ABSTRACT SECURITY CLASSIFICATION
☐ UNCLASSIFIED/UNLIMITED ☒ SAME AS RPT ☐ DTIC USERS	Unclassified
22a. NAME OF RESPONSIBLE INDIVIDUAL: Lt. Col. Robert Carter, Jr.	22b. TELEPHONE (Include Area Code): (202) 767-4931; 22c. OFFICE SYMBOL: NE

DD Form 1473, JUN 86 — Previous editions are obsolete.

SECURITY CLASSIFICATION OF THIS PAGE
UNCLASSIFIED

TABLE OF CONTENTS

SECTION		PAGE
1	INTRODUCTION	1
2	TASK 1: TIME-RESOLVED PHOTOLUMINESCENCE AND TRANSIENT-ABSORPTION SPECTROSCOPY OF MBE-GROWN TERNARY ALLOYS	3
3	TASK 2: TIME-RESOLVED PHOTOLUMINESCENCE AND TRANSIENT-ABSORPTION SPECTROSCOPY OF MULTIPLE QUANTUM WELLS	7
4	TASK 3: THEORY OF DRESSED EXCITONS IN MULTIPLE QUANTUM WELLS	9
5	TASK 4: ABSORPTIVE BISTABILITY	11
6	PUBLICATIONS AND PRESENTATIONS	15

APPENDICES

A	Time-Resolved Photoluminescence Measurements in $Al_xGa_{1-x}As$ Under Intense Picosecond Excitation	17
B	Picosecond Investigations of High-Density Carrier Dynamics in Alloy Semiconductors	21
C	Nonlinear Optical Properties of the Electron-Hole Plasma in $Al_{0.52}Ga_{0.48}As$	35
D	Renormalization of Direct and Indirect Band Gaps in Highly Excited $Al_xGa_{1-x}As$	41
E	Picosecond Observation of the Photorefractive Effect in GaAs	53
F	Picosecond Photorefractive Beam Coupling in GaAs	59
G	Picosecond Photorefractive Effect in $BaTiO_3$	63
H	Theory of Transient Energy Transfer in Gallium Arsenide	67
I	Picosecond Photorefractive and Free-Carrier Transient Energy Transfer in GaAs at 1 μm	101

TABLE OF CONTENTS (Continued)

SECTION		PAGE
J	A Hybridly Mode-Locked CW Laser with Brewster Prisms	155
K	Generation of 55-fs Pulses and Variable Spectral Windowing in a Linear-Cavity Synchronously Pumped CW Dye Laser	161
L	Variable Intracavity Spectral Windowing in a Synchronously Pumped Femtosecond CW Dye Lase	165
M	Tunable Near-Infrared Picosecond Pulses from a Short-Cavity Dye Laser	169
N	Femtosecond Pulse Generation in the Red/Deep Red Spectral Region	177
O	Femtosecond Synchronously Pumped Pyridine Dye Lasers	183
P	Picosecond and Femtosecond Pulse Generation near 1000 nm from a Frequency-Doubled Nd:YAG-Pumped CW Dye Laser	187
Q	Cavity Length Detuning Effects and Stabilization of a Synchronously-Pumped Femtosecond Linear Dye Laser	191
R	Photoreflectance of GaAs Doping Superlattices	205
S	Observation of Symmetry Forbidden Transitions in the Room Temperature Photoreflectance Spectrum of a GaAs/GaAlAs Multiple Quantum Well	211

SECTION 1

INTRODUCTION

This document is the Final Report on the AFOSR contract entitled "Nonlinear Optical Properties and Subpicosecond Dynamics of Excitons and Electron-Hole Plasmas in Multiple Quantum Well Structures. In August of 1986, this program was descoped to consist of the following four tasks: Task 1 - Time-Resolved Photoluminescence and Transient-Absorption Spectroscopy of MBE-Grown Ternary Alloys; Task 2 - Time-Resolved Photoluminescence and Transient-Absorption Spectroscopy of Multiple Quantum Wells; Task 3 - Theory of Dressed Excitons in Multiple Quantum Wells; and Task 4 - Absorptive Bistability. Progress on the program prior to descoping was reported in the August 1986 Annual Report. We briefly report progress on the descoped program in the sections to follow. More detail may be found in Appendices A-D, which consist of reprints of publications (published, accepted, or submitted). Under the descoped work statement, Hughes Research Laboratories (HRL) has also agreed to provide AFOSR with unrestricted access to results on research performed on related HRL IR&D projects. These include studies of (1) Ultrafast Photorefractive Effects; (2) Ultrafast Laser Development; (3) Photoreflective Characterization of MBE-Grown Structures; and (4) Calculation of Bandgap Renormalization in MQW. Progress in these areas has been discussed in the Bimonthly Reports, and relevant reprints are included here in the Appendices.

This report consists of six sections and 19 Appendices. In Sections 2-5, we describe Tasks 1-4, respectively, of the descoped program and briefly summarize progress on each. In Section 6, we list the publications and presentations associated with the descoped program. Appendices A-D consist of reprints of publications that have resulted from research supported by AFOSR. Three additional manuscripts are in preparation and copies will be supplied to AFOSR upon completion. Appendices E-S contain reprints of publications that have resulted from work performed under related HRL IR&D projects.

SECTION 2

TASK 1: TIME-RESOLVED PHOTOLUMINESCENCE AND TRANSIENT-ABSORPTION SPECTROSCOPY OF MBE-GROWN TERNARY ALLOYS

The goal of this task is to use picosecond time-resolved photoluminescence and picosecond transient absorption spectroscopy to investigate bandgap narrowing, alloy scattering, nonlinear diffusion, and bulk and surface recombination in MBE-grown heterostructures. The specific materials system chosen for these studies was $Al_xGa_{1-x}As$ grown by MBE. This technologically important material is both electronically and optically well-characterized, and high-quality samples are available in-house at HRL. $Al_xGa_{1-x}As$ also has an interesting band structure. It is a direct-gap semiconductor for $x<0.43$ and an indirect-gap semiconductor for $x>0.43$. For x-values near the direct-to-indirect-gap crossover composition ($x=0.43$), intense optical excitation produces an electronic distribution that occupies multiple conduction band valleys. This effect has been demonstrated to produce novel features in the luminescence spectra and interesting optical nonlinearities in the near-band-edge absorption spectra.

Materials with x-values ranging from 0.23 to 0.54 have been studied. We find that materials that are clearly direct-gap exhibit luminescence features typical of direct gap semiconductors. That is, we observe a single luminescence peak with a spectral width characterized by the carrier number density, a high-energy tail characterized by the carrier temperature, and a low-energy edge characterized by the renormalized band gap. We find that the carrier temperature has cooled to that of the lattice essentially immediately after the passage of the excitation pulse. The measured value of the renormalized band gap is found to be in excellent agreement with that predicted by the universal formula of Vashishta and Kalia. Materials with alloy compositions near x_c exhibit dramatically

different spectra consisting of multiple peaks, one arising from direct transitions from the Γ band, one arising from transitions from the indirect X bands, and in the case of indirect-gap materials, one arising from a phonon side band. The observation of strong luminescence peaks from the X bands is a result of alloy disorder, which perturbs the crystal symmetry and relaxes k-conservation allowing zero-phonon or quasi-direct transitions from the side valleys. The observation of multiple peaks in the spectra has allowed us to independently measure the renormalization of both direct and indirect gaps in a given semiconductor. We find that the renormalization of the fundamental (indirect) gap in materials with $x>0.43$ is also in excellent agreement with the theory of Vashishta and Kalia, but the fundamental (direct) gap in samples with x near to but less than 0.43 experiences considerably more renormalization than predicted. This is a consequence of alloy disorder, which mixes the heavy side valleys with the light Γ valley, evidently modifying the density of states of the latter. Analysis of the renormalization of the higher lying Γ valley in the indirect-gap materials indicates that electron exchange does not contribute. This is reasonable since the population of this valley is very low. All other effects associated with Coulomb interactions and hole exchange are expected to contribute in full, as observed.

We have also observed stimulated emission in indirect-gap $Al_xGa_{1-x}As$ with x-values as high as 0.52. This, again, is a consequence of alloy disorder, which greatly increases the transition rate out of the indirect valleys. Simultaneous stimulated emission from both direct and indirect valleys has been observed in a sample with an x-value of 0.45.

Finally, we have observed strong, optically-induced, changes in the near-band-edge absorption spectrum of an $x=0.52$ sample at a temperature of 15K. These measurements were performed by illuminating the sample with an intense picosecond pulse at 532 nm (well above the direct gap) and observing the absorption

spectrum at various time delays later using a picosecond continuum pulse. Three features were observed: (1) strong bleaching above the unexcited absorption edge as a result of band filling in the valence band; (2) induced absorption below the unexcited absorption edge as a consequence of band-gap renormalization; and (3) a shift of the Fabry-Perot fringes resulting from the strong index changes associated with the modifications to the absorption spectrum. An index change of 0.1 was extracted from the fringe shift.

The above results are described in greater detail in Appendices A-D. Further details will be supplied in two manuscripts that are currently in preparation.

SECTION 3

TASK 2: TIME-RESOLVED PHOTOLUMINESCENCE AND TRANSIENT-ABSORPTION SPECTROSCOPY OF MULTIPLE QUANTUM WELLS

The purpose of this task is to extend the studies of Task 1 to MQW structures and to contrast the results with those from the bulk ternary heterostructures. This task was to be performed only if time permitted. We have demonstrated picosecond saturation of the excitonic resonances in an MQW supplied by an outside vendor, and we are now currently routinely growing high-quality MQW material and have developed and demonstrated etching procedures for substrate removal in-house at HRL. We routinely characterize the MQWs using photoreflectance facilities developed under HRL IR&D. Also, since we can remove the thick GaAs substrate, room-temperature linear transmission measurements are routinely performed. In addition to high-quality MQWs, we now have access to materials that exhibit 3-dimensional confinement, i.e., quantum dots. These are fabricated at HRL using focused ion beam technology. The spectroscopy of these structures should be extremely fruitful. We are now clearly in a position to complete this task, and it will be continued under HRL IR&D support.

SECTION 4

TASK 3: THEORY OF DRESSED EXCITONS IN MULTIPLE QUANTUM WELLS

The purpose of this task is to perform calculations of the nonlinear optical response of the exciton in multiple quantum wells when the laser is tuned below the spectral linewidth of the exciton. An exact theory of the influence on a MQW exciton of a radiation field of arbitrary intensity was constructed. We find that each unperturbed excitonic energy level is split into two symmetrically displaced dressed-exciton energies. The separation between the dressed states is given by the generalized Rabi flopping frequency. The dressed-exciton states are given as a linear coherent superposition of the basis (unperturbed) states. The solutions are valid for all intensity regimes provided that the laser detuning from resonance is outside the exciton spectral linewidth. The emission process of the dressed-exciton showed gain in the absence of a real population inversion for radiation down shifted from the pump by the generalized Rabi flopping frequency. This has led to the prediction of broad-band self-pumped phase conjugation in MQW. Further details of this work will be provided in a paper that is in preparation.

SECTION 5

TASK 4: ABSORPTIVE BISTABILITY

The objective of this task is to investigate absorptive bistability in $Al_xGa_{1-x}As$ using band-gap renormalization in an indirect-gap alloy as the mechanism. For excitation just below the direct absorption edge, electron-hole pairs are generated by direct absorption through band tail states, by two-photon absorption, and by indirect absorption (either phonon assisted or zero-phonon quasi-direct) with electrons being promoted into the X and L valleys. Any electrons generated into the direct Γ band immediately relax by phonon emission into the energetically lower lying X valleys. As more and more electrons populate these side valleys, the indirect gap renormalizes through exchange and correlation effects. More importantly, however, a test charge placed in the Γ conduction band "sees" a renormalized direct gap due to Coulomb correlation and hole exchange effects (the electron exchange will not be present). Thus, the direct gap will be moved closer to resonance with the exciting radiation. We performed measurements to determine whether this effect would lead to an increasing absorption and, potentially, intrinsic optical bistability. This could, in principle, provide a bistable material for wavelengths from 410 to 620 nm by choosing indirect-gap AlGaAs with appropriate x values.

For these studies we excited an indirect-gap $Al_xGa_{1-x}As$ sample (x=0.52) at T=15K with 10-ps, 588-nm pulses from a tunable short cavity dye laser (SCDL). Under these conditions, the excitation occurs at roughly 9 meV below the direct absorption edge, which at this temperature is dominated by a broad excitonic absorption. We then probed the absorption spectrum at various time delays later using a broad-band picosecond continuum pulse generated by tightly focusing a part of the pump into a water cell. We find that at an excitation level of 7 mJ/cm^2 a weak but clearly observable induced absorption occurs below the unexcited

absorption edge, extending into the region of the pump. These results are illustrated in Figure 1. Also notice that bleaching of the absorption occurs above the unexcited absorption edge. This induced bleaching is clearly partially responsible for the weakness of the induced absorption. That is, under the conditions described, the optically-coupled states are located very near the Brillouin zone center. As such, band filling in the valence band can easily saturate the near-band-edge absorption even though the Γ band is never filled. In fact, this effect is so severe that the induced absorption illustrated in Figure 1 could not be achieved if the direct gap did not shrink to below the excitation energy during the excitation pulse. Despite this significant band-gap renormalization, the competition between band filling induced bleaching and induced absorption caused by band-gap renormalization reduces the potential for intrinsic absorptive bistability in these materials.

The situation is much more favorable, however, for optical excitation slightly above the direct absorption edge. Under these conditions we take advantage of the large number of electrons that we can generate into the side valleys (via the direct valley) and the concomitant band filling that results from an equal number of holes in the valence band. Results of this type of measurement are shown in Figure 2. Here, the SCDL is tuned to 596 nm and excitation spectra are shown for delays of 0 and 150 ps at fluences of 16 and 18 mJ/cm^2, respectively. Clearly, a very strong bleaching of the absorption is observed at the excitation wavelength even during the excitation pulse, i.e., zero delay. We also observe a strong shift of the Fabry-Perot fringes indicating large index changes. An important point to emphasize is that these measurements were conducted at room temperature. These results indicate a clear potential for the use of $Al_xGa_{1-x}As$ in room temperature, dispersive or absorptive, optically bistable devices.

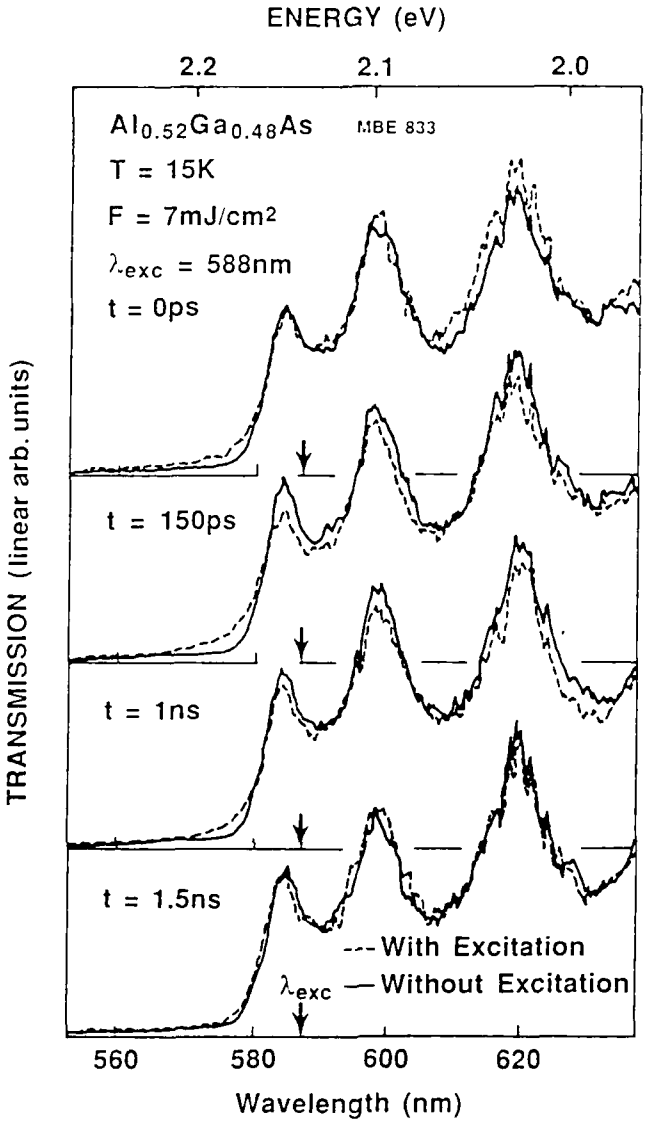

Figure 1. Time-Resolved Transmission Spectra for $Al_{0.52}Ga_{0.48}As$ with picosecond excitation slightly below the direct absorption edge.

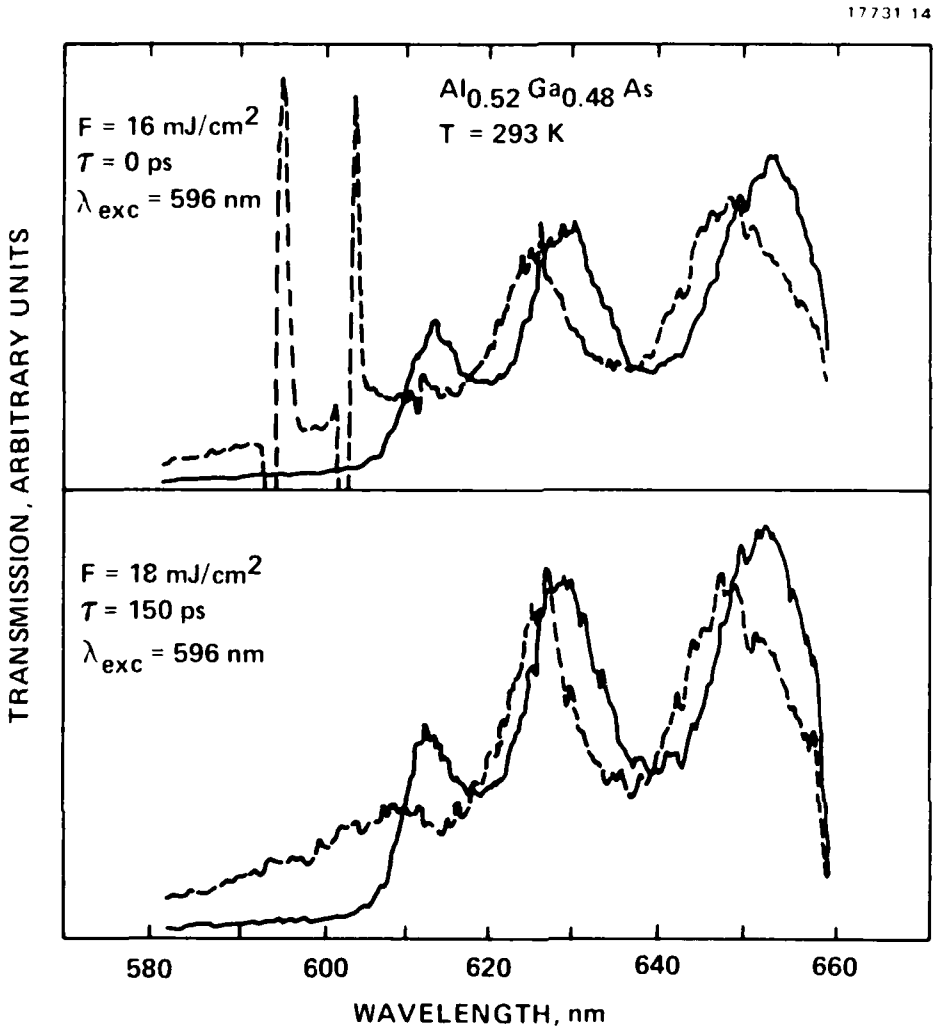

Figure 2. Time-Resolved Transmission Spectra of $Al_{0.52}Ga_{0.48}As$ with picosecond excitation slightly above the direct absorption edge.

SECTION 6

PUBLICATIONS AND PRESENTATIONS

1. K. Bohnert, H. Kalt, D.P. Norwood, T.F. Boggess, A.L. Smirl, R.Y. Loo, "Time-resolved photoluminescence measurements in $Al_xGa_{1-x}As$ under intense picosecond excitation," in **Ultrafast Phenomena V**, G.R. Fleming and A.E. Siegman, Eds. (Springer-Verlag, 1986) p 207.

2. J.F. Lam, R.C. Lind, R.A. McFarlane, S.C. Rand, A.L. Smirl, "Self-pumped phase conjugation in resonant systems," XIV International Quantum Electronics Conference, San Francisco, CA, June, 1986.

3. K. Bohnert, H. Kalt, Thomas F. Boggess, Arthur L. Smirl, R.Y. Loo, "Dynamics of Hot Carrier Relaxation, Carrier Recombination, and Band Gap Renormalization in the Ternary Semiconductor $Al_xGa_{1-x}As$," presented at the XIV International Quantum Electronics Conference, San Francisco, CA, June, 1986.

4. K. Bohnert, H. Kalt, Thomas F. Boggess, Arthur L. Smirl, R.Y. Loo, "Time Resolved Photoluminescence Measurements in $Al_xGa_{1-x}As$ Under Intense Picosecond Excitation," presented at the Fifth Topical Meeting on Ultrafast Phenomena, Snowmass Village, CO, June, 1986.

5. INVITED; T.F. Boggess, H. Kalt, K. Bohnert, D.P. Norwood, A.L. Smirl, I.J. D'Haenens, "Picosecond investigations of high-density carrier dynamics in alloy semiconductors," Proc. of SPIE Ultrafast Lasers Probe Phenomena in Bulk and Microstructure Semiconductors, **793**, p. 37, 1987.

6. H. Kalt, K. Bohnert, D.P. Norwood, T.F. Boggess, A.L. Smirl, I.J. D'Haenens, "Nonlinear optical properties of the electron-hole plasma in $Al_{0.52}Ga_{0.48}As$," J. Appl. Phys., 62, p. 4187, 1987.

7. K. Bohnert, H. Kalt, T.F. Boggess, D.P. Norwood, A.L. Smirl,I.J. D'Haenens, "Renormalization of direct and indirect band gaps in highly excited $Al_xGa_{1-x}As$," to be published Phys. Rev. Lett. 1988.

8. INVITED; T.F. Boggess, K. Bohnert, H. Kalt, D.P. Norwood, A.L. Smirl, I.J. D'Haenens, "Picosecond investigations of high-density carrier dynamics in alloy semiconductors," presented at the SPIE Symposium on Advances in Semiconductors and Semiconductor Structures, Bay Point, FL, March 1987.

9. K. Bohnert, H. Kalt, D.P. Norwood, T.F. Boggess, A.L. Smirl, "Nonlinear optical properties of the electron-hole plasma in $Al_{0.52}Ga_{0.48}As$," presented at the American Physical Society Meeting, New York City, NY, March 1987.

10. H. Kalt, K. Bohnert, D.P. Norwood, T.F. Boggess, A.L. Smirl, "Band-gap renormalization in $Al_xGa_{1-x}As$," presented at the American Physical Society Meeting, New York City, NY, March 1987.

11. K. Bohnert, H. Kalt, D.P. Norwood, T.F. Boggess, A.L. Smirl, "Band-gap renormalization in $Al_xGa_{1-x}As$ after strong picosecond excitation," presented at the German Physical Society Meeting, Munster, West Germany, March 1987.

12. H. Kalt, K. Bohnert, D.P. Norwood, T.F. Boggess, A.L. Smirl, I.J. D'Haenens, "Investigation of band-gap renormalization in $Al_xGa_{1-x}As$ using picosecond time-resolved photoluminescence," presented at the XVth International Quantum Electronics Conference, Baltimore, MD, April 1987.

13. H. Kalt, D.P. Norwood, T.F. Boggess, A.L. Smirl, "Stimulated emission in indirect $Al_xGa_{1-x}As$," presented at the 1987 Annual Meeting of the Optical Society of America, Rochester, NY, October 1987.

14. J.F. Lam, "Theory of the dynamic Stark effect in semiconductor multiple quantum wells," to be submitted to Phys. Rev. B 1987.

15. H. Kalt, A.L. Smirl, T.F. Boggess, "Stimulated emission in indirect-gap $Al_xGa_{1-x}As$," to be submitted to J. Appl. Phys. 1987.

16. H. Kalt, K. Bohnert, D.P. Norwood, A.L. Smirl, T.F. Boggess, "Optical nonlinearities in highly excited, indirect $Al_xGa_{1-x}As$," to be presented at the Spring Meeting of the German Physical Society, March 14-18, 1988, Karlsruhe, Germany.

17. H. Kalt, A.L. Smirl, T.F. Boggess, "Stimulated emission in the indirect semiconductor $Al_xGa_{1-x}As$ ($x > 0.43$)," to be presented at the Spring Meeting of the German Physical Society, March 14-18, 1988, Karlsruhe, Germany.

Appendix A: Time-Resolved Photoluminescence Measurements in $Al_xGa_{1-x}As$ Under Intense Picosecond Excitation.

A reprint of a paper published in Ultrafast Phenomena V, G.R. Fleming and A.E. Siegman, Eds. (Springer-Verlag, New York, 1986) pp 207-209.

ULTRAFAST PHENOMENA V, (SPRINGER-VERLAG, NY, 1986)

Time-Resolved Photoluminescence Measurements in $Al_xGa_{1-x}As$ Under Intense Picosecond Excitation

K. Bohnert[1], *H. Kalt*[1], *D.P. Norwood*[1], *T.F. Boggess*[1], *A.L. Smirl*[2], *and R.Y. Loo*[2]

[1]Center for Applied Quantum Electronics, Department of Physics, North Texas State University, Denton, TX 76203, USA
[2]Hughes Research Laboratories, 3011 Malibu Canyon Road, Malibu, CA 90265, USA

The ternary semiconductor alloy $Al_xGa_{1-x}As$ exhibits a direct-indirect gap crossover with increasing aluminum concentration x at x_c=0.435 [1]. By varying the alloy composition, the relative energy separation between direct and indirect gaps in the vicinity of the crossover composition can be varied, and the distribution of photo-excited electrons among direct and indirect conduction band valleys can be externally controlled. In the following, we report preliminary results that illustrate the influence of the variation of the band structure with composition on the nature and dynamics of radiative carrier recombination following intense picosecond excitation. We further analyzed the photoluminescence with respect to bandgap renormalization which influences the spectral position of the emission bands. For appropriate energy separations between direct and indirect gaps (at compositions near x_c), the number of photo-excited electrons in the energetically higher lying conduction band valley(s) can be arranged to be significantly smaller than in the lower valley(s). The electron exchange contribution to the renormalization of the larger gap then is strongly reduced, whereas the lower gap is renormalized by full exchange and correlation effects. This, in principle, allows one to experimentally separate correlation and exchange contributions to band gap renormalization.

The investigated $Al_xGa_{1-x}As$ layers were grown on GaAs substrates by liquid phase or molecular beam epitaxy. Their thicknesses ranged between 2 and 10 μm. The samples were mounted in a closed-cycle refrigerator for temperature-dependent measurements. The excitation source was a frequency doubled, actively/passively mode-locked Nd:YAG laser, providing single pulses with a temporal width of 32 ps (FWHM) at 532 nm. The photoluminescence from the center of the 700 μm (FWHM) excitation spot was dispersed in a 0.25 m spectrometer and time-resolved with a highly sensitive streak camera. The temporal resolution was determined by the width of the selected time window (typically between 30 and 70 ps).

Initially, an alloy composition well within the direct gap regime (x=0.23) was investigated where a significant interference by indirect band extrema was excluded. Plasma luminescence typical for a direct-gap semiconductor was observed. The temporal evolution of the spectrally-resolved emission was measured on a picosecond time scale, and carrier density and temperature were extracted as a function of time. The temporal evolution of the carrier temperature in room temperature $Al_{0.23}Ga_{0.77}As$ is shown in Fig. 1a. The exciting fluence was 2 mJ/cm^2. The initial excess energy of the photo-excited electron-hole pairs was 630 meV. The temperature during the pulse maximum (t=0 ps) is around 450 K. This

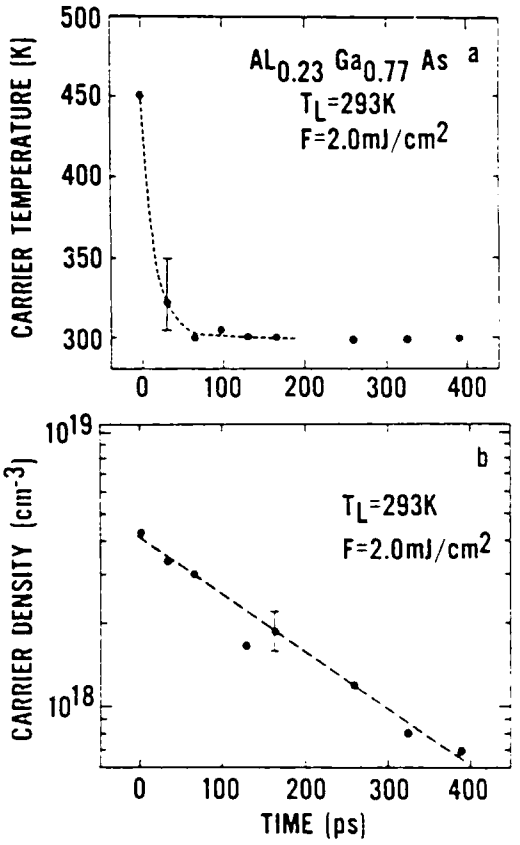

Figure 1. Temperature (a) and density (b) of the photoexcited carriers for room temperature $Al_{0.23}Ga_{0.77}As$ as a function of time

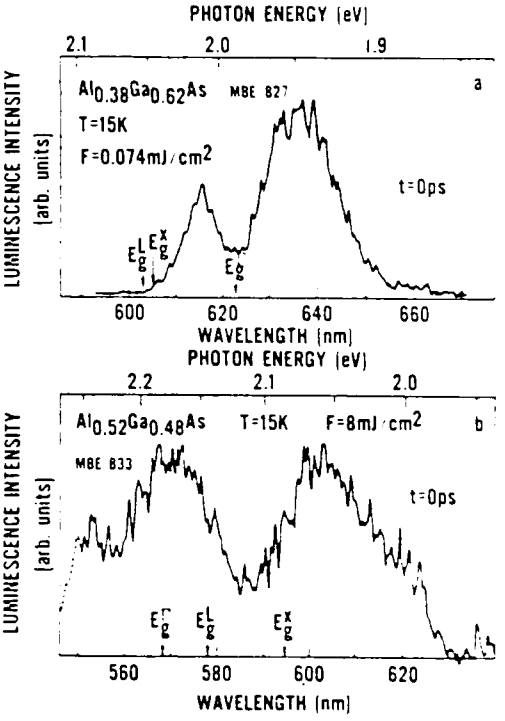

Figure 2. Low temperature photoluminescence spectra at t=0 ps for $Al_{0.38}Ga_{0.62}As$ (a) and $Al_{0.52}Ga_{0.48}As$ (b)

indicates that the carriers lost most of their initial excess energy on a time scale short compared to the pulsewidth. The carrier temperature reaches lattice temperature essentially as soon as excitation ends. On time scales given by our temporal resolution, no definite evidence for a reduced carrier cooling rate due to screening of the carrier-phonon interaction [2] and/or the build-up of a nonequilibrium phonon distribution [3] at high densities of photo-excited carriers was found. The carrier density (Fig. 1b) shows essentially an exponential decay with a time constant of ~200 ps.

Figure 2a shows a low temperature photoluminescence spectrum for $Al_{0.38}Ga_{0.62}As$ at t=0 ps. For this alloy composition the direct conduction band valley is only approximately 60 meV below the indirect X-valleys. The nonrenormalized gaps are indicated by arrows. The low and high energy peaks in this spectrum are attributed to recombination from direct and indirect valleys, respectively. The decay times for the direct and indirect emission bands are 105 ps and 60 ps, respectively. Emission from indirect valleys for alloy compositions near the direct-indirect crossover occurs predominantly without participation of phonons due to an electron scattering by random potential fluctuations [4]. The relative intensity of the indirect emission band indicates a high efficiency for this recom-

bination channel. The shorter decay time for the indirect emission is consistent with electron transitions from the indirect valleys to the lower Γ-valley which help to adjust an intervalley equilibrium distribution for the photo-excited electrons.

Figure 2b shows a luminescence spectrum at t=0 ps for x=0.52. For this composition, the lowest conduction band edge occurs at the X-point. It is separated from the direct Γ-minimum by approximately 100 meV. The non-renormalized band gaps are indicated by arrows. Again two distinct emission bands are observed. The direct emission (high energy band) is observed only during excitation, i.e., during the relaxation of the photo-excited electrons to the bottom of the bands. The decay time for the indirect emission now is increased to 640 ps. This is consistent with a decreasing probability for no-phonon transitions with increasing direct-indirect gap separation in the indirect gap regime [5].

An examination of band gap renormalization shows an enhanced renormalization of the Γ-gap for compositions below but close to x_c. This is explained by an increase of the effective electron mass due to multivalley effects [6]. The renormalization of gaps above the lowest gap appears to be reduced due to a reduced exchange contribution.

In conclusion, for alloy compositions near the direct-indirect gap crossover, emission from direct and indirect conduction band valleys is observed simultaneously. The relative intensity of the indirect (no-phonon) emission band indicates a high radiative recombination rate due to random potential fluctuations. Bandgap renormalization near x_c is influenced by disorder effects and by the distribution of the photo-excited electrons among several conduction band valleys.

References

1. R. Dingle, R. A. Logan, and J. R. Arthur: In GaAs and Related Compounds, ed. by C. Hilsum (Institute of Physics, London, 1977), p. 210
2. M. J. Zarrabi and R. R. Alfano: Phys. Rev. B 32, 3947 (1985)
3. H. M. van Driel: Phys. Rev. B 19, 5928 (1979)
4. E. Conen, M. D. Sturge, M. A. Olmstead, and R. A. Logan: Phys. Rev. B 22, 771 (1980)
5. A. W. Pikhtin: Fiz. Tekh. Polyprovodn. 11, 425 (1977) [Sov. Phys. Semicond. 11, 245 (1977)]
6. P. J. Pearah, W. T. Masselink, J. Klem, T. Henderson, H. Morkoc, C. W. Litton, D. C. Reynolds: Phys. Rev. B 32, 3857 (1985)

Appendix B: Picosecond Investigations of High-Density Carrier Dynamics in Alloy Semiconductors.

A reprint of a paper published in SPIE, 793, 37 (1987).

Reprinted from SPIE Vol. 793—Ultrafast Lasers Probe Phenomena in Bulk and Microstructure Semiconductors

Invited Paper

Picosecond investigations of high-density carrier dynamics in alloy semiconductors

Thomas F. Boggess, H. Kalt, K. Bohnert, D. P. Norwood, and Arthur L. Smirl*

Department of Physics, Center for Applied Quantum Electronics
North Texas State University, Denton, TX 76203

and

Irnee D'Haenens

Hughes Research Laboratories, 3011 Malibu Canyon Road
M/S RL65, Malibu, CA 90265

Abstract

We examine the influence of dense electron-hole plasmas on the optical properties of $Al_xGa_{1-x}As$ for a variety of x-values using transient transmission spectroscopy and time-resolved photoluminescence. The measurements provide evidence for band-filling, nonlinear refraction, induced absorption, alloy disorder, and band-gap renormalization. The band gap renormalization is compared to existing theory, and good agreement is obtained by considering the influence of alloy disorder and the separate contributions of exchange and correlation.

Introduction

The continuing widespread use of the ternary semiconductor alloy $Al_xGa_{1-x}As$ in the electronics and electro-optics industry has resulted in the extensive investigation of the electrical and optical properties of this material. By varying the aluminum concentration, x, of this solid solution, the band gap can be adjusted[1] while maintaining a good lattice match to GaAs. This makes $Al_xGa_{1-x}As$ an ideal material for use in, e.g., double-heterostructure lasers and multiple quantum well structures. The alloy composition further determines the nature of the band gap, materials with $x<x_c\simeq0.43$ being direct gap and those with $x>x_c$ being indirect gap semiconductors.

Intense optical excitation of materials with x-values near x_c results in the creation of a dense electron-hole plasma (EHP) with the electrons distributed among both direct and indirect minima. Many-body effects[2] create a narrowing of both direct and indirect gaps, although the magnitude of the renormalization of each gap is influenced by the distribution of electrons among the various conduction band minima. In addition, alloy disorder[3] leads to an admixture of the heavy side valleys with the lighter central valley, an effect that leads to an enhanced direct exciton binding energy[4] and also, evidently, strongly influences the renormalization for x-values near x_c. This disorder also relaxes k-conservation, allowing no-phonon[5] transitions and even stimulated emission[5,6] from the indirect minima. Finally, the presence of such a dense EHP inevitably alters the states available for optical transitions through band filling and screening of the exciton continuum states.

Here, we discuss the influence of dense EHP on the optical properties of several epitaxial layers of $Al_xGa_{1-x}As$, one with a composition well into the direct-gap regime (x=0.23), one nominally direct-gap (x=0.38), and one nominally indirect-gap (x=0.52). The EHP in each sample was produced by intense optical excitation using 30 ps pulses at 532 nm provided by a frequency-doubled, actively-and-passively

*Presently on leave from Hughes Research Laboratories, Malibu, California.

modelocked Nd:YAG laser. The dynamics of the absorption spectra were studied by probing the excited region of the samples with a time-delayed picosecond continuum pulse.[7] The emission spectra were studied using a combination of a spectrometer, streak camera, and optical multichannel analyzer to achieve simultaneous spectral and temporal resolution. These measurements provide information regarding band filling, band-gap renormalization, and alloy scattering in these alloy semiconductors.

Samples

The x=0.23 sample was grown by liquid-phase epitaxy (LPE) on a GaAs substrate. The epi-layer thickness was a few microns. The x=0.38 and x=0.52 samples were grown by molecular beam epitaxy (MBE) in the following manner. First, a 1 μm layer of AlAs was grown on a semi-insulating GaAs substrate. A 2 μm layer of $Al_xGa_{1-x}As$ was then grown, and a 10 nm GaAs cap followed to prevent oxidation. The AlAs layer served as a potential barrier to prevent carrier diffusion from the region of interest ($Al_xGa_{1-x}As$) into the substrate. Furthermore, a portion of the x=0.52 sample was prepared for transmission measurements by selectively etching small (~1 mm^2) windows through the GaAs substrate. In this case the AlAs served as an etch-stop layer. For each sample, the quoted x-value was arrived at by determining the unperturbed band gap by using photoreflectance, low-excitation luminescence, reflection, and (for the x=0.52 sample) transmission measurements and then extracting the aluminum concentration from the work of Casey.[1] The samples were mounted in a closed-cycle He refrigerator that allowed us to vary the lattice temperature from 15-300 K, although most of the data reported here were taken at 15K.

Luminescence measurements

The radiative recombination from each sample was measured following excitation with intense picosecond pulses at 532 nm. The central 100 μm of the 800 μm excited region was imaged onto the entrance slit of the spectrometer where the radiation was spectrally dispersed. The luminescence was then imaged onto the entrance slit of the streak camera where it was temporally resolved. In this manner a complete record of the temporal development of the emission spectrum was obtained for each excitation, although for adequate signal-to-noise ratios several hundred shots were averaged. The data were corrected for the vidicon dark current and the spectral response and the linearity of the streak camera.

An example of the results of one such measurement for the x=0.23 direct-gap sample is shown in Fig. 1 for an excitation level of 2 mJ/cm^2, a time delay t=0 ps, and a lattice temperature of 293 K. The features of the luminescence are typical of a direct-gap semiconductor. The solid line in the figure represents a fit to the experimental data using a k-conserving model with essentially three fit parameters: the carrier density, carrier temperature, and the renormalized band gap. The fit focuses on the peak and the high energy tail, ignoring the low energy region where band tailing occurs. Our results indicate the presence of a thermalized distribution with an elevated temperature during the excitation pulse. Measurements at longer time delays indicate that the elevated temperature drops to approximately lattice temperature immediately (on a 30 ps time scale) after excitation, and the EHP recombines on a time scale of ~200 ps. This measurement also clearly shows a red shift of the band gap in the presence of the dense EHP. Stimulated emission is observed at excitation levels slightly above 2 mJ/cm^2.

In Fig. 2 we show the results of measurements at 15 K on the direct-gap x=0.38 MBE-grown sample. In this case, we observe two distinct peaks in the luminescence. The energetically lower peak we associate with recombination from the direct minimum, while we attribute the higher energy peak to recombination from the X-valleys. The L-band densities are too low to significantly influence the spectra. The decay of each peak is also shown; the direct recombination decays with a time constant of roughly 100 ps, and the indirect signal decays with a somewhat shorter lifetime of approximately 60 ps. The strength of the indirect gap signal is a direct result of alloy disorder, which allows no-phonon or

quasi-direct transitions from the indirect minima.[5] The short lifetime of the indirect signal is a consequence of the quasi-direct nature of the recombination and real transitions to the energetically lower lying direct minimum through LO phonon and alloy scattering. The data were fit in this case by assuming relaxed k-conservation for both the Γ and X-bands and neglecting phonon participation.[5] A single electron Fermi level and a single electron carrier temperature were used. Again, the analysis indicated elevated carrier temperatures in both bands only during excitation.

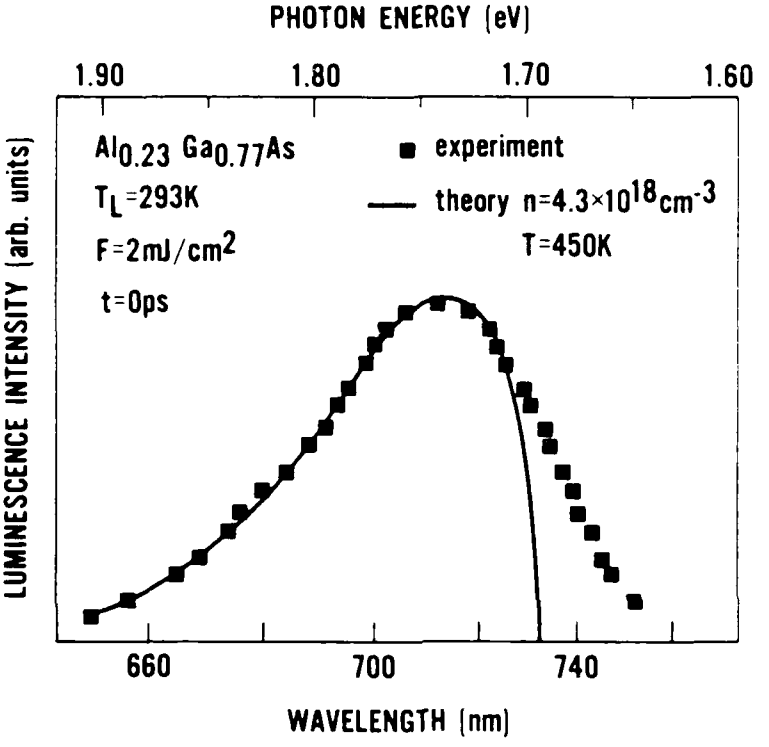

Figure 1. Measured luminescence profile and theoretical fit for the x = 0.23 sample.

An example of the results of measurements at 15 K on the x=0.52 sample is shown in Fig. 3. These data were obtained from the sample backed with a GaAs substrate. Again, we observe two distinct emission peaks, the energetically lower peak arising now from the X-band and the higher energy peak from the direct gap. Again, although the L-band electrons are included in our analysis, we find their density to be too low to significantly influence the observed spectra. The higher energy peak (direct gap) is now observed only during excitation, while the low energy peak (indirect gap) is present for more than a nanosecond. For this measurement, a sharp-cut color filter was used to block the 532 nm laser line. This accounts for the steep edge in the luminescence profile at approximately 550 nm. The feature centered near 2.25 eV is a remnant of the laser line. An additional shoulder is observed on the low energy side of the no-phonon indirect gap emission. We attribute this to a phonon side band. Recall that there was no observable phonon side band in the x=0.38 sample luminescence. The strength of the no-phonon line is dramatically reduced in the x=0.52 sample compared to the x=0.38 sample, and the relative strength of the phonon sideband is, therefore, enhanced. We attribute this reduced alloy mixing to the fact that the occupied states in the X-band are no longer resonant with real states in the Γ-band. The remaining features of these data are consistent with the following development of the EHP. Initially, electrons are deposited high in the central valley where they rapidly thermalize primarily by carrier-carrier scattering. These hot thermalized electrons rapidly scatter to the side valleys where they

cool and recombine by both phonon-assisted indirect transitions and no-phonon quasi-direct transitions. Of course, as long as carriers are present in the central valley (i.e., on these time scales, only while carriers are still being generated) there is some probability that they will recombine with holes in the valence band. This accounts for the Γ-band luminescence observed during the pulse.

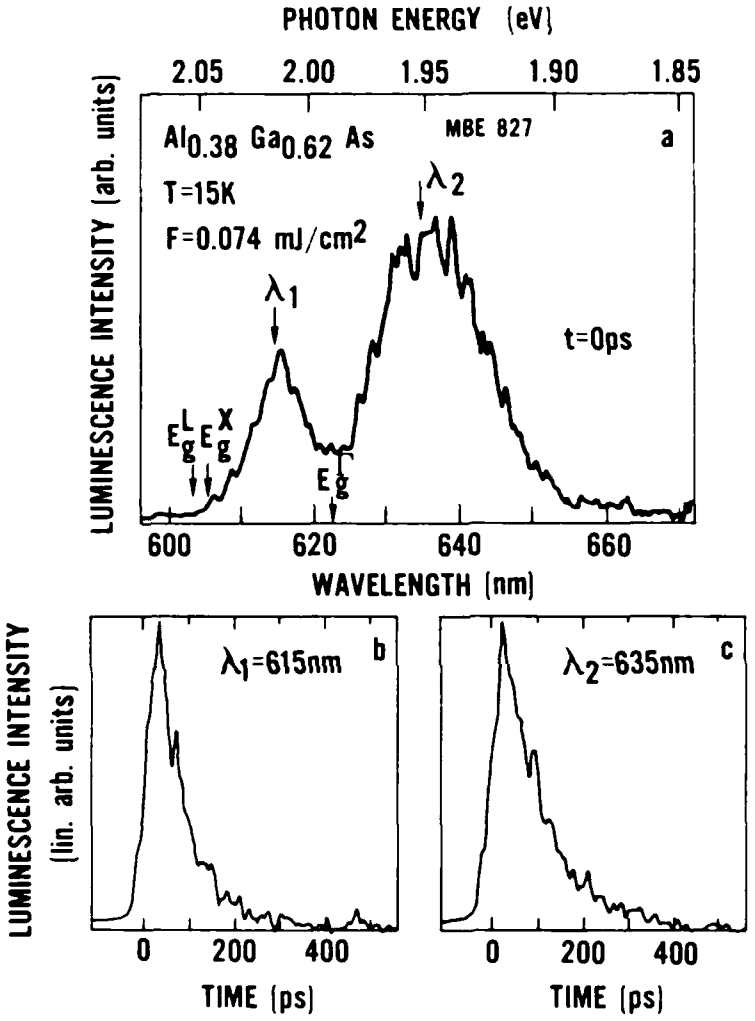

Figure 2. Time-resolved emission spectrum (a) and decay curves for the (b) indirect-and (c) direct-gap luminescence bands in $Al_{0.38}Ga_{0.62}As$.

Similar measurements on the semitransparent windows of the x=0.52 sample indicate that the strength of the no-phonon line relative to the phonon side band and Γ-band luminescence is considerably greater than in material overlying a GaAs substrate. This, together with the resonator-like structure formed by the etched window, produces stimulated emission from the indirect gap at high excitation levels.

A significant consequence of observing simultaneous Γ- and X-band emission in samples with $x \sim x_c$ is that analysis of the data provides independent determination of the renormalization of both the direct and indirect band gap in each sample. Our study of band-gap renormalization and the consequences of alloy disorder and the distribution of electrons among the various conduction band minima will be discussed in detail below.

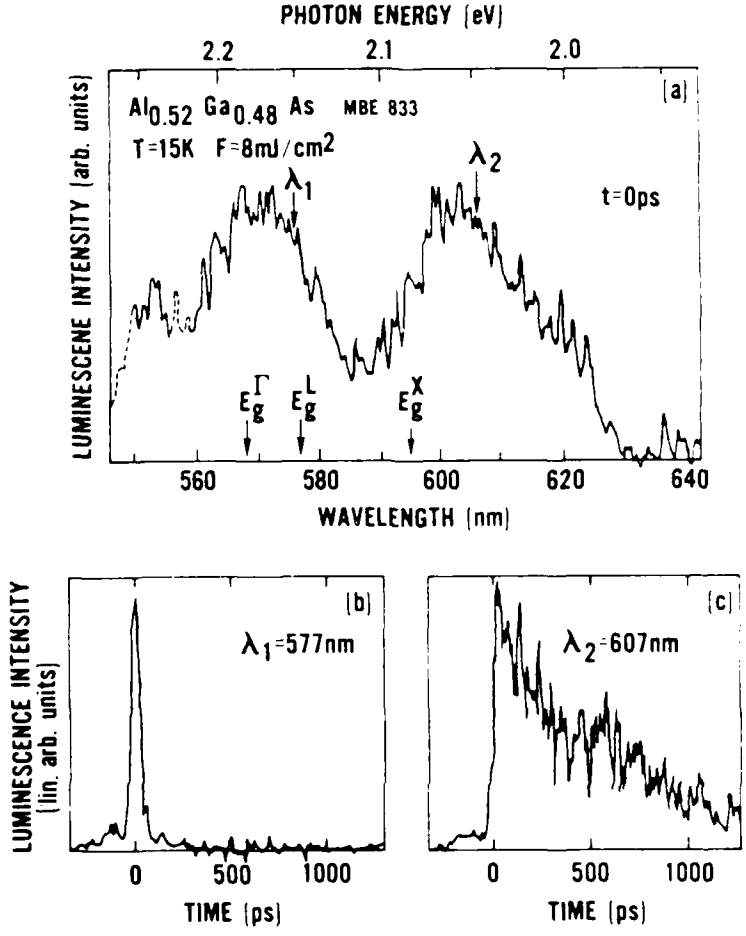

Figure 3. Time-resolved emission spectrum (a) and decay curves for the (b) direct and (c) indirect luminescence bands in $Al_{0.52}Ga_{0.48}As$.

Transmission measurements

The residual 1.06 μm pulse remaining after frequency doubling was amplified and tightly focused into a water cell to produce a very broad-band picosecond continuum pulse.[7] A variable delay was placed in this probe beam path to provide temporal resolution for these measurements. One portion of the probe was focused on the central region of the excited area of a semitransparent window on the x=0.52 sample. The transmitted probe was dispersed in a 0.25-m spectrometer, passed through a streak camera, and then detected on a vidicon. A small part of the continuum probe was time-delayed, directed around the sample, and then arranged to follow the same path as the transmitted probe. This reference pulse was then used to compensate for shot-to-shot fluctuations in the continuum. Although temporal resolution in this measurement was achieved by mechanically changing the probe path length, the streak camera provided excellent sensitivity and a convenient means for eliminating scattered pump light and for isolating the time-delayed reference beam. The transmission was measured as a function of time using various excitation fluences.

The results of one such measurement at 15 K are shown in Fig. 4 for excitation with a 532 nm, 30 ps, pulse with a fluence of 11 mJ/cm^2. The solid lines in the figure indicate the transmission of the unexcited sample. The modulation of the long wavelength transmission is a consequence of the Fabry-Perot etalon formed by the 2-μm-thick $Al_xGa_{1-x}As$ layer. The absorption edge is determined by the direct gap; the weak absorption of the indirect gap, which is ~100 meV lower in energy than the direct gap, is not evident in such thin samples. Three distinct features are observed in the transmission spectra of the excited sample. The most obvious is a strong and persistent (lasting longer than 1 ns) bleaching of the direct absorption, the second is a clear increase in the absorption below the unexcited absorption edge, and the final feature is a shift of the Fabry-Perot fringes to higher energies. We will now discuss the origin of each of these features.

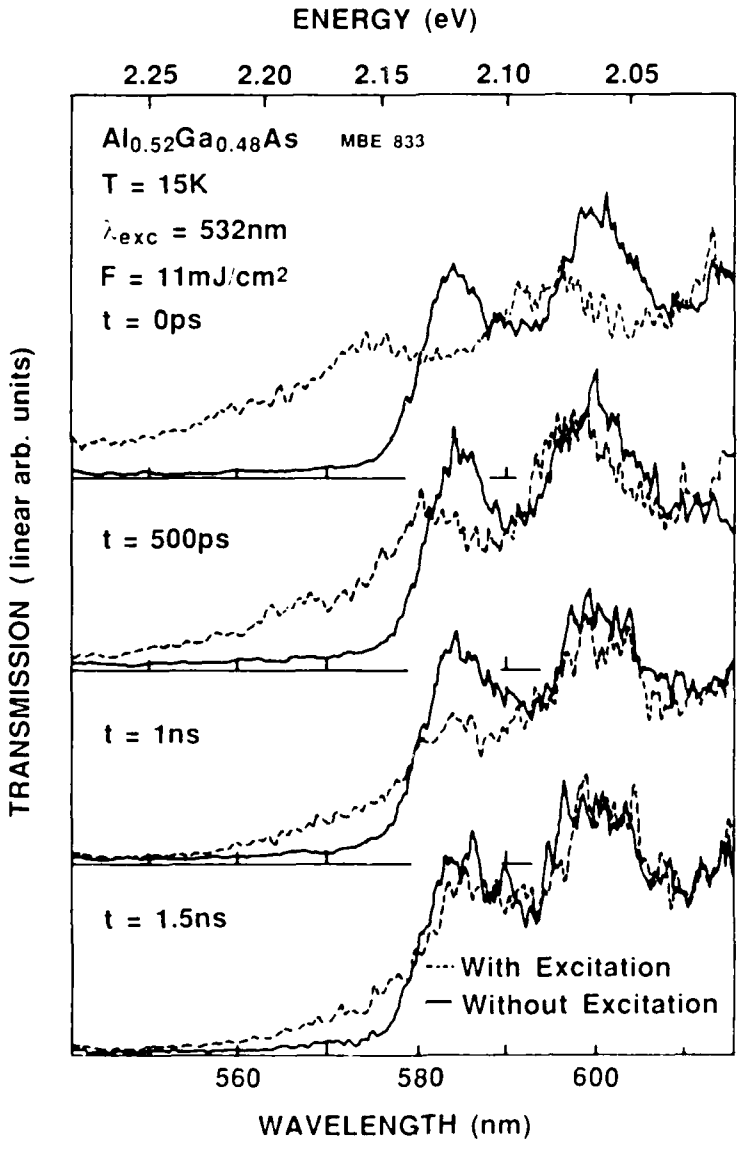

Figure 4. Time-resolved transmission spectra obtained for the x = 0.52 sample using a picosecond continuum.

The saturation of the direct absorption is a result of the occupation by the EHP of states that were previously optically coupled in the unexcited material. Analysis of the luminescence data for this sample indicates that the bleaching primarily arises from band filling of the valence band where the Fermi level is ~80 meV below the valence band edge; the electron distribution in the Γ-valley is nondegenerate. Additional bleaching can occur due to screening of the exciton continuum states. The duration of the bleaching is consistent with the lifetime of the indirect-gap luminescence. The radiative recombination replenishes the empty valence states with electrons and prevents complete saturation. This incomplete saturation coupled with renormalization of the direct gap results in the induced absorption at energies just below the unexcited absorption edge. Finally, strong changes in the absorption spectrum are always accompanied by modifications of the refractive index. The fringe shift observed in the spectra shown in Fig. 4 corresponds to a decrease of the refractive index. This is consistent with the observation that the influence of band filling and screening on the absorption spectrum far outweighs that of band-gap renormalization in this material.

Band-gap renormalization

As high densities of electrons and holes are deposited in a semiconductor, we can no longer neglect interactions between the carriers.[2] For example, consider electrons in the conduction band. At very high electron concentrations, a given electron experiences strong Coulombic repulsive forces from the surrounding electrons. The electrons adjust their configuration so as to screen such forces. This, in effect, creates a virtual positive charge around the given electron and, thereby, reduces its potential energy. Similar interactions occur between the electron and surrounding holes. In addition to these correlation effects, an electron within a given band tends to repel electrons of like spin state through the exchange interaction (Pauli exclusion principle). Similar arguments can be applied to a hole in the valence band. The net result of these many-body effects is to reduce the single-particle potential energy, which translates in the band-structure model to a reduction of the band gap energy.

Many models have been put forth to account for these many-body effects. One that is widely accepted and easily applied is the universal formula of Vashishta and Kalia (VK)[8] which is based on the results of the self-consistent mean field theory of Singwi and Tosi.[9] In the VK model, the so-called exchange-correlation energy is given by[8]

$$E_{xc} = \frac{a+br_s}{c+dr_s+r_s^2} Ry^* \quad , \tag{1}$$

where a = -4.8316, b = -5.0879, c = 0.0152, and d = 3.0426, and r_s is the normalized mean interparticle distance

$$r_s = \left(\frac{3}{4\pi n a_x^3}\right)^{1/3} \quad . \tag{2}$$

In Eq. (2), n is the carrier density and a_x is the excitonic Bohr radius,

$$a_x = \left(\frac{\epsilon(0)\hbar^2}{me^2}\right) \quad . \tag{3}$$

The Ry^* in Eq. (1) is the Rydberg or exciton binding energy given by

$$Ry^* = \frac{e^4 m}{2\epsilon(o)^2 \hbar^2} \quad . \tag{4}$$

In Eqs. (3) and (4), m is the reduced optical mass and $\epsilon(o)$ is the static dielectric constant.

The chemical potential after excitation is[2]

$$\mu = E_g' + \frac{\hbar^2 k_f^2}{2m} + \mu_{xc} \quad , \tag{5}$$

where E_g' is the renormalized band gap, and the change in the chemical potential resulting from exchange and correlation is

$$\mu_{xc} = E_{xc} + n \frac{\partial E_{xc}}{\partial n} = E_g - E_g' \quad . \tag{6}$$

Thus, a knowledge of the carrier density, which we can extract from fits to our luminescence data, the band parameters, and Eqs. (1)-(6), allows us to calculate the expected shift in the band gap. Notice that Eq. (1) is referred to as a universal formula in the sense that when it is applied, a plot of $E_g - E_g'$ (in units of the Rydberg) versus r_s produces a curve that is independent of band structure parameters (e.g., anisotropy, the ratio of the electron and hole effective masses, and valley degeneracy).[8]

Such a plot is shown in Fig. 5 along with values of the band-gap shift at various carrier densities obtained from analysis of the x=0.23 sample luminescence. Although data are available only over a very limited range of densities, the agreement with theory (using no adjustable parameters) is quite satisfying and provides confidence in both the model and our data.

Similar excellent agreement is obtained for the renormalization of the X-band of the x=0.52 sample. Application of the model to the Γ-band of this sample, however, produced very poor agreement with the measured renormalization. For total carrier densities in the range 3-6 x 10^{19} cm^{-3}, e.g., the measured renormalization was roughly 50 meV less than predicted by the model. This discrepancy can be explained in the following manner. In this indirect-gap sample, the electron density in the X-band is much greater than that in the Γ-band. The indirect gap renormalizes through full exchange and correlation, but the electron exchange contribution to the direct-gap renormalization is negligible because of the low carrier density. The Γ-band electrons do, however, experience full correlation effects since they are localized in the same space as the X-band electrons. The electron exchange energy can be estimated from[10]

$$E_x^e = - \frac{0.916\ \phi(\rho_e)}{r_s\ \nu_e^{1/3}} Ry^* \quad , \tag{7}$$

where ν_e is the valley degeneracy factor, and ϕ is an anisotropy factor[10]

$$\phi(\rho_e) = \rho_e^{1/6} \frac{\sin^{-1}[(1-\rho_e)^{1/2}]}{(1-\rho_e)^{1/2}} \quad , 0 \le \rho_e \le 1 \quad . \tag{8}$$

The quantity ρ_e is the ratio of the transverse to longitudinal electronic effective mass. The electron exchange contribution to the renormalization is then

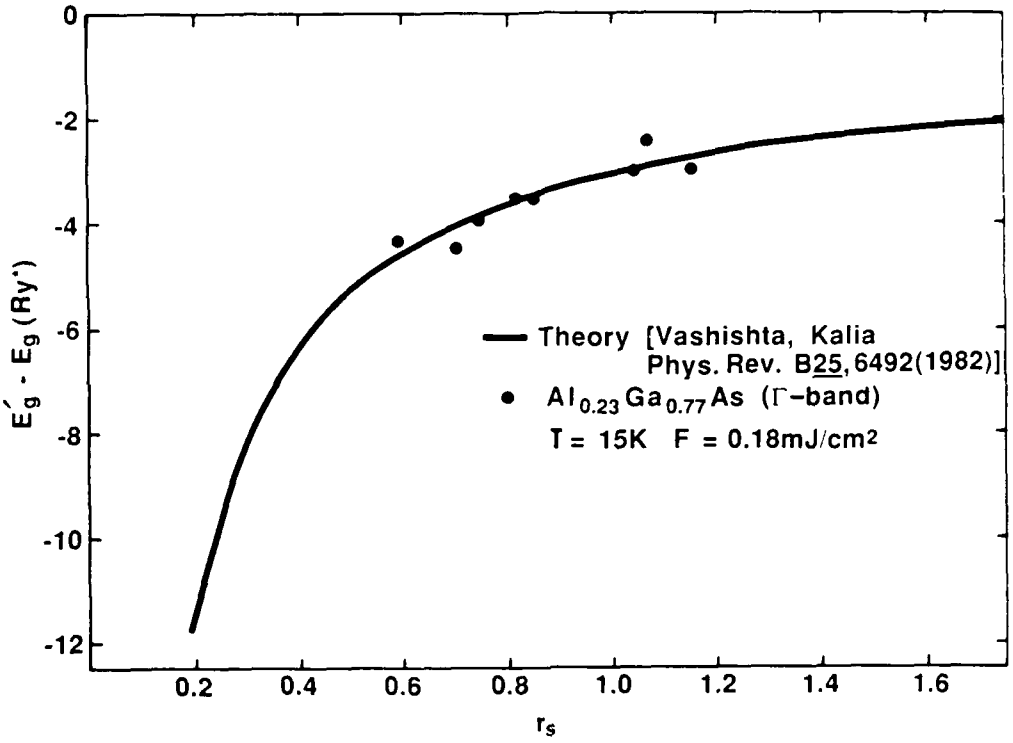

Figure 5. Comparison of VK formula to the measured band-gap renormalization in $Al_{0.23}Ga_{0.77}As$.

$$\mu_x^e = E_x^e + n \frac{\partial E_x^e}{\partial n} \quad , \tag{9}$$

in analogy with Eq. (6). We find that subtracting this contribution from the total exchange-correlation renormalization energy predicted by the VK formula produces a renormalized band gap that is in excellent agreement with our measured value.

We also find poor agreement between the simple VK model and the measured renormalization of both the Γ-band and X-bands in the x=0.38 sample, the measured renormalization in each case being larger than predicted. Renormalization in this sample is complicated by the strong admixture of the Γ-and X-bands which results from random potential fluctuations. This band mixing has been used to explain the superlinear increase with x of the direct exciton binding energy as x approaches x_c from below.[4] If we attribute this enhanced binding energy to an enhanced Γ-band optical mass (which is equivalent to the density of states mass), then the electron density in the Γ-band (and the total electron density) would be larger than otherwise predicted. This, of course, would lead to a larger band-gap renormalization. Note that, although band mixing occurs in the x=0.52 sample as well, most of the carriers reside in the heavy mass side valleys, and the mixing therefore has a negligible effect on the carrier density.

In Fig. 6, we again show the universal VK curve along with data for the Γ-band of the x=0.38 sample. Clearly, the data are in poor agreement with theory. These data, are plotted using a Rydberg of 6.54 meV obtained by using a reduced optical mass calculated from linear extrapolations of the various band masses for GaAs and AlAs for x=0.38. We can bring our data into excellent agreement

with the theory if we increase the Rydberg by roughly a factor of four and adjust the density accordingly. This new Rydberg value is in good agreement with that obtained by Pearah et al.[4] (~32 meV) from excitonic absorption measurements at the same x-value.

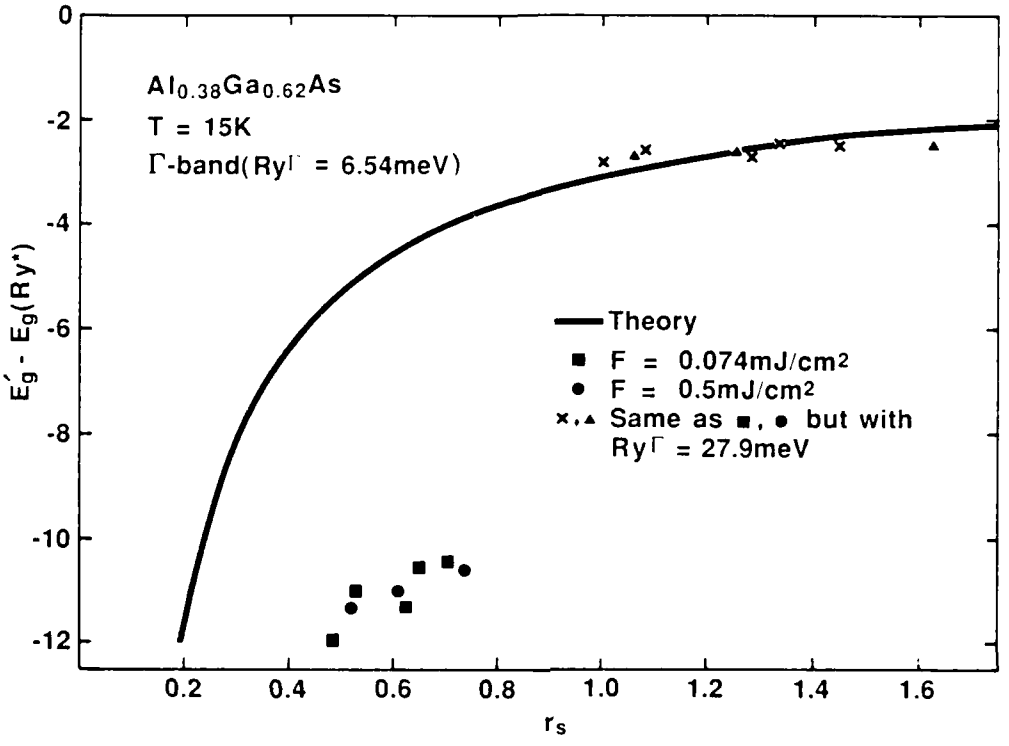

Figure 6. Comparison of VK formula to the measured Γ-band renormalization in $Al_{0.38}Ga_{0.62}As$. Also shown are the data as corrected for alloy disorder.

The X-band in this sample is energetically higher lying and therefore has a much smaller carrier density than the Γ-valley. As shown in Fig. 7, we can account for the renormalization of this band by adjusting for the reduced electron exchange contribution (in analogy to the Γ-band in the x=0.52 sample) and by using the Γ-band density determined by the procedure described in the preceding paragraph.

Summary

We have described our studies of the influence of dense EHP on the optical properties of direct and indirect gap $Al_xGa_{1-x}As$. Time-resolved photoluminescence has been discussed for samples with x=0.23, 0.38, and 0.52. The direct gap x=0.23 sample displayed luminescence typical of a direct-gap semiconductor, and the measured band-gap renormalization was found to be in excellent quantitative agreement with the VK model.[8] Luminescence from both the indirect and direct gaps was measured simultaneously for the x=0.38 and x=0.52 samples. Renormalization of the X-band in the x=0.52 sample also agreed well with the VK model. The renormalization of the Γ-band in this sample can be described by the VK model if we consider the reduced electron-exchange contribution in this band. To our knowledge, this is the only experimental evidence presently available which indicates a clear separation of the electron-exchange energy from the total self energy. The renormalization of the Γ-band in the x=0.38 sample can be explained in terms of the VK model if we account for the mass enhancement of this band that results from mixing by alloy disorder with the heavy side valleys. The mass-enhancement

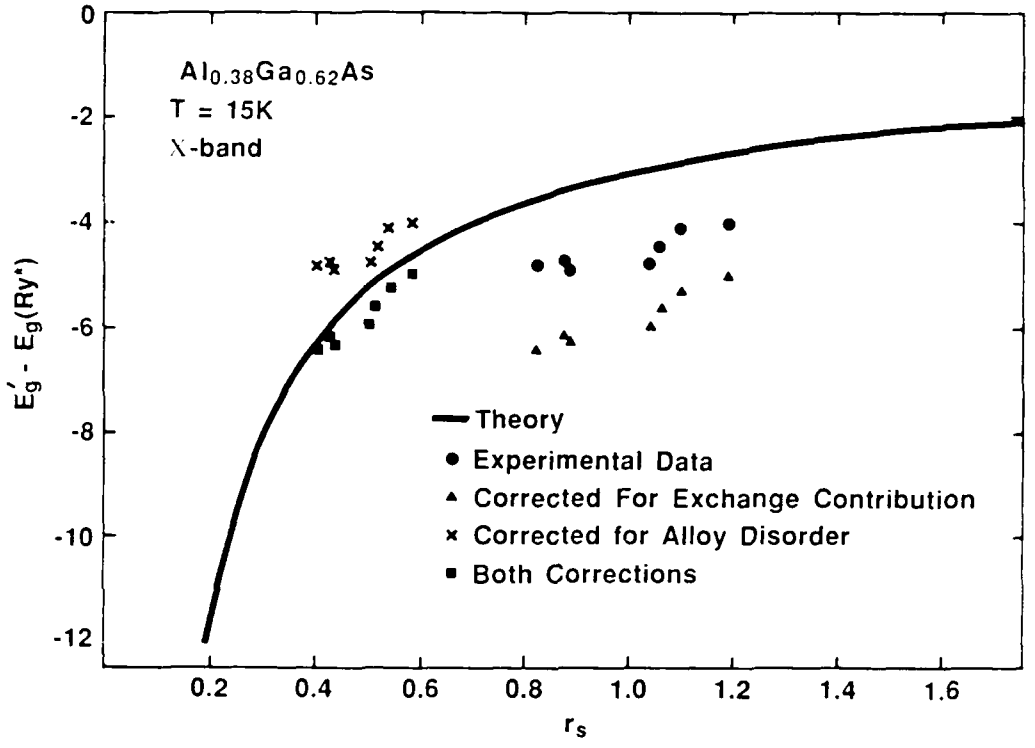

Figure 7. Comparison of VK formula to the measured renormalization of the X-band in $Al_{0.38}Ga_{0.62}As$. Also shown are the data corrected for reduced exchange energy, alloy disorder, and both effects simultaneously.

factor extracted from these measurements is consistent with the enhanced exciton binding energy obtained from absorption measurements.[4] By taking into account both the increased carrier density that arises from this mass enhancement and the reduced exchange contribution for higher lying bands, the VK model can be used to describe the renormalization of the X-band in the x=0.38 sample. Transient transmission spectroscopy of the bandedge of $Al_{0.52}Ga_{0.48}As$ shows strong bleaching of the direct absorption and induced absorption below the unrenormalized absorption edge. These observations indicate a potential for nonlinear optical device application for these materials. The observed features of the excited absorption spectra are in complete agreement with the EHP properties determined by luminescence measurements.

Acknowlegements

This research was sponsored in part by the U. S. Office of Naval Research, the Air Force Office of Scientific Research, and The Robert A. Welch Foundation.

References

1. H. C. Casey, Jr., J. Appl. Phys. 49, 3684 (1978).
2. See, e.g., H. Haug and S. Schmitt-Rink, Prog. Quant. Electr. 9, 3 (1984).
3. J. R. Hauser, M. A. Littlejohn, and T. H. Glisson, Appl. Phys. Lett. 28, 458 (1976).
4. P. J. Pearah, W. T. Masselink, J. Klem, T. Henderson, H. Morkoc, C. W. Litton, and D. C. Reynolds, Phys. Rev. B 32, 3857 (1985).

5. E. Cohen, M. D. Sturge, M. A. Olmstead, and R. A. Logan, Phys. Rev. B 22, 771 (1980).
6. R. Sarfaty, Arza Ron, E. Cohen, and R. A. Logan, J. Appl. Phys. 59, 780 (1986).
7. R. R. Alfano and S. L. Shapiro, Phys. Rev. Lett. 24, 584 (1970).
8. P. Vashishta and R. K. Kalia, Phys. Rev. B 25, 6492 (1982).
9. K. S. Singwi and M. P. Tosi, Solid State Physics 36, 177 (1981).
10. W. F. Brinkman and T. M. Rice, Phys. Rev. B 7, 1508 (1973).

Appendix C: Nonlinear Optical Properties of the Electron-Hole Plasma in $Al_{0.52}Ga_{0.48}As$.

A reprint of a paper published in J. Appl. Phys. 62, 4187 (1987).

Nonlinear optical properties of the electron-hole plasma in $Al_{0.52}Ga_{0.48}As$

H. Kalt, K. Bohnert,[a] D. P. Norwood, and Thomas F. Boggess
Center for Applied Quantum Electronics, Department of Physics, North Texas State University, Denton, Texas 76203

Arthur L. Smirl,[b] I. J. D'Haenens
Hughes Research Laboratories, 3011 Malibu Canyon Road, Malibu, California 90265

(Received 5 June 1987; accepted for publication 29 July 1987)

A dense electron-hole plasma is created in $Al_{0.52}Ga_{0.48}As$ using picosecond excitation with high excess energy. Its properties are studied by time-resolved photoluminescence and transient transmission spectroscopy. Simultaneous emission out of the indirect X and the direct Γ band is observed. Alloy disorder strongly influences the bimolecular recombination by allowing for quasidirect transitions and stimulated emission out of the indirect X band. The electron-hole plasma, whose electrons reside mainly in the X valleys, causes strong optical nonlinearities at the direct absorption edge. A persistent absorption bleaching and large induced refractive-index changes due to band filling of the valence band and induced absorption due to band-gap renormalization are observed.

I. INTRODUCTION

Solid solutions of semiconductors are widely used as components of multiple quantum-well structures, heterostructures, and related optoelectronic devices. Despite these extensive applications, little information is available on ultrafast phenomena in $Al_xGa_{1-x}As$, especially under high optical excitation. $Al_xGa_{1-x}As$ materials with x values close to the direct-to-indirect gap semiconductor crossover composition, $x_c \simeq 0.43$, have a variety of unique electronic and optical properties. Using an appropriate excess energy and excitation levels, one can create a dense electron-hole plasma, with the optically excited carriers distributed among various different conduction bands. This allows one, for example, to simultaneously study the renormalization of direct and indirect band gaps in the same material and to isolate electron exchange from the other many-body contributions to the band-gap renormalization.[1] In $Al_{0.52}Ga_{0.48}As$ (like in all materials with $x > x_c$), the majority of excited electrons reside in the X band, which is the lowest conduction band. We shall demonstrate that the most significant optical nonlinearities, however, occur at the absorption edge of the central valley which is essentially not occupied. Degenerate populations of electrons in the X band and holes in the valence band result in strong bleaching of the direct absorption, large changes in the refractive index, and induced absorption below the Γ band gap.

The recombination of the electron-hole plasma in indirect AlGaAs is strongly influenced by alloy disorder. The random distribution of Al and Ga atoms on the appropriate lattice sites leads to local potential fluctuations and mixes the wave functions of states in the Γ and the X valleys. This allows quasidirect transitions, i.e., recombination of electrons in the indirect band with holes in the valence band without participation of phonons. Even stimulated emission out of an indirect valley has been reported[2] in nanosecond experiments for $x \leqslant 0.46$. Although the strength of the band mixing[3] should fall off like $1/\Delta^2$ (where Δ is the energy separation of X and Γ band), we shall demonstrate that picosecond excitation in $Al_{0.52}Ga_{0.48}As$ creates sufficiently high carrier densities to allow stimulated X-band emission despite $\Delta = 96$ meV.

After a description of the experimental procedures in Sec. II, we discuss the results of time-resolved photoluminescence measurements and describe a model to fit the observed spectra (Sec. III). The nonlinearities at the direct absorption edge are studied by transient transmission spectroscopy and possible applications are pointed out (Sec. IV.) The paper is summarized in Sec. V.

II. EXPERIMENTAL PROCEDURES

We studied the nonlinear optical properties of the electron-hole plasma in $Al_{0.52}Ga_{0.48}As$ by time-resolved photoluminescence and transient transmission spectroscopy. The electron-hole plasma was excited with high excess energy by 32-ps pulses at 532 nm from a frequency-doubled, actively and passively and mode-locked Nd:YAG laser. Alternatively, to achieve excitation energies close to the direct band gap, we used the output of an amplified short-cavity-dye laser pumped by the picosecond 532-nm pulses. This provided us with 5–15 ps pulses tunable in the range of 570–850 nm. The excitation spot (800 μm diameter) was imaged onto the entrance of a 0.25-m spectrometer. Due to an appropriate choice of the entrance slit, we sampled luminescence only from the central 100 μm of the excited region to attain spatially homogeneous excitation conditions. The spectrum was temporally dispersed by a streak camera and analyzed by an optical multichannel analyzer. Thus, we were able to record both the spectral and temporal development of the luminescence signal. Luminescence spectra were taken at different times t after excitation ($t = 0$ ps corresponds to the maximum of the pump pulse) using the temporal window Δt of

[a] Present address: BBC Forschungszentrum, CH-5405 Baden, Switzerland.
[b] Presently on leave at NTSU.

 0021-8979/87/224187-05$02.40

typically 30–65 ps. Measurements of decay curves at a fixed luminescence wavelength λ had a spectral resolution $\Delta\lambda$ of 2–4 nm.

The residual 1.06-μm pulse remaining after frequency doubling was separated from the green pulse by a dichroic mirror, amplified, and tightly focused into a water cell. The resulting broadband picosecond continuum was used to probe the sample transmission in the center of the excitation spot. Part of the probe beam was directed around the sample and used as a reference to account for shot-to-shot intensity fluctuations. Here, the streak camera not only separates probe and reference beam but also eliminates the scattered light of the strong excitation beam.

The sample is a 2-μm-thick layer of nominally undoped $Al_{0.52}Ga_{0.48}As$ grown by molecular-beam epitaxy on a semi-insulating GaAs substrate. The active layer and the substrate are separated by a barrier layer of AlAs to prevent diffusion of photoexcited carriers into the substrate. A 100-Å GaAs cap layer protects the AlGaAs from oxidation. For transmission measurements the substrate has been locally etched away creating an array of 1×1 mm windows. The samples were mounted on a cold finger in a closed-cycle He refrigerator and cooled to a lattice temperature of $T_L = 15$ K.

III. TIME-RESOLVED PHOTOLUMINESCENCE MEASUREMENTS

As mentioned above, $Al_{0.52}Ga_{0.48}As$ is an indirect-gap semiconductor, where the X band is the lowest conduction-band minimum with an energy gap of $E_g^X = 2.085$ eV at $T = 5$ K.[4] The next higher-lying valleys are at the L point ($E_g^L = 2.148$ eV) and at the Γ point ($E_g^\Gamma = 2.181$ eV). Irradiation of this material with picosecond pulses at 2.33 eV (532 nm) excites electrons mostly into the Γ band. These electrons rapidly scatter into the side valleys due to interaction with longitudinal optical (LO) phonons and the strong band mixing induced by alloy disorder. Carrier-carrier scattering leads to a thermalization of the electron and hole distributions. Quasi-Fermi levels (and a common temperature) for electrons and holes are established on a timescale of less than 100 fs,[5] with an excess energy of the electron-hole plasma of about 5 LO-phonon energies (compared to E_g^X). The electron-hole plasma cools mainly by emission of LO phonons. Although these ultrafast processes are not directly resolved in our experiments, their impact is still clearly reflected.

Figure 1 shows photoluminescence spectra taken at different time delays after excitation. The spectra consist of two distinct luminescence bands which we attribute to bimolecular recombination of electrons in the X (lower energy) and Γ band (higher energy). While the X-band luminescence decays with a time constant of about 650 ps, the higher-energy emission is visible only during the presence of the excitation pulse. This reflects the rapid scattering of Γ-band electrons into the side valleys. Recombination of electrons in the L bands gives no significant contribution to the luminescence spectra due to the low carrier density and transition probability in this band.

We are able to extract the carrier densities and temperatures from fits to the spectral line shapes (see below). For spectra taken during the excitation process (e.g., $t = 16$ ps), the average carrier temperature in the X band is $T = 120$ K. This corresponds to an excess energy well below one LO phonon energy and is consistent with a fast initial cooling of the electron-hole plasma. A fit to the Γ-band luminescence assuming common Fermi levels and temperatures is not possible, however. The spectral width and the slope of the high-energy luminescence indicate a higher temperature in this band. The Γ band is populated significantly only during the initial "hot" phase of the electron-hole plasma. Thus, the luminescence out of this band shows up only because of the large transition probabilities compared to the indirect bands. In contrast to the short lifetime in the central valley, the majority of electrons in the X band have time enough to cool before they recombine. Thus, the recorded temperature difference for both bands is merely an artifact of our time resolution of tens of picoseconds. The electron-hole plasma cools to $T = 65$ K but does not reach lattice temperature within an observation time of 1.6 ns. This reflects the rather inefficient cooling due to emission of acoustic phonons. The carrier density, however, does not change significantly within the same time interval. This observation supports similar experimental findings of Cohen *et al.*[2] Although there is no real proof for the existence of a stable liquid phase in indirect AlGaAs, the experiments seem to indicate a formation of electron-hole droplets.

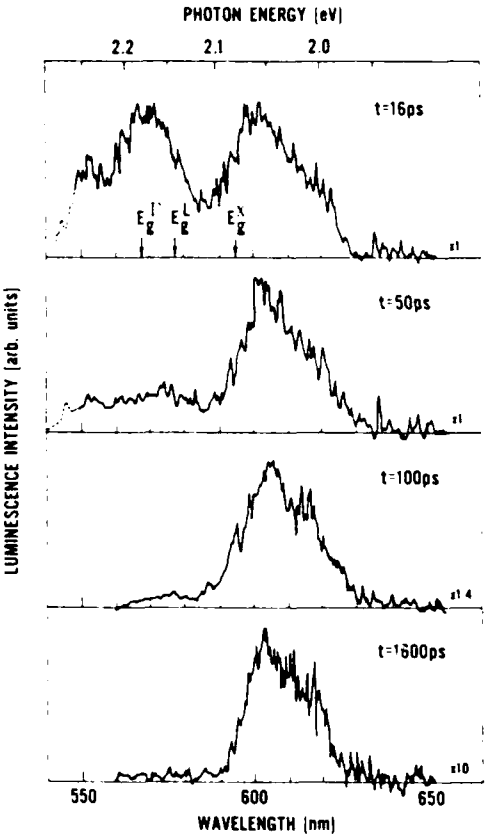

FIG. 1. Photoluminescence spectra of $Al_{0.52}Ga_{0.48}As$ for an excitation fluence $F = 8$ mJ/cm^2 at different times t after excitation.

Exchange and correlation effects in the electron-hole system lead to a reduction of the single-particle energies and thus to a shrinkage of the direct and indirect band gaps in the presence of an electron-hole plasma. These band-gap reductions show up as red shifts of the low-energy tails of the plasma luminescence compared to the unrenormalized band gaps as indicated in Fig. 1. A comparison[1] of those experimental band-gap shifts with the universal formula of Vashishta and Kalia[6] shows that the X band is renormalized due to full correlation and exchange effects, whereas in the Γ band the electron exchange is negligible. This is a result of the confinement of exchange interactions to carriers within the same valley and the relatively low carrier density in the Γ band. Those few electrons in the central valley see, however, the Coulomb interaction with all other excited electrons and holes independent of the band in which they reside. Thus, all many-body effects, other than electron exchange, still contribute to the renormalization of this band.

More detail of the X-band luminescence is given in Fig. 2. The experimental spectrum has been taken well after the excitation pulse has ended and the Γ-band has decayed completely. The spectrum is actually a superposition of a no-phonon line and a phonon sideband. We achieve a very good fit to the experimental spectrum by using a two-band model where the no-phonon line and sideband have the same line shape and are separated by the AlAs-like LO-phonon energy (48 meV)[7] for this x value. The line-shape fits are based on quasidirect recombination for the no-phonon line. We assume a common quasi-Fermi level for all conduction-band valleys and take into account the heavy- and light-hole bands in the valence band structure. The fit does not include band tailing due to alloy disorder which is negligible[3] or resonance damping which leads to some deviations at the low-energy sides of each emission band. The omission of resonance broadening is, however, not critical[8] for the determination of n and T, and the renormalized band-gap E_g' can be determined with an accuracy of $\pm 5\%$. The extracted values from this fit are $n = 1.4\times 10^{19}$ cm^{-3}, $T = 99$ K, and $E_g'^{X} = 2.035$ eV.

The structure of the X-band emission spectrum is a clear measure of the strength of alloy disorder effects for this alloy composition. The no-phonon line is due to quasidirect transitions allowed by alloy disorder.[2,9] Its relative intensity is of the same order of magnitude as the phonon sideband, and its decay time ($t = 620$ ps) is only slightly smaller than for the sideband ($t = 700$ ps). This shows that for $x = 0.52$ the alloy disorder is, as expected, less effective than for x values just above the crossover composition, $x_c = 0.43$, where the no-phonon line is predominant at short delay times.[2] It is also evident that band mixing due to alloy disorder in indirect AlGaAs is reduced compared to samples with x values near to but less than x_c. In such materials the X-band states couple resonantly with states at the Γ point, and the quasidirect recombination is nearly as effective as the direct recombination out of the Γ band.[1]

Despite this relative weakness of alloy disorder in $Al_{0.52}Ga_{0.48}As$, the band mixing is still strong enough to result in stimulated emission out of the indirect X band at high excitation levels. By increasing the excitation fluence, one is able to pass the threshold for stimulated emission and the line shape of the X-band luminescence changes dramatically (Fig. 3). A narrow, intense, emission line appears just as the low-energy side of the no-phonon line. This corroborates our modeling of the X-band spectra and emphasizes the

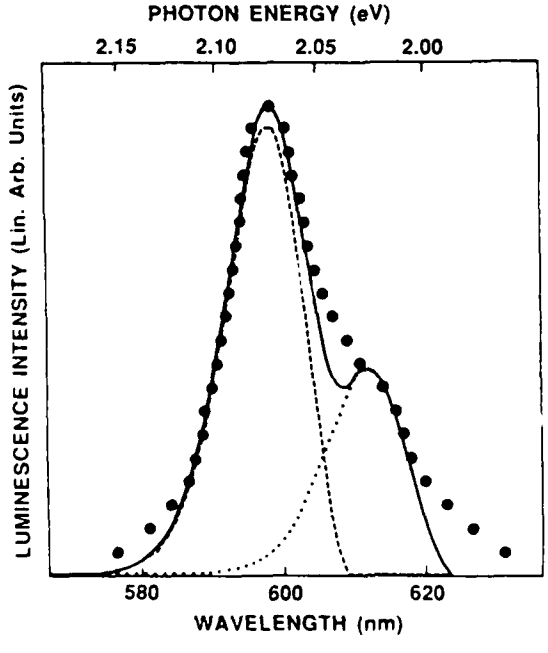

FIG. 2. Fit (solid line) to an experimental luminescence spectrum (large dots) for $F = 5.4$ mJ/cm^2 and $t = 150$ ps. The no-phonon line and the phonon sideband are represented by the dashed and the dotted line, respectively.

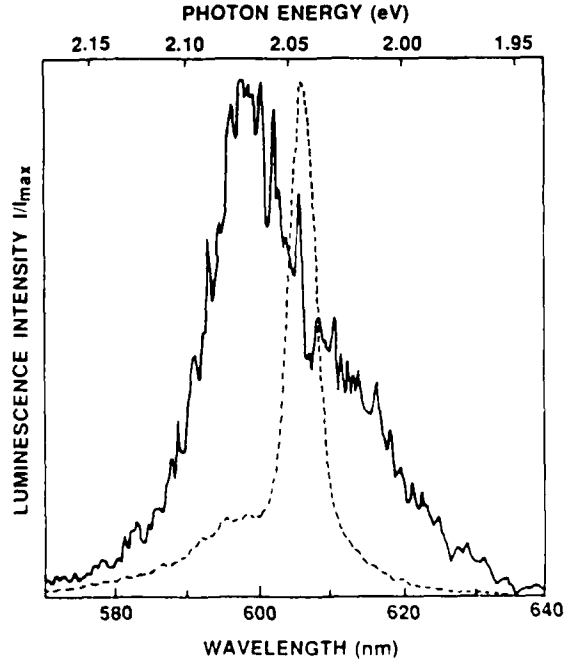

FIG. 3. Comparison of spontaneous (solid line) and stimulated (dashed line) emission taken for $F = 5.4$ mJ/cm^2, $t = 150$ ps and $F = 12$ mJ/cm^2, $t = 0$ ps, respectively.

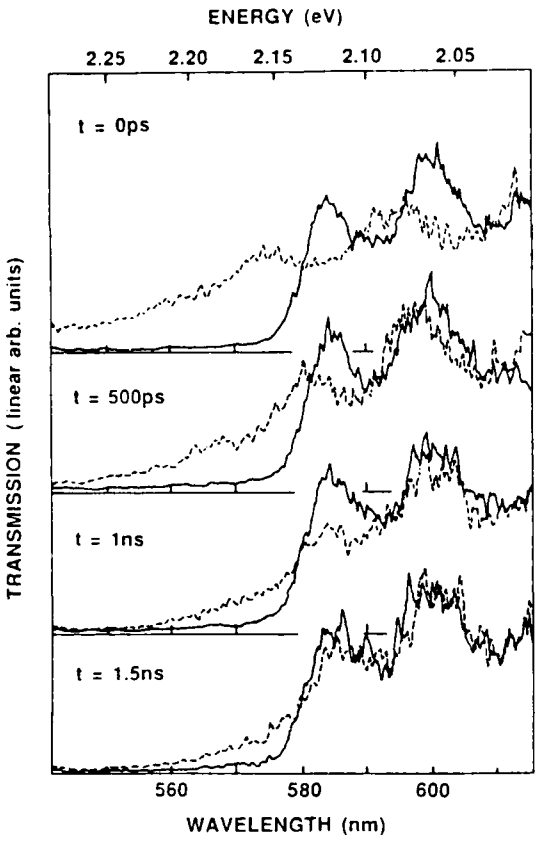

FIG. 4. Transmission of $Al_{0.52}Ga_{0.48}As$ in the vicinity of the direct absorption edge without excitation (solid line) and with an excitation of $F = 11$ mJ/cm^2 at 532 nm (dashed line) for different times t.

importance of the band-mixing effects associated with alloy disorder in AlGaAs. Although the strength of this mixing falls off like $1/\Delta^2$, we still obse.ve quasidirect emission for a relatively large band-edge separation of $\Delta = 96$ meV.

When the excitation fluence at 532 nm is chosen to be just below the onset of stimulated emission, carrier densities up to $n = 5.5\times10^{19}$ cm^{-3} at $t = 0$ ps are extracted from our fit. The density at which a degenerate distribution is reached in the valence band is $n_c = 3.6\times10^{18}$ cm^{-3} for an appropriate carrier temperature of $T = 120$ K. Thus, the carrier distribution in the valence band is highly degenerate and the quasi-Fermi level for the holes lies 86 meV within the band. This strong band filling is easily confirmed by transient transmission spectroscopy.

IV. TRANSIENT TRANSMISSION SPECTROSCOPY

The transmission of $Al_{0.52}Ga_{0.48}As$ in the area of the direct band gap with and without excitation is shown in Fig. 4 for various delay times after excitation. The absorption to the central Γ valley governs the transmission without excitation. Absorption sets in below the direct band gap due to excitonic effects, but no sharp excitonic resonance is resolved because of alloy-disorder-induced line broadening. Absorption to the indirect bands is negligible in this thin layer. Note that the quasidirect luminescence bands of Figs. 1–3 occur in a spectral region where the sample is essentially transparent. The modulation of the transmission below the Γ gap is caused by Fabry–Perot interference within the sample. When an electron-hole plasma is excited in the sample the transmission spectra change dramatically. Three different features are obvious in Fig. 4: A strong persistent bleaching of the absorption to the Γ-band, an induced absorption below the direct gap, and a significant blue shift of the Fabry–Perot fringes.

The absorption bleaching confirms the strong band filling in the valence band already deduced from our luminescence measurements. No band filling, however, occurs in the Γ band because the carrier distribution in this valley is nondegenerate and the carrier density is only $\sim10^{15}$ cm^{-3} once the excitation pulse has ended. Thus, this bleaching in the absorption to the Γ band is caused by an excited dense electron-hole plasma whose electrons reside in the side valleys. Note that, although $Al_{0.52}Ga_{0.48}As$ is an intrinsic semiconductor, the blocking of the transitions between valence and Γ band is caused by only one sort of excited carrier, i.e., the holes. Thus, indirect AlGaAs has more similiarities with Ge (Ref. 10) than with the GaAs system. Furhermore, the excited electron-hole plasma screens the Coulomb enhancement of the excitonic continuum at the Γ point[10] which leads to an additional reduction of the absorption in the spectral range above the renormalized Γ band gap. The duration of the bleaching is consistent with the lifetime of the electron-hole plasma determined by the decay of photoluminescence.

With several times 10^{19} cm^{-3} carriers in the sidevalleys, the Γ band is renormalized by electron correlation as well as hole correlation and hole exchange effects. This results in an induced absorption below the direct absorption edge with decreases with decaying carrier density. This effect, however, is still visible for delay times of about $t = 1$ ns. The shift of the absorption edge in Fig. 4 is in excellent agreement with the band-gap shift of about 40 meV extracted from the Γ-band luminescence. This value is also confirmed in experiments where the electron-hole plasma is excited using a laser energy below the direct absorption edge. The short-cavity-dye laser allows us to tune the excitation energy E_{exc} across E_g^Γ. The strength of the absorption bleaching decreases monotonically when $E_g^\Gamma - E_{exc}$ increases, but significant bleaching is still achieved for E_{exc} down to 2.100 eV. The carrier densities necessary for bleaching can only be reached when the Γ-absorption edge shifts below E_{exc} during the excitation process due to band-gap renormalization.

The blue shift of the Fabry–Perot modes can be used to calculate the strong plasma-induced changes of the refractive index. These changes reach values up to $\Delta n = -9.9\times10^{-2}$ just below the Γ gap for $t = 0$ ps in Fig. 4. This negative Δn (or blue shift) shows that band filling of the valence band and screening dominate the induced index changes rather than band-gap renormalization.

In order to examine the applicability of these nonlinearities at the direct absorption edge for optical bistability, we excited the sample with the tunable short-cavity-dye laser. As discussed above, an induced absorption due to band-gap renormalization is observed below the absorption edge. Although this induced absorption is partially reduced by the

simultaneously occurring bleaching, it might be feasible for optical switching by an intrinsic absorptive bistability.[11,12] The situation, however, is much more favorable for excitation just above the direct absorption edge. Here, changes of the refractive index and bleaching of the absorption on the same order of magnitude as for excitation at 532 nm were achieved for sample temperatures of 15 as well as 300 K. These large nonlinearities should be easily applicable for optical switching based on dispersive bistability or bistability due to bleaching of absorption.[12]

V. SUMMARY

In summary, the nonlinear optical properties of a dense electron-hole plasma in $Al_{0.52}Ga_{0.48}As$ have been examined by picosecond photoluminescence and transient transmission spectroscopy. An initial carrier distribution among different central and side valleys of the conduction band leads to distinct luminescence bands due to bimolecular recombination of Γ- and X-band electrons. The importance of alloy disorder in this solid solution is manifested in quasidirect recombination and stimulated emission out of the indirect X band. The excited electron-hole plasma, whose majority of electrons reside in the indirect X valleys, induces strong optical nonlinearities at the direct absorption edge. Induced absorption due to band-gap renormalization, a persistent bleaching of absorption and large changes of the refractive index due to band filling of the valence band and screening effects are observed.

ACKNOWLEDGMENTS

The work at NTSU was supported by the U.S. Office of Naval Research and the Robert A. Welch Foundation. The research at Hughes was sponsored in part by the Air Force Office of Scientific Research.

[1] K. Bohnert, H. Kalt, T. F. Boggess, D. P. Norwood, and A. L. Smirl (unpublished).

[2] E. Cohen, M. D. Sturge, M. A. Olmstead, and R. A. Logan, Phys. Rev. B **22**, 771 (1980); and R. Sarfaty, Arza Ron, E. Cohen, R. A. Logan, J. Appl. Phys. **59**, 780 (1986).

[3] A. N. Pikhtin, Fiz. Tech. Poluprovodn. **11**, 425 (1977) [Sov. Phys. Semicond. **11**, 245 (1977)].

[4] D. J. Wolford, W. Y. Hsu, J. D. Dow, and B. G. Streetman, J. Lumin. **18/19**, 863 (1978).

[5] C. H. Brito-Cruz, R. L. Fork, and C. V. Shank, *XVth International Conference on Quantum Electronics Technical Digest Series 1987* (Optical Society of America, Washington, DC, 1987), Vol. 21, p. 82.

[6] P. Vashishta and R. K. Kalia, Phys. Rev. B **25**, 6492 (1982).

[7] M. Ilegems and G. L. Pearson, Phys. Rev. B **1**, 1576 (1970).

[8] K. Bohnert, M. Anselment, G. Kobbe, C. Klingshirn, H. Haug, S. W. Koch, S. Schmitt-Rink, and I. F. Abraham, Z. Phys. B **42**, 1 (1981).

[9] R. A. Faulkner, Phys. Rev. **175**, 991 (1968).

[10] H. Schweizer, A. Forchel, A. Hangleiter, S. Schmitt-Rink, J. P. Löwenau, and H. Haug, Phys. Rev. Lett. **51**, 698 (1983).

[11] K. Bohnert, H. Kalt, and C. Klingshirn, Appl. Phys. Lett. **43**, 1088 (1983).

[12] For a recent review, see H. M. Gibbs, *Optical Bistability: Controlling Light with Light* (Academic, New York, 1985).

Appendix D: Renormalization of Direct and Indirect Band Gaps in Highly Excited $Al_xGa_{1-x}As$.

A preprint of a paper accepted for publication in Phys. Rev. Lett. 1987.

Submitted to Phys. Rev. Lett.

RENORMALIZATION OF DIRECT AND INDIRECT BAND GAPS IN HIGHLY EXCITED $Al_xGa_{1-x}As$

K. Bohnert,[a] H. Kalt, Arthur L. Smirl, D. P. Norwood,
Center for Applied Quantum Electronics
Department of Physics
North Texas State University
Denton, Texas 76203

and

Thomas F. Boggess, I. J. D'Haenens
Hughes Research Laboratories
3011 Malibu Canyon Road
Malibu, California 90265

Abstract

Band-gap renormalization due to many-particle effects has been investigated at the Γ- and X-points of the Brillouin zone in $Al_xGa_{1-x}As$ as a function of alloy composition. The composition dependence of the distribution of the photo-excited electrons among direct and indirect conduction-band valleys has been used to experimentally separate the electron-exchange contribution to band-gap narrowing.

(a) Present Address: BBC Forschungszentrum, CH-5405 Baden, Switzerland

For more than a decade, band-gap renormalization in semiconductors in the presence of laser generated electron-hole plasmas has been a field of considerable interest. The renormalization arises primarily from exchange and correlation interactions in the electron-hole system. Previous theoretical and experimental studies focused on the renormalization of the fundamental band gap, i.e., the gap at the Γ-point in direct materials or the gaps at the X- or L-points in indirect materials. A good quantitative understanding of the underlying physics has been obtained for low-temperature degenerate distributions [1]. So far, however, little interest has been given to the renormalization of gaps above the fundamental band gap. In this letter we report what is to our knowledge the first experimental investigation of band-gap renormalization at both the Γ- and X-points of the Brillouin zone of a given semiconductor. These studies have lead to an experimental verification of the electron-exchange energy in the $Al_xGa_{1-x}As$ alloy system. Previous measurements in semiconductors have not been able to distinguish between the various contributions to the band-gap renormalization.

$Al_xGa_{1-x}As$ is a material that is particularly well-suited for these investigations. By varying the mole fraction, x, of AlAs, it can be grown as either a direct- ($x < x_c \simeq 0.43$) or an indirect-gap ($x > x_c$) semiconductor. The relative energy separation of the direct and indirect gaps can thus be systematically controlled by adjusting the x-value. For x-values near x_c, intense optical excitation results in the distribution of photo-excited electrons not only in the lowest conduction-band valley but also in higher-lying valleys as well. The emission spectrum of an electron-hole plasma in this case will be composed of two (rather than one) luminescence bands which correspond to the bimolecular recombination from the direct and indirect conduction band valleys. Analysis of these distinct luminescence bands allows us to determine the energetic position of each renormalized gap.

The measurements reported here were performed using intense 30-psec pulses at 532 nm from a mode-locked and frequency-doubled Nd:YAG laser. Eight $Al_xGa_{1-x}As$ samples with x-values of 0.23, 0.30, 0.38, 0.42, 0.49, 0.51, 0.52, and 0.55 were studied. Each sample was 2-μm thick, nominally undoped, and prepared by molecular-beam epitaxy on a GaAs substrate. The active layers were separated from the substrate by an AlAs barrier. All measurements were

conducted at 15 K. The luminescence from the central 100 μm of a 700 μm excitation spot was dispersed with a spectrometer and time resolved with a streak camera. The temporal resolution was determined by the width of the selected time window (typically between 30 and 65 ps). By this procedure, spatially homogenous and quasi-stationary conditions of excitation were achieved. The exciting fluence, F, was varied between 0.01 mJ/cm^2 and 12 mJ/cm^2. Care was taken to record the spectra at excitations below the threshold for stimulated emission.

For aluminum contents significantly below x_c, the indirect conduction-band valleys are far above the direct gap, and only the valley at the fundamental Γ-gap is populated with excited electrons. In these cases, plasma luminescence typical of a direct-gap semiconductor was observed consisting of a single spectrally broad emission band. In contrast, for alloy compositions near x_c where direct and indirect conduction bands were populated, the luminescence spectra exhibited two distinct emission bands. Examples of such (time-resolved) spectra are shown in Fig. 1 for x=0.38 ($x<x_c$) and x=0.52 ($x>x_c$) [2]. The selected time invervals coincide with the excitation-pulse maximum (t=0 ps). In the direct-gap material (Fig. 1a), the low-energy band arises from bimolecular recombination from the Γ-conduction band while the high-energy band results from bimolecular recombination from the indirect X-valleys. The comparatively strong indirect luminescence is a consequence of alloy disorder which allows electrons in indirect conduction bands to recombine with holes in the valence band without phonon participation [3,4]. The indirect emission, therefore, is not phonon-shifted. (A possible phonon side-band, which for $x<x_c$ should contribute only very weakly, could be embedded within the direct emission band.)

For x=0.52 (Fig. 1b), the spectral sequence of the two emission bands is reversed, the lower energy feature now being associated with emission from the indirect gap and the energetically higher feature with the direct gap. The absolute luminescence intensity is strongly reduced relative to the 0.38 sample reflecting the decreasing probability for quasi-direct transitions from the indirect valleys as x increases above x_c [5]. While the decay times of the two emission bands are similar in the direct alloy (τ~100 ps), they are drastically different in the indirect alloy. Here, the direct luminescence is observed essentially only during excitation compared to a lifetime of τ= 650 ps for

the indirect emission. For $x>x_c$ a weak shoulder can be observed on the low energy side of the indirect luminescence band. This feature is due to additional phonon-assisted electron-hole recombination from the indirect X-valleys [2]. (Note that an analysis of the spectra for both the x=0.52 and the x=0.38 sample shows that the electron populations of the indirect L-valleys and their relative transition probabilities are such that these bands contribute only weakly to the overall luminescence intensity.) For the purposes of this Letter, the features in Fig. 1 that we particularly wish to emphasize are the pronounced red shifts of the emission bands relative to the unrenormalized gaps (indicated by arrows).

The renormalized band gaps, E_g', the corresponding carrier densities, n, and the plasma temperatures, T, were extracted by fitting the data using a simple model assuming electron transitions with relaxed k-conservation [6]. This appears to be appropriate in the presence of strong alloy disorder. The model in ref. [6] was extended to account for bimolecular recombination from two conduction band valleys. For $x>x_c$, a third term was added to account for the LO-phonon side-band using the appropriate LO-phonon energies. The relative intensities of the various emission bands were treated as adjustable parameters. A common quasi-chemical potential for all involved conduction bands was assumed, since the time scales for carrier-carrier scattering, intraband carrier relaxation, and interband scattering are short compared to our pulsewidth. The heavy- and light-hole bands were approximated by a single parabolic band. The effective mass parameters were taken from refs. [7-10].

The dots in Fig. 1 are the results of the line-shape analysis. For x=0.38, both emission bands could be fit reasonably well. The small deviation at the low-energy edge may be due to collision broadening which was not included in our model. (Commonly, this is introduced only phenomenologically and has only a minor effect on the extracted parameters.) For x=0.52 a satisfying fit was achieved for the indirect emission band. Note that the computed spectrum is composed of the quasi-direct contribution and a LO-phonon sideband (solid and dashed line, respectively). The direct emission band could not be fit with the asumption of a common temperature and Fermi distribution for all conduction bands. This is an artifact of our limited time

resolution which is long compared to the lifetime of the electrons in the Γ-valley. These electrons scatter into the side valleys on a time scale of less than 100 fsec. While the long-lived carriers in the X-band have time enough to cool before they recombine, the emission out of the Γ-valley reflects an earlier (hotter) stage in the relaxation process. The determination of the reduced direct gap is not influenced by this effect, and the fit to the indirect emission provides a good approximation to the total number of carriers and their distribution even during excitation.

From the line shape analysis, we extracted the renormalized band gaps with an accuracy of approximately ±5 meV. The position of the renormalized X-gap for $x>x_c$ has been further confirmed by stimulating the "quasi-direct" emission from the X-valleys [2]. Characteristic ranges of carrier densities were 10^{18} - $5{\cdot}10^{18}$ cm^{-3} and 10^{19} - $3{\cdot}10^{19}$ cm^{-3} in the direct- and indirect-gap regimes, respectively. The higher densities achievable for $x>x_c$ are explained by the reduced radiative recombination rate as well as the higher density of states in the indirect-gap regime. The results are summarized in Fig. 2 where the bold (thin) vertical bars represent the measured renormalized band-gap energies for the fundamental (higher-lying) gaps. In each case, the length of the bar indicates the uncertainty of the extracted value. We comment that the unrenormalized band gaps were determined from low-excitation luminescence, transmission from regions where the substrate had been etched away, and photoreflectance. The x-values were then assigned using the reported compositional dependences of the gaps according to Casey [7]. The energy band gaps at the Γ- and X-points at low temperatures are represented by the solid lines in Fig. 2 [11]. In all cases the strong plasma-induced reduction of the band gaps is clearly evident.

We model the band-gap renormalization using the formalism of Ref. [1], where the renormalized band gap is given by

$$E_g'(n) = E_g + E_{xc}(n) + n \frac{\partial}{\partial n} E_{xc}(n) \quad . \tag{1}$$

The exchange-correlation energy is given by the universal formula [1]:

$$E_{xc}(r_s) = (a+br_s)/(c+dr_s+r_s^2)\ R_y^* \quad , \tag{2}$$

where the normalized interparticle separation is $r_s=(3/4\pi na_x^3)^{1/3}$ and $a=-4.8316$, $b=-5.0879$,

c=0.0152, and d=3.0426. R_y^* and a_x are the excitonic Rydberg and Bohr radius, respectively, for the direct exciton in the case $x(x_c$ and for the indirect exciton in the case $x)x_c$. Although this formalism was developed for the renormalization of the fundamental gap, we shall demonstrate that it can evidently be applied to the higher-lying band gap if the electron-exchange energy is properly handled.

The heavily-dotted bands in Fig. 2 are a result of applying Eqs. (1) and (2) to the fundamental gap for carrier densities appropriate to our experimental conditions, i.e., 10^{18} - $5x10^{18}$ cm^{-3} for $x(x_c$ and 10^{19} - $3x10^{19}$ cm^{-3} for $x)x_c$. We find agreement between theory and experiment for materials that are clearly direct-gap (x=0.23 and 0.30) and for all of the indirect-gap materials.

For alloy compositions just below x_c, the renormalization of the Γ-gap becomes significantly larger than calculated. Similar results were reported for like x-values in Ref. [12]. We attribute this enhancement to alloy disorder effects. The disorder potential leads to an admixture of heavy X-band states to the lighter Γ-band states [13]. This possibly results in a modification of the density of states and the effective carrier density in the Γ-band which leads to an enhanced renormalization of the Γ- and also the higher X-gap. This is consistent with the superlinear increase of the excitonic binding energy with x, which has been observed for $0.3<x<0.4$ by Pearah et al. [13]. The effect of bandmixing on the large effective mass of the X-band for $x>x_c$ is negligible.

The lightly-dotted bands in Fig. 2 were obtained by assuming that all electrons reside in the higher lying valley(s) and again applying Eqs. (1) and (2). For the moment, let's focus on the Γ-band of the indirect-gap ($x>x_c$) materials. Clearly, the theory grossly overestimates the band-gap shrinkage. This result is not surprising since in reality nearly all of the electrons are distributed in the lower-lying X-valleys. In fact, our analysis reveals that typically fewer than one percent of all electrons are in the Γ-valley. For these conditions, we would expect the hole-exchange energy to remain unchanged since it will not be influenced by our choice of conduction bands. Likewise, the correlation energy will not be changed since the Coulomb interaction between the Γ-valley electrons and all other excited carriers is still present [14]. By contrast, the sparce population of the Γ-valley

implies that the electron-exchange energy for this band should be negligible. With these considerations, we can estimate the renormalization of the Γ-gap in these indirect-gap materials by calculating E_g' according to Eqs. (1) and (2) using the appropriate Γ-band parameters and then subtracting the (missing) electron-exchange contribution. The latter is given by

$$\Delta E_g^{ex,e} = E_{ex}^e + n \frac{\partial}{\partial n} E_{ex}^e \quad , \tag{3}$$

where the electron-exchange energy for the Γ-band is simply $E_{ex}^e = -0.916\ r_s^{-1}\ R_y^*$ [15]. The striped band in Fig. 2 is a result of this procedure. We find that this simple yet physically reasonable adjustment to this well-known formalism provides remarkable agreement with the data, and thus, allows the direct experimental separation of the electron-exchange contribution to the bandgap narrowing.

Finally, we comment that the renormalization of the X-band in direct-gap materials with x-values near x_c (see x=0.38 data Fig. 2) is particularly complicated. This band has a reduced (though non-negligible) electron-exchange energy and is also influenced by alloy disorder. A detailed analysis of the renormalization of this band requires a better understanding of the influence of alloy disorder on the density of states, effective mass, excitonic Rydberg, etc.

In summary, plasma-induced bandgap renormalization in direct and indirect AlGaAs has been measured at different points of the Brillouin zone from time-resolved photoluminescence measurements. Whereas the fundamental gaps are renormalized by full exchange and correlation energies, the renormalization of the energetically larger gaps is found to be reduced as a result of the missing electron-exchange contribution. At alloy compositions just below the direct-to-indirect band crossover, evidence was found that disorder effects enhance the band gap shrinkage.

This work was supported in part by the Office of Naval Research, The Robert A. Welch Foundation, and the Air Force Office of Scientific Research.

References

[1] P. Vashishta and R. K. Kalia, Phys. Rev. **B25**, 6492 (1982) and references therein.

[2] H. Kalt, K. Bohnert, D. P. Norwood, T. F. Boggess, A. L. Smirl, and I. J. D'Haenens, to be published in J. Appl. Phys.

[3] R. A. Faulkner, Phys. Rev. **175**, 991 (1968).

[4] E. Cohen, M. D. Sturge, M. A. Olmstead, and R. A. Logan, Phys. Rev. **B22**, 771 (1980).

[5] M. V. Klein, M. D. Sturge, and E. Cohen, Phys. Rev. **B25**, 4331 (1982).

[6] G. Lasher and F. Stern, Phys. Rev. **133**, A553 (1964).

[7] H. C. Casey, J. Appl. Phys. **49**, 3684 (1978).

[8] N. Lifshitz, A. Jayaraman, R. A. Logan, and H. C. Card, Phys. Rev. **B21**, 670 (1980).

[9] J. S. Blakemore, J. Appl. Phys. **53**, R123 (1982).

[10] P. Lawaetz, Phys. Rev. **B4**, 3460 (1971).

[11] D. J. Wolford, W. Y. Hsu, J. D. Dow, B. G. Streetman, J. Lumin. **18/19**, 863 (1978).

[12] M. Capizzi, S. Modesti, A. Frova, J. L. Staehli, M. Guzzi, and R. A. Logan, Phys. Rev. **B29**, 2028 (1984).

[13] P. J. Pearah, W. T. Masselink, J. Klem, T. Henderson, H. Morkoc, C. W. Litton, and R. C. Reynolds, Phys. Rev. **B32**, 3857 (1985).

[14] Strictly speaking, the correlation energy is modified by the number of degenerate valleys and the effective mass of the X-bands where they actually reside. This effect is small, however (on the order of our experimental uncertainty), and we neglect it. See Ref. [1].

[15] M. Combescot and P. Nozieres, J. Phys. **C5**, 2369 (1972), P. Vashista, P. Bhattacharyya, and K. S. Singwi, Phys. Rev. **B10**, 5108, (1974).

Figure Captions

Figure 1. Time-resolved luminescence spectra and line-shape fits (dots) for alloy compositions below (a) and above (b) the direct-indirect band crossover. The solid and dashed curves in (b) represent contributions from quasidirect and phonon-assisted transitions, respectively.

Figure 2. Band-gap energies at the Γ- and X-points versus alloy composition, x. Solid lines represent unrenormalized gaps, vertical bars measured renormalized gaps, dotted bands theoretical values according to Ref. [1], striped band corrected for missing electron-exchange energy.

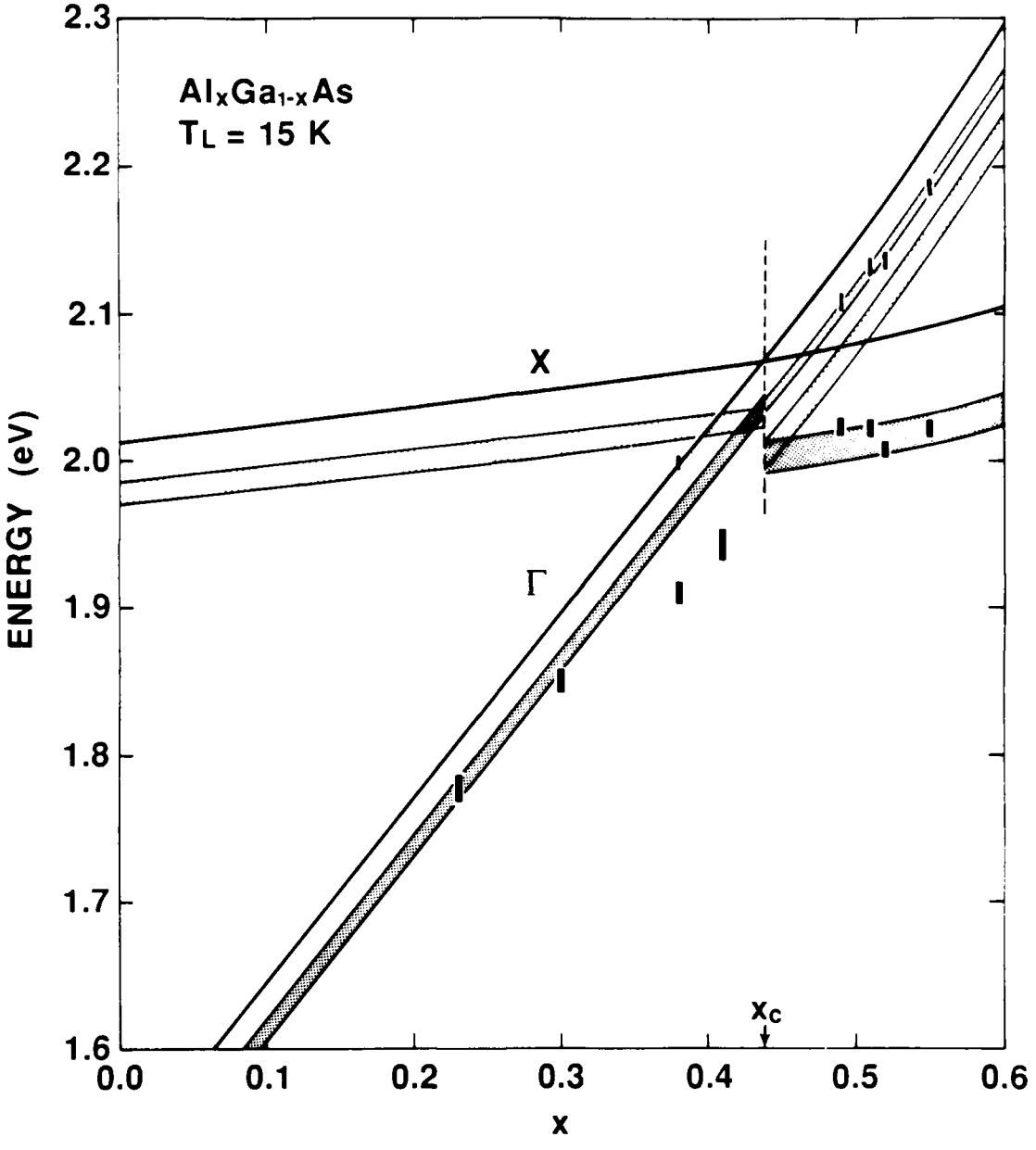
$Al_xGa_{1-x}As$
T_L = 15 K
ENERGY (eV)
2.3
2.2
2.1
2.0
1.9
1.8
1.7
1.6
X
Γ
x_c
0.0
0.1
0.2
0.3
0.4
0.5
0.6
x

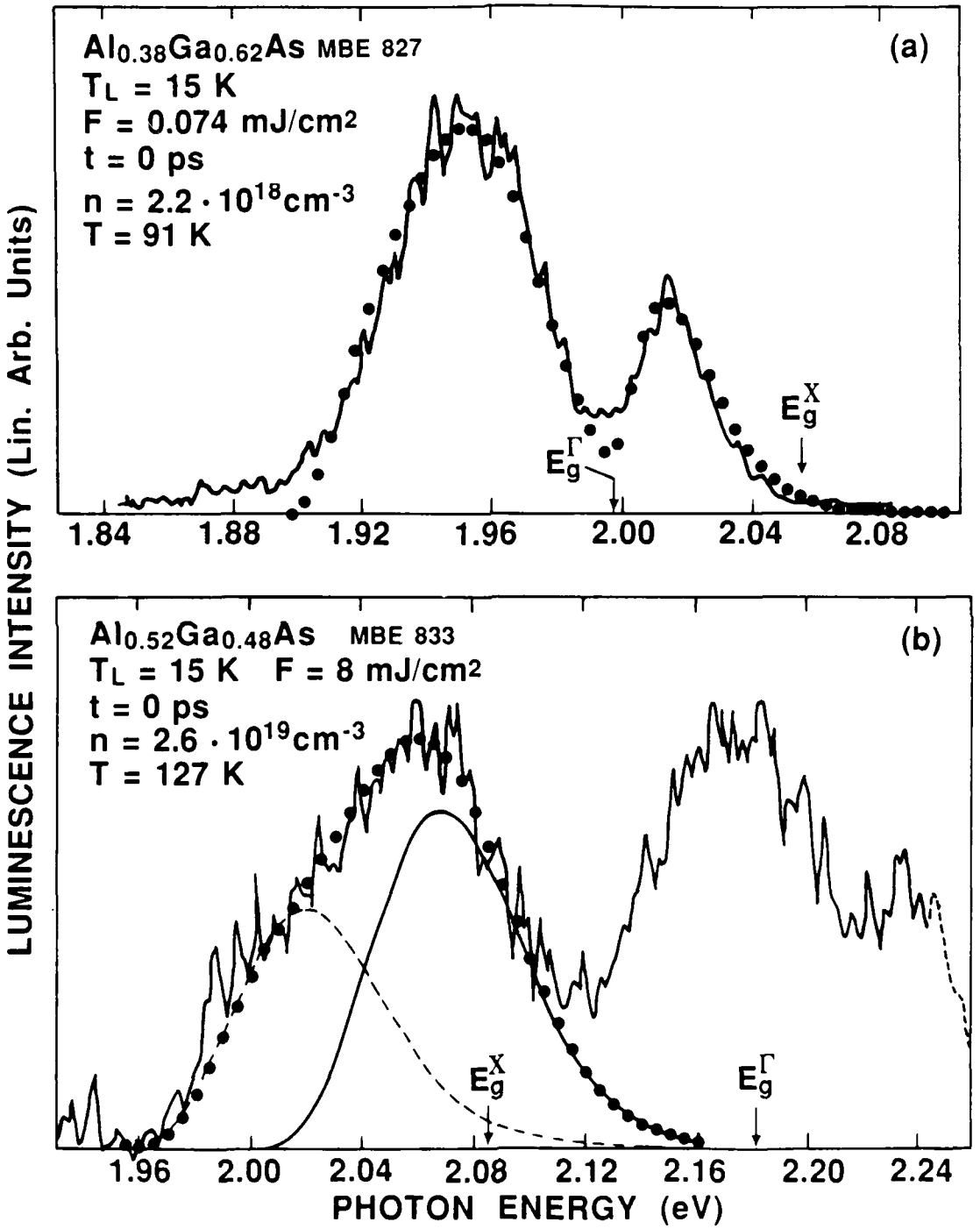
Al0.38Ga0.62As MBE 827
(a)
TL = 15 K
F = 0.074 mJ/cm2
t = 0 ps
n = 2.2 · 10^18 cm^-3
T = 91 K
Eg^X
Eg^Γ
1.84
1.88
1.92
1.96
2.00
2.04
2.08
Al0.52Ga0.48As MBE 833
(b)
TL = 15 K F = 8 mJ/cm2
t = 0 ps
n = 2.6 · 10^19 cm^-3
T = 127 K
Eg^X
Eg^Γ
1.96
2.00
2.04
2.08
2.12
2.16
2.20
2.24
PHOTON ENERGY (eV)
LUMINESCENCE INTENSITY (Lin. Arb. Units)

Appendix E: Picosecond Observation of the Photorefractive Effect in GaAs.

A reprint of a paper published in Ultrafast Phenomena V, G.R. Fleming and A.E. Siegman, Eds. (Springer-Verlag, New York, 1986) pp 203-206.

ULTRAFAST PHENOMENA V, (SPRINGER-VERLAG, NY, 1986)

Picosecond Observation of the Photorefractive Effect in GaAs

A.L. Smirl[1], *G.C. Valley*[1], *M.B. Klein*[1], *K. Bohnert*[2], *and T.F. Boggess*[2]

[1]Hughes Research Laboratories, 3011 Malibu Canyon Road, Malibu, CA 90265, USA

[2]Center for Applied Quantum Electronics, North Texas State University, Denton, TX 76203, USA

For more than 15 years, photorefractive materials such as $LiNbO_3$, $BaTiO_3$ and $Bi_{12}SiO_{20}$ have been widely investigated for applications in holographic storage, optical data processing, and phase conjugation [1]. Previously, however, transient studies in these materials have been limited to time scales of ns or longer and to investigations of the photorefractive effect where the space charge field is produced between one-photon-ionized donors or acceptors and charged traps [2-4]. Although picosecond pulses and trains of pulses have been used to provide the large fields necessary for two-photon ionization of donors in $LiNbO_3$ [5,6] and potassium tantalate niobate (KTN) [7], no subnanosecond time resolution of the photorefractive processes was reported. More recently, the photorefractive effect has been demonstrated in the semiconductors GaAs, InP, and CdTe on time scales from 250 μs to steady state [8-11]. Here, we report (to the best of our knowledge) the first investigations of the photorefractive effect on picosecond time scales.

In our experiments, we measured the energy transferred between two 1.06 μm pulses that were spatially and temporally coincident in a GaAs sample. The laser source for our experiments was an actively and passively mode-locked Nd:YAG laser operating in the fundamental transverse mode. A single pulse was switched from the train of pulses and amplified. The pulse was then divided into two parts and recombined at a small angle in the sample. The optical pulse width was measured to be 43 ps (full width at e^{-1} of the intensity). We wish to emphasize that the crystal studied here is the same one that was used by KLEIN [9] in his cw experiments. The crystal cross section was 6 mm x 5 mm, and the thickness was 4 mm. The crystal orientation was identical to that used by KLEIN [9]. That is, the grating wave vector (sample surface) was along the (100) direction; both pulses were polarized along (110); and the surface normal was parallel to $(\bar{1}10)$. The beam diameters at the sample surface were 5 mm (full width e^{-1} of the maximum intensity), as determined by pinhole scans.

We measured the beam coupling as a function of the ratio of the energies in the two pulses, the total fluence, time delay between the two pulses, and crystal orientation. We found the direction of energy transfer between two equal beams to depend definitively on crystal orientation, an unambiguous signature of the photorefractive effect. Moreover, we measured photorefractive gains for weak picosecond signal pulses of a few percent using pump fluences of less than 0.2 mJ/cm^2 (i.e., 2pJ/μm^2). At these low fluences and times too short for significant carrier-trap recombination to occur, the space charge field is established between ionized donors and mobile free carriers, in contrast to the cw photorefractive effect where the space charge field is between immobile ionized donors and immobile traps. As a consequence, for picosecond pulses, the space charge field in this regime is limited by the number of available donors; whereas, for cw radiation the limiting field is determined by the trap density. The former

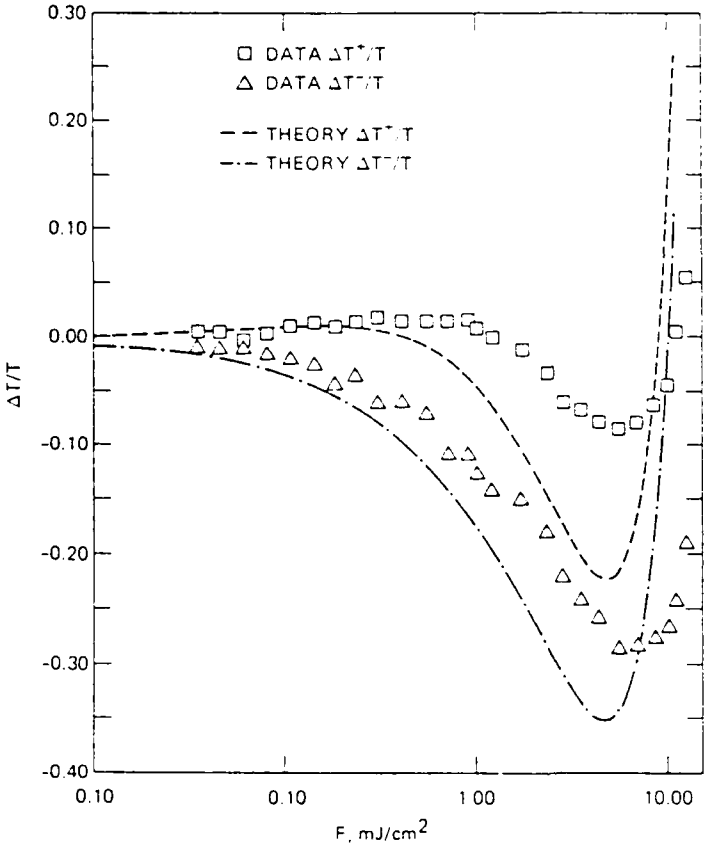

Fig. 1. The normalized change in the probe transmission for the sample oriented for photorefractive energy transfer from strong to weak beam, $\Delta T^+/T$ (squares), and the normalized change in probe transmission for the sample oriented for photorefractive energy transfer from weak to strong, $\Delta T^-/T$ (triangles), as a function of the pump fluence for a grating spacing of 1.7 μm and a constant pump-to-probe ratio of 20:1. The dashed and dashed-dot curves are the results of theoretical calculations for the two orientations, respectively.

is believed to be an order of magnitude larger than the latter. For higher fluences and these pulsewidths, investigations of the photorefractive gratings are complicated by the onset of two-photon absorption and the accompanying absorptive and refractive index changes. In fact, at the highest fluences, the photorefractive energy transfer is dominated by a space charge field that originates from the separation between mobile free electrons and mobile free holes generated by two-photon absorption.

An example of such measurements is shown in Fig. 1. Here, the normalized change in probe transmission $\Delta T/T$ is shown as a function of pump fluence for a pump-to-probe ratio of 20:1. The quantity $\Delta T/T$ is defined as the probe energy transmission with the pump present minus the probe transmission without the pump, both divided by the probe energy transmission without the pump:

$$\Delta T/T = [T \text{ (with pump)} - T \text{ (without pump)}]/T \text{ (without pump)}. \quad (1)$$

The squares ($\Delta T^+/T$) represent data acquired with the crystal oriented such that photorefractive energy transfer is from the strong to the weak beam; the triangles ($\Delta T^-/T$) represent data taken after the crystal was rotated 180° about the surface normal that bisects the angle between the two beams. We have performed theoretical calculations based on a simple set of materials equations combined with Maxwell's equations. The materials equations used here differ from those used previously [12,13,14] in that they were modified to include two-photon absorption and neglect recombination. The results of such a numerical calculation for the two crystal orientations

are shown by the dashed and dot-dashed curves in Fig. 1. We wish to emphasize that these curves are the result of a zero-fit-parameter calculation. That is, all material parameters were either taken from the literature or independently measured for this sample. Quantitative agreement between experiment and theory can be easily achieved by varying these material parameters within reasonable uncertainties, but without additional independent measurements there is no justification for such a forced fit. In any event, qualitative agreement between calculated and measured data is quite satisfactory.

The qualitative interpretation of the data of Fig. 1 that emerges from such studies is as follows. For the top curve, photorefractive gain initially competes with loss from two photon absorption. For the lowest fluences, photorefractive transfer is larger than the two-photon loss, and a net gain is observed. Eventually, as the fluence is increased, all of the EL2 donors are ionized, and two-photon absorption begins to dominate, with a zero crossing near 1 mJ/cm^2. Finally, however, we note that two-photon absorption is accompanied by the generation of electron-hole pairs. That is, a free-carrier grating is produced. Because the real part of the Drude index of refraction is much larger than the imaginary part, an index grating is created that is in phase with the modulated intensity profile. It is well known that such a grating cannot transfer energy in steady state; however, in the transient regime, there is a higher-order transfer that is always from strong to weak beam [15]. This transient transfer was found to dominate at the higher fluences, resulting in probe gain for fluences larger than approximately 10 mJ/cm^2, as shown. For the lower curve, the photorefractive energy transfer is from probe to pump, and photorefractive effects as well as two photon absorption contribute to increasing probe loss with increasing fluence. Again, however, at the highest fluences, transient energy transfer begins to dominate and to reverse the sign of the slope.

Finally, we can isolate and separate the photorefractive contributions from those of two-photon absorption and free-carrier transient energy transfer by recognizing that (in the small signal limit) only photorefrac-

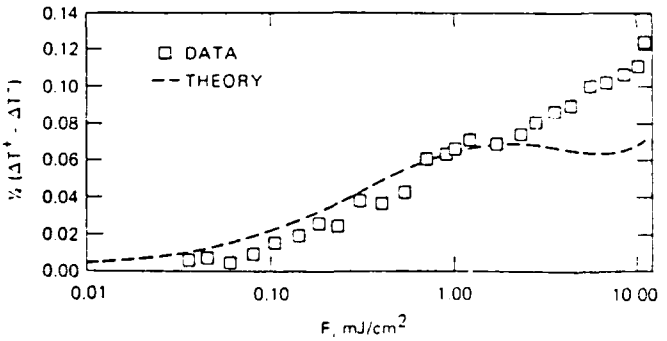

Fig. 2. Half the difference between the normalized change in the probe transmission for the sample oriented for photorefractive probe gain ($\Delta T^+/T$) and the change in the probe transmission for the sample oriented for photorefractive probe loss ($\Delta T^-/T$) as a function of pump fluence for a grating spacing of 1.7 μm and a constant pump-to-probe ratio of 20:1 (i.e., half the difference between the squares and the triangles in Fig. 1). The dashed curve is one half the corresponding difference between the two theoretical curves of Fig. 1.

tive energy transfer explicitly depends on crystal orientation. When the crystal is oriented for weak to strong beam transfer, the photorefractive grating contributes to probe loss; when the crystal is rotated 180° about the surface normal, the photorefractive energy transfer is reversed and is from strong to weak, while the other two contributions maintain their sign. Consequently, twice the photorefractive energy transfer is obtained by subtracting the two curves shown in Fig. 1. The photorefractive energy transfer obtained in this way is shown in Fig. 2. We emphasize that there are two distinct contributions to the photorefractive transfer. At low fluences, the space charge field is primarily between one-photon-generated mobile free electrons and immobile ionized EL2$^+$ donors. At higher fluences, the space charge field (i.e. Dember field) between two-photon-generated free electrons and free holes also contributes.

References

1. P. Gunter, Phys. Repts. **93**, 200 (1983).
2. C.-T. Chen, D.M. Kim, and D.von der Linde, Appl. Phys. Lett. **34**, 321 (1979).
3. L.K. Lam, T.Y. Chang, J.Feinberg, and R.W. Hellwarth, Opt. Lett. **6**, (1981).
4. J.P. Hermann, J.P. Herriau, and J.P. Huignard, Appl. Opt. **20**, 2173 (1981).
5. D. Von Der Linde, A.M. Glass, and K.F. Rodgers, Appl. Phys. Lett. **25**, 155 (1974).
6. D. von der Linde, O.F. Schirmer, and H. Kurz, Appl. Phys. **15**, 167 (1978).
7. D. von der Linde, A.M. Glass, and K.F. Rodgers, Appl. Phys. Lett. **26**, 22 (1975).
8. A.M. Glass, A.M. Johnson, D.H. Olson, W. Simpson and A.A. Ballman, Appl. Phys. Lett. **44**, 948 (1984).
9. M.B. Klein, Opt. Lett. **9**, 350 (1984).
10. J. Strait and A.M. Glass, J. Opt. Soc. Am.B **3**, 342 (1986); A.M. Glass, M.B. Klein, and G.C. Valley, Electron. Lettr. **211**, 220 (1985).
11. J. Strait and A.M. Glass, Appl. Opt. **255** 338 (1986).
12. V.L. Vinetskii and N.V. Kukhtarev, Sov. Phys. Solid State, **165**, 2414 (1975).
13. N.V. Kukhtarev, Pis'ma Zh. Tekh. Fiz. **2**, 1114 (1976) [Sov. Tech. Phys. Lett **2**, 438 (1976)]; G.C. Valley, IEEE J. Quantum Electron., QE-19, 1637 (1983).
14. G.C. Valley, J. Appl. Phys. **59**, 3363 (1986); F.P. Strohkendl, J.M.C. Jonathan, and R.W. Hellwarth, Opt. Lett. **11**, 312 (1986).
15. V.L. Vinetskii, N.V. Kukhtarev, and M.S. Soskin, Sov. J. Quantum Electron. **7**, 230 (1977).

Appendix F: Picosecond Photorefractive Beam Coupling in GaAs.

A reprint of a paper published in Optics Letters 11, 647 (1986).

Reprinted from Optics Letters, Vol. 11, page 647, October 1986

Picosecond photorefractive beam coupling in GaAs

George C. Valley, Arthur L. Smirl, and M. B. Klein

Hughes Research Laboratories, Malibu, California 90265

K. Bohnert and Thomas F. Boggess

Center for Applied Quantum Electronics, North Texas State University, Denton, Texas 76203

Received June 12, 1986; accepted July 16, 1986

We report the first observation to our knowledge of the photorefractive effect on picosecond time scales. Photorefractive beam coupling in GaAs with picosecond, 1.06-μm pulses is observed owing to charge separation between electrons and the ionized defect $EL2^+$ at low fluences and to separation between free electrons and holes created by two-photon interband absorption for high fluences. The accompanying processes of linear absorption, two-photon absorption, and transient energy transfer are also observed.

Photorefractive materials such as $LiNbO_3$, $BaTiO_3$, and $Bi_{12}SiO_{20}$ have been widely investigated over the past 15 years for applications in holographic storage, optical data processing, and phase conjugation.[1] Recently the photorefractive effect was demonstrated in the semiconductors GaAs, InP, and CdTe on time scales from 250 μsec to steady state.[2-5] Here we report the observation of beam coupling in GaAs due to the photorefractive effect with single 43-psec pulses of 1.06-μm radiation. Our results are attributed to the charge separation between photoionized, untrapped electrons and the ionized donor level $EL2^+$ at low fluences F ($F < 0.3$ mJ/cm^2) and to the separation between untrapped electrons and holes created by two-photon absorption for high fluences ($F > 3$ mJ/cm^2).

Previously, the photorefractive effect due to one-photon ionization and charges trapped at donor or acceptor sites has been observed with pulses as short as 10 nsec in $LiNbO_3$, $BaTiO_3$, and $Bi_{12}SiO_{20}$.[6-8] Moreover, the photorefractive effect due to two-photon ionization of donors has been produced by trains of picosecond pulses in $LiNbO_3$ (Refs. 9 and 10) and by a single picosecond pulse and trains in potassium tantalate niobate (KTN).[11] The minimum time needed to produce a grating was observed to be less than a few nanosceconds[7] to less than 2 nsec,[10] limited by the time resolution of the experiments. Our results in GaAs show that it is possible to produce a photorefractive effect a factor of 100 to 1000 times faster than these time scales. In addition, our results show for the first reported time that a photorefractive effect can be produced by the charge separation between untrapped electrons and ionized donor levels ($EL2^+$) and also by the charge separation of electrons and holes created by two-photon interband absorption.

Our experiments were performed using the same sample of semi-insulating, undoped GaAs and the same experimental configuration reported previously.[3] The sample is 5 mm × 5.5 mm × 3.3 mm with the 3.3-mm length along the direction of propagation. Properties of our sample were reported in Ref. 3 or inferred from the literature as given in Table 1. The deep level $EL2$,[17,18] which exists in both a neutral and a positively ionized state, was identified as the source of the steady-state photorefractive effect by the excellent agreement between the measurement of the ionized $EL2$ number density N^+ from conductivity as a function of temperature ($N^+ = 1.4 \times 10^{15}$ cm^{-3}) and from photorefractive beam coupling ($N^+ = 1.3 \times 10^{15}$ cm^{-3}).[3] In addition, the absorption spectrum of our sample is similar to the $EL2$ absorption spectrum reported in Ref. 18.

The laser source for our experiments was an actively and passively mode-locked Nd:YAG laser operating in the fundamental transverse mode. A single pulse was switched from the train of pulses and amplified. The average pulse width, measured on a shot-by-shot basis, was 43 psec full width at $1/e$ of the peak irradiance. After amplification the pulse was divided into two parts and recombined at an angle to give a grating period of 1.7 μm in the crystal. As in Ref. 3, both pump and probe were polarized along the (110) direc-

Table 1. Parameters of the GaAs Crystal Used for Picosecond Beam Coupling

Parameter	Value	Reference
Refractive index, n_b	3.48	12
Dielectric constant, ϵ/ϵ_0	12.9	13
Electro-optic coefficient, r_{41}	1.43 pm/V	14
Absorption coefficient, α	1.2 cm^{-1}	3
Two-photon absorption coefficient, β	26. cm/GW	15
Free-carrier cross section, s_{fc}	3×10^{-18}	15
Electron Hall mobility, μ_H	5800 cm^2/Vs	3
Electron drift mobility, μ_n	$\mu_H/\mu_n = 1.175$	16
Hole drift mobility, μ_p	$\mu_n/\mu_p = 13$	17
Total $EL2$ density, N	1.3×10^{16} cm^{-3}	18[a]
Ionized $EL2$ ($EL2^+$) density, N^+	1.4×10^{15} cm^{-3}	3
$EL2$ cross section, s_e	$<\alpha/(N - N^+)$	[b]
$EL2^+$ cross section, s_h	$s_e/4$	17

[a] This value is extrapolated from Fig. 2 of Ref. 18 using the absorption coefficient of 1.2 cm^{-1} measured in our sample.

[b] $s_e = \alpha/(N - N^+)$ when the quantum efficiency for mobile electron generation from $EL2$ donors is one and there is no other absorption processes in the material.

0146-9592/86/100647-03$2.00/0

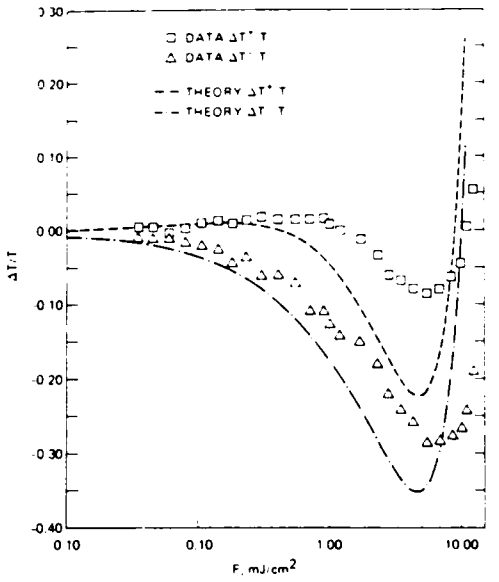

Fig. 1. Normalized change in transmission of the probe beam $\Delta T/T$ as a function of the peak pump fluence for a grating spacing of 1.7 μm and a constant pump-to-probe ratio 23:1. The sample was rotated 180° about the surface normal between measurements represented by the squares and triangles. The dashed and dotted-dashed lines represent theoretical fits using the parameters of Table 1.

tion and the grating wave vector pointed in the (001) direction. The beam diameters at the sample were 5 mm (full width at e^{-1} of the maximum irradiance), as determined by pinhole scans performed in both the horizontal and vertical directions.

For fluences sufficient for observation of significant energy transfer, investigation of the photorefractive effect is complicated by two-photon absorption and free-carrier refractive-index changes. This is illustrated in Fig. 1, where the quantity $\Delta T/T$ is plotted as a function of peak pump fluence with the incident probe-to-pump energy ratio held constant at 4.4%. The quantity $\Delta T/T$ is defined as the probe energy transmission with the pump present minus the transmission without the pump, all divided by the probe energy transmission T without the pump:

$$\frac{\Delta T}{T} = \frac{T(\text{with pump}) - T(\text{without pump})}{T(\text{without pump})}. \quad (1)$$

Note that for small gain or loss the quantity $\Delta T/T$ is independent of linear absorption [e.g., if we could write the photorefractive gain simply as $\exp(\Gamma L)$ and the loss as $\exp(-\alpha L)$, $\Delta T/T$ would equal ΓL for small ΓL]. The two curves shown in Fig. 1 are for two orientations of the crystal. The top curve (squares) represents data acquired with the crystal oriented such that protorefractive energy transfer is from pump beam to probe; the bottom curve (triangles) represents data taken after the crystal was rotated by 180° about the surface normal that bisects the angle between the two beams. Figure 1 shows that the energy transfer depends on crystal orientation, an unambiguous signature of the photorefractive effect. In the top curve the photorefractive gain competes with loss from two-photon absorption at fluences below 3 mJ/cm^2 with a zero crossing at 1 mJ/cm^2, while in the lower curve both effects cause probe loss. At fluences above 3 mJ/cm^2 transient energy transfer[19] by the free-carrier grating transfers energy from the strong to the weak beam in each orientation.

In order to isolate the photorefractive effect, we subtract the data for the two orientations given in Fig. 1. If the two-photon absorption and the free-carrier transient energy transfer are independent of the photorefractive effect (which is true for sufficiently small energy transfer and no pump depletion, conditions of our experiments), then the difference between $\Delta T/T$ for the two orientations should be twice the energy transfer due to the photorefractive effect alone. These data points are shown by the squares in Fig. 2.

We have performed detailed numerical calculations to determine if the data in Fig. 2 are consistent with the photorefractive effect due to production and transport of charge carriers, an internal space-charge field due to charge separation, and a change in the refractive index through the electro-optic effect. Our calculations also include saturation of the $EL2$ absorption, the free-carrier absorption and refractive index, and two-photon absorption, all of which contribute to $\Delta T/T$. The set of materials equations used for this modeling differs from that used previously[20,21] by the addition of the two-photon ionization and the neglect of recombination, which is not important in GaAs on time scales less than 100 psec (Ref. 22):

$$\partial N^+/\partial t = s_e I(N - N^+/(h\nu) - s_h I N^+/(h\nu), \quad (2)$$

$$\partial p/\partial t = -(1/e)\partial j_p/\partial z + \beta I^2/(2h\nu) + s_h I N^+ f(h\nu), \quad (3)$$

$$\partial n/\partial t = (1/e)\partial j_n/\partial z + \beta I^2/(2h\nu) + s_e I(N - N^+)/(h\nu), \quad (4)$$

$$j_p = e\mu_p E p - \mu_p k_B T \partial p/\partial z, \quad (5)$$

$$j_n = e\mu_n E n + \mu_n k_B T \partial n/\partial z, \quad (6)$$

$$\partial E/\partial z = (e/\epsilon)(p + N^+ - n - N_A), \quad (7)$$

where z is the coordinate perpendicular to the direction of propagation, I is the irradiance, p, n, j_p, and j_n

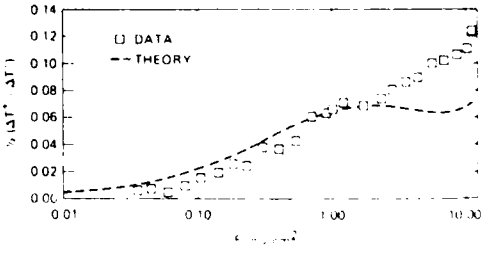

Fig. 2. Normalized change in probe transmission for the sample oriented for energy transfer from the strong to the weak beam $(\Delta T/T)^+$ minus that for transfer from weak to strong $(\Delta T/T)^-$ as a function of peak pump fluence for a grating spacing of 1.7 μm and a constant pump-to-probe ratio of 23:1. The dashed line indicates numerical calculations made using rate and transport equations combined with Maxwell's equations.

are the hole and electron number and current densities, $h\nu$ is the photon energy, and k_BT is Boltzmann's constant times temperature. N_A is the number density of negative ions that compensate for the charge of N^+ in the dark but that cannot be photoionized (these are thought to be carbon ions). The remainder of the parameters are defined in Table 1. These equations are combined with Maxwell's equations including the effects listed above and solved numerically.

Results of the numerical calculations for the two crystal orientations are shown by the dashed and dotted–dashed curves in Fig. 1. These curves use one unknown parameter, the quantum efficiency of the $EL2$ donor, as a fitting parameter. The calculations shown in Fig. 1 use a quantum efficiency of 0.58, which is consistent with other photorefractive studies[23] and other studies of $EL2$.[24] In our calculations we have modeled the free-carrier index with and without the interband correction factor.[25] The results shown in Fig. 1 are without the interband correction factor; results with the correction factor fit the data quite poorly. Excellent quantitative agreement between experiment and theory can be achieved easily by varying the other material parameters within physically reasonable limits, but without additional independent measurements there is no justification for such a forced fit. In particular, the high-fluence region of the curve is very sensitive to the hole mobility, the two-photon absorption coefficient, and the interband correction factor.

The qualitative interpretation from comparison of the calculations with the data in Fig. 1 is quite clear. For the top curve, photorefractive gain initially competes with loss from two-photon absorption, and a net gain is observed. Eventually, as the fluence is increased, all the $EL2$ donors are ionized, and two-photon absorption begins to dominate, with a zero crossing near 1 mJ/cm^2. Finally, the electron and hole densities become sufficiently large that the free-carrier grating (the real part of the Drude index) can transfer energy from the strong beam to the weak beam.[19] This results in probe gain for fluences larger than about 10 mJ/cm^2, as shown. For the lower curve, the photorefractive energy transfer is from probe to pump, and this and two-photon absorption contribute to increasing probe loss with increasing fluence. Again, however, at the highest fluences, transient energy transfer begins to dominate and to reverse the sign of the slope of $\Delta T/T$ as a function of F.

Finally, we can isolate the photorefractive contributions from those of two-photon absorption and free-carrier transient energy transfer by recognizing that (in the small-signal limit) only photorefractive energy transfer explicitly depends on crystal orientation. When the crystal is oriented for weak to strong beam transfer, the photorefractive grating contributes to probe loss; when the crystal is rotated 180° about the surface normal, the photorefractive energy transfer is reversed and is from strong to weak beam, while the other contributions maintain their signs. Consequently, twice the photorefractive part of $\Delta T/T$ is obtained by subtracting the two curves shown in Fig. 1. Both the experimental data and the theoretical calculations are shown this way in Fig. 2. At low fluences the space-charge field leading to the photorefractive effect is primarily between one-photon-generated mobile electrons and immobile ionized $EL2^+$ donors. At higher fluences, the space-charge field between two-photon-generated free electrons and holes also contributes. At the highest fluences, transient energy transfer and the photorefractive effect appear to interact in a nonlinear way.

The authors are grateful to A. Hunter of Hughes Research Laboratories for helpful discussions of the properties of GaAs. The work at North Texas State University was supported by the U.S. Office of Naval Research and the Robert A. Welch Foundation; the work at Hughes Research Laboratories, in part by the U.S. Air Force Office of Scientific Research.

References

1. P. Günter, Phys. Rep. **93**, 199 (1983).
2. A. M. Glass, A. M. Johnson, D. H. Olson, W. Simpson, and A. A. Ballman, Appl. Phys. Lett. **44**, 948 (1984).
3. M. B. Klein, Opt. Lett. **9**, 350 (1984).
4. J. Strait and A. M. Glass, J. Opt. Soc. Am. B **3**, 342 (1986); A. M. Glass, M. B. Klein, and G. C. Valley, Electron. Lett. **21**, 220 (1985).
5. J. Strait and A. M. Glass, Appl. Opt. **25**, 338 (1986).
6. C.-T. Chen, D. M. Kim, and D. von der Linde, Appl. Phys. Lett. **34**, 321 (1979).
7. L. K. Lam, T. Y. Chang, J. Feinberg, and R. W. Hellwarth, Opt. Lett. **6**, 475 (1981).
8. J. P. Hermann, J. P. Herriau, and J. P. Huignard, Appl. Opt. **20**, 2173 (1981).
9. D. von der Linde, A. M. Glass, and K. F. Rodgers, Appl. Phys. Lett. **25**, 155 (1974).
10. D. von der Linde, O. F. Schirmer, and H. Kurz, Appl. Phys. **15**, 167 (1978).
11. D. von der Linde, A. M. Glass, and K. F. Rodgers, Appl. Phys. Lett. **26**, 22 (1975).
12. D. T. F. Marple, J. Appl. Phys. **35**, 1241 (1964).
13. K. S. Champlin, R. J. Erlandson, G. H. Glover, P. S. Hauge, and T. Lu, Appl. Phys. Lett. **11**, 348 (1967).
14. M. Sugie and K. Tada, Jpn. J. Appl. Phys. **15**, 421 (1976).
15. T. F. Boggess, Jr., A. L. Smirl, S. C. Moss, I. W. Boyd, and E. W. van Stryland, IEEE J. Quantum Electron. **QE-21**, 488 (1985).
16. J. S. Blakemore, J. Appl. Phys. **53**, R123 (1982).
17. W. Walukiewicz, J. Lagowski, and H. C. Gatos, Appl. Phys. Lett. **43**, 192 (1983).
18. G. M. Martin, Appl. Phys. Lett. **39**, 747 (1981).
19. V. L. Vinetskii, N. V. Kukhtarev, and M. S. Soskin, Kvantovaya Elektron. (Moscow) **4**, 420 (1977) [Sov. J. Quantum Electron. **7**, 230 (1977)].
20. N. V. Kukhtarev, Pis'ma Zh. Tekh. Fiz. **2**, 1114 (1976) [Sov. Tech. Phys. Lett **2**, 438 (1976)]; G. C. Valley, IEEE J. Quantum Electron. **QE-19**, 1637 (1983).
21. G. C. Valley, J. Appl. Phys. **59**, 3363 (1986); F. P. Strohkendl, J. M. C. Jonathan, and R. W. Hellwarth, Opt. Lett. **11**, 312 (1986).
22. J. S. Weiner and P. Y. Yu, J. Appl. Phys. **55**, 3889 (1984).
23. R. A. Mullen and R. W. Hellwarth, J. Appl. Phys. **58**, 40 (1985).
24. M. Kaminska, M. Skowronski, J. Lagowski, J. M. Parsey, and H. C. Gatos, Appl. Phys. Lett. **43**, 302 (1983).
25. R. K. Jain and M. B. Klein, in *Optical Phase Conjugation*, R. A. Fisher, ed. (Academic, New York, 1983), Chap. 10, p. 307.

Appendix G: Picosecond Photorefractive Effect in $BaTiO_3$.

A reprint of a paper published in Optics Letters 12, 501 (1987).

Reprinted from Optics Letters, Vol. 12, page 501, July 1987.

Picosecond photorefractive effect in $BaTiO_3$

Arthur L. Smirl, George C. Valley, and Ruth Ann Mullen

Hughes Research Laboratories, Malibu, California 90265

K. Bohnert, C. D. Mire, and Thomas F. Boggess

Center for Applied Quantum Electronics, Department of Physics, North Texas State University, Denton, Texas 76203

Received January 26, 1987; accepted March 30, 1987

We report the observation of photorefractive index gratings written and read out in $BaTiO_3$ using single pulses of 30-psec duration and fluences of 1 to 15 mJ/cm^2 at a wavelength of 0.532 μm. While the photorefractive gratings are masked during formation by a large free-carrier grating, they are clearly seen from 50 psec to many minutes following the peak in the writing beams. The rapid and complete formation of the photorefractive grating and the complete decay of the free-carrier grating on a scale of 50 to 100 psec indicate either that the carrier-recombination time in our sample of $BaTiO_3$ is less than 100 psec or that the mobility of the carriers is >23 cm^2/V sec.

In a typical photorefractive measurement, two noncollinear light beams interfere in the material to produce a spatial modulation of the optical irradiance with period Λ_g. The conventional explanation of the photorefractive effect, which has proved widely applicable to both cw and nanosecond pulsed observations,[1] is that the absorption of this light produces (by photoionization) a spatially modulated carrier distribution with the same period; that the carriers then diffuse from regions of higher concentration to regions of lower concentration (or drift in an applied field) and are eventually retrapped; and that this is accompanied by the formation of a periodic space-charge field within the crystal. The space-charge field then modulates the refractive index through the electro-optic effect. The time required for grating formation is thus determined by the rate at which carriers are generated, by their drift or diffusion rates, and by their recombination lifetimes. The maximum space-charge field will be obtained if the carriers diffuse (or drift) one-half grating period. If the recombination lifetime is sufficiently short, however, the carriers will move only a fraction of a grating period before being retrapped, and a weaker space-charge field will be established.

For short-pulsed excitation, the carrier-generation rate can exceed significantly the recombination rate, and large densities of photoionized (or free) carriers can be produced. These free carriers are the source of a second index grating through the usual Drude (or band-filling) contribution to the index of refraction. In contrast to the case of a photorefractive grating, here carrier diffusion or drift is not required to establish the free-carrier index change. Moreover, while the diffusion of carriers for roughly one-half grating period produces an optimal photorefractive response, diffusion over this distance totally destroys the free-carrier modulation. Thus a large mobility generally indicates a larger photorefractive sensitivity and a faster response but dictates a shorter free-carrier grating lifetime. By comparison, a shorter carrier-recombination time can lessen the photorefractive response and will hasten the free-carrier grating decay.

We recently reported observation of the photorefractive effect in GaAs on picosecond time scales.[2] These results are of interest but are not completely surprising because the large electron mobility in GaAs (~6000 cm^2/V sec) leads to diffusion times of the order of 5 psec for the 1.7-μm grating period reported in Ref. 2. Thus there was ample time for carriers to diffuse one or more grating periods during our 43-psec pulses, and the charge separation necessary for establishing the photorefractive effect could be obtained. Here we report the writing of free-carrier and photorefractive gratings in $BaTiO_3$ with 30-psec pulses and find that the photorefractive grating is fully formed and that the free-carrier grating has decayed within 50 to 100 psec after the peak intensity of the writing beams. This suggests either that the carriers have diffused roughly one-half grating period or that they have recombined in this time. Since the mobilities of both electrons and holes in $BaTiO_3$ (as measured by conventional transport techniques) are widely reported to be of the order of 1 cm^2/V sec or less,[3] at least 2 nsec should be required for diffusion to destroy the 0.48-μm-period free-carrier gratings used in our $BaTiO_3$ experiments. If the mobility of our charge carriers is less than 1 cm^2/V sec, our photorefractive grating must be produced by excitation of a large number of carriers and by their diffusion for a small fraction of a grating period.

The basic geometry used in our experiments is shown in Fig. 1. Two 30-psec (full width at e^{-1} of the intensity) pulses, labeled PUMP 1 and PUMP 2, that were derived from a single frequency-doubled pulse produced by a mode-locked Nd:YAG laser interfered in the crystal to form a grating of period 0.48 μm. The grating formation and decay were interrogated by a third, time-delayed probe pulse that was counterpropagating to one of the writing pulses. The writing pulses were *p* polarized, and the probe was *s* polarized. Initially, the 1.82-mm-thick crystal was oriented so that the grating *k* vector was parallel to the *c* axis ($\mathbf{k}_g \parallel \mathbf{c}$). Subsequently, the crystal was rotated so that the *k* vector was perpendicular to the *c* axis ($\mathbf{k}_g \perp \mathbf{c}$).

0146-9592/87/070501-03$2.00/0

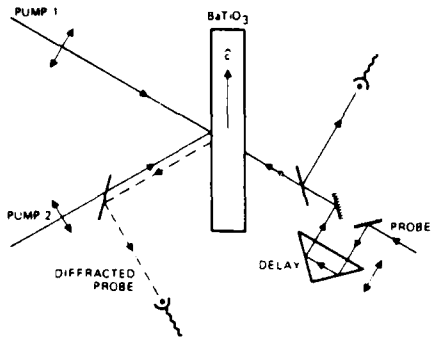

Fig. 1. Experimental geometry.

Figure 2 shows the measured diffraction efficiency as a function of probe delay for the case in which the fluence of each writing pulse was 6 mJ/cm^2. In Fig. 2(A), the data were acquired with the crystal as shown in Fig. 1 ($\mathbf{k}_g \parallel \mathbf{c}$), so that the probe pulse could sense a change in the refractive index due to the internal space-charge field and the r_{13} electro-optic coefficient (photorefractive effect). To obtain the data shown in Fig. 2(B), the crystal was rotated by 90° ($\mathbf{k}_g \perp \mathbf{c}$), so that any internal space-charge field produced by the pump beams would not produce a refractive-index variation that would be sensed by an s-polarized probe.

Two distinct features are evident in the data shown in Fig. 2. The first is a strong peak with a width of approximately 50 psec, roughly consistent with the intensity autocorrelation time of our pulses. The strength and the duration of this peak are independent of crystal orientation and are consistent with diffraction from a free-carrier index grating generated by single-photon absorption. The short duration and the symmetry of the peak suggest that the free-carrier grating decays by either diffusion or recombination in less than 50 psec.

The second feature, a relatively constant, long-lasting diffraction efficiency, is roughly 50 times weaker than the peak and is present only in the ($\mathbf{k}_g \parallel \mathbf{c}$) geometry—a definitive signature of the photorefractive effect. The flat nature of this signal for tens of nanoseconds following excitation suggests that photorefractive grating formation is essentially complete shortly after the end of the excitation pulses. From this and from the rapid decay of the free-carrier peak, we conclude that the free-carrier grating is generated and decays by diffusion and recombination to form a long-lived photorefractive grating in less than 50 psec.

Our observations and conclusions can be explained by invoking either a carrier-recombination time τ_R of less than 100 psec or a mobility parallel to the c axis, $\mu_\parallel$, sufficiently large to ensure that the time required for diffusion to destroy a sinusoidal free-carrier grating is less than 100 psec. This diffusion time is given by

$$\tau_D = \frac{e\Lambda_g^2}{4\pi^2 k_B T \mu_\parallel}, \qquad (1)$$

where e is the elementary charge, k_B the Boltzmann constant, and T the temperature. We emphasize that, solely on the basis of the data shown in Fig. 2, we cannot tell which (or what combination) of these two processes is responsible for the picosecond photorefractive response of our crystal. Let us first examine the implications of assuming that the free-carrier grating decay is dominated by recombination, i.e., $\tau_R < 100$ psec and $\tau_R \ll \tau_D$. By substituting Eq. (1) into the latter inequality, one immediately finds that a recombination-dominated grating decay also implies a mobility–lifetime product of $\mu_\parallel \tau_R \ll 2.3 \times 10^{-9}$ cm^2/V. By comparison, assuming a diffusion-dominated grating decay ($\tau_D \ll \tau_R$) implies a mobility $\mu_\parallel > 23$ cm^2/V sec and a mobility–lifetime product of $\mu_\parallel \tau_R \gg 2.3 \times 10^{-9}$ cm^2/V. Clearly recombination and diffusion contribute equally when $\mu_\parallel \tau_R = 2.3 \times 10^{-9}$ cm^2/V.

These mobility–lifetime products can be compared with previous measurements of the mobility–lifetime product in $BaTiO_3$. Tzou *et al.*[4] used 8-nsec pulsed illumination to measure photorefractive grating erasure as a function of time. From this, they obtained a mobility–lifetime product parallel to the c axis of $\mu_\perp \mu_R = 5 \times 10^{-10}$ cm^2/V and a trap density $N_T = 2 \times 10^{16}$ cm^{-3} in their sample of $BaTiO_3$. Since the recombination time, $\tau_R = 1/(\gamma_R N_T)$ (where γ_R is the recombination rate coefficient), is inversely proportional to the trap density and since our sample has a trap density measured at $\lambda = 442$ nm of $N_T = 10^{17}$ cm^{-3}, we expect our mobility–lifetime product to be a factor of 5 smaller, $\mu_\perp \tau_R \simeq 10^{-10}$ cm^2/V. If this value is accurate, it is smaller than the $\mu_\parallel \tau_R = 2.3 \times 10^{-9}$ cm^2/V calculated in the preceding paragraph, and it indicates a recombination-dominated decay with $\tau_R < 100$ psec.

Moreover, if $\mu_\parallel \tau_R = 10^{-10}$ cm^2/V is taken to be correct and if the free-carrier grating decay τ_G is assumed to be determined approximately by $\tau_G = (1/\tau_R + 1/$

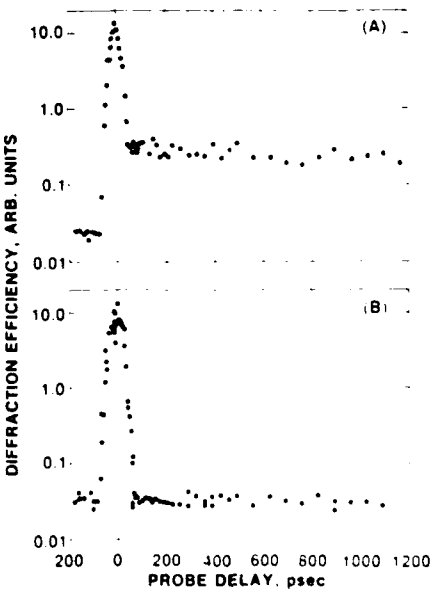

Fig. 2. Diffraction efficiency of a 0.48-μm laser-induced grating as a function of time delay for a crystal of $BaTiO_3$ oriented with the grating wave vector (a) parallel and (b) perpendicular to the c axis.

Table 1. Comparison of Parameters of 43-psec Experiments with Those of 20-nsec Experiments

Parameter	This Work	Lam *et al.*[a]
Wavelength, λ	0.532 μm	0.532 μm
Pulse length, τ_P	43 psec (FW $1/e$)	20 nsec
Total fluence, F	12 mJ/cm^2	400 mJ/cm^2
Grating period, Λ_g	0.48 μm	0.43 μm
Trap density, N_T	10^{17} cm^{-3} (0.442 μm)	2×10^{16} cm^{-3} (0.51 μm)
Writing polarization	p	s
Reading polarization	s	p
Diffraction efficiency, η	3×10^{-6}	5×10^{-3}
Recombination time, τ_R	<100 psec	<1 nsec
Interaction length	1.8 mm	1.2 mm

[a] Ref. 5.

$\tau_D)^{-1} < 100$ psec, then these two conditions when considered together yield the two inequalities $\tau_R < 100$ psec and $\mu_i > 1$ cm^2/Vsec, and they also dictate that the grating decay cannot be dominated by diffusion but must be dominated by recombination. Two examples of limiting cases serve to illustrate these points. First, consider a recombination time $\tau_R \sim 100$ psec. In this case, a mobility–lifetime product of $\mu\ \tau_R \sim 10^{-10}$ cm^2/V implies a mobility of $\mu_i \sim 1$ cm^2/V sec, which corresponds to a diffusion time of $\tau_D \sim 2$ nsec. Clearly, the free-carrier grating decay rate is determined by recombination. Not only is a mobility value of $\mu_i \sim 1$ cm^2/V sec consistent with the picosecond observations shown in Fig. 2 and with the values suggested by Tzou *et al.* for the hole mobility in their sample, but also it is a value that is in the range of those reported when conventional transport techniques are used.[3] Second, we take the mobility μ = 23 cm^2/V sec, from which a diffusion time of $\tau_D \sim 100$ psec can be calculated. Under these circumstances, a mobility–lifetime product $\mu_i \tau_R \sim 10^{-10}$ cm^2/V yields a recombination lifetime $\tau_R \sim 4$ psec. The free-carrier grating decay is again dominated by recombination. Consequently, if $\mu_i \tau_R \sim 10^{-10}$ cm^2/V and if the free-carrier grating decays simply by diffusion and recombination, then it will be dominated by recombination regardless of the value chosen for the mobility. All this comparison is dependent, of course, on the assumption that the rate coefficient and the mobility in our sample are roughly the same as in that used by Tzou *et al.*, a plausible assumption since both crystals were obtained from Sanders and Associates.

One concern with this interpretation is that Tzou *et al.* found the mobility perpendicular to the c axis to be 18 times larger than that parallel to the c axis, and mobilities > 18 cm^2/V sec are larger than the tabulated measurements of either electron or hole mobilities in $BaTiO_3$ by conventional techniques.[3]

Our results can be compared with the similar measurements made previously with 20-nsec pulses at 0.532 μm.[5] Table 1 gives the parameters of each experiment. The major differences in the experiments besides the pulse length are the trap density in the crystal, the writing energy, and the polarization of the reading pulse. The diffraction efficiencies observed by Lam *et al.* can be compared qualitatively with ours by scaling them as the square of the product of the fluence, the trap density, the interaction length, and the electro-optic coefficient. Performing such a scaling on the 20-nsec diffraction efficiency, one obtains a predicted efficiency that is more than an order of magnitude higher than those that we observed with our 30-psec pulses.

Comparison with our results in GaAs can be made by noting that, at a fluence of 7 mJ/cm^2, we obtained[6] a diffraction efficiency for GaAs of $\sim 3 \times 10^{-3}$. By scaling as the square of the fluence, we estimate an efficiency of roughly 10^{-2} for GaAs at 12 mJ/cm^2. Note that the comparison is further complicated by the fact that our $BaTiO_3$ results are for a grating period of 0.48 μm, whereas those in GaAs are for a period of 1.7 μm. The lower-than-expected measured efficiencies reported in this and the preceding paragraph tend to support the view that photorefractive grating formation with picosecond pulses in our crystal is limited by rapid recombination of the carriers following their diffusion for a small fraction of a grating period rather than by rapid diffusion of the carriers for a full half-grating period before recombination. If the opposite were true, then we would have expected comparable diffraction efficiencies since the two materials have comparable values for the factor $n^3 r/\epsilon$ (where ϵ is the dielectric constant).[7]

In summary, we have observed the formation of a photorefractive grating in $BaTiO_3$ in less than 100 psec by using 43-psec pulses at 0.532 μm. This suggests either a recombination time in $BaTiO_3$ of less than 100 psec or a much larger effective carrier mobility for picosecond time scales or for our sample than has been measured previously by conventional techniques in different samples. The magnitude of the grating indicates a less efficient photorefractive effect than that found in $BaTiO_3$ with cw or nanosecond illumination or than found in GaAs with picosecond pulses.

The authors wish to acknowledge many useful conversations with M. B. Klein. This work is supported in part by the U.S. Office of Naval Research and The Robert A. Welch Foundation.

References

1. G. C. Valley, IEEE J. Quantum Electron. **QE-19**, 1637 (1983).
2. G. C. Valley, A. L. Smirl, M. B. Klein, K. Bohnert, and T. F. Boggess, Opt. Lett. **11**, 647 (1986).
3. M. B. Klein, in *Photorefractive Materials and Applications*, P. Günter and J. P. Huignard, eds. (Springer-Verlag, Heidelberg, 1987), Chap. 7, Table 7-2.
4. C.-P. Tzou, T. Y. Chang, and R. W. Hellwarth, Proc. Soc. Photo-Opt. Instrum. Eng. **613**, 11-1 (1986).
5. L. K. Lam, T. Y. Chang, J. Feinberg, and R. W. Hellwarth, Opt. Lett. **6**, 475 (1981).
6. A. L. Smirl, K. Bohnert, G. C. Valley, and T. F. Boggess, submitted to IEEE J. Quantum Electron.
7. A. M. Glass, A. M. Johnson, D. H. Olson, W. Simpson, and A. A. Ballman, Appl. Phys. Lett. **44**, 948 (1984).

Appendix H: Theory of Transient Energy Transfer in Gallium Arsenide.

A preprint of a paper accepted for publication in IEEE J. Quantum Electron., January , 1988.

Theory of Transient Energy Transfer in Gallium Arsenide

George C. Valley and Arthur L. Smirl*

Hughes Research Laboratories

3011 Malibu Canyon Road

Malibu, CA 90265

Abstract

Numerical calculations are given for optical two-beam coupling in undoped, semi-insulating GaAs using picosecond pulses. Absorption at the intrinsic defect EL2, two-photon absorption, free-carrier absorption, photorefractive gratings, free carrier gratings, and absorption gratings are included. Results for normalized probe transmission as a function of pump fluence and as a function of pump-probe delay show that the major effects are energy transfer from pump to probe or from probe to pump (depending on crystal orientation) due to the photorefractive effect, two-photon absorption, and free carrier transient energy transfer from the pump to the probe.

Accepted for publication in IEEE Journal of Quantum Electronics, January 1988

* Presently on leave at the Center for Quantum Electronics, Department of Physics, North Texas State University

1. INTRODUCTION

When two picosecond pulses from an optical beam form an interference pattern in GaAs, several separate physical processes produce energy transfer from one beam to the other [1]. These include the photorefractive effect, Drude refractive index gratings, and absorption gratings. In addition, two-photon absorption and saturation of linear absorption produce an apparent energy transfer when one makes the usual measurement of probe (or weak beam) transmission with and without the presence of a pump (or strong beam). The purpose of this paper is to derive a set of consistent equations for all of these effects and to solve these equations numerically in order to investigate interactions between the effects.

In the photorefractive effect [2] a spatial variation in the optical irradiance pattern is transferred to the mobile charge carriers in a material through photoionization. These carriers drift and diffuse leading to an internal space charge field that modulates the refractive index of the material through the electro-optic effect. In GaAs, as in other photorefractive materials [3], both electrons and holes participate in the charge transport process, and the fact that their photoionization rates and mobilities are unequal leads to an internal space charge field. Observations of four-wave mixing and beam coupling in GaAs with cw beams [4], [5] were accurately modeled by one-photon ionization of a single species of charge carriers. For ps beams, two-photon absorption simultaneously produces both electrons and holes, and in addition the irradiances are sufficiently high that the donor or acceptor levels responsible for the photorefractive effect can be saturated. The

effect of this is that a defect such as EL2, which is primarily a donor and electron trap for cw beams in n-type semi-insulating (SI) GaAs, also acts as an acceptor and a hole trap at high irradiances.

The production of large numbers of conduction band electrons also modifies the refractive index of the material through the plasma nonlinearity [6],[7]. This process, which is negligible in SI GaAs with cw beams, competes with the photorefractive energy transfer observed with ps beams. This competition has been observed previosly in CdS with 70-ns pulses from a Ruby laser [6].

In addition to the photorefractive and free-carrier refractive index gratings, intensity-dependent absorption coefficients lead to gratings in the donor/acceptor absorption and in the free-carrier absorption. These gratings and the saturation of absorption processes lead to changes in the transmission of a probe beam in the presence of a pump. To obtain a self-consistent treatment of probe transmission all of these processes are included in the numerical calculations discussed in this paper. In the next section the basic equations used to model ps transient energy transfer are given. Properties of GaAs used in the calculations are discussed in Section 3 and results are presented in Section 4. Two sets of results are given: (1) probe transmission as a function of fluence for zero delay between pump and probe and (2) probe transmission as a function of delay between pump and probe for a single fluence. A detailed comparison between these results and the experimental observations is given in the companion paper [8].

2. BASIC EQUATIONS

The energy level model that we have applied to GaAs is shown in Fig. 1. In semi-insulating, undoped samples of GaAs, the donor-trap system that gives rise to the photorefractive effect is believed to be the EL2/EL2$^+$ deep level located 0.82 eV below the conduction band. The positively charged fraction of EL2 (EL2$^+$) is balanced by compensating acceptors (labeled A$^-$). Electrons of density n are produced by photoionization from the donor level EL2 at a rate $s_e I/(h\nu)$ where s_e is the cross section of the EL2, I is the optical irradiance, and $h\nu$ is the energy per photon. Likewise, optical energy is absorbed by EL2 with an absorption coefficient $s_e(N-N^+)$ where N is the total EL2 density and N^+ is the density of EL2$^+$. Absorption with a coefficient $s_h N^+$ also produces holes of density p from EL2$^+$ (the EL2$^+$ cross section is s_h). The acceptors A$^-$ of density N_A are assumed not to participate in photoionization processes. Electrons and holes are also produced by band-to-band two-photon ionization with a two-photon absorption coefficient β. Including all of these processes plus diffusion and drift of electrons and holes, one may write the rate equations, current equations and Poisson's equation for the space charge field in the GaAs, $\mathbf{E}_{sc}$:

$$\partial N^+/\partial t = s_e I(N-N^+)/(h\nu) - s_h I N^+/(h\nu) \tag{1}$$

$$\partial p/\partial t = -(1/e)\nabla\cdot\mathbf{j}_p + \beta I^2/(2h\nu) + s_h I N^+/(h\nu) \tag{2}$$

$$\partial n/\partial t = (1/e)\nabla\cdot\mathbf{j}_n + \beta I^2/(2h\nu) + s_e I(N-N^+)/(h\nu) \tag{3}$$

$$\mathbf{j}_p = e\mu_p \mathbf{E}_{sc} p - \mu_p k_B T\ \nabla p \tag{4}$$

$$\mathbf{j}_n = e\mu_n \mathbf{E}_{sc} n + \mu_n k_B T\ \nabla n \tag{5}$$

$$\nabla\cdot\mathbf{E}_{sc} = (e/\epsilon)(p + N^+ - n - N_A) \tag{6}$$

where e is the charge on the electron. μ_n and μ_p are the electron and hole mobilities, k_BT is Boltzmann's constant times temperature, and ϵ is the low-frequency dielectric constant. Note that recombination has been omitted from Eqs. (1)-(3). As discussed in Section 3, this is a good approximation for high quality GaAs on time scales of 100 ps or less.

Equations (1)-(6) must be supplemented with a wave equation for the optical field. If the amplitude E of the optical frequency electric field is slowly varying compared to a wavelength and if the beams can be approximated by plane waves propagating at a small angle to the z direction, then the wave equation can be written

$$\cos\theta\ \partial E/\partial z = i\delta_{PR}E_{sc}E + i\delta_D En - n_b\epsilon_o c\beta|E|^2E - s_{fc}nE/2 - s_e(N-N^+)E/2 - s_hN^-E/2 - \alpha_{np}E/2. \quad (7)$$

where θ is the angle between the direction of propagation and the z axis inside the crystal and $E_{sc} = |\mathbf{E}_{sc}|$ (The coordinate system is defined with the z axis normal to the surface of the crystal, the pump and probe propagating in the x-z plane and polarized in the y direction). The photorefractive coupling coefficient δ_{PR} is given by

$$\delta_{PR} = \pi r n_b^3/\lambda \quad (8)$$

where r is the effective electro-optic coefficient, n_b is the background refractive index, and λ is the vacuum wavelength. In addition, the Drude-Lorentz or free-carrier plasma coupling coefficient δ_D is given by [7]

$$\delta_D = -[\omega/(2cn_bN)]\omega_p^2/[\omega^2(1-\omega^2/\omega_g^2)] \quad (9)$$

where the plasma frequency for a number density N is given by $\omega_N^2 = e^2N/(\epsilon_o m_e^*)$, ω is the optical frequency, ω_g is the band gap energy divided by $\hbar$ (Planck's constant divided by 2π), and m_e^* is the electron effective mass. The other parameters in eq. (7) are the free carrier absorption cross section s_{fc} and the non-photorefractive absorption coefficient α_{np}. The time coordinate does not appear in eq. (7) if one uses retarded time coordinates. All time derivatives in eqs. (1)-(6) are then actually derivatives in the frame moving with the pulse.

The geometry of the transient energy transfer process in GaAs is shown in Fig. 2. Two beams, E_{-1} and E_{-1}, are incident on the crystal with an angle between the beams of $2\theta'$. This produces an interference pattern in the crystal of period $\Lambda_g = \lambda/(2\sin\theta') = \lambda/(2n_b\sin\theta)$ (2θ is the angle between the beams inside the crystal). The slowly varying amplitude of the optical field can be written:

$$E(t,z) = E_{+1}(t,z)\exp(-ik_x x) + E_{-1}(t,z)\exp(+ik_x x) \tag{10}$$

where $k_x = 2\pi n_b \sin\theta/\lambda = \pi/\Lambda_g$ ($k_g = 2\pi/\Lambda_g$). The irradiance can also be written in the form

$$I(t,x,z) = I_0(t,z) + I_{+2}(t,z)\exp(-i2k_x x) + I_{-2}(t,z)\exp(i2k_x x) \tag{11}$$

where $I_0 = 2n_b\epsilon_o c(|E_{+1}|^2 + |E_{-1}|^2)$ and $I_{+2} = I_{-2}^* = 2n_b\epsilon_o c E_{+1}E_{-1}^*$. In addition, it is useful to define two other properties of the optical field at the $z = 0$ face of the crystal: the ratio of the irradiance in the -1 beam to that

in the +1 beam, f_r, and the sum of the fluences in the two pulses $F_0 = \pi^{1/2}\tau_p I_0(0,0)$ where τ_p is the pulse length of the Gaussian pulse. F_0 is also the fluence averaged spatially over the fringes at the z = 0 surface.

In order to solve eqs. (1)-(7), we will assume that the beam ratio f_r is small and that the transient energy transfer is sufficiently small that f_r remains small. In this approximation one may neglect Fourier components of order higher than those given by eq. (10) in the optical fields, and one may assume a solution for n, p, N^- and $\mathbf{E}_{sc}$ of the form [the current densities may be eliminated immediately from eqs. (1)-(6)]

$$n(t,x,z) = n_0(t,z) + n_{+2}(t,z)\exp(-i2k_x x) + n_{-2}(t,z)\exp(+i2k_x x) \tag{12}$$

The derivatives with respect to z in the materials equations are neglected relative to $2k_x$; this is equivalent to the assumption that the quantities change slowly in the direction of propagation in a distance equal to the grating period. These assumptions yield three equations for the zeroth-order quantities (there is no zeroth-order space charge field) and four equations for the amplitudes of the grating terms:

$$\partial N_0^-/\partial t = s_e I_0(N-N_0^-)/(h\nu) - s_h I_0 N_0^-/(h\nu) \tag{13}$$

$$\partial p_0/\partial t = \beta I_0^2/(2h\nu) + s_h I_0 N_0^-/(h\nu) \tag{14}$$

$$\partial n_0/\partial t = \beta I_0^2/(2h\nu) + s_e I_0(N-N_0^-)/(h\nu) \tag{15}$$

$$\partial N_2^-/\partial t = -s_e I_0 N_2^-/(h\nu) + s_e I_2(N-N_0^-)/(h\nu) - s_h I_2 N_0^-/(h\nu) - s_h I_0 N_2^-/(h\nu) \tag{16}$$

$$\partial p_2/\partial t = +ik_g \mu_p E_{sc2} p_0 - k_g^2 \mu_p k_B T p_2/e + \beta I_0 I_2/(h\nu) + s_h I_2 N_0^-/(h\nu) - s_h I_0 N_2^-/(h\nu) \tag{17}$$

$$\partial n_2/\partial t = -ik_g\mu_n E_{sc2} n_0 - k_g^2 \mu_n k_B T n_2/e + \beta I_0 I_2/(h\nu)$$
$$+s_e I_2(N-N_0^+)/(h\nu) - s_e I_0 N_2^-/(h\nu) \quad (18)$$

$$E_{sc2} = ie(p_2 + N_2^- - n_2)/(k_g \epsilon) \quad (19)$$

The boundary conditions for these equations are $N_0^-(z,t=-\infty) = N_A$ and $p_0(z,t=-\infty) = n_0(z,t=-\infty) = N_2^-(z,t=-\infty) = p_2(z,t=-\infty) = n_2(z,t=-\infty) = E_{sc2}(z,t=-\infty) = 0$. As these conditions and eqs. (1)-(6) indicate, dark conductivity and dark generation of conduction band electrons are ignored. This is a good approximation since the electron number density generated by picosecond pulses rapidly exceeds the dark number density.

The field equations for E_{-1} and E_{-1} are given by

$$\cos\theta\ \partial E_{-1}/\partial z = i\delta_{PR} E_{sc2} E_{-1} + i\ \delta_D E_{+1} n_0 + i\delta_D E_{-1} n_2$$
$$- 2n_b \epsilon_o c\beta(|E_{+1}|^2/2 + |E_{-1}|^2)E_{+1}$$
$$-s_e(N-N_0^+)E_{-1}/2 - s_h N_0 E_{-1}/2 - s_{fc} n_0 E_{+1}/2$$
$$-\alpha_{np} E_{-1}/2 + (s_e - s_h) N_2^- E_{-1}/2 - s_{fc} n_2 E_{-1}/2 \quad (20)$$

$$\cos\theta\ \partial E_{-1}/\partial z = i\delta_{PR} E_{sc-2} E_{-1} + i\ \delta_D E_{-1} n_0 + i\delta_D E_{+1} n_{-2}$$
$$- 2n_b \epsilon_o c\beta(|E_{-1}|^2/2 + |E_{-1}|^2)E_{-1}$$
$$-s_e(N-N_0^+)E_{-1}/2 - s_h N_0^- E_{-1}/2 - s_{fc} n_0 E_{-1}/2$$
$$-\alpha_{np} E_{-1}/2 + (s_e - s_h) N_{-2}^- E_{-1}/2 - s_{fc} n_{-2} E_{-1}/2 \quad (21)$$

The first term on the right hand side of eqs. (20) and (21) gives photorefractive energy transfer. The second term gives a time-dependent phase shift due to the zeroth order free carrier index. The third term gives transient energy transfer due to the free carrier index grating. The fourth

term consists of the two-photon grating and absorption terms. The fifth through seventh terms are saturable absorption in the EL2, $EL2^{-}$, and free carriers respectively. The eighth term is the non-photorefractive absorption, while the last two terms represent absorption gratings. Similar equations have been used to describe transient energy transfer in CdS using 70-ns pulses [6].

3. PROPERTIES OF SEMI-INSULATING GaAs

Numerical solutions to the equations presented in the previous section require a large number of parameters of SI GaAs. Unlike many other photorefractive materials, most of these parameters are quite well known for SI GaAs. Table 1 gives values for these parameters and the references from which that the values are obtained. Many of these parameters have been given previously [1], but without detailed discussion of how they were obtained.

Consider first the absorption. The coefficient 1.2 cm^{-1} was measured at 1.06 μm for the sample of GaAs used in our beam coupling experiments [1], [5]. This value is typical of undoped SI GaAs [9]. The attribution of this absorption to the "native level" EL2 is based on the exact superposition of the absorption spectrum measured on our sample [5] with the spectrum measured by Martin ([9], Fig. 1). At low temperatures or for sufficiently short times, some of the absorption in SI GaAs may produce an excited state of EL2 [10], but for cw illumination at 300°K all of the absorption is thought to produce conduction band electrons and valence band holes [10]-[12]:

$$\alpha = s_e(N\text{-}N^-) + s_h N^- \quad . \tag{23}$$

Values for the electron and hole cross sections of EL2 and $EL2^-$ are difficult to obtain. At 1.06 μm Martin [9] obtained $\alpha(85°K) = \alpha(300°K)$. Since $N\text{-}N^- >> N^-$ and $s_e \geq s_h$, it is inferred that $s_e(85°) \simeq s_e(300°K)$ [12].

From Martin's data, a cross section $s_e = 1.0\ 10^{-16}$ cm^2 can be obtained [12]. The data of Kaminska et al. [11] yield $s_e(80°K) = 1.3x10^{-16}$ cm^2 while Mitonneau and Mircea [10] obtained $s_e(100°K) = 1.5x10^{-16}$ cm^2. Following Dobrilla and Blakemore [12], we use s_e(1.06 μm, 300°K) = $1.0x10^{-16}$cm^2. The hole cross section is much more difficult to obtain [12]. The following ratios of electron to hole cross section, s_e/s_h, have appeared in the literature: 1.7(80°K, 300°K) [13],[14], 3.3(no temperature given) [15], and 10.7 (100°K) [10]. In view of this discrepancy, we will present results using $s_e/s_h = 2$ and 10.

The free carrier cross section is obtained from the review of Blakemore [16] while the two-photon absorption coefficient was measured by Boggess et al. [17].

The EL2 density is obtained directly from the absorption coefficient and the photoionization cross section. The small uncertainty indicated is due to the uncertainty in the ratio of the electron to hole cross section. The value of the $EL2^-$ density is obtained in two ways. First, it is obtained from measurements of conductivity as a function of temperature. Second, it is obtained from cw beam coupling gain as a function of grating period. In the sample used for the ps measurements the values are $1.4x10^{15}cm^{-3}$ and $1.3x10^{15}cm^{-3}$ respectively [5].

The electron and hole recombination cross sections, s_{Re} and s_{Rh}, are obtained from the review of Martin and Makram-Ebeid [18]; earlier values of the electron recombination cross section given by Lang and Logan [19] for the O level (now thought to be EL2) are within a factor of two of the values given in [18]. Combining these parameters with the EL2 and $EL2^-$ densities and the thermal velocities given by Blakemore [16] yields recombination times

of 38 ns for the electrons and 3.2 μs for the holes. Much shorter recombination times have been reported in the literature [20], but we attribute these times to measurements on samples with a larger impurity concentration than found in our sample. A value of the direct electron-hole recombination coefficient of $\gamma_D = 2 \cdot 10^{-10}$ cm^3/s has been given by Von Lehmen and Ballantyne [21]. This leads to a direct recombination time of 1 ns for a carrier density of 5×10^{18} cm^{-3}. From these estimates of recombination times we conclude that the omission of all recombination processes on time scales less than 100 ps is justified.

Estimates of the electron and hole mobilities for crystals such as ours are obtained as follows. To obtain the electron drift mobility, we first measured the electron Hall mobility and then used Blakemore's [16] value for the weak-field Hall factor (the ratio of electron Hall to electron drift mobility) to obtain the drift mobility. Knowledge of the hole mobility in n-type GaAs is derived from theoretical work and extrapolation of p-type GaAs data [22]. Our ionized impurity concentration is approximately 3×10^{15} cm^{-3} ($EL2^-$ density of 1.4×10^{15} plus compensating acceptors--negative carbon ions--of about the same density). From Fig. 3 of Ref. [22] one obtains an electron Hall mobility of 6000 cm^2/Vs for an ionized impurity density of 3×10^{15} cm^{-3} that is consistent with our measured value of 5800. This figure also yields a mobility ratio of $\mu_n/\mu_p = 12$ for an ionized impurity concentration of 3×10^{15} cm^{-3}. This yields a hole mobility of 400 cm^2/Vs which is consistent with the measurements on p-GaAs in Fig. 2 of Ref. [22].

4. RESULTS

Equations (13)-(21) are solved numerically by the following procedure. First, eqs. (13)-(19) are integrated in time using the fields specified at the incident face of the crystal. Second, the field equations (20) and (21) are integrated a step Δz in the direction of propagation (the angle between the beams, $\theta' = 5.1°$ inside the crystal, is sufficiently small that the fields E_{-1} and E_{-1} are nearly co-propagating). Then the time integration of eqs. (13)-(19) is repeated using the fields at Δz. The process is repeated for n z steps until n Δz equals the length of the crystal in the direction of propagation, 3.3 mm for the crystal used in our experiments [1]. Both the time step and the z step are decreased until no change in the calculated fields is obtained to three significant figures. Calculations are given for wavelength = 1.06μm, pulse length 21.5 ps (half-width 1/e of the intensity), grating period Λ_g = 1.7 μm, and probe-to-pump ratio 0.044.

The quantity of interest for comparison to experimental results is the probe transmission through the crystal in the presence of the pump minus the probe transmission without the pump divided by the probe transmission without the pump, $\Delta T/T$. The physical significance of this quantity can be seen by writing $\Delta T/T$ for a situation in which the probe undergoes absorption independent of the pump $\exp(-\alpha l)$, absorption that depends on the pump $\exp(-\Delta\alpha l)$ and photorefractive gain $\exp(\Gamma l)$ that depends on the pump. $\Delta T/T$ is then given by

$$\Delta T/T = [\exp(-\alpha l - \Delta\alpha l + \Gamma l) - \exp(-\alpha l)]/\exp(-\alpha l) \qquad (24)$$

$$= \exp(-\Delta\alpha l + \Gamma l) - 1$$

$$\simeq -\Delta\alpha l + \Gamma l, \text{ for } \Delta\alpha l << 1 \text{ and } \Gamma l << 1.$$

The photorefractive gain can be separated from all other sources of probe gain or loss that depend on the pump intensity by performing experiments (and calculations) for two crystal orientations. In the first orientation, the sign of the charge carriers and the electro-optic effect is such that the photorefractive effect transfers energy from the pump to the probe (i.e. $\Gamma > 0$). The second orientation is obtained by rotating the crystal by 180° so that the photorefractive effect transfers energy from the probe to the pump [6].

Figs. 3 and 4 show calculations of $\Delta T/T$ as a function of fluence inside the crystal for a hole to electron cross section ratio of 1/2 and 1/10. The upper curve in each figure corresponds to photorefractive gain for the probe. The separation of the curves gives twice the magnitude of the photorefractive gain-coefficient-length product Γl. Note that at low fluences the curves are nearly symmetric about $\Delta T/T = 0$, indicating that only the photorefractive effect is important. The large dip in all curves that reaches a minimum around $F = 2$ mJ/cm^2 is due to two-photon absorption. The large increase in $\Delta T/T$ for $F > 3$ MJ/cm^2 is caused by the transient energy transfer of the free-carrier refractive index grating.

Fig. 5 shows similar calculations for $\delta_D = 0$ and $s_e/s_h = 2$. Note that the curves do not turn up for $F > 3$ mJ/cm^2. In Fig. 6 all effects are included except the EL2 and EL2$^-$ absorption. Note that the two curves nearly overlap for $F < 0.1$ mJ/cm^2, indicating that in this fluence range the photorefractive effect is totally dependent on the charge carriers generated

from EL2. Fig. 6 also shows that for F > 0.3 mJ/cm^2, there is a strong photorefractive effect from the charge carriers generated by two-photon absorption. Setting the two-photon absorption coefficient equal to zero yields the curves shown in Fig. 7. The large upturn in both curves for F > 0.3 mJ/cm^2 is caused by transient energy transfer in the free carrier grating for the electrons generated from EL2.

Calculations of $\Delta T/T$ as a function of probe delay relative to the pump are shown in Figs. 8 and 9. All of the features seen in Figs. 3 to 7 are now evident as a function of probe delay. The separation of the curves for a given fluence is again due to the photorefractive effect. The separation (and the photorefractive effect) is greater for negative delays. This can be understood by noting that for negative delay the probe interferes with the leading edge of the pump. This means that most of the pump energy is available for reading out the grating and being transferred into the probe. The peak at delays of about -1.0 are caused by transient energy transfer. This process causes the minima in the curves, which would have been symmetric about zero delay for two-photon absorption, to be shifted to positive delay. For large delays, the grating effects become unimportant and the probe samples the medium after the pump has propagated through the medium. The positive values of $\Delta T/T$ for delays greater than 2.5 are caused by the unequal values of the electron and hole cross sections. If the cross sections were equal, the only effect at large delays (in the absence of recombination) would be the free carrier absorption. Since we have assumed that the EL2 cross section is larger than that of $EL2^-$, photo-ionizing electrons from EL2 decreases the probe absorption from that obtained with no pump. The largest effect of this kind is seen for F = 2.0 mJ/cm^2 and $s_h = s_e/10$.

5. CONCLUSIONS

Numerical solutions of the materials equations and optical field equations for two-beam coupling on picosecond time scales in GaAs have been given. Solutions are given for the normalized probe beam transmission as a function of fluence and as a function of probe delay. In a companion paper the same computer codes are used to model specific experiments and discrepancies between numerical results and the results of those experiments are discussed [8].

The numerical results show that three main effects are important in undoped, semi-insulating GaAs: photorefractive energy transfer that can transfer energy either from pump to probe or from probe to pump depending on the crystal orientation, two-photon absorption, and transient energy transfer from the strong pump to the weak probe due to the free carrier refractive index grating. At fluences less than 0.1 mJ/cm^2 only the photorefractive effect is important. At fluences above 0.3 mJ/cm^2 two-photon absorption is important in addition. At fluences above 2 mJ/cm^2 transient energy transfer dominates.

Results as a function of probe delay show that the photorefractive effect and free-carrier transient energy transfer are maximized for negative delays (i.e probe ahead of the pump) of about one pulse length. The two-photon absorption is symmetric about zero delay. At large positive delays the dominant effect is the change in the EL2 absorption caused by changes in the relative population of EL2 and $EL2^+$ and unequal electron and hole cross sections.

Acknowledgements

This work was supported in part by the Office of Naval Research and The Robert A. Welch Foundation. We are grateful to Drs. A. Hunter and M.B. Klein for many helpful discussions.

FIGURE CAPTIONS

Fig. 1 Schematic energy level diagram for undoped semi-insulating GaAs. Absorption at EL2 produces $EL2^+$ and a free electron in the conduction band. Absorption at $EL2^+$ produces EL2 and a free hole in the valence band. Band-to-band two-photon absorption produces both an electron and a hole while free carrier absorption raises an electron higher in the conduction band.

Fig. 2 Beam coupling geometry in GaAs. Energy is transferred between pump and probe by the free carrier grating, the photorefractive grating, and absorption gratings.

Fig. 3 The quantity $\Delta T/T$ as a function of fluence for hole cross section equal to half the electron cross section. The upper curve is for the case in which the photorefractive energy transfer is from pump to probe while the lower curve is for photorefractive transfer from probe to pump.

Fig. 4 The quantity $\Delta T/T$ as a function of fluence for hole cross section equal to one-tenth the electron cross section. The upper curve is for the case in which the photorefractive energy transfer is from pump to probe while the lower curve is for photorefractive transfer from probe to pump.

Fig. 5 The quantity $\Delta T/T$ as a function of fluence for hole cross section equal to one-half the electron cross section and with the coupling coefficient for the free-carrier refractive index, δ_p, set to zero. The upper curve is for

the case in which the photorefractive energy transfer is from pump to probe while the lower curve is for photorefractive transfer from probe to pump.

Fig. 6 The quantity $\Delta T/T$ as a function of fluence for electron and hole cross sections set equal to zero. The upper curve is for the case in which the photorefractive energy transfer is from pump to probe while the lower curve is for photorefractive transfer from probe to pump.

Fig. 7 The quantity $\Delta T/T$ as a function of fluence for hole cross section equal to one-half the electron cross section and with the two-photon absorption coefficient β set equal to zero. The upper curve is for the case in which the photorefractive energy transfer is from pump to probe while the lower curve is for photorefractive transfer from probe to pump.

Fig. 8 The quantity $\Delta T/T$ as a function of delay divided by pulse length for fluences F = 0.5, 1.0, and 2.0 mJ/cm^2. The hole cross section is set equal to one-half of the electron cross section. The upper curve is for the case in which the photorefractive energy transfer is from pump to probe while the lower curve is for photorefractive transfer from probe to pump

Fig. 9 The quantity $\Delta T/T$ as a function of delay divided by pulse length for fluences of 0.5, 1.0, and 2.0 mJ/cm^2. The hole cross section is set equal equal to one-tenth the electron cross section. The upper curve is for the case in which the photorefractive energy transfer is from pump to probe while the lower curve is for photorefractive transfer from probe to pump.

References

1. G.C. Valley, A.L. Smirl, M.B. Klein, K. Bohnert, and T.F. Boggess, "Picosecond photorefractive beam coupling in GaAs," Opt. Lett. **11**, 647-649 (1986).

2. P. Günter, "Holography, coherent light amplification and optical phase conjugation with photorefractive materials," Phys. Repts. **93**, 199-299 (1982).

3. G.C. Valley, "Simultaneous electron/hole transport in photorefractive materials," J. Appl. Phys. **59**, 3363-3366 (1986); F.P. Strohkendl, J.M.C. Jonathan, and R.W. Hellwarth, Hole-electron competition in photorefractive gratings," Opt. Lett. **11**, 312-314 (1986).

4. A.M. Glass, A.M. Johnson, D.H. Olson, W. Simpson, and A.A. Ballman, "Four-wave mixing in semi-insulating InP and GaAs using the photorefractive effect," Appl. Phys. Lett. **44**, 948-950 (1984).

5. M.B. Klein, "Beam coupling in undoped GaAs at 1.06 μm using the photorefractive effect," Opt. Lett. **9**, 350-352 (1984).

6. V.L. Vinetskii, N.V. Kukhtarev, and M.S. Soskin, "Transformation of intensities and phases of light beams by a transient 'undisplaced' holographic grating," Kvantovaya Elektron. (Moscow) **4**, 420-425 (1977) [Engl. Trans. Sov. J. Quantum Electron. **7**, 230-233 (1977)]; V.L. Vinetskii, N.V. Kukhtarev, E.N.

Sal'kova, and L.G. Sukhoverkhova, "Mechanisms of dynamic conversion of coherent optical beams in CdS," Kvantovaya Elektron. (Moscow) **7** 1191-1198 (1980) [Engl. trans. Sov. J. Quantum Electron. **10**, 684-688 (1980)].

7. R.K. Jain and M.B. Klein, "Degenerate four-wave mixing in semiconductors. Chap. 10, pp. 307-415 in **Optical Phase Conjugation**, ed. by R.A. Fisher (Academic Press, New York) (1983).

8. A.L. Smirl, G.C. Valley, K. Bohnert, T.F. Boggess, submitted to IEEE J. Quantum Electronics, 1987.

9. G.M. Martin, "Optical assessment of the main electron trap in bulk semi-insulating GaAs," Appl. Phys. Lett., **39**, 747-749 (1981).

10. A. Mitonneau and A. Mircea, "Auger de-excitation of a metastable state in GaAs," Solid State Comm. **30**, 157-162 (1979).

11. M. Kaminska, M. Skowronski, J. Lagowski, J.M. Parsey, and H.C. Gatos, "Intracenter transitions in the dominant deep level (EL2) in GaAs," Appl. Phys. Lett. **43**, 302-304 (1983).

12. P. Dobrilla and J.S. Blakemore, "Experimental requirements for quantitative mapping of midgap flaw concentration in semi-insulating GaAs wafers by measurement of near-infrared transmittance," J. Appl. Phys. **58**, 208-218 (1985).

13. G. Vincent, D. Bois, and A. Chantre. "Photoelectric memory effect in GaAs," J. Appl. Phys. **53**, 3643-3649 (1982).

14. A. Chantre, G. Vincent, and D. Bois. "Deep-level optical spectroscopy in GaAs," Phys. Rev. B, **23**, 5335-5359 (1981).

15. G. Martin. "Key electrical parameters in semi-insulating materials: the methods to determine them in GaAs," in **Semi-Insulating III-V Materials** ed. by G.J. Rees (Shiva, Nantwich U.K., 1980) pp. 13-28.

16. J.S. Blakemore. "Semiconducting and other major properties of gallium arsenide," J. Appl. Phys. **53**, R123-R181 (1982).

17. T.F. Boggess, Jr., A.L. Smirl, S.C. Moss, I.W. Boyd, and E.W. van Stryland. "Optical limiting in GaAs," IEEE J. Quant. Electron. **QE-21**, 488-494 (1985).

18. G.M. Martin and S. Makram-Ebeid. "The mid-gap donor level EL2 in GaAs," Chap. 6 in **Deep Centers in Semiconductors. A State-of-the-Art Approach**, ed. by S.T. Pantelides, (Gordon and Breach, New York, 1986), pp. 399-487.

19. D.V. Lang and R.A. Logan. "A study of deep levels in GaAs by capacitance spectroscopy," J. Electron. Materials, **4**, 1053-1065 (1975).

20. J.S. Weiner and P.Y. Yu. "Free carrier lifetime in semi-insulating GaAs from time-resolved band-to-band photoluminescence," J. Appl. Phys. **55**, 3889-3891 (1984).

21. A. Von Lehmen and J.M. Ballantyne. "Investigation of the nonlinearity in the luminescence of GaAs under high-density picosecond photoexcitation," J. Appl. Phys. **58**, 958-962 (1985).

22. W. Walukiewicz, L. Pawlowicz, J. Lagowski and H.C. Gatos, "Characterization of semi-insulating GaAs," in **Semi-insulating III-V Materials**, ed. S. Makram-Ebeid and B. Tuck (Shiva, Nantwich, 1982) pp. 121-127.

23. D.T.F. Marple, J.Appl.Phys. **35**, 1241 (1964).

24. K.S. Champlin, R.J.Erlandson, G.H. Glover, P.S. Hauge, and T. Lu, "Search for resonance behavior in the microwave dielectric constant of GaAs," Appl. Phys. Lett. **11**, 348-349 (1967).

25. M. Sugie and K. Tada., "Measurements of the Linear Electrooptic Coefficients and Analysis of the Nonlinear Susceptibilities in Cubic GaAs and Hexagonal CdS," Jpn. J. Appl. Phys. **15**, 421-431 (1976).

Table 1. Parameters of GaAs used in transient energy transfer calculations.

Parameter	Value	Ref.
Refractive index, n_b	3.48	[23]
Dielectric constant, ϵ/ϵ_o	12.9	[24]
Electro-optic coefficient, r_{41}	1.43 pm/V	[25]
Absorption coefficient, α	1.2 cm^{-1}	[5]
Two-photon absorption coefficient, β	26 cm/GW	[17]
EL2 cross section, s_e	$1.0x10^{-16}cm^2$	[12]
$EL2^-$ cross section, s_h	$s_e/2$, $s_e/10$	[10],[14]
Free-carrier cross section, s_{fc}	$6.x10^{-18}$ cm^2	[16]
Total EL2 density, N	$1.2x10^{16}$ cm^{-3}	
Ionized EL2 ($EL2^-$) density, N^-	$1.4x10^{15}$ cm^{-3}	[5]
Electron recombination cross section, s_{Re}	$4.3x10^{-16}$ cm^2	[18]
Hole recombination cross section, s_{Rh}	$2x10^{-18}$ cm^2	[18]
Direct electron-hole recombination coefficient, γ_D	$2x10^{-10}$ cm^3/s	[21]
Electron thermal velocity, v_n	$4.4x10^7$ cm/s	[16]
Hole thermal velocity, v_p	$1.7x10^7$ cm/s	[16]
Electron Hall mobility, μ_H	5800 cm^2/Vs	[5]
electron drift mobility, μ_n	5000 cm^2/Vs	[5],[16]
Hole drift mobility, μ_p	400 cm^2/Vs	[22]

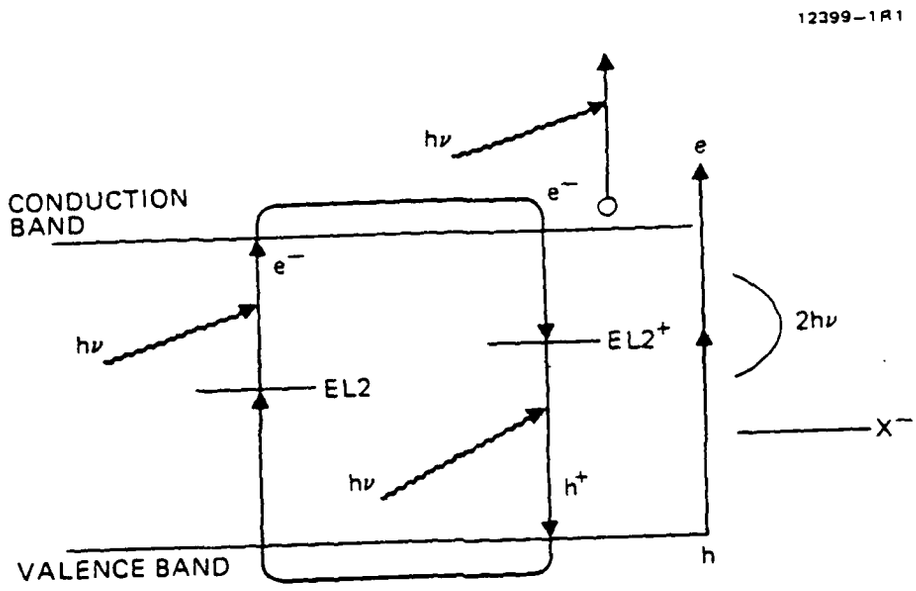
12399-1R1
hν
e
e⁻
CONDUCTION BAND
e⁻
hν
EL2⁺
2hν
EL2
X⁻
hν
h⁺
VALENCE BAND
h

Fig. 1

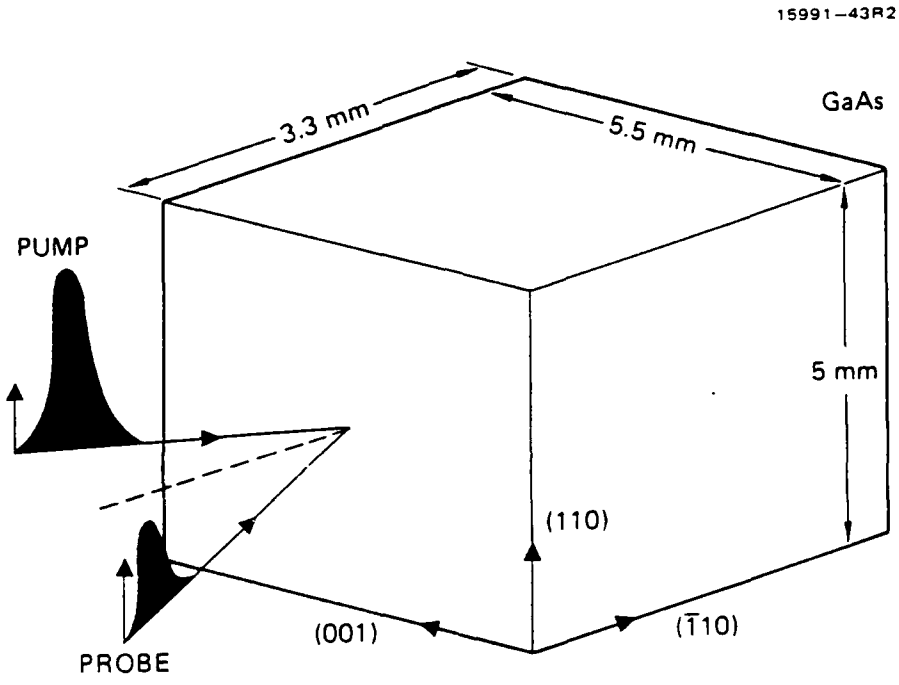

Fig. 2

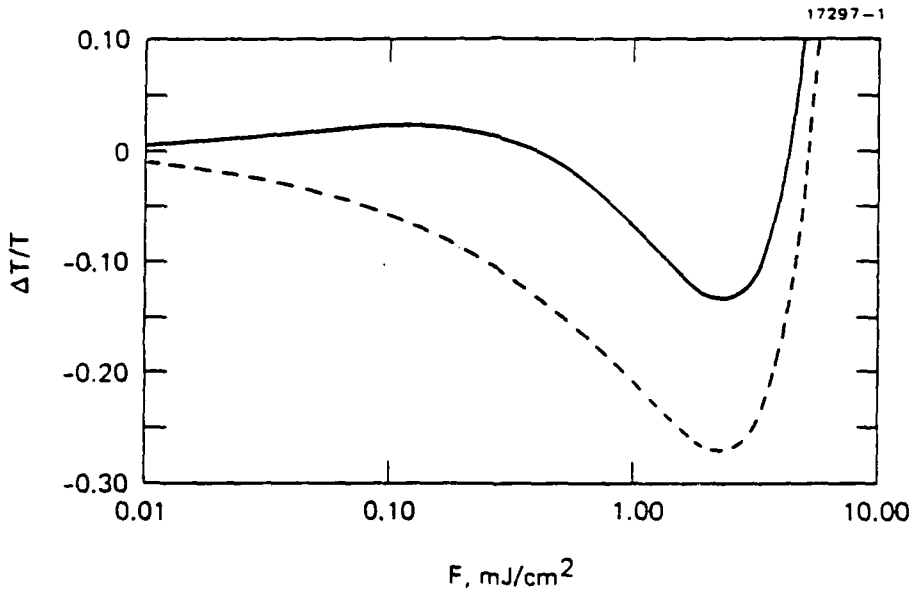

Fig. 3

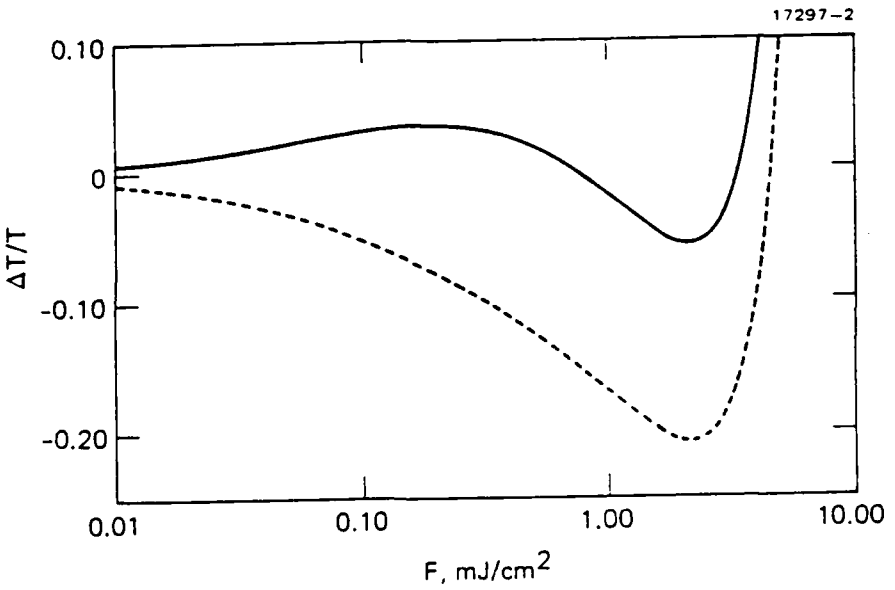

Fig. 4

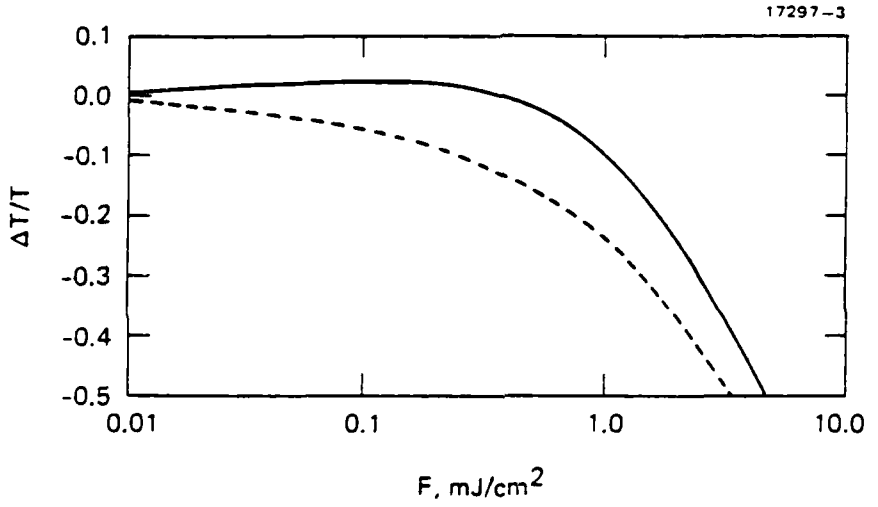

Fig. 5

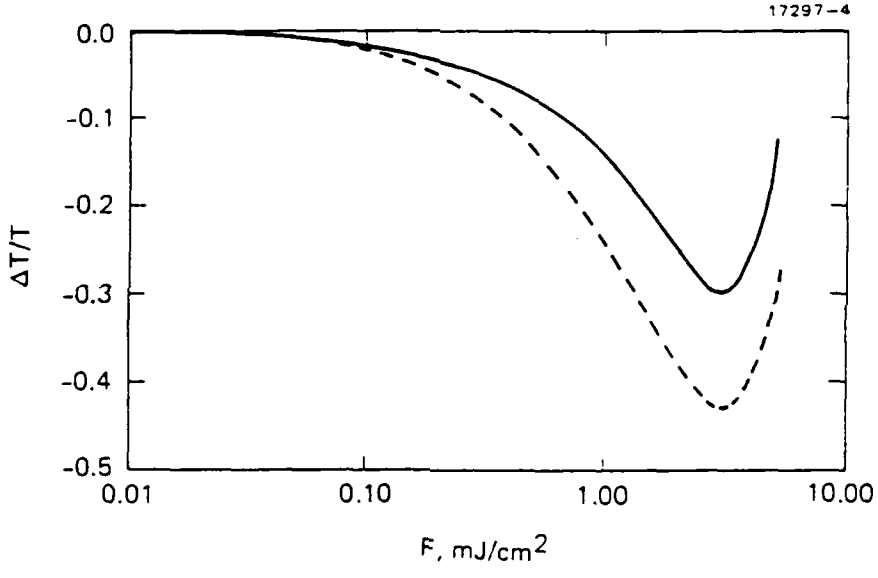

Fig. 6

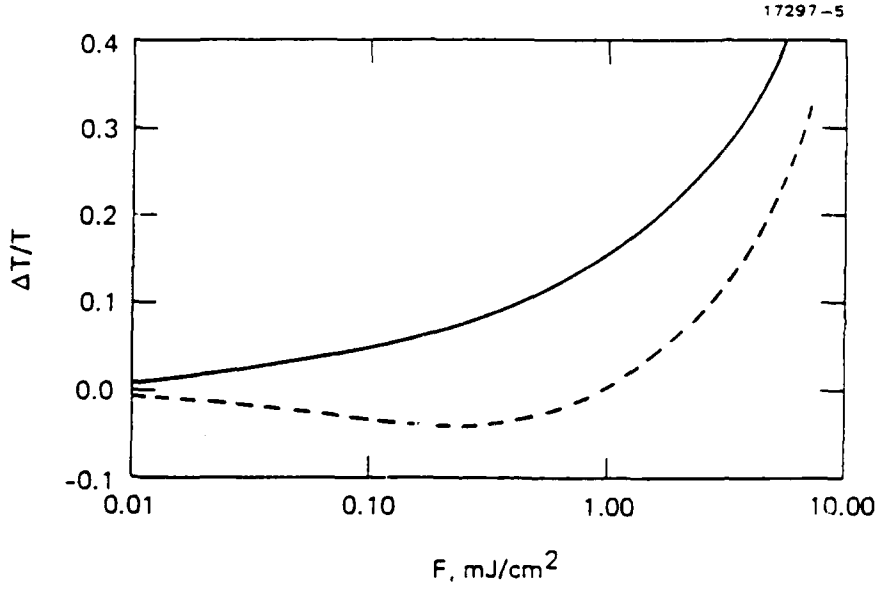

Fig. 7

AD-A191 926 NONLINEAR OPTICAL PROPERTIES AND SUBPICOSECOND DYNAMICS 2/3
OF EXCITONS AND E..(U) ARMY LAB COMMAND WATERTOWN MA
MATERIAL TECHNOLOGY LAB T F BOGGESS ET AL. DEC 87
UNCLASSIFIED MAC-REF-F4767 AFOSR-TR-88-0012 F/G 20/12 NL

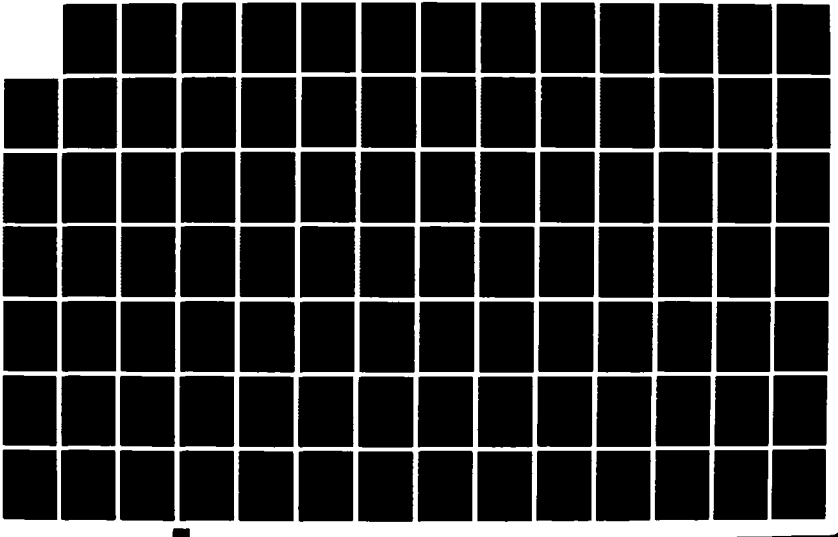

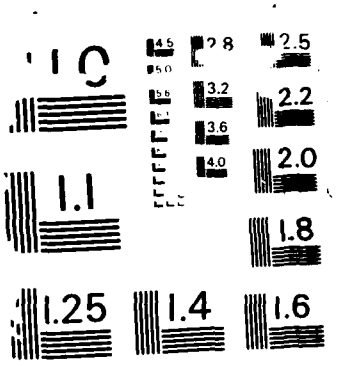

TEST CHART

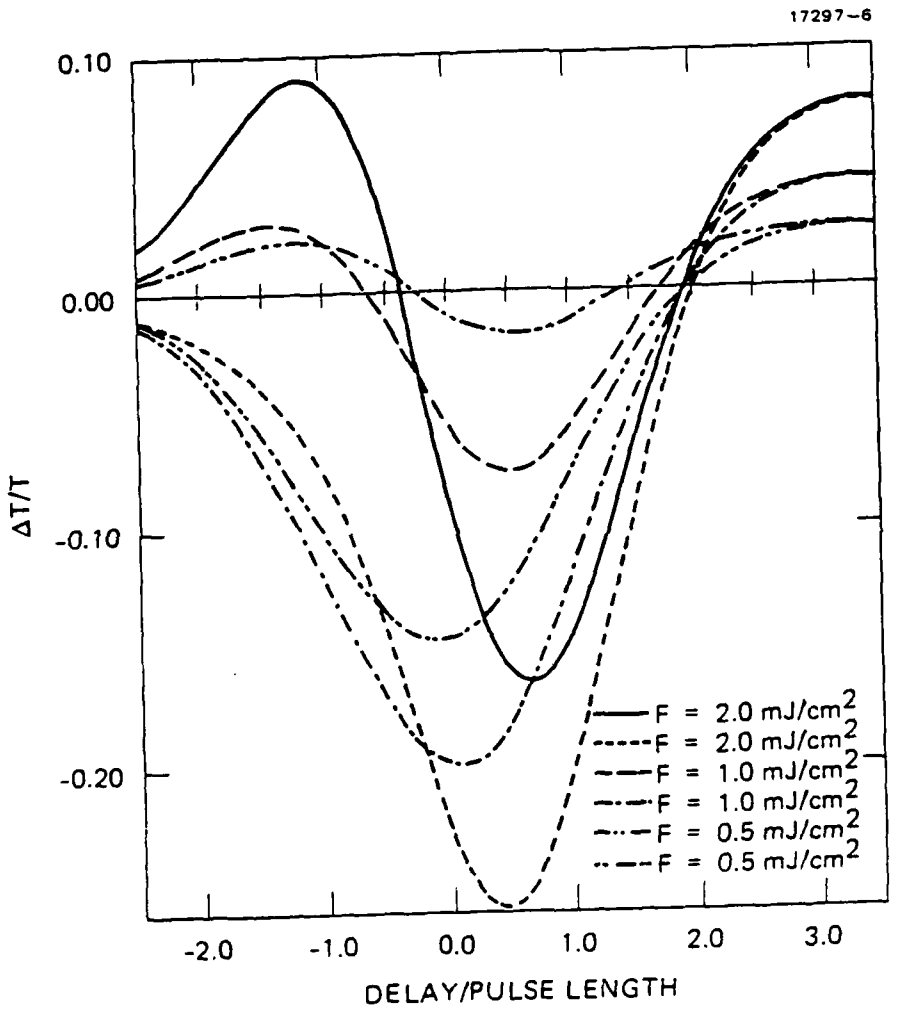
17297-6
0.10
0.00
-0.10
-0.20
ΔT/T
-2.0
-1.0
0.0
1.0
2.0
3.0
DELAY/PULSE LENGTH
F = 2.0 mJ/cm2
F = 2.0 mJ/cm2
F = 1.0 mJ/cm2
F = 1.0 mJ/cm2
F = 0.5 mJ/cm2
F = 0.5 mJ/cm2

Fig. 8

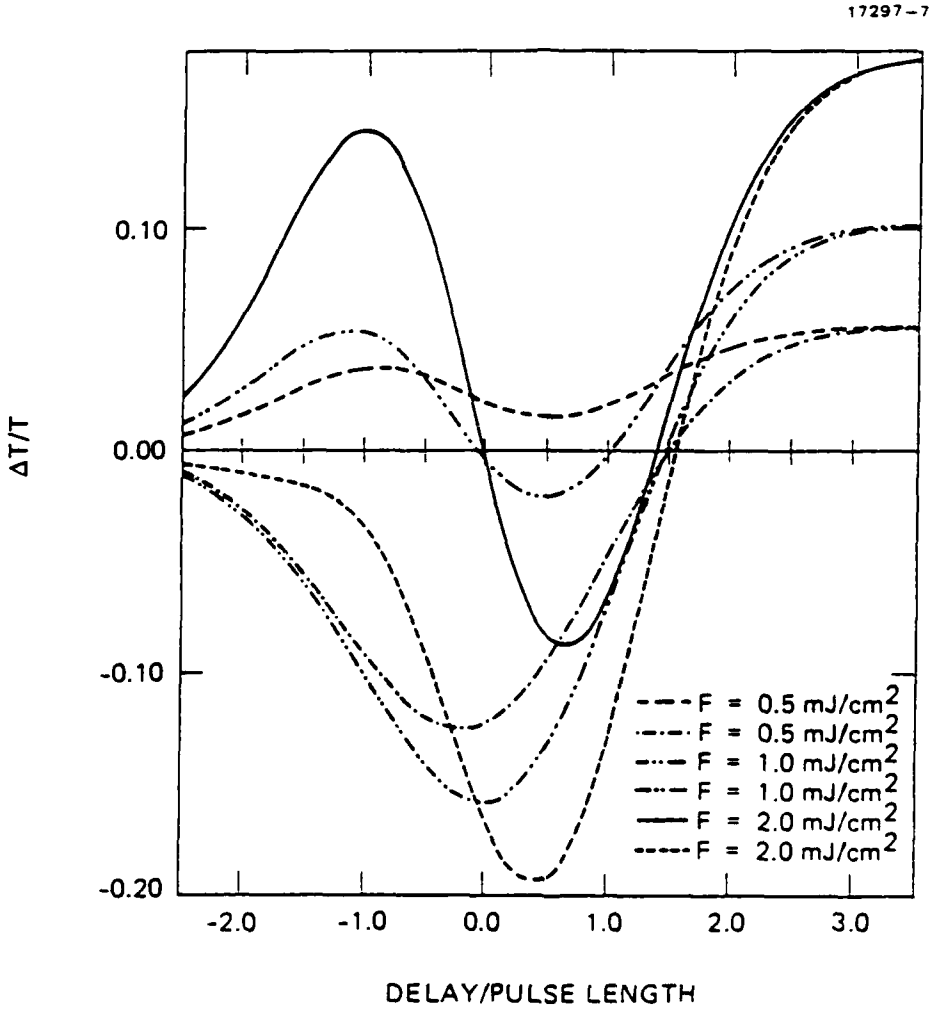
17297-7
0.10
0.00
-0.10
-0.20
ΔT/T
-2.0
-1.0
0.0
1.0
2.0
3.0
DELAY/PULSE LENGTH
F = 0.5 mJ/cm2
F = 0.5 mJ/cm2
F = 1.0 mJ/cm2
F = 1.0 mJ/cm2
F = 2.0 mJ/cm2
F = 2.0 mJ/cm2

Fig. 9

Appendix I: Picosecond Photorefractive and Free-Carrier Transient Energy Transfer in GaAs at 1 μm.

A preprint of a paper accepted for publication in IEEE J. Quantum Electron., January, 1988.

INVITED PAPER IEEE J. QUANTUM ELECTRON.

Picosecond Photorefractive and Free-Carrier Transient Energy Transfer in GaAs at 1 μm

Arthur L. Smirl* and George C. Valley
Hughes Research Laboratories
3011 Malibu Canyon Road
Malibu, CA 90265

K. Bohnert† and Thomas F. Boggess
Center for Applied Quantum Electronics
Department of Physics
North Texas State University
Denton, TX 76203

ABSTRACT

The strength, formation, and decay of photorefractive and free-carrier gratings written in GaAs by 43-ps pulses at a wavelength of 1 μm are investigated using picosecond time-resolved two-beam coupling, transient grating and degenerate-four-wave-mixing techniques. Photorefractive weak-beam gains of a few percent are measured at fluences of a few pJ/μm² (0.1 mJ/cm²), and gain from transient energy transfer is observed at fluences larger than ~10 mJ/cm² in the beam coupling experiments. The roles of saturation and two-photon absorption in determining the final electron, hole and ionized-donor populations and the roles of drift and diffusion in determining the quasi-steady-state photorefractive and free-carrier index modulations are discussed.

*Presently on leave of absence at North Texas State University.

†Now with BBC Brown Boveri Research Laboratories, CH-5405 Baden-Dattwil, Switzerland.

INTRODUCTION

There is a continuing need for sensitive, fast nonlinear optical materials and mechanisms that can be used to construct optical devices for a variety of potential applications in optical communication, data processing, and computing systems. In partial response to this need, photorefractive effects in ferroelectric and cubic oxide crystals such as $BaTiO_3$ [1], $Bi_{12}SiO_{20}$ [2], $K(TaNb)O_3$ [3,4], $(SrBa)Nb_2O_6$ [5], and $LiNbO_3$ [6,7] have been studied extensively for applications in holographic storage and optical data processing and have been used to construct phase-conjugate resonators [8], image amplifiers [9], real-time interferometers and beam steering devices [10], to demonstrate convolution and correlation [11], and most recently, to phase-lock multiple lasers [12,13,14]. To date, these oxides have exhibited low free-carrier mobilities and relatively short carrier lifetimes. These small mobility-lifetime products can severely limit both speed and sensitivity in processing with either cw radiation or ultrashort pulses [15]. Consequently, these oxides show the most promise for applications that require a high degree of parallel processing, where the requirements on the material response time can be relaxed. Moreover, such commonly-used ferroelectric materials have shown a useful response only in the visible region of the spectrum at wavelengths below ~700 nm.

Recently, the photorefractive responses of the compound III-V semiconductors GaAs and InP and the II-VI semiconductor CdTe to cw laser radiation at 1 μm have been reported [16-19]. Compound semiconductors such as these are of interest because their operating wavelengths are compatible with those of semiconductor diode and Nd:YAG lasers and with low-loss propagation in fibers and because their high mobilities and large mobility-lifetime products indicate a potential for faster responses and increased sensitivities. Specifically, degenerate four-wave mixing was used by Glass et al. [16] to observe the photorefractive response of semi-insulating InP:Fe and GaAs:Cr as a function of an externally applied field. Klein [17] used a two-beam-mixing geometry to measure the weak-beam gain as a function of grating spacing in undoped GaAs with EL2 centers, from which he extracted the concentration of ionized EL2 donors, and he determined the photorefractive response time of his sample to be 20 μs at an intensity of 4 W/cm^2. Subsequently, Glass et al. [18]

determined, from the direction of energy transfer in two-beam photorefractive mixing experiments, that the majority photocarriers in InP:Fe and undoped GaAs were electrons. The steady-state grating-formation time and the dependence of the two-beam mixing gain on grating period have also been investigated in GaAs:Cr by Albanese et al. [19]. From these measurements, they extracted a trap density and determined grating formation times that, when scaled, were comparable to those observed by Klein [17] in undoped material. The first time-resolved, pulsed photorefractive measurements in semiconductors were reported by Strait and Glass [20]. In the latter measurements, the authors demonstrated that photorefractive gratings could be written and erased in less than a microsecond in In:Fe and CdTe:In. Most recently, Valley et al. have demonstrated photorefractive beam coupling gain in semi-insulating GaAs with single 43-ps pulses [21].

Here, we report detailed measurements of the photorefractive response of GaAs on picosecond time scales using two-beam mixing, three-beam transient grating and four-wave mixing techniques. We also measure and separate the contributions of two-photon absorption and transient energy transfer to the energy loss and transfer.

ENERGY TRANSFER and LOSS MECHANISMS

Typically, in photorefractive experiments and, specifically, for the experimental geometries to be described here, two beams are spatially coincident in a sample with an angle of $2\theta'$ between the two beams, as illustrated in Fig. 1. When this is so, a number of separate processes can cause the transmission of one beam to be modified by the presence of the other, or the transmission of a third beam (not shown) to be modified by the presence of the two coincident beams. For example, one beam can induce nonlinear irradiance- or fluence-dependent changes in the absorption coefficient that are then sensed by the second beam, or the interference of the two beams can produce spatially-periodic changes in the index of refraction or the absorption coefficient that can cause energy to be exchanged between the two beams or cause light from a third beam to be diffracted. Here, we report investigations of such energy transfer, loss and gain mechanisms in GaAs on picosecond time scales and at a wavelength of 1.06 μm.

The sample used in our experiments is an undoped semi-insulating GaAs crystal grown by the liquid-encapsulated Czochralski process and is the same one used by Klein [17] in his cw measurements at 1.06 μm. As reported earlier [17], this sample has a dark resistivity $\rho = 6.3 \times 10^7$ Ωcm and an electron Hall mobility $\mu = 5800$ cm^2/Vs. The energy level model that we adopt for GaAs is shown schematically in Fig. 2a. Absorption at 1.06 μm in GaAs is believed to arise from the photoionization of deep levels. Although deep levels in GaAs can be produced by intentionally adding dopants such as Cr, they can also arise from stoichiometric defects. The dominant defect in undoped material is a donor level called EL2 that is located roughly 0.8 eV below the conduction band edge. In undoped GaAs, these EL2 donors provide the charge compensation necessary for the growth of semi-insulating samples. Consequently, in the dark, the density of ionized $EL2^+$ must exactly equal the density of negatively-charged acceptors, A^-, in order to ensure charge neutrality and complete compensation.

The steady-state photorefractive effect that is observed under cw and long-pulse excitation is initiated by the single-photon ionization of electrons from these EL2 donors. The direct absorption of the spatially varying optical irradiance produces a periodic distribution of mobile

electrons. These electrons diffuse from regions of higher concentration to regions of lower concentration (or drift in an applied field) and, finally, recombine with the $EL2^+$ traps to produce neutral EL2 donors. Since the density of photoionized electrons in the conduction band under steady-state conditions is relatively small compared to the density of ionized donors, the principal effect of this generation, diffusion and recombination of carriers is to produce a spatially-periodic modulation of the $EL2^+$ ionized donor (or trap) population. That is, near the grating peak, photoionization produces more $EL2^+$ than needed to compensate the negatively charged acceptors, and in regions away from the grating peak, recombination neutralizes $EL2^+$ so that there are too few to compensate for the acceptors. In this way, a periodic space-charge field is established between two immobile species: the excessive ionized donors near the peaks in the interference pattern and the uncompensated acceptors away from these peaks. We emphasize that it is the ionized $EL2^+$ donor population that is periodically modulated above and below the density required to compensate the acceptors. There is no modulation of the acceptor population. Also, notice that the maximum space-charge density in steady-state is limited by the density of available electron traps (measured without illumination) and that the dark density of traps is determined by the acceptor density. This space-charge field then periodically modulates the refractive index through the electro-optic effect. For later comparison, notice that the initial photoionized distribution of carriers and, thus, the periodic distribution of charge are both spatially in-phase with the incident irradiance profile. By contrast, the space-charge field, which is proportional to the integral of the charge distribution, and the index profile, which is proportional to the space-charge field, are shifted by $\pi/2$ with respect to the irradiance pattern. It is well known that this shift is optimum for steady-state energy transfer from an index grating in two-beam coupling experiments. The time required for this process to reach steady-state (i.e., the response time) is determined by the photoionization rate, the electron mobility, the electron-trap recombination rate, the grating spacing, and the applied electric field, if any. Ultimately, the electron mobility or the recombination time will limit the response time; however, in the experiments performed to date, the response time has been determined by the generation rate and grating spacing. For example, in our sample, at an

irradiance of 4 W/cm² and a grating spacing of 1 μm, a response time of 20 μs has been measured [17].

One way in which our picosecond measurements differ from earlier cw and nanosecond experiments is the enhanced time resolution (see, e.g., [22]). Another is that the generation rate can significantly exceed the recombination rate, and a large density of free photoionized carriers can be produced. In this case, the initial space-charge field responsible for the photorefractive effect will be between immobile ionized donors $EL2^+$ and mobile free electrons, as illustrated in Fig. 2b. The Drude-Lorentz (or band-filling) change in the refractive index associated with these free carriers is the source of a second refractive-index grating. The sign of this index change is negative, and the magnitude is proportional to the charge density. Thus, in contrast to the photorefractive grating, the free-carrier index grating is spatially out of phase with the incident irradiance distribution by π. It is well known that such an index grating can not transfer energy in two-beam coupling experiments in steady state or for equal beams. Even in the transient regime, the nominally unshifted free-carrier index grating will result in no energy transfer in first order (in perturbation theory). In higher orders, however, there is significant energy transfer when the pulse length is on the order of (or shorter than) the grating relaxation time [23]. This process is called transient energy transfer. Clearly, there is also a Drude absorption grating associated with the generation of free-carriers. This grating is nominally in phase with the incident irradiance pattern and will cause a first order transfer of energy between two beams. Even so, the absorption grating is much weaker than the index grating in GaAs for our experimental conditions, and our calculations show that the higher order transient energy transfer from the free-carrier index grating exceeds the first-order transfer from the Drude absorptive grating.

The time required for formation of the free-carrier grating is totally determined by the carrier generation rate; unlike the photorefractive grating formation, diffusion is not required. In the absence of a space-charge field, the free-electron grating would decay by electronic diffusion and recombination, and its strength would be determined by the total incident fluence and by the relative rates for generation, diffusion and recombination. For typical mobilities in undoped semi-

insulating GaAs and for grating spacings of a few microns, diffusive decay would destroy the electronic density modulation before recombination could deplete the carrier population, if there were no space-charge field. The presence of a space-charge field between the electrons and stationary ionized donors $EL2^+$, however, will prevent the total decay of the free-carrier grating by diffusion. That is, the free-carrier grating will decay only until the diffusive current associated with the density gradient exactly balances the drift current that is associated with the space-charge field. Eventually, the remaining free-carrier grating will decay by recombination.

Notice that the processes that cause the decay of the free-carrier grating are the ones required to establish a photorefractive grating. That is, the time required for photorefractive grating formation in high-quality semi-insulating GaAs on picosecond time scales is determined primarily by the carrier generation rate and the diffusion (or drift) rate. In this case, the maximum space-charge field will be obtained if the carriers diffuse one-half of a grating period. Thus, recombination is not necessary for photorefractive grating formation and will not occur on ps time scales for high-quality undoped material. In fact, recombination times in high quality GaAs can be greater than 10 ns. However, if the recombination lifetime is sufficiently short or the grating spacing sufficiently large, the carriers will move only a fraction of a grating period before being retrapped, and a less than optimum space-charge field will be established. This occurs in $BaTiO_3$, for example, as we have recently reported [15]. Thus, a large mobility generally indicates a larger photorefractive sensitivity and a faster response. By comparison, a shorter recombination time can lessen the magnitude of the photorefractive response and will hasten the free-carrier grating decay. Although recombination will destroy the free-carrier grating and deplete the electronic population, it will not destroy the photorefractive grating. Instead, the recombining electrons neutralize the $EL2^+$ to reduce the excess (compared to the dark density) $EL2^+$ population near the peaks of the grating and to leave uncompensated negatively-charged immobile acceptors A^- away from the peaks. Thus, when recombination is complete, the $EL2^+$ trap population is modulated above and below that required for compensating the acceptors. The net effect of recombination is that a transient photorefractive grating caused by the space-charge field between the mobile electrons and the

ionized $EL2^+$ donors will be transformed into a long-lived photorefractive grating where the field is between the excess $EL2^+$ (near the grating peaks) and the uncompensated immobile acceptors A^- (away from the peaks). The latter is analogous to the steady-state photorefractive grating described in connection with Fig. 2a and will persist until erased by the dark current (~0.1 ms). Also, like the steady-state grating, the maximum space-charge density for this long-lived grating is limited by the dark density of $EL2^+$ traps (which is equal to the acceptor density A^-).

Another difference between cw and picosecond photorefractive experiments is the saturation of the absorption coefficient that is caused by the extremely high generation rates that accompany short-pulsed excitation. In fact, the fluences used in our experiments are sufficiently high near the peaks of the irradiance pattern to photoionize the entire EL2 donor population. This leads to a bleaching of the linear absorption near the grating peaks and, thus, to the formation of an absorption grating. Notice that, in the case of a strong pump pulse and a weak probe, some degree of spatially uniform background bleaching will be present and will be sensed as apparent gain by the probe. Once ionized, the $EL2^+$ can absorb electrons from the valence band (or if you prefer, holes are generated in the valence band) to again produce neutral EL2 donors. The donors that are neutralized in this way are once again capable of providing electrons to the conduction band by single-photon absorption. At high excitation rates, these valence-band-to-$EL2^+$ and EL2-to-conduction-band transitions provide an effective mechanism for stepwise two-photon absorption. Also, the repopulation of donor states by absorption from the valence band limits the degree of bleaching of the donor states that can be achieved in practice. The exact degree of saturation is determined by the ratio of the electron (i.e., EL2-to-conduction band) and hole (i.e., valence band-to-$EL2^+$) cross sections.

Still another difference between cw and ps photorefractive experiments is the limitation on the number density of the space charge responsible for the internal electric field. Under cw conditions, the limiting space charge density is the number density of the trapped charge, which is equal to the acceptor number density. For illumination pulses short compared to the electron recombination time (~10 ns), the number density of positively charged centers is limited by the total

EL2 density, while the number density of electrons is potentially unlimited provided that the hole cross section of the $EL2^+$ is non-zero. If the hole cross section of $EL2^+$ is zero, then the limit on the electron number density is equal to the density of the electrons trapped at EL2 before illumination. In addition, if direct two-photon absorption is important, this is another source of conduction band electrons and valence band holes.

At the fluences needed to produce a significant photorefractive grating, picosecond beam-coupling and transient-grating measurements in GaAs are further complicated by the onset of two-photon absorption (Fig. 2c). One obvious consequence of two-photon absorption is that a weak probe pulse will experience a larger loss in the presence of a strong pulse than it would encounter alone. That is, two-photon absorption enhances probe loss. Another consequence of two-photon absorption is the generation of electron-hole pairs. As a result, an initially unshifted electron-hole free-carrier grating is produced that contributes to transient energy transfer in much the same way as the electron free-carrier grating generated by linear absorption. The former is still higher order than the latter, since the electron-hole grating is generated by a nonlinear absorption process. Once created, the electrons and holes diffuse from regions of high concentration to regions of low concentration. The electrons have the higher mobility and attempt to diffuse faster than the holes, thus, setting up a space-charge field between the electrons and holes. This field tends to accelerate the holes and to decelerate the electrons. The separation between the electrons and holes and the magnitude of the field will increase until the two are constrained to move together. The field that we have described is simply the well-known Dember field that is responsible for establishing ambipolar diffusion, but it can also modulate the refractive index through the electro-optic effect. A key point is that, in contrast to the space-charge field established between electrons and traps as a result of linear absorption, the field produced here is between two mobile species: electrons and holes generated by two-photon absorption. Consequently, the electron-hole space-charge field can decay completely by ambipolar diffusion and bimolecular recombination. This is in contrast to the transient electron-trap space-charge field, which decays by recombination into a steady-state donor-trap space-charge field. Also, in contrast to the one-photon-generated gratings, here the processes

that destroy the two-photon free-carrier grating (i.e., ambipolar diffusion and bimolecular recombination) also destroy the photorefractive grating. As we shall show, ambipolar diffusion can destroy an electron-hole grating with a period of a few microns in several tens of ps. Consequently, two-photon absorption is a second source for transient free-carrier and photorefractive gratings in GaAs, and both of these gratings can be switched on and off on picosecond time scales.

THEORETICAL MODEL

All of the processes described in the preceding section can be incorporated into a set of rate equations for the electron density n, the hole density p, and the density of ionized EL2 traps N^+, a pair of equations for the electron current j_n and hole current j_p, and Poisson's equation for the space charge field, E_{sc}:

$$\partial n/\partial t = (1/e)\nabla\cdot j_n + s_e I(N-N^+)/(h\nu) + \beta I^2/(2h\nu) - \gamma_{et} n N^+ - \gamma_{eh} np \quad , \tag{1}$$

$$\partial p/\partial t = -(1/e)\nabla\cdot j_p + s_h I N^+/(h\nu) + \beta I^2/(2h\nu) - \gamma_{hd} p(N-N^+) - \gamma_{eh} np \quad , \tag{2}$$

$$\partial N^+/\partial t = s_e I(N-N^+)/(h\nu) - s_h I N^+/(h\nu) - \gamma_{et} n N^+ + \gamma_{hd} p(N-N^+) \quad , \tag{3}$$

$$j_n = e\mu_n E_{sc} n + \mu_n k_B T \nabla n \quad , \tag{4}$$

$$j_p = e\mu_p E_{sc} p - \mu_p k_B T \nabla p \quad , \tag{5}$$

$$\nabla\cdot E_{sc} = (e/\epsilon)(p + N^+ - n - N_A) \quad , \tag{6}$$

where e is the elementary charge on the electron, μ_n and μ_p are the electron and hole mobilities, $k_B T$ is Boltzmann's constant times temperature, ϵ is the low frequency dielectric constant, the constant N is the total EL2 defect density, and N_A is the density of acceptors A^-. The first terms on the right hand side of Eqs. (1) and (2) are merely an expression of continuity. The second term in Eq. (1) and the first in Eq. (3) account for the production of electrons and photoionization of EL2 donors at a rate $s_e I(N-N^+)/(h\nu)$, where s_e is the absorption cross section of the EL2, I is the optical irradiance, $(N-N^+)$ is the density of unionized EL2, and $h\nu$ is the energy per photon. The third terms in Eqs. (1) and (2) allow for the generation of electron-hole pairs by band-to-band two-photon absorption with a coefficient β. The second terms in Eqs. (2) and (3) describe the production of holes in the valence band and the repopulation of the $EL2^+$ traps by valence band-to-$EL2^+$ transitions that occur at a rate of $s_h N^+ I/(h\nu)$, where s_h is the $EL2^+$ (or hole) cross section. Finally, the terms $\gamma_{eh} np$, $\gamma_{et} n N^+$, and $\gamma_{hd} p(N-N^+)$ describe bimolecular electron-hole, electron-trap, and hole-donor recombination processes with coefficients γ_{eh}, γ_{et}, and γ_{hd}, respectively. Notice that the acceptors A^- are assumed not to interact with the optical field.

Of course, the materials equations (1)-(6) must be solved self-consistently with the wave equation for the optical field. If the amplitude E of the optical electric field is slowly varying in

space compared to a wavelength and in time compared to the optical period, then the reduced wave equation can be written in retarded time coordinates as

$$\cos\theta\ \partial E/\partial z = i\delta_{PR}E_{SC}E + i\delta_D nE - n_b\epsilon_0 c\beta|E|^2E - s_{fc}nE/2 - s_e(N-N^+)E/2$$
$$- s_h N^+E/2 - \alpha_{np}E/2 \quad , \tag{7}$$

where 2θ is the angle between the two beams inside the sample. The first term here is the result of photorefractive coupling with a coefficient given by

$$\delta_{PR} = \pi r n_b^3/\lambda \quad , \tag{8}$$

where r is the effective electro-optic coefficient, n_b is the background refractive index, and λ is the vacuum wavelength. The second represents the Drude-Lorentz change in index of refraction associated with the generation of free-carriers. There are several contributions included in this term. The first is the Drude change in index associated with the production of free, unbound charge carriers. The second is the refractive change caused by the saturation of band-to-band transitions as a result of bandfilling. Both of these can be included in a single coupling coefficient δ_D, which can be written in the form [24]

$$\delta_D = -[\omega/(2cn_bN)]\omega_N^2/[\omega^2(1-\omega^2/\omega_g^2)] \quad , \tag{9}$$

where the plasma frequency for a number density N is given by $\omega_N^2 = e^2N/(\epsilon_0 m_e)$, ω is the optical frequency, ω_g is the band gap energy divided by $\hbar$, and m_e is the electron effective mass. For simplicity, we have ignored the contributions of the holes to the free-carrier refractive index change both because the majority of the holes have a larger effective mass and because the electron density is larger than the hole density over the fluence range of concern here. We estimate that this approximation contributes an error of less than 15% to our calculation of the free-carrier index change. This is a negligible error given the other approximations inherent in the use of Eq. (9). For example, the effect on the index of refraction of filling or depleting the EL2 donor sites is not taken into account explicitly by Eq. (9), but this contribution could be phenomenologically included by treating δ_D as a fit parameter. If the cross sections for the EL2-to-conduction-band and valence-band-to-$EL2^+$ absorption are roughly equal, then we would expect the latter effect to be

small, since each time a nearly-resonant oscillator is removed from the index profile, it is replaced by another nearly-resonant oscillator of approximately the same strength. The third term in Eq. (7) allows for two-photon absorption, and the final four terms account for the linear absorption associated with the free-carriers, EL2-to-conduction-band, valence-band-to-$EL2^+$, and non-photorefractive transitions, respectively. Here, s_{fc} and α_{np} are the free-carrier cross section and the non-photorefractive absorption coefficient, respectively.

General analytical solutions to Eqs. (1)-(7) are not available in the transient regime. The numerical procedures that we used to solve these equations are discussed in detail in a companion paper [25]. Here, we have used the same computer codes described in that paper to model selected experiments and to provide a direct comparison between theory and experiment. The values and origins of the values of the GaAs materials parameters that were used for the numerical solution of (1) through (7) are given in Table 1 and discussed in Section 3 of Ref. [25].

TWO-BEAM COUPLING

The geometry used for our two-beam mixing experiments is shown in Fig. 1. Here, a single amplified pulse at 1.06 μm was switched from a train of pulses produced by an actively and passively mode-locked Nd:YAG laser. The pulse was divided into two parts by a beam-splitter, and a variable time delay was introduced into one path as shown. The two pulses were then recombined with an external angle of $2\theta'=36^0$ between the two beams, corresponding to a grating period of 1.7 μm. A variable attenuator consisting of a half-wave plate placed between crossed polarizers was inserted into each beam path and allowed the amplitude of each pulse to be continuously adjusted. The polarizers and the half-wave plate located in the probe path also allowed the probe polarization to be continuously rotated. The optical pulse width was measured on a shot-by-shot basis by monitoring the ratio of the second harmonic energy produced by an angle-matched KDP crystal to the square of the incident fundamental energy. This ratiometer was calibrated by using conventional second-harmonic autocorrelation scans, and its accuracy checked against a streak camera having 2 ps time resolution. For the data reported here, the average pulse width was determined to be 43 ps (full width at e^{-1} of the intensity). An automated data acquisition system ensured that data were accepted only when the pulse width was within ±10% of this value. Temporal coincidence of the two pulses (i.e., zero delay) was determined indirectly by maximizing the second harmonic signal from a KDP crystal. We believe the absolute values of our measured delays to be accurate to within ±2 ps and relative delays (i.e., differences in delays) to roughly 10^{-3} ps. The spatial profiles were measured and spatial overlap of the pulses ensured by scanning the beams in the horizontal and vertical directions with a small diameter pinhole and by observing the profiles on a vidicon. The spatial profiles of the pump pulse and the probe pulse at the sample were determined to be Gaussian and equal with measured radii of 2.5 mm (half-width e^{-1} of the intensity, HW1/eI). The crystal had dimensions of 5.5, 5.0, and 3.3 mm in the (001), (110), and ($\bar{1}$10) directions, respectively, and was initially oriented as shown in Fig. 1.

The quantity measured was the normalized change in probe transmission, which is defined as the difference in the probe transmissions with and without the pump present divided by the probe

transmission without the pump:

$$\Delta T/T = [T_{pr}(\text{with pump}) - T_{pr}(\text{without pump})]/T_{pr}(\text{without pump}) \quad . \tag{10}$$

This quantity was measured in the configuration shown in Fig. 1 as a function of the ratio of pump to probe energies, total fluence, time delay between pump and probe, probe polarization, and crystal orientation. Specifically, the normalized change in probe transmission was investigated for four sample orientations. Initially, the sample was oriented such that the photorefractive energy transfer was from pump to probe; for this case,we denote the normalized change in probe transmission as $\Delta T^0/T$. Next, the sample was rotated 180° about the bisector of the two beams, so that the photorefractive energy transfer was from probe to pump ($\Delta T^{\pi}/T$). Finally, data were acquired with the sample rotated ±90° ($\Delta T^{\pm\pi/2}/T$).

The quantity that was measured experimentally was the normalized change in the probe transmission $\Delta T/T$, but the quantity that we wish to discuss is the net change in probe absorbance, ΔA. Since the probe absorbance A_{pr} is defined as the negative natural logarithm of the probe transmission, $-\ln(T_{pr})$, the relationship between the two quantities is

$$\begin{aligned}\Delta A &\equiv A_{pr}\,(\text{with pump}) - A_{pr}\,(\text{without pump}) \\ &= \ln\,[T_{pr}\,(\text{without pump})/T_{pr}\,(\text{with pump})] \\ &= -\ln\,(\Delta T/T+1) \quad .\end{aligned} \tag{11}$$

The physical significance of the change in probe absorbance ΔA can be seen most easily by writing the probe transmission in the presence of the pump, T_{pr} (with pump), in the simple exponential form $\exp(-\alpha\ell + \Gamma\ell \pm \Delta\alpha\ell)$, where α is the linear absorption coefficient in the absence of the pump, Γ is the photorefractive gain coefficient for two-wave mixing, ℓ is the crystal thickness, and $\Delta\alpha$ is meant to represent the net non-photorefractive nonlinear loss, gain, or energy transfer that might be present. For the transient conditions that obtain here, Γ and $\Delta\alpha$ vary in time at each position in the sample. Since both a spatial and temporal integration is performed by measuring the probe energy, $\Gamma\ell$ and $\Delta\alpha\ell$ must be viewed as averaged or net quantities even at low fluences. Under these limited conditions, the change in absorbance is given by

$$\Delta A = \ln [\exp(-\alpha\ell)/\exp(-\alpha\ell + \Gamma\ell \pm \Delta\alpha\ell)]$$

$$= -(\Gamma\ell \pm \Delta\alpha\ell) \quad . \tag{12}$$

Notice that in the limit of small net changes in probe transmission the normalized change in probe transmission is approximately equal to the negative change in absorbance:

$$\Delta T/T \simeq -\Delta A = \Gamma\ell \pm \Delta\alpha\ell \quad , \quad \text{for } \Delta T/T << 1 \quad . \tag{13}$$

All normalized changes in probe transmission that will be reported here are less than 0.3. Consequently, the approximate equality given by Eq. (13) will hold with an accuracy of better than 15% for even the most extreme data presented. Note, however, that for a large net probe loss or gain, $\Delta T/T$ does not accurately represent the negative absorbance change $-\Delta A$.

Since only the photorefractive mechanisms reverse sign with crystal orientation, non-photorefractive contributions to the net change in probe absorbance can be eliminated by subtracting the absorbance change ΔA^0 measured with the crystal oriented for photorefractive energy transfer from pump-to-probe (photorefractive probe gain) from ΔA^π measured with the crystal rotated 180° and oriented for photorefractive energy transfer from probe-to-pump (photorefractive probe loss). This procedure yields twice the photorefractive probe gain:

$$\Delta A^\pi - \Delta A^0 = 2\Gamma\ell$$

$$\simeq \Delta T^0/T - \Delta T^\pi/T \quad , \quad \text{for } \Delta T^0/T, \Delta T^\pi/T << 1 \quad . \tag{14}$$

Similarly, the sum of these two quantities eliminates photorefractive effects to allow the investigation of non-photorefractive nonlinear energy transfer and loss mechanisms:

$$\Delta A^\pi + \Delta A^0 = \pm 2\Delta\alpha\ell$$

$$\simeq -(\Delta T^0/T + \Delta T^\pi/T) \quad , \quad \text{for } \Delta T^0/T, \Delta T^\pi/T << 1 \quad . \tag{15}$$

We emphasize that the quantity $\Delta T^0/T - \Delta T^\pi/T$ provides for a separation of photorefractive and non-photorefractive contributions to the net absorbance only for small changes in normalized probe transmissions [i.e., when Eq. (13) is valid]. This can be illustrated by writing this difference again assuming that the probe transmissions can be represented by simple exponentials:

$$\Delta T^0/T - \Delta T^\pi/T = 2 \sinh(\Gamma\ell) \exp(\pm\Delta\alpha\ell) \quad . \tag{16}$$

Clearly, this quantity gives twice the photorefractive gain $2\Gamma\ell$ (independent of non-photorefractive gain or loss, $\pm\Delta\alpha\ell$) only for $\Gamma\ell << 1$ and $\Delta\alpha\ell << 1$. We repeat that for all data presented here, the approximate equality given by Eq. (13) is accurate to better than 15%, and the normalized change in probe transmission $\Delta T/T$ and negative net change in absorbance $-\Delta A$ can be used interchangeably with the same accuracy.

The results of measuring the normalized change in probe transmission as a function of probe-to-pump ratio for a constant incident (or external) fluence of 0.4 mJ/cm² and a grating spacing of 1.7 μm are shown in Fig. 3. The dots represent data acquired with the crystal oriented for photorefr tive probe gain ($\Delta T^0/T$); the triangles represent data acquired with the crystal rotated and oriented for photorefractive probe loss ($\Delta T^\pi/T$). Clearly, the direction of energy transfer depends on crystal orientation--an unambiguous signature of the photorefractive effect. Moreover, probe gains of a few percent have been achieved on picosecond time scales using an irradiance of a few pJ/μm². Also, notice that probe gain and loss are not symmetric about 0, illustrating that nonphotorefractive energy transfer and loss mechanisms are important even at fluences as low as 0.4 mJ/cm². In fact, when the fluence is increased, probe loss is observed for both crystal orientations. The latter point is illustrated in Fig. 4, where the measurements of Fig. 3 have been repeated for an incident fluence of 2.4 mJ/cm².

The contributions of the nonphotorefractive processes are more evident if the data are acquired and displayed differently. In Fig. 5, then, $\Delta T/T$ is plotted for the same two sample orientations as a function of incident fluence for a constant pump-to-probe ratio of 23:1. The dashed and dot-dashed curves in Fig. 5 are the results of numerical solutions to Eqs. (1)-(9) for the two-beam mixing geometry of Fig. 1 and for the same two crystal orientations as the data in Fig. 5. There is clearly good qualitative agreement between theory and experiment. The materials constants used in the numerical solutions are listed in our companion paper [25]. We emphasize that these curves are the result of calculations in which all materials parameters were either taken directly from the literature or independently measured for our sample. In this sense, these are zero-fit-

parameter calculations. We have achieved better quantitative agreement between experiment and theory by varying these materials parameters within reasonable uncertainties, but without additional independent measurements of the materials parameters there is no justification for such forced fits. The trends in the data shown in Fig. 5 can be understood qualitatively in terms of the mechanisms discussed in the preceding section by considering the order of the nonlinearity associated with each process included in the wave equation [Eq. (7)]. Our discussions will emphasize the photorefractive energy transfer, two-photon absorption, the transient energy transfer associated with the Drude-Lorentz index grating, and bleaching of the EL2 donor absorption.

The photorefractive contribution to the wave equation is given by the first term in Eq. (7), $i\delta_{PR}E_{SC}E$. For small fluences, most of the carriers are produced by single-photon ionization of the EL2 donors at a rate given by the second term of Eq. (1), $s_e(N-N^+)I/(h\nu)$. At low fluences and in the absence of two-photon absorption, the space-charge field E_{SC} can be shown to be proportional to the time integral of the gradient in the carrier density, ∇n, and thus, linear in fluence for a fixed pump-to-probe ratio. In fact, the photorefractive component of the energy transfer can be separated from the other processes by taking the difference in the two sets of data for the two crystal orientations shown in Fig. 5. The quantity $(\Delta T^0/T - \Delta T^\pi/T)/2$ is plotted in Fig. 6. Notice that both ordinate and abscissa scales are logarithmic. The large scatter in the data at the lowest fluences is the result of weak signals and poor signal-to-noise ratios at those fluences. At the lower fluences, the photorefractive gain increases roughly linearly with fluence, consistent with the production of electrons by single-photon ionization of the donors. At a fluence of ~0.5 mJ/cm², however, a distinct saturation of the gain is observed. There are two reasons for this saturation. The first is a reduction of the electron generation rate that accompanies the saturation of the EL2-to-conduction-band absorption coefficient $s_e(N-N^+)$ because of a depletion of the EL2 unionized population. By setting the total donor density (10^{16} cm^{-3}) equal to the time-integrated generation rate [i.e., $s_e(N-N^+)F/(h\nu)$, where $F/(1-R)$ is the incident fluence and R the crystal reflectivity], we estimate that 1 mJ/cm² is the incident fluence at which one-half of the donors (at the front sample surface and the center of the beam) are photoionized.

The second (and more important) source for this saturation of the photorefractive gain is related to the dynamics of grating formation. Before recombination occurs and in the absence of two-photon absorption, the quasi-steady state photorefractive and free-carrier grating strengths are determined by a balance between the diffusion current ($\mu_n k_B T \nabla n$), which tries to increase the space-charge field and destroy the electron free-carrier grating, and the drift current ($e\mu_n E_{sc} n$), which tries to decrease the space-charge field and preserve the free-carrier modulation. In the absence of a drift current, diffusion would destroy a sinusoidal electron grating in GaAs in approximately 2 ps. Consequently, under these conditions, it is roughly correct to assume that a quasi-steady state exists in which the drift and diffusion currents are approximately equal,

$$e\mu_n E_{sc} n \sim \mu_n k_B T \nabla n \quad , \tag{17}$$

throughout the 43 ps excitation process. That is, once established a gradient in electron density ∇n will quickly be reduced and the space charge increased by the diffusion current until the two currents are roughly equal. Although it is not immediately obvious from Eq. (17), at the lower fluences, the diffusion current reduces the electron gradient ∇n to a very small value compared to the gradient in ionized donors, ∇N^+, and the space charge field can be viewed as arising from a modulation of the $EL2^+$ concentration in the presence of an almost uniform negatively-charged free electron population. Thus, at low fluences both the diffusion current and the space charge field increase linearly with fluence. By comparison, the drift current contains an additional fluence dependence through the carrier density n and initially increases roughly as the square of the fluence. Consequently, the drift current increases more rapidly with fluence than the diffusion current and eventually limits the magnitude of the space charge field.

These tendencies can be seen most easily by considering the solution to the materials equations, Eqs. (1)-(6), for a highly idealized situation. Specifically, an initial carrier density of the form

$$n(t=0,x,z) = n_0(t=0,x,z) + n_{+2}(t=0,x,z)\exp(-2k_x x) + n_{-2}(t=0,x,z)\exp(+2k_x x) \quad , \tag{18}$$

(where x(z) is the direction parallel (perpendicular) to the sample face in Fig. 1 and k_x is the magnitude of the x-component of the light propagation vectors) is assumed to be created on a time

scale short compared to the time required for significant diffusion. If two-photon absorption is neglected, then the quasi-steady state solution for the space charge field before recombination occurs is reduced to solving Eq. (17) together with Poisson's equation, Eq. (6). If the space-charge field E_{sc} is written in a form similar to Eq. (18), one readily finds the amplitude of the steady-state space charge fieid and carrier density gradient in the limit of small modulation ratio (i.e., $n_{+_2}/n_0 << 1$) to be

$$E_{sc_2}(t=\infty,x,z) = [-ien_{+_2}(t=0,x,z)/(2k_x\epsilon)]/[1 + n_0(t=0,x,z)/n_{sat}] \quad (19)$$

and

$$n_{+_2}(t=\infty,x,z) = n_{+_2}(t=0,x,z)/[1 + n_{sat}/n_0(t=0,x,z)] \quad , \quad (20)$$

respectively, where $n_{sat} \equiv \epsilon(2k_x)^2k_B/e^2$ is defined as the saturation density. Notice that at low excitation levels, the initial carrier density is much smaller than the saturation density: $n_0(t=0) << n_{sat}$. In this limit, the magnitude of the space-charge field is given by $en_{+_2}(t=0)/(2k_x\epsilon)$, which is directly proportional to the initial gradient in the carrier density and, thus, proportional to the fluence. Also, notice that the drift current cannot balance the diffusion current before the latter has essentially destroyed the free-carrier grating [i.e., $n_{+_2}(t=\infty) << n_{+_2}(t=0)$]. Thus, at these fluences the free-carrier modulation $n_{+_2}(t=\infty)$ is negligible compared to the modulation in $EL2^+$ concentration, N^+. Notice, however, that for low fluences the drift current increases as the square of the fluence (because of the additional fluence dependence of the conductivity $e\mu_n n$), while the diffusion current increases linearly. Eventually, then, as the carrier density $n_0(t=0)$ becomes comparable to the saturation density, the drift current becomes strong enough to significantly limit the decay of the free-carrier grating and the magnitude of the space-charge field. In fact, in the high excitation regime, where $n_0(t=0) >> n_{sat}$, there will be negligible decay of the free-carrier grating [i.e., $n_{+_2}(t=\infty) \sim n_{+_2}(t=0)$] and the space-charge field approaches a constant value given by $en_{sat}[n_{+_2}(t=0)/n_0(t=0)]$, which is proportional to the probe-to-pump ratio. Because the 43-ps pump pulses used in our experiments are not short compared to the electron diffusion times of ~2 ps and because the effects two-photon absorption are not negligible, these results are not directly applicable. Nevertheless, this simple calculation illustrates the role of the background conductivity

$e\mu_n n_0$ in limiting the magnitude of the space-charge field and in limiting the decay of the free-carrier index grating. These same tendencies are seen in our numerical results and also can be seen by carefully inspecting the full linearized materials equations given in Ref. [26].

In addition to the initial linear increase in probe gain with fluence and the eventual saturation shown in Fig. 6, our numerical studies indicate that for external fluences below ~3 mJ/cm² the principal space-charge field is between single-photon-generated free electrons and immobile ionized $EL2^+$ donors, while above this fluence, there is a significant contribution from the Dember field associated with mobile electron-hole pairs created by two-photon absorption.

For comparison, the **nonlinear** loss and energy transfer processes that do not depend on crystal orientation are illustrated in Fig. 7. Here, one-half the negative sum of the two sets of data shown in Fig. 5, $-(\Delta T^0/2T + \Delta T^\pi/2T)$, is plotted on a logarithmic scale. At low fluences, two-photon absorption is the dominate nonlinear absorption process. Since the absorption coefficient βI is linear in intensity, an initial linear dependence on fluence is expected and observed. The reversal of slope and apparent reduction of absorbance observed at the higher fluences above ~2 mJ/cm² is caused by the onset of transient energy transfer associated with the free-carrier index grating. The strength of the Drude-Lorentz index change $\delta_D n$ also is proportional to the time-integral of the intensity I; however, in the two-beam mixing geometry, this process does not contribute in the same order as the photorefractive and two-photon effects. As we discussed previously, the reason for this is that the free-carrier index grating is unshifted to first order and will not transfer energy in this configuration. It will, however, contribute in higher order [23]. Two beam mixing is sensitive to spatial shifts in the grating sources because the pump light scattered from the gratings is coherently superposed with the transmitted probe pulse, making this technique sensitive to the phase of the scattered light. Notice that the numerical solutions shown in Fig. 7 are in excellent agreement with the observations, adding further support to the interpretation presented in this paragraph.

Consequently, for the lowest fluences shown in Fig. 5 and for the crystal oriented for photorefractive probe gain (upper curve), the photorefractive gain competes with loss from two-photon absorption. Initially, the photorefractive energy transfer is larger than two-photon loss, and

a net gain is observed. As the fluence is increased, the photorefractive gain saturates, and two-photon absorption begins to dominate, with a zero crossing at ~1 mJ/cm². Between roughly 1 and 5 mJ/cm², two-photon absorption dominates. Eventually, however, as sufficient carriers are generated by one- and two-photon absorption, the transient energy transfer associated with the free-carrier index grating is found to dominate at the highest fluences, causing a change in slope and resulting in probe gain for fluences larger than ~10 mJ/cm², as shown. For the lower curve, the photorefractive energy transfer is from probe-to-pump, and photorefractive effects as well as two-photon absorption contribute to increasing probe loss with increasing fluence. Again, however, at the highest fluences, transient energy transfer begins to dominate and reverses the sign of the slope.

TIME-RESOLVED TWO-BEAM COUPLING

The normalized change in probe transmission was also measured as a function of time delay for the geometry shown in Fig. 1. These time-resolved beam-coupling measurements were performed for several pump fluences, two probe polarizations, and four crystal orientations. The results of one such measurement are shown in Fig. 8, where $\Delta T/T$ is plotted as a function of time delay between pump and probe for a fixed fluence of 2.3 mJ/cm^2, a pump-to-probe ratio of 23:1, and two crystal orientations. Again, the dots correspond to data acquired with the crystal oriented for photorefractive probe gain, the triangles to data acquired with the crystal oriented for photorefractive probe loss, and the solid curves represent numerical solutions of Eqs. (1)-(9).

Since the quantitative agreement between the theory and the data is rather poor in Fig. 8, it is useful to attempt to understand the major features qualitatively in terms of the same three principal mechanisms used to describe Fig. 5: photorefractive energy transfer, two-photon absorption, and transient energy transfer associated with the free-carrier grating. There are three properties of each of these that are known qualitatively: the sign of $\Delta T/T$, the approximate width of the change in time, and the symmetry (or lack thereof) about zero delay. Other information, such as the magnitudes of the various effects, can be extracted either directly or indirectly from the data in Fig. 8 or estimated from separate measurements. We extract and illustrate each of these contributions roughly in Figs. 9-11.

The photorefractive contribution to $\Delta T/T$ is either positive or negative, depending on crystal orientation; it is expected to have a width roughly $\sqrt{2}$ times the optical pulse width; and it is expected to be asymmetric and skewed slightly toward negative delays. The maximum lags zero delay because the photorefractive grating has a lifetime comparable to or larger than the pulsewidth, so that a trailing pump scatters from the grating for a longer time than a leading pump. As for Fig. 6, the photorefractive component can be extracted unambiguously from the experimental results by subtracting the two sets of data in Fig. 8 for the two crystal orientations and dividing by 2. The resulting photorefractive gain is given by the dots in Fig. 9. The solid line is a shifted-Gaussian fit

to the data (not a theoretical calculation), that we subsequently use in Fig. 11 to schematically represent the photorefractive component of the two-beam gain. Notice that the measured photorefractive gain curve is temporally narrower than the expected $\sqrt{2}$ x 43 ps.

The other two principal components of the nonlinear loss and gain are independent of crystal orientation. Free-carrier transient energy transfer is always positive for the weak probe pulse and is slightly larger for a trailing pump pulse, again, because the free-carrier grating lifetime is comparable to or longer than the pulse width. Two-photon absorption is always negative, and since it is instantaneous, its contribution is symmetric about zero delay. The magnitude of the two-photon absorbance at zero delay can be estimated using our separate knowledge of the two-photon absorption coefficient [26]. The critical magnitude, however, is the difference in the strengths of two-photon absorption and free-carrier transient energy transfer. The combined effects of loss from two-photon absorption and gain from transient energy transfer can be extracted directly from Fig. 8 as 1/2 the sum of the two sets of data for the two orientations. The data so obtained are given by the circles in Fig. 10. Next, We obtain a representation for the free-carrier transient energy transfer and the two-photon loss by fitting the data in Fig. 10 by a positive shifted and a negative unshifted (with respect to zero delay) Gaussian, respectively. The dashed and dot-dashed curves in Fig. 10 are the resulting Gaussian curves, and the solid curve is the resulting sum and fit to the data.

Finally, the representations for photorefractive and free-carrier transient energy transfer and two-photon loss are shown together in Fig. 11. The three contributions can be added to obtain the two solid curves for the total $\Delta T/T$ for the two crystal orientations. These curves illustrate schematically how these processes can produce the qualitative tendencies observed in the data.

The results of a zero-fit-parameter numerical solution to Eqs. (1)-(9), allowing for probe delay and using the same materials parameters as Fig. 5, are given by the solid lines in Fig. 8. There is fair qualitative agreement between the theoretical and experimental features, but quantitative agreement is lacking. Better agreement can be obtained by varying either the

experimental or materials parameters slightly [25]. The major discrepancy, however, is that the experimental features are consistently narrower in time than the corresponding theoretical features. Although we do not presently understand this, we speculate that the experimental results fall off more rapidly than predicted at negative delays because our pulses are not bandwidth-limited. That is, our pulses may have a coherence time that is slightly less than their width, thus, precluding contributions from the grating terms for the longer delays. Experiments are underway to investigate this possibility.

Next, the time-resolved measurements of Fig. 8 were repeated for orthogonally polarized pulses. The results are displayed in Fig. 12, for an s-polarized pump and a p-polarized probe and for three fluences. Rotating the probe polarization by 90° "turns off" all grating sources that depend on a modulation of the intensity or carrier or donor population densities. The circles, crosses, and triangles represent the data in Fig. 12. The solid, dot-dashed, and dashed curves are the results of numerical solutions to Eqs. (1)-(9) in which all two-photon, photorefractive, and free-carrier grating terms have been set to zero. Only EL2-to-conduction-band, valence-band-to-$EL2^+$, two-photon, and free-carrier absorption and saturation of the donor and trap populations were included in the numerical solutions. The rather good agreement between the calculated and measured curves suggests that the various absorption cross sections entered into the code are correct. Notice that good agreement between theory and experiment are achieved for both sets of data where coherence is not an issue: that is, in Figs. 5-7, where grating sources are important, but there is no time delay between the two pulses and, in Fig. 10, where time delay is important, but grating terms are absent. This further suggests that the discrepancy between theory and experiment in Fig. 8 may not be a problem with the model, but rather an experimental artifact related to the coherence in the wings of our pulses.

TIME-RESOLVED DEGENERATE-FOUR-WAVE MIXING

The final set of measurements were obtained with a three-pulse transient grating geometry. As shown in Fig. 13, two 43-ps, 1.06-μm, s-polarized pulses write the grating. The grating is then read with a time-delayed probe pulse, as shown. The diffraction efficiency was measured in this geometry as a function of time-delay, writing fluence, crystal orientation, and probe polarization. An important difference between this technique and the two-beam-coupling shown in Fig. 1 is that here the scattered probe light is measured in a background-free direction, and consequently, a time-delayed and orthogonally-polarized probe pulse will be equally sensitive to shifted (e.g., photorefractive) and unshifted (e.g., free-carrier) gratings. Thus, the Drude-Lorentz free-carrier index grating, which could contribute to the two-beam energy transfer only in higher order, can contribute here in first order.

As an example of one such measurement, the grating diffraction efficiency is shown in Fig. 14 as a function of time delay for equal writing fluences, a total incident writing fluence of 3.6 mJ/cm^2, a p-polarized probe and a probe fluence of 0.12 mJ/cm^2. Here, the diffraction efficiency is defined as the ratio of diffracted probe energy to incident probe energy, as opposed to the ratio of diffracted-to-transmitted energy, for example. A two-component decay is observed. The initial fast decay is on the order of the optical pulse width. This is followed by a slower decay, lasting many nanoseconds. These measurements were repeated for an s-polarized probe and for various crystal orientations, including rotating the crystal by 90° about the bisector of the writing beams. While the latter orientation does not completely eliminate the photorefractive effect, it was found to reduce the photorefractive gain in the two-beam coupling geometry by a factor of 5 to 10. To within our present experimental accuracy, both the narrow peak and the slower feature were independent of crystal orientation and probe polarization. From this, we conclude that the free-carrier Drude-Lorentz index grating is larger than and dominates the photorefractive index grating at all delays. In fact, for the data shown in Fig. 14, the probe polarization and crystal orientation were chosen so that the probe should have been totally insensitive to photorefractive effects [i.e.,

both E_{SC} and the probe field along (001)].

In order to investigate the writing efficiency associated with the formation of this free-carrier grating, we measured the diffraction efficiency as a function of fluence with the probe delay fixed, first, at 40 ps near the peak diffraction efficiency and, then, at 400 ps in the slowly varying region. The results are shown in Fig. 15. The diffraction efficiency at a delay of 40 ps increases roughly as the square of the fluence. Since the diffraction efficiency is proportional to the square of the index modulation, this indicates a linear change in index with fluence. By comparison, the diffraction efficiency at 400 ps increases consistent with a squared dependence on fluence for the lower fluences, but exhibits a slight saturation near ~2 mJ/cm².

Consider first the peak at 40 ps in Figs. 14 and 15 which is associated with the diffraction of the probe pulse from a free-carrier index grating. At low fluences, the electrons will be generated by single-photon ionization of the EL2 donors, which is consistent with the fluence-squared dependence of the diffraction efficiency. As the fluence is increased, however, one might expect the onset of two-photon absorption and a deviation from this squared dependence. For example, the external incident fluence at which the linear absorption coefficient α becomes equal to the instantaneous two-photon absorption coefficient βI (at the center of the beam and at the front surface of the sample) is 2.5 mJ/cm². It is the electron density, however, that determines the magnitude of the index change. (Note: The holes contribute little to the index change because of their relatively large mass.) The carrier density generated by two-photon absorption becomes equal to that generated by linear absorption (again, at the front sample surface and at the beam center) at a fluence of ~7 mJ/cm², which differs from the equal absorption fluence by $2^{3/2}$, where a factor of 2 comes from the fact that two photons must be absorbed to produce an electron and a factor of $\sqrt{2}$ from the time integration. Integration over the Gaussian spatial profile of the pulse produces another factor of 2 for a total incident fluence of ~14 mJ/cm². Thus, although two-photon absorption begins to play a role in our measurements at fluences of approximately 2 mJ/cm², the majority of the carriers are produced by single-photon absorption for all data shown in Fig. 15.

The onset of the effects of two-photon absorption as discussed in the preceding paragraph are further offset by the depletion of the EL2 donor population and the accompanying saturation of the EL2-to-conduction-band absorption. The compensating effects of donor saturation can be seen most easily by considering Eq. (1) for the electron density n and Eq. (3) for the ionized donor density N^+, allowing for linear and two-photon absorption while excluding all other effects (i.e. drift, diffusion, and valence-band-to-$EL2^+$ absorption):

$$\partial n/\partial t = s_e I(N-N^+)/(h\nu) + \beta I^2/(2h\nu) \tag{21}$$

$$\partial N^+/\partial t = s_e I(N-N^+)/(h\nu). \tag{22}$$

In this case, the ionized-donor density is given by

$$N^+(t) = N\left\{1 - \exp\left[-\int_{-\infty}^{t}(I/F_S)dt\right]\right\} \quad , \tag{23}$$

where the saturation fluence is defined as $F_S=h\nu/s_e$ and has a value of 1.6 mJ/cm² for our sample. In the weak saturation limit, then, the equation for the electron density can be written approximately as

$$\partial n/\partial t \simeq (s_e NI/(h\nu))\left[1-\int_{-\infty}^{t}(I/F_S)dt\right] + \beta I^2/(2h\nu) \quad , \tag{24}$$

which can be integrated to obtain the final carrier density at the front surface following a Gaussian pulse:

$$n(z=0^+,\ t=+\infty) = s_e NF/(h\nu) - s_e NF^2/(2h\nu F_S) + \beta F^2/\left(2\sqrt{2\pi}\tau h\nu\right) \quad , \tag{25}$$

where F/(1-R) is the external incident fluence used to label our figures. From Eq. (25), it is clear that saturation and two-photon effects have opposite signs and somewhat compensate one another at moderate fluences. For our pulse width and sample parameters, the ratio of the third-to-second terms is ~0.6. Furthermore, the total density of carriers produced (at the surface) by strictly linear absorption (first term) will be larger than the net density lost or gained by saturation and two-

photon absorption combined if the incident fluence is less than 12 mJ/cm². Finally, valence-band-to-EL2$^+$ transitions, which have been omitted from our analysis here and which replenish the EL2 population, will further moderate and limit the saturation of the electron population. The net effect of including the latter transitions is to allow for the stepwise two-photon generation of electron-hole pairs, whereby a hole is generated and a neutralized EL2 produced by the valence-band-to-EL2$^+$ transition and an electron is subsequently produced by the photoionization of the EL2. Summarizing, although we expect the onset of saturation and two-photon absorption at approximately 2 mJ/cm², we do not expect that together they will substantially alter the power law for electron production for fluences below roughly 10 mJ/cm², consistent with the fluence dependence of the diffraction efficiency maximum as shown in Fig. 15.

The writing efficiency shown in Fig. 15 and the fast decay shown in Fig. 14 are consistent with a free-carrier grating in which electrons are generated into the conduction band by single-photon ionization of the EL2 donors and by two-photon absorption and holes are produced in the valence band by two-photon absorption and by valence-band-to-EL2$^+$ transitions. In addition to the free-carrier grating, of course, a modulation of the immobile ionized donor density EL2$^+$ is produced. The final number of electrons produced (when summed over space) will be approximately equal to the number of holes plus the number of EL2$^+$. Thus, there are more electrons than holes. The initial fast decay of the diffraction efficiency shown in Fig. 14 is consistent with the diffusion of the electrons in the presence of the mobile holes and stationary ionized EL2$^+$ donors. In overly simplistic terms, the electron-hole portion of the grating decays by ambipolar diffusion, which in the absence of the space-charge field from the immobile EL2$^+$, would occur in a characteristic time given by $\tau_A = \Lambda_g^2/(4\pi^2 D_A) \simeq 40$ ps, where D_A is the ambipolar diffusion coefficient. The free-electron grating cannot decay completely, however, because of the presence of the charged EL2$^+$. In fact, the grating decay can proceed only to the point where the diffusion current ($\mu_n k_B T \nabla n$) exactly balances the drift current ($e\mu_n E_{sc} n$). That is, the overall electron density gradient ∇n will decrease and the space charge E_{sc} will increase until

$$E_{sc} = -(k_B T/e)(\nabla n/n) \quad . \tag{26}$$

This quasi-steady state density modulation ∇n will be maintained until (on a time scale of tens-of-ns) recombination reduces the space-charge by depleting the $EL2^+$ population. When considered alone, this process should equilibrate on a time scale of at most the electronic diffusion time given by $\tau_D = \Lambda_g^2/(4\pi D_n) \simeq 5$ ps, where D_n is the diffusion coefficient for the electrons. Of course, these two processes do not equilibrate independently, but evolve together as dictated by Eqs. (1)-(6).

The reason for the saturation in the diffraction efficiency at 400 ps shown in Fig. 15 is now evident. The magnitude of the gradient in electron density that can be maintained on nanosecond time scales is determined by the space-charge field, as indicated by Eq. (26). The growth of the space charge with fluence, however, is limited eventually by the number of available donors, $\sim 10^{16}$ cm^{-3} for the sample used here. As discussed in a preceding paragraph, this donor population would begin to saturate at an incident fluence of approximately 2 mJ/cm^2. The final $EL2^+$ population following excitation will be determined by the incident fluence and by the strength of the valence-band-to-$EL2^+$ absorption, since the latter tends to repopulate the $EL2^+$.

CONCLUSIONS

The data and theoretical analyses presented in the previous sections are consistent with the following picture of two- and four-wave mixing in undoped semi-insulating GaAs. The normalized transmission, $\Delta T/T$, of a weak probe in the two-wave mixing geometry is sensitive to three major processes: photorefractive energy transfer in a direction controlled by the crystal axes, transient energy transfer from the strong beam to the weak beam due to the Drude-Lorentz free-carrier refractive index grating, and two-photon absorption. Saturation of linear absorption and absorption gratings also occur but with a much smaller effect. At fluences below 1 mJ/cm^2, the photorefractive effect dominates. As the total fluence is increased, the photorefractive space-charge field saturates because the donor population is depleted and the background conductivity increases. At this point two-photon absorption causes probe loss for all crystal orientations. Finaliy, above ~5 mJ/cm^2, transient energy transfer caused by the free-carrier grating, which contributes only to higher order in intensity, begins to dominate.

By contrast, the three-pulse transient grating geometry used for our experiments is sensitive to the strength of the refractive index grating and not to whether the grating is shifted by 90^0 from the intensity interference pattern (photorefractive component) or by 180^0 (free-carrier component). Our measurements indicate that the index change associated with the free-carrier grating is larger than and dominates the photorefractive grating for all time delays and for all fluences. These free-carrier gratings exhibit an initial fast diffusive decay time of less than 100 ps, but complete decay is prevented by the space-charge field (and drift current) associated with the immobile ionized donors.

ACKNOWLEDGEMENTS

The authors wish to acknowledge many useful conversations with M. B. Klein and A. T. Hunter. This work was supported in part by the U.S. Office of Naval Research and The Robert A. Welch Foundation.

REFERENCES

[1] J. Feinberg, D. Heiman, A. R. Tanguay, Jr., and R. W. Hellwarth, "Photorefractive effects and light-induced charge migration in barium titanate," J. Appl. Phys., vol. 51, pp. 1297-1305, 1980.

[2] J. P. Huignard and F. Micheron, "High-sensitivity read-write volume holographic storage in $Bi_{12}SiO_{20}$ and $Bi_{12}GeO_{20}$ crystals," Appl. Phys. Lett., vol. 29, pp. 591-593, 1976.

[3] D. von der Linde, A. M. Glass, and K. F. Rodgers, "High-sensitivity optical recording in KTN by two-photon absorption," Appl. Phys. Lett., vol. 26, pp. 22-24, Jan. 1975.

[4] P. Günter and A. Krumins, "High-sensitivity read-write volume holographic storage in reduced $kNbO_3$ crystals," Appl. Phys., vol. 23, pp. 199-207, 1980.

[5] B. Fisher, M. Cronin-Golomb, J. O. White, and A. Yariv, "Amplifying continuous wave phase conjugate mirror with strontium barium niobate," Appl. Phys. Lett., vol. 40, pp. 863-865, 1982.

[6] F. S. Chen, J. T. LaMacchia, and D. B. Frazer, "Holographic storage in lithium niobate," Appl. Phys. Lett., vol. 13, pp. 223-225, 1968.

[7] D. von der Linde, A. M. Glass, and K. F. Rodgers, "Multiphoton photorefractive processes for optical storage in $LiNbO_3$," Appl. Phys. Lett., vol. 25, pp. 155-157, Aug. 1974.

[8] J. Feinberg and R. W. Hellwarth, "Phase-conjugating mirror with continuous-wave gain," Opt. Lett., vol. 5, pp. 519-521, Dec. 1980.

[9] J. P. Huignard and A. Marrakchi, "Two-wave mixing and energy transfer in $Bi_{12}SiO_{20}$ crystals: Application to image amplification and vibration analysis," Opt. Lett., vol. 9, pp. 622-624, Dec. 1981.

[10] J. P. Huignard, H. Rajbenbach, Ph. Refregier, and L. Solymar, "Wave mixing in photorefractive bismuth silicon oxide crystals and its applications," Opt. Eng., vol. 24, pp. 586-592, 1985.

[11] J. O. White and Amnon Yariv, "Real time image processing via four-wave mixing in a photorefractive medium," Appl. Phys. Lett., vol. 37, pp. 5-7, July 1980.

[12] M. Cronin-Golomb, A. Yariv, and I. Ury, "Coherent coupling of diode lasers by phase conjugation," Appl. Phys. Lett., vol. 48, pp. 1240-1242, 1986.

[13] J. Feinberg and G. D. Bacher, "Phase-locking lasers with phase conjugation," Appl. Phys. Lett., vol. 48, pp. 570-572, 1986.

[14] J. O. White, G. C. Valley, and R. A. McFarlane, "Coherent coupling of pulsed dye oscillators using nonlinear phase conjugation," Appl. Phys. Lett., vol. 50, pp. 880-882, 1987.

[15] A. L. Smirl, G. C. Valley, R. A. Mullen, K. Bohnert, C. D. Mire, and T. F. Boggess, "Picosecond photorefractive effect in $BaTiO_3$," Opt. Lett., vol. 12, pp. xxx-xxx, 1987.

[16] A. M. Glass, A. M. Johnson, D. H. Olson, W. Simpson, and A. A. Ballman, "Four-wave mixing in semi-insulating InP and GaAs using the photorefractive effect," Appl. Phys. Lett., vol. 44, pp. 948-950, May 1984.

[17] M. B. Klein, "Beam coupling in undoped GaAs at 1.06 μm using the photorefractive effect," Opt. Lett., vol. 9, pp. 350-352, Aug. 1984.

[18] A. M. Glass, M. B. Klein, G. C. Valley, "Photorefractive determination of the sign of photocarriers in InP and GaAs," Electron. Lett., vol. 21, pp. 220-221, Mar. 1985.

[19] G. Albanese, J. Kumar, and W. H. Steier, "Investigation of the photorefractive behavior of chrome-doped GaAs by using two-beam coupling," Opt. Lett., vol. 11, pp. 650-652, Oct. 1986.

[20] J. Strait and A. M. Glass, "Time-resolved photorefractive four-wave mixing in semiconductor materials," J. Opt. Soc. Am. B, vol. 3, pp. 342-344, Feb. 1986.

[21] G. C. Valley, A. L. Smirl, M. B. Klein, K. Bohnert, and T. F. Boggess, "Picosecond photorefractive beam coupling in GaAs," Opt. Lett., vol. 11, pp. 647-649, 1986.

[22] G. C. Valley, "Short-pulse grating formation in photorefractive materials," IEEE J. Quantum Electron., vol. QE-19, pp. 1637-1645, 1983.

[23] V. L. Vinetskii, N. V. Kukhtarev, and M. S. Soskin, "Transformation of intensities and phases of light beams by transient 'undisplaced' holographic gratings," Sov. J. Quantum Electron., vol. 7, pp. 230-233, Feb. 1977.

[24] R. K. Jain and M. B. Klein, "Degenerate four-wave mixing in semiconductors," in Optical Phase Conjugation, ed. by R. A. Fisher (Academic Press, New York, 1983), pp. 307-415.

[25] G. C. Valley and A. L. Smirl, "Theory of transient energy transfer in gallium arsenide," IEEE J. Quantum Electron., this issue, 1987.

[26] T. F. Boggess, A. L. Smirl, S. C. Moss, and Ian W. Boyd, "Optical limiting in GaAs," IEEE J. Quantum Electron., vol. QE-21, pp. 488-494, 1985.

FIGURE CAPTIONS

Figure 1. Generic geometry for two-beam coupling experiments.

Figure 2. Schematic of energy level diagram for undoped semi-insulating GaAs illustrating (a) steady-state photorefractive grating formation and ultrafast free-carrier and photorefractive grating formation resulting from (b) single-photon ionization of donors and (c) two-photon absorption.

Figure 3. The normalized change in probe transmission $\Delta T/T$ as a function of probe-to-pump ratio for a constant total incident fluence of 0.4 mJ/cm². The circles represent data acquired with the crystal oriented for photorefractive energy transfer from pump-to-probe ($\Delta T^0/T$) and the triangles from probe-to-pump ($\Delta T^\pi/T$).

Figure 4. The normalized change in probe transmission $\Delta T/T$ as a function of the ratio of probe-to-pump for a constant total incident fluence of 2.4 mJ/cm². The circles represent data acquired with the crystal oriented for photorefractive probe gain ($\Delta T^0/T$) and the triangles for a photorefractive probe loss ($\Delta T^\pi/T$).

Figure 5. The normalized change in probe transmission $\Delta T/T$ as a function of incident fluence for a fixed probe-to-pump ratio of 0.044. Again, the circles represent data acquired with the crystal oriented for photorefractive probe gain ($\Delta T^0/T$) and the triangles for photorefractive probe loss ($\Delta T^\pi/T$). The dashed and dot-dashed curves are results of numerical solutions of Eqs. (1)-(9).

Figure 6. The photorefractive probe gain as a function of total incident fluence for a fixed probe-to-pump ratio of 0.044, obtained by calculating 1/2 the difference of the two curves shown in Fig. 5 [i.e., $1/2(\Delta T^0/T - \Delta T^\pi/T)$]. The circles represent the data, and the dashed line indicates the numerical solution of Eqs. (1)-(9). A line with a slope of 1 is shown for comparison.

Figure 7. The nonlinear probe loss, as determined by taking 1/2 the negative sum of the two curves shown in Fig. 5 [i.e., $-1/2(\Delta T^0/T + \Delta T^\pi/T)$], as a function of total incident fluence for a probe-to-pump ratio of 0.044. The circles represent the data, and the dashed line indicates the numerical solution of Eqs. (1)-(9). A line with a slope of 1 is shown for comparison.

Figure 8. The normalized change in probe transmission $\Delta T/T$ as a function of time delay in units of the pulsewidth (21.5 ps, half-width at e^{-1} of the intensity) for a constant probe-to-pump ratio of 0.044 and for a constant incident fluence of 2.3 mJ/cm². The circles represent data acquired with the crystal oriented for photorefractive probe gain $\Delta T^0/T$ and the triangles for photorefractive probe loss $\Delta T^\pi/T$. The solid curves are numerical solutions to Eqs. (1)-(9) for the same two orientations.

Figure 9. The photorefractive probe gain as a function of time delay for a constant incident fluence of 2.3 mJ/cm² and a fixed probe-to-pump ratio of 0.044. These data are obtained by calculating 1/2 the difference of the two sets of data in Fig. 8, $[1/2(\Delta T^0/T - \Delta T^\pi/T)]$. The solid curve is a numerical fit to the data using a shifted (with respect to zero delay) Gaussian.

Figure 10. The nonlinear, nonphotorefractive probe loss as a function of time delay for a total incident fluence of 2.3 mJ/cm² and a probe-to-pump ratio of 0.044. The data (circles) were obtained by calculating 1/2 the sum of the two sets of data in Fig. 8 [i.e., $1/2(\Delta T^0/T + \Delta T^\pi/T)$]. The solid curve is a representation of the total nonlinear probe loss obtained by fitting the data with a shifted Gaussian for the transient energy transfer (TET) and an unshifted Gaussian for the two-photon absorption (T^pA).

Figure 11. A schematic illustration of the manner in which photorefractive gain (PR^0), photorefractive loss (PR^π), two-photon absorption (TPA), and transient energy transfer (TET) can be combined to account for the observed tendencies in the normalized change in probe transmission $\Delta T/T$ for the two crystal orientations (solid curves). The data from Fig. 8 are reproduced for comparison.

Figure 12. The normalized change in probe transmission $\Delta T/T$ as a function of time delay for orthogonally polarized pump and probe, a fixed probe-to-pump ratio of 0.044, and for three fluences: 2.3, 5.5, and 11.5 mJ/cm^2. Notice that the time delay is normalized by the pulse length (i.e., 21.5 ps half width at e^{-1}). The solid, dashed and dot-dashed lines represent numerical solutions to Eqs. (1)-(9).

Figure 13. Schematic representation of the geometry for time-resolved transient grating (or degenerate-four-wave mixing) experiments.

Figure 14. The diffraction efficiency of a p-polarized weak probe pulse as a function of time delay following two s-polarized writing pulses, each having a fluence of 1.8 mJ/cm^2 (i.e., total fluence of 3.6 mJ/cm^2).

Figure 15. The diffraction efficiency of the weak p-polarized probe pulse as a function of the total writing fluence for fixed time delays of 40 ps (circles) and 400 ps (triangles).

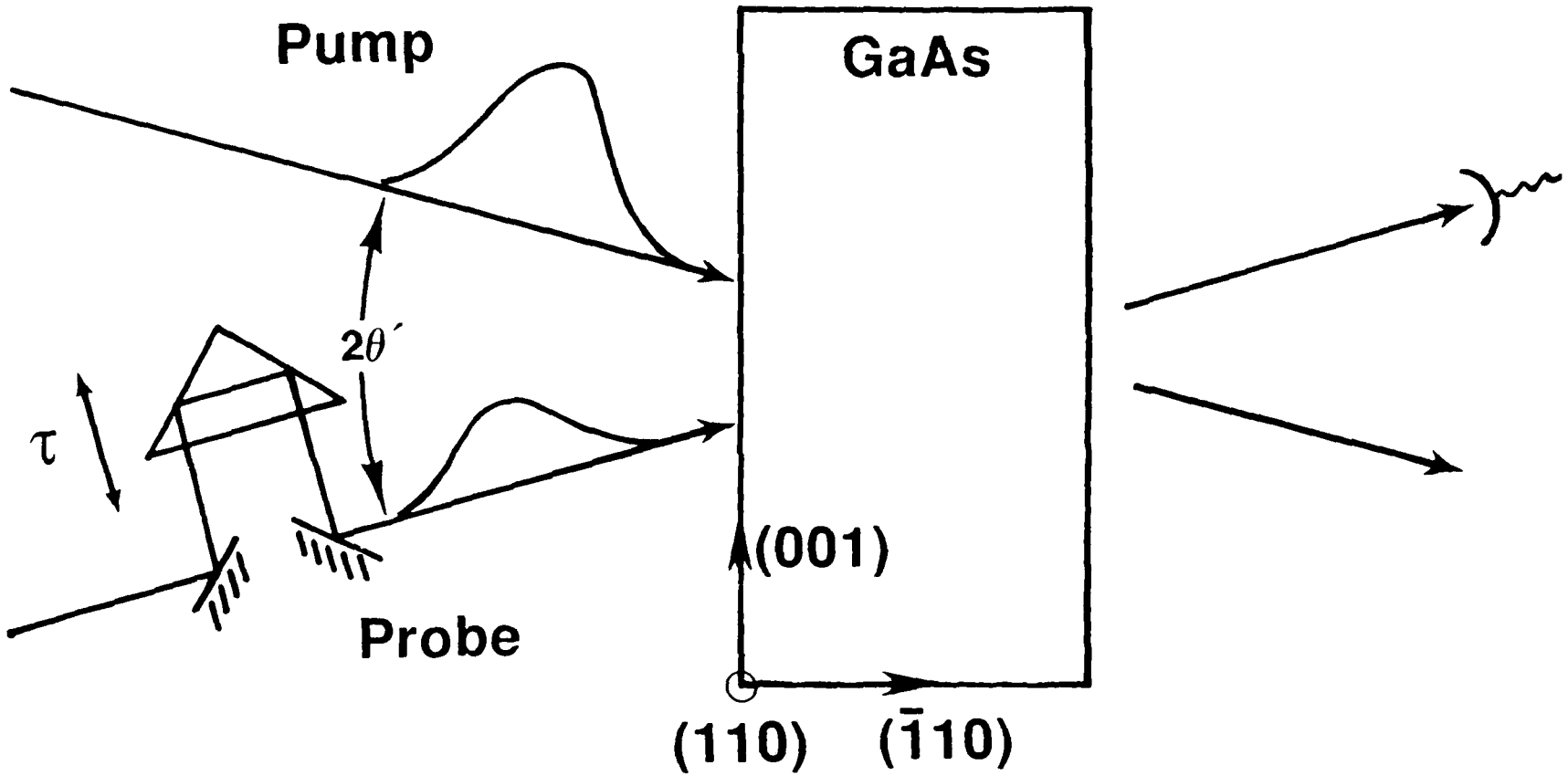
Pump
GaAs
$2\theta'$
τ
(001)
Probe
(110)
$(\bar{1}10)$

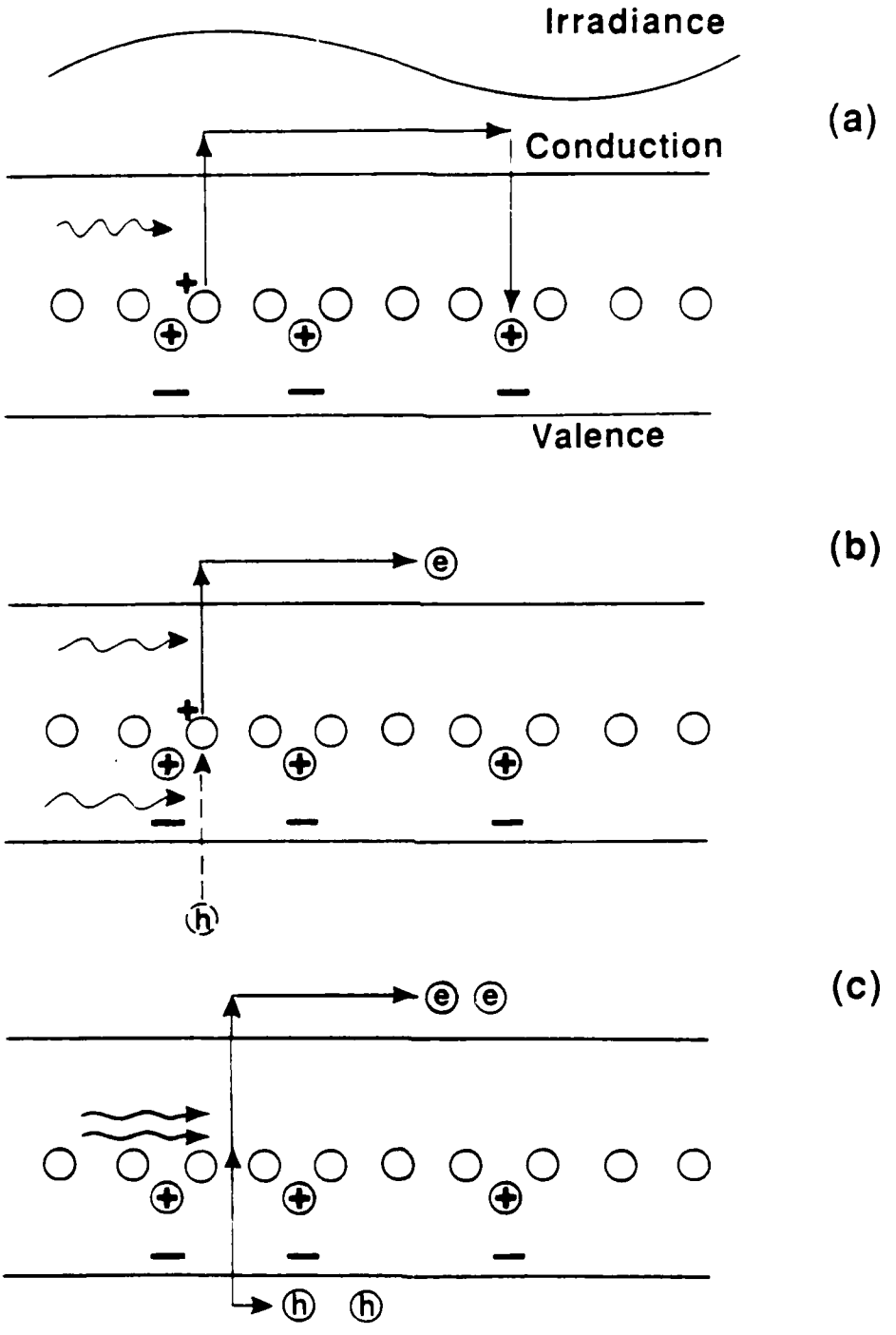
Irradiance
(a)
Conduction
Valence
(b)
e
h
(c)
e e
h h
○Neutral EL2 Donors
⊕Ionized EL2+ Donors (Traps)
– Charged Acceptors
ⓔ Electrons
ⓗ Holes

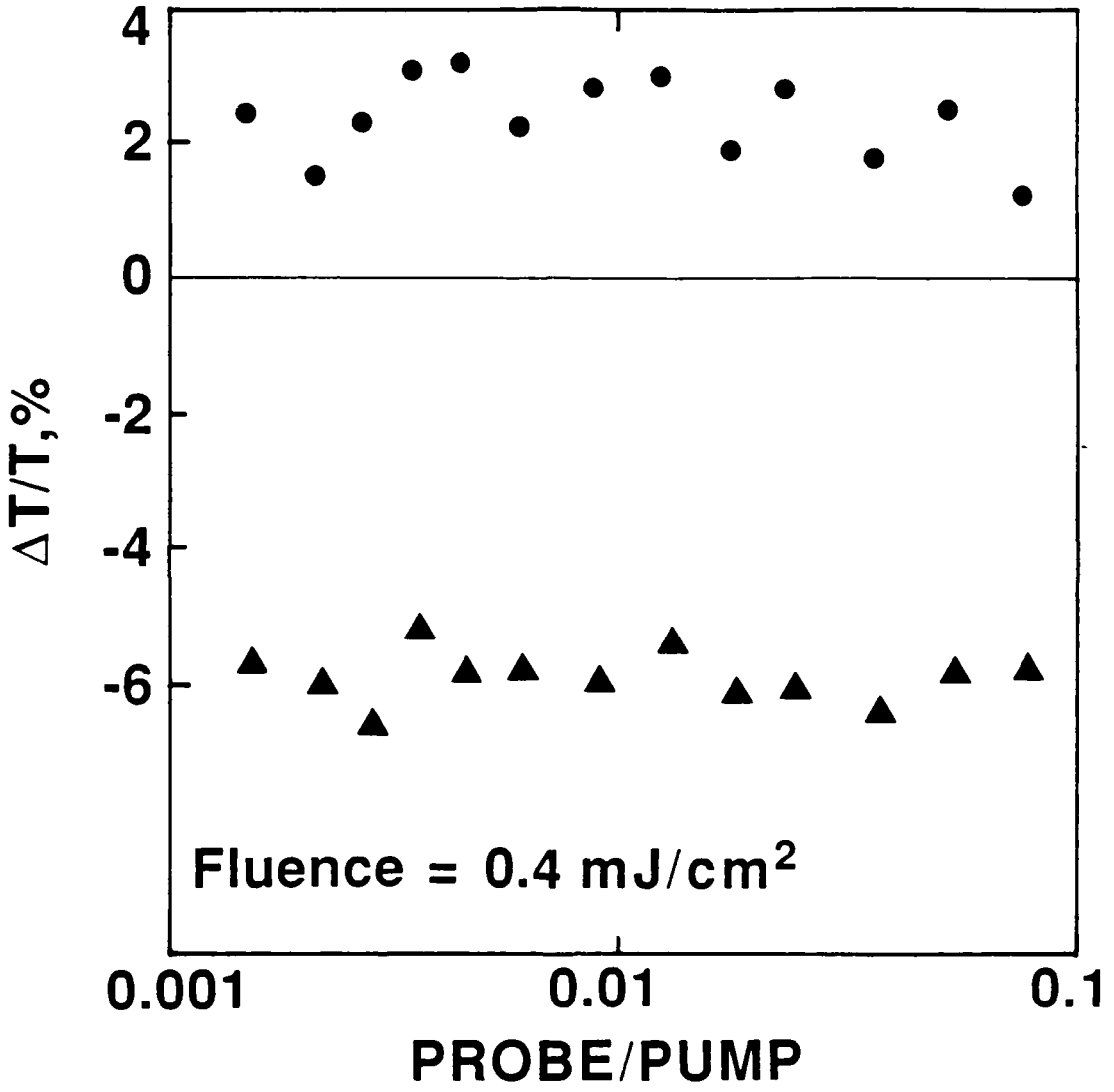
4
2
0
-2
-4
-6
ΔT/T,%
Fluence = 0.4 mJ/cm²
0.001
0.01
0.1
PROBE/PUMP

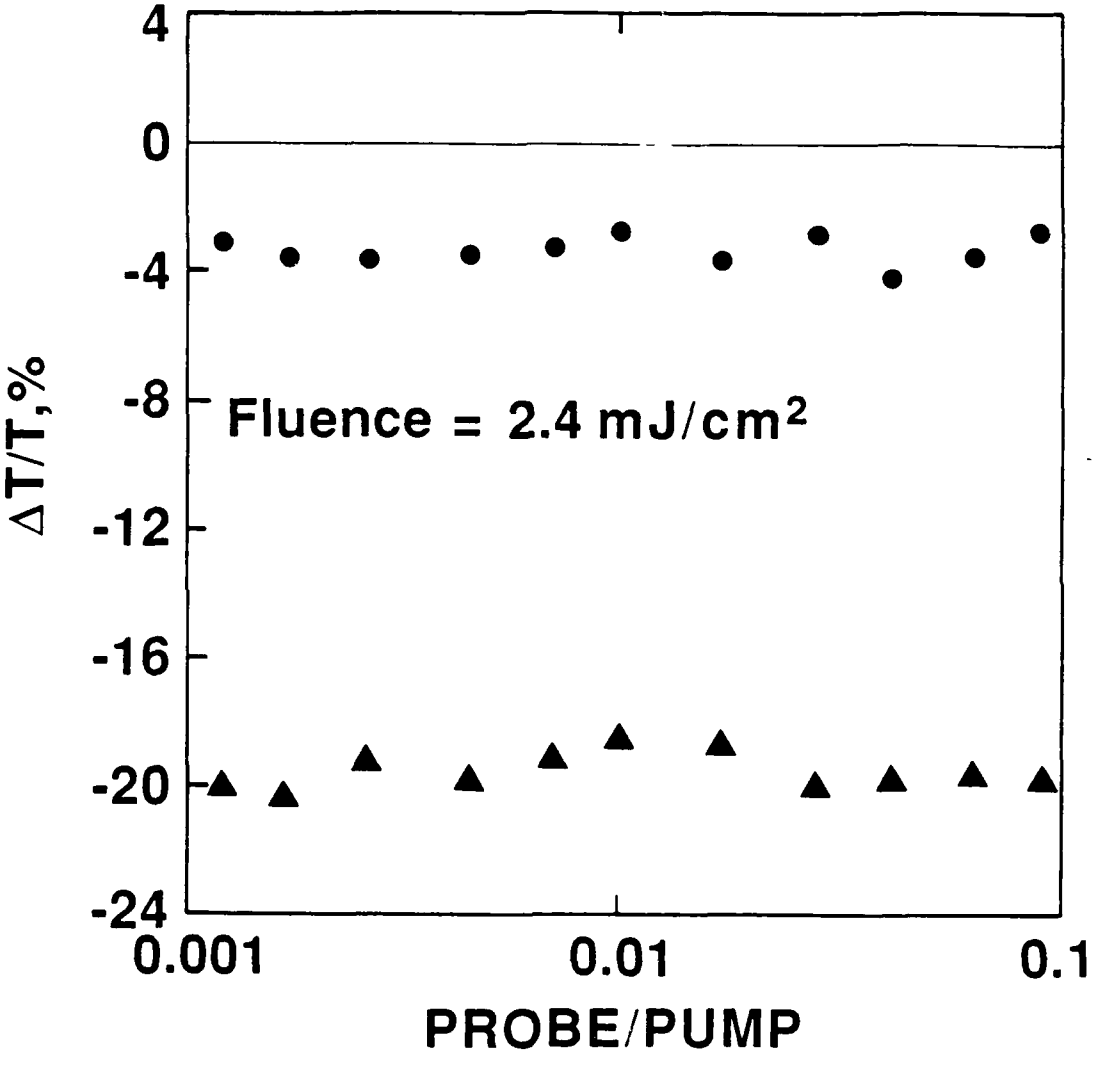
4
0
-4
-8
-12
-16
-20
-24
ΔT/T,%
Fluence = 2.4 mJ/cm²
0.001
0.01
0.1
PROBE/PUMP

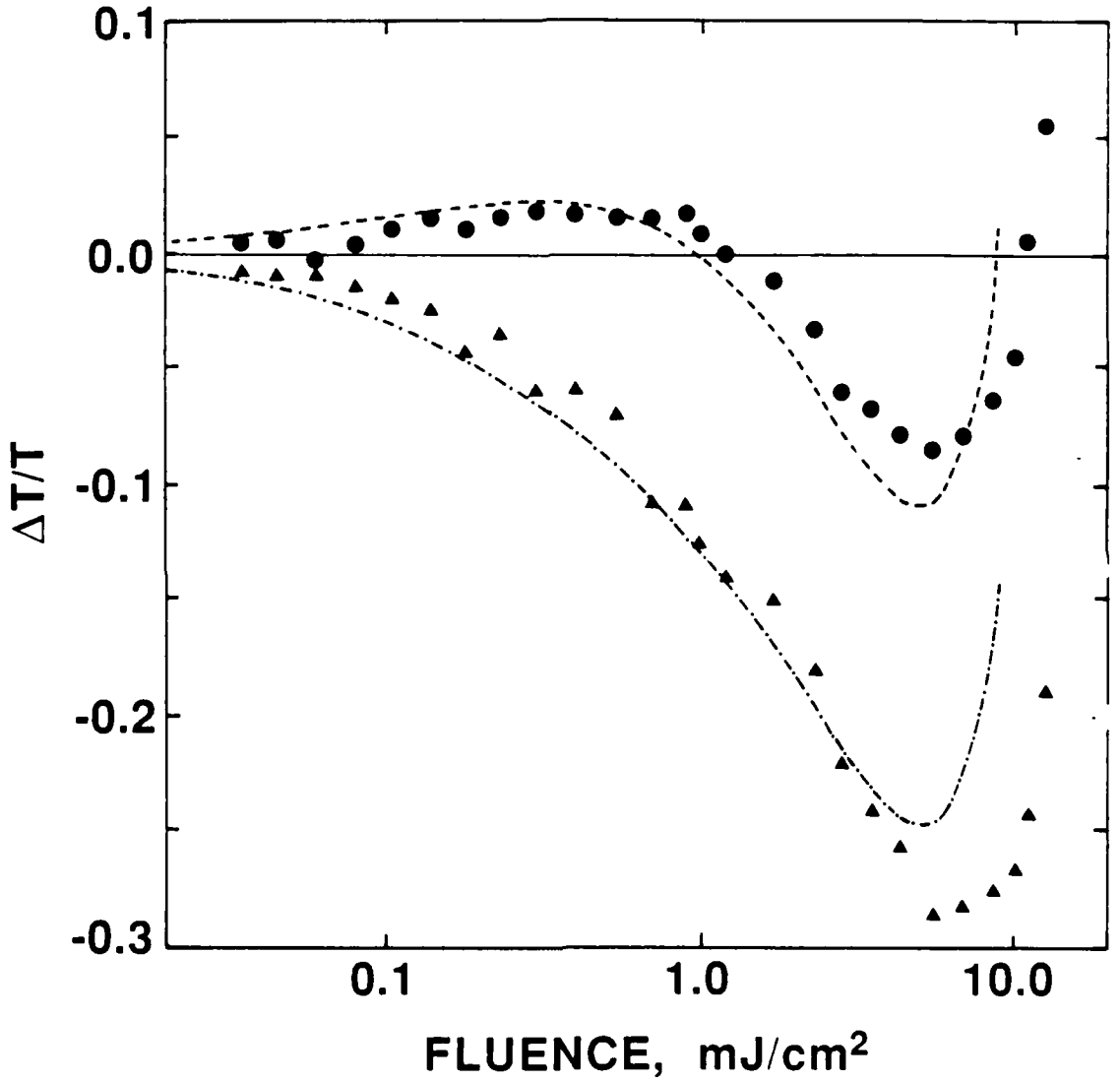
0.1
0.0
-0.1
-0.2
-0.3
ΔT/T
0.1
1.0
10.0
FLUENCE, mJ/cm²

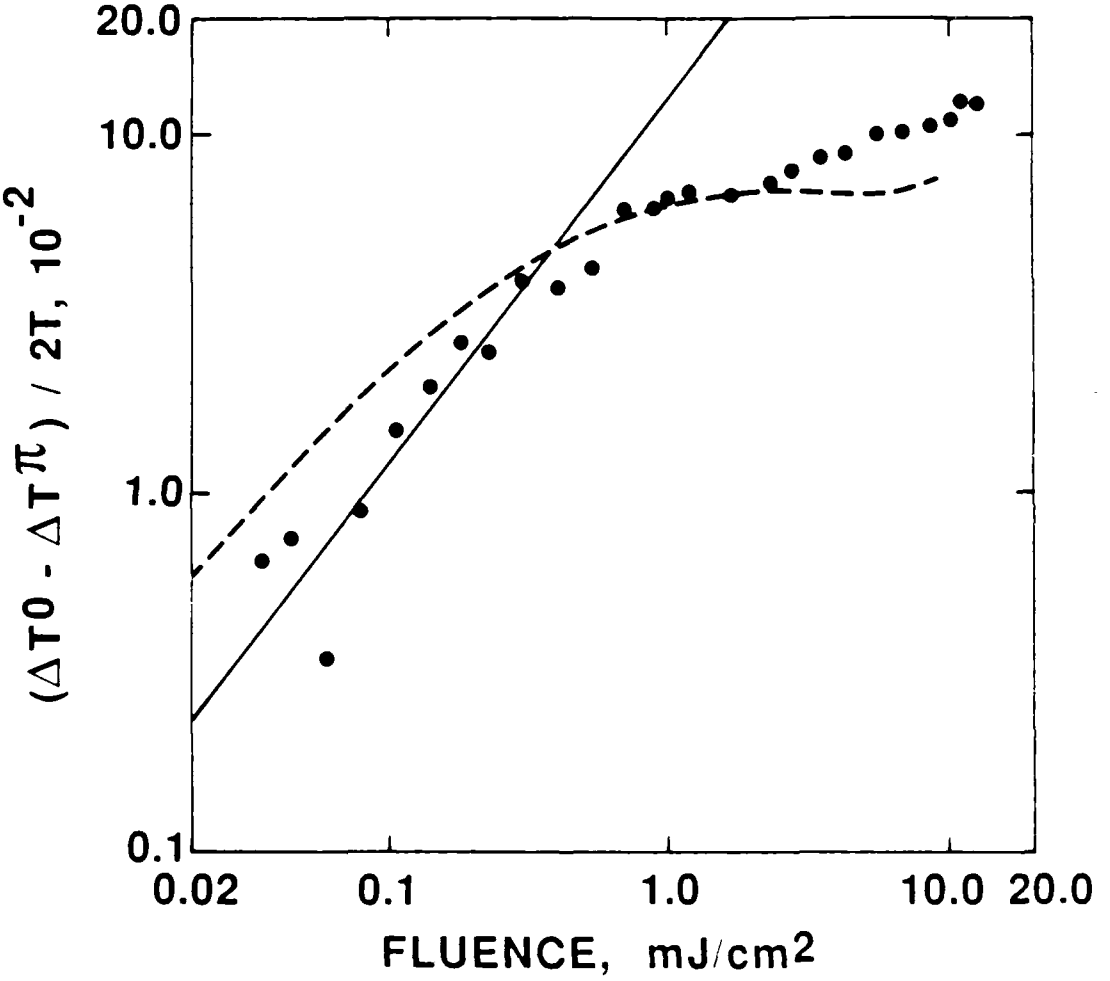
20.0
10.0
1.0
0.1
0.02
0.1
1.0
10.0
20.0
(ΔT0 - ΔTπ) / 2T, 10-2
FLUENCE, mJ/cm2

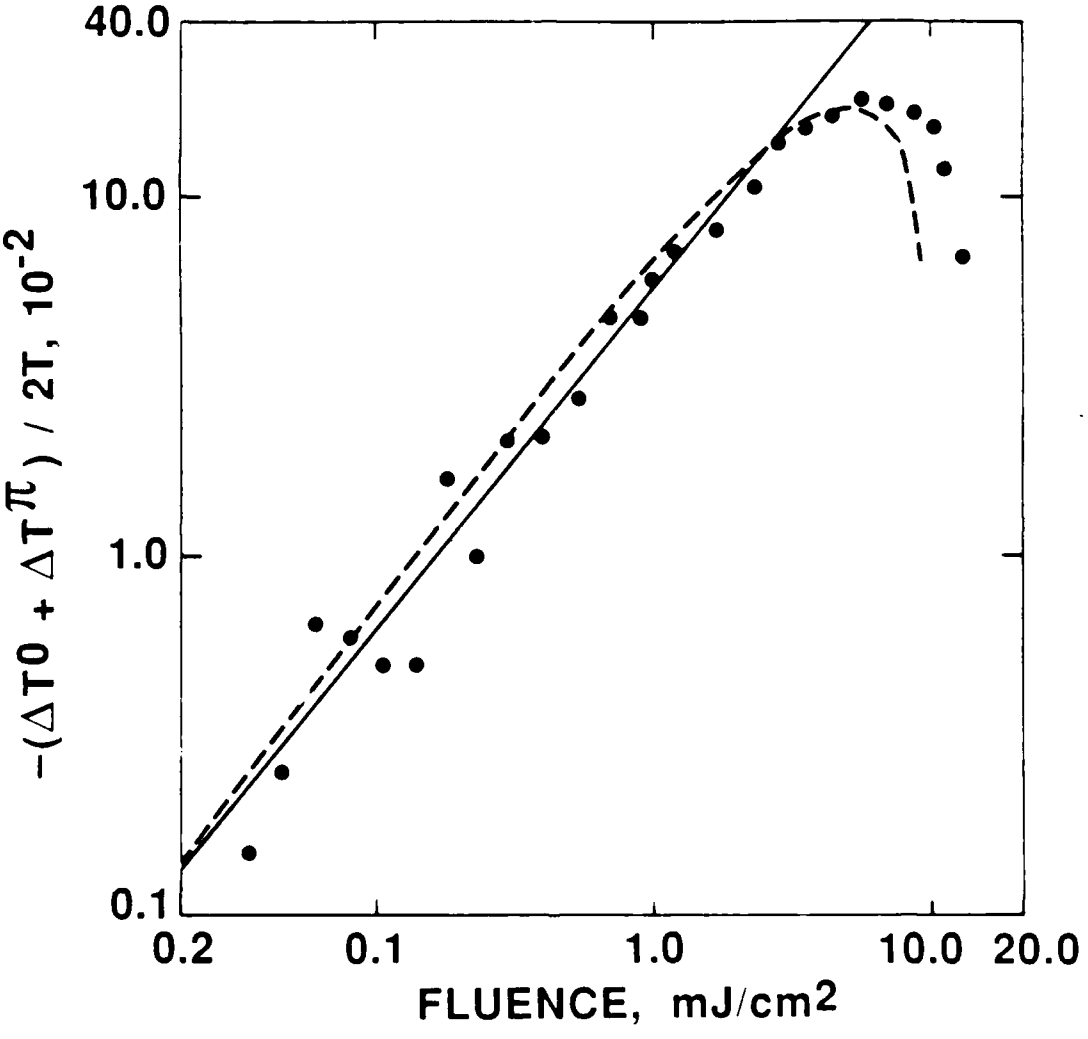
40.0
10.0
1.0
0.1
0.2
0.1
1.0
10.0
20.0
$-(\Delta T0 + \Delta T^{\pi}) / 2T, 10^{-2}$
FLUENCE, mJ/cm2

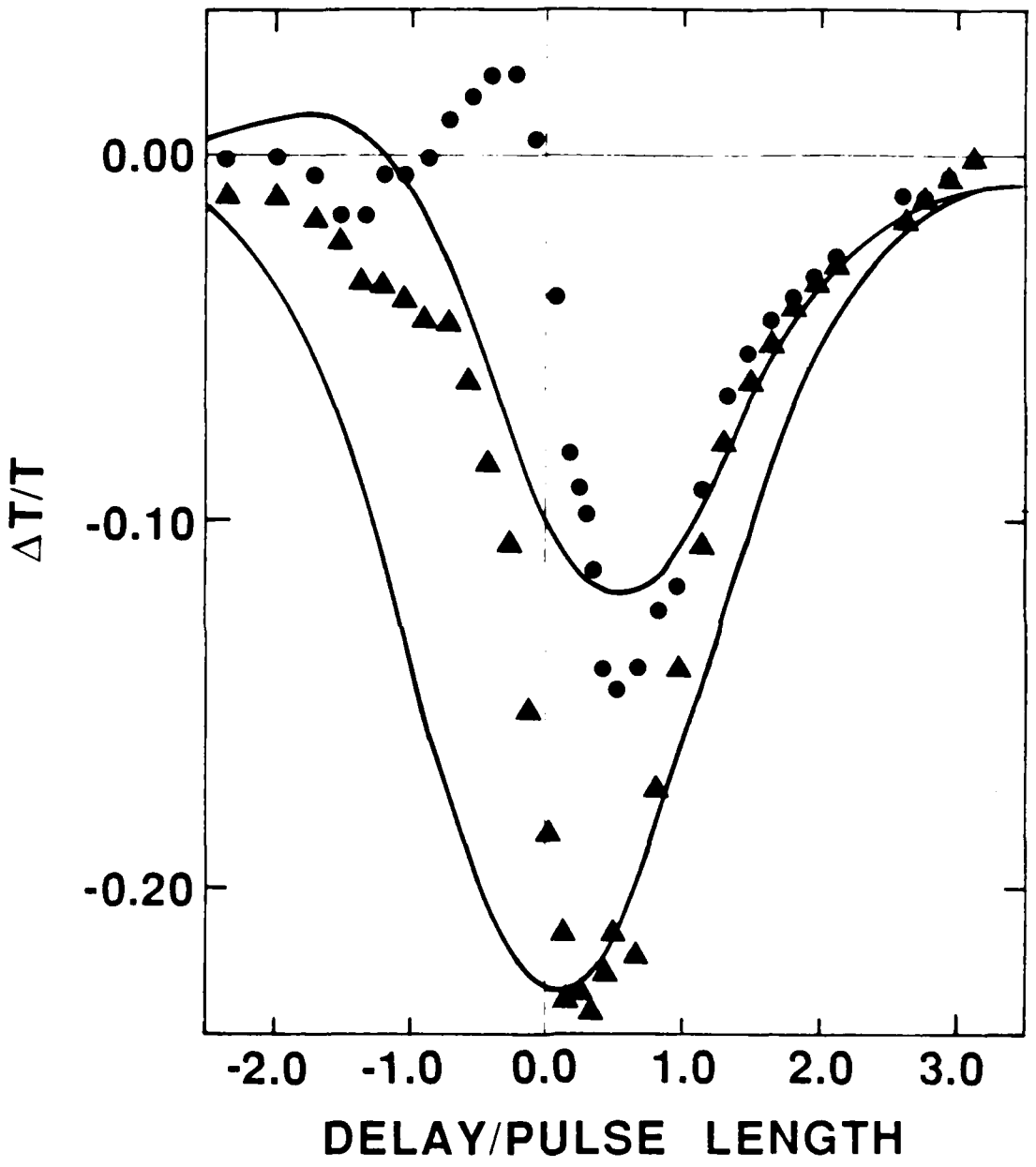
0.00
-0.10
-0.20
ΔT/T
-2.0
-1.0
0.0
1.0
2.0
3.0
DELAY/PULSE LENGTH

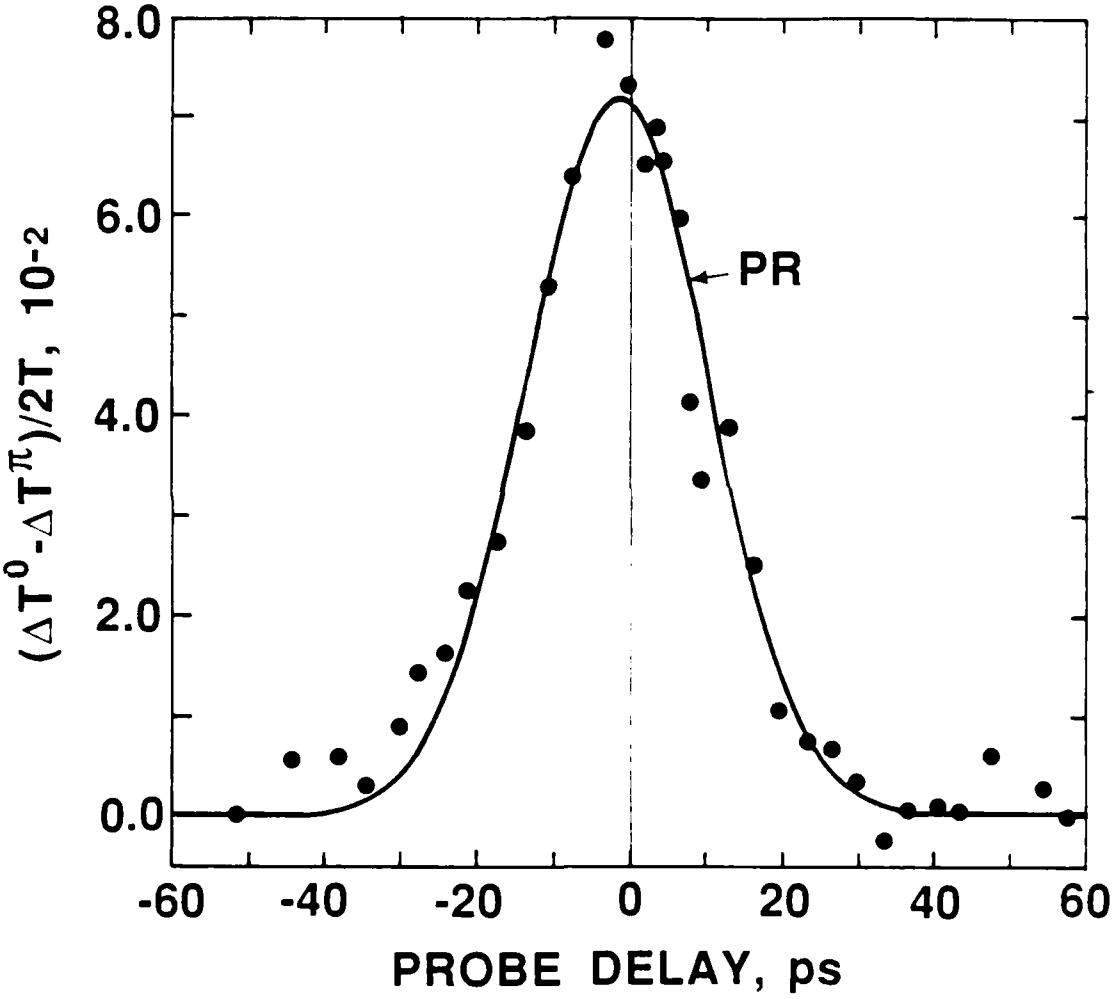
8.0
6.0
4.0
2.0
0.0
-60
-40
-20
0
20
40
60
PR
$(\Delta T^0 - \Delta T^\pi)/2T$, 10^{-2}
PROBE DELAY, ps

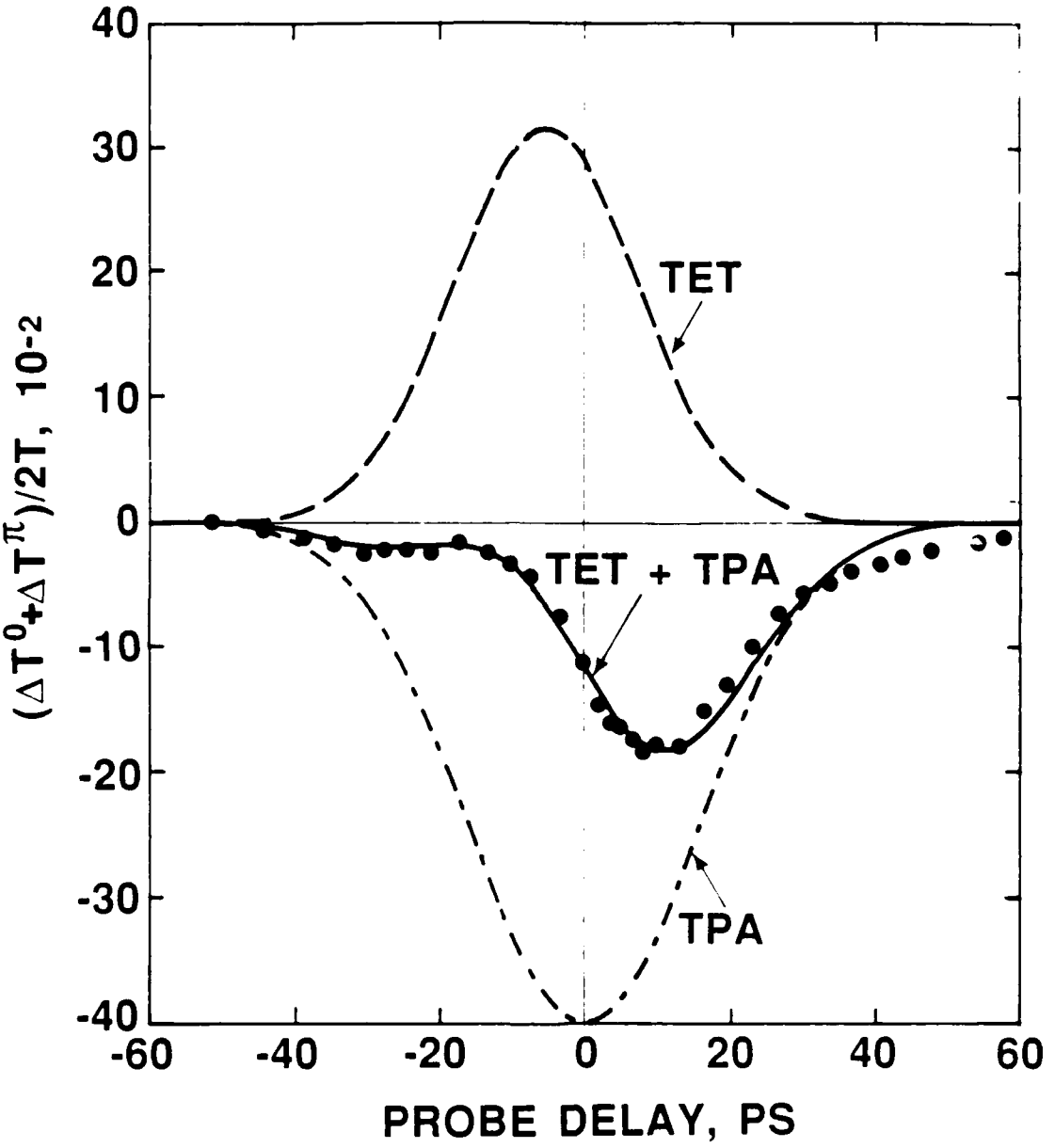
40
30
20
10
0
-10
-20
-30
-40
-60
-40
-20
0
20
40
60
TET
TET + TPA
TPA
$(\Delta T^0+\Delta T^\pi)/2T,\ 10^{-2}$
PROBE DELAY, PS

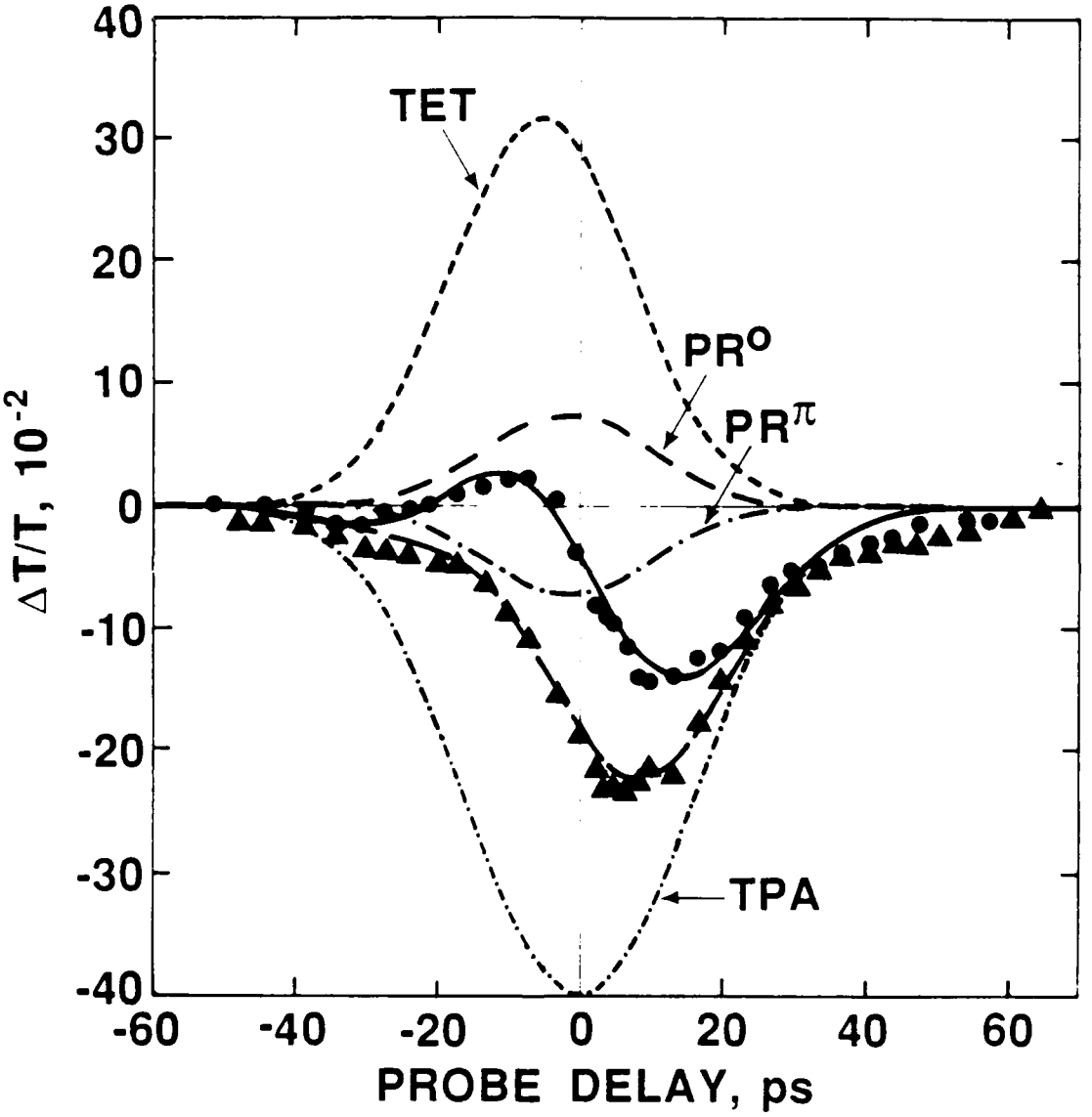
40
30
20
10
0
-10
-20
-30
-40
-60
-40
-20
0
20
40
60
ΔT/T, 10-2
PROBE DELAY, ps
TET
PRO
PRπ
TPA

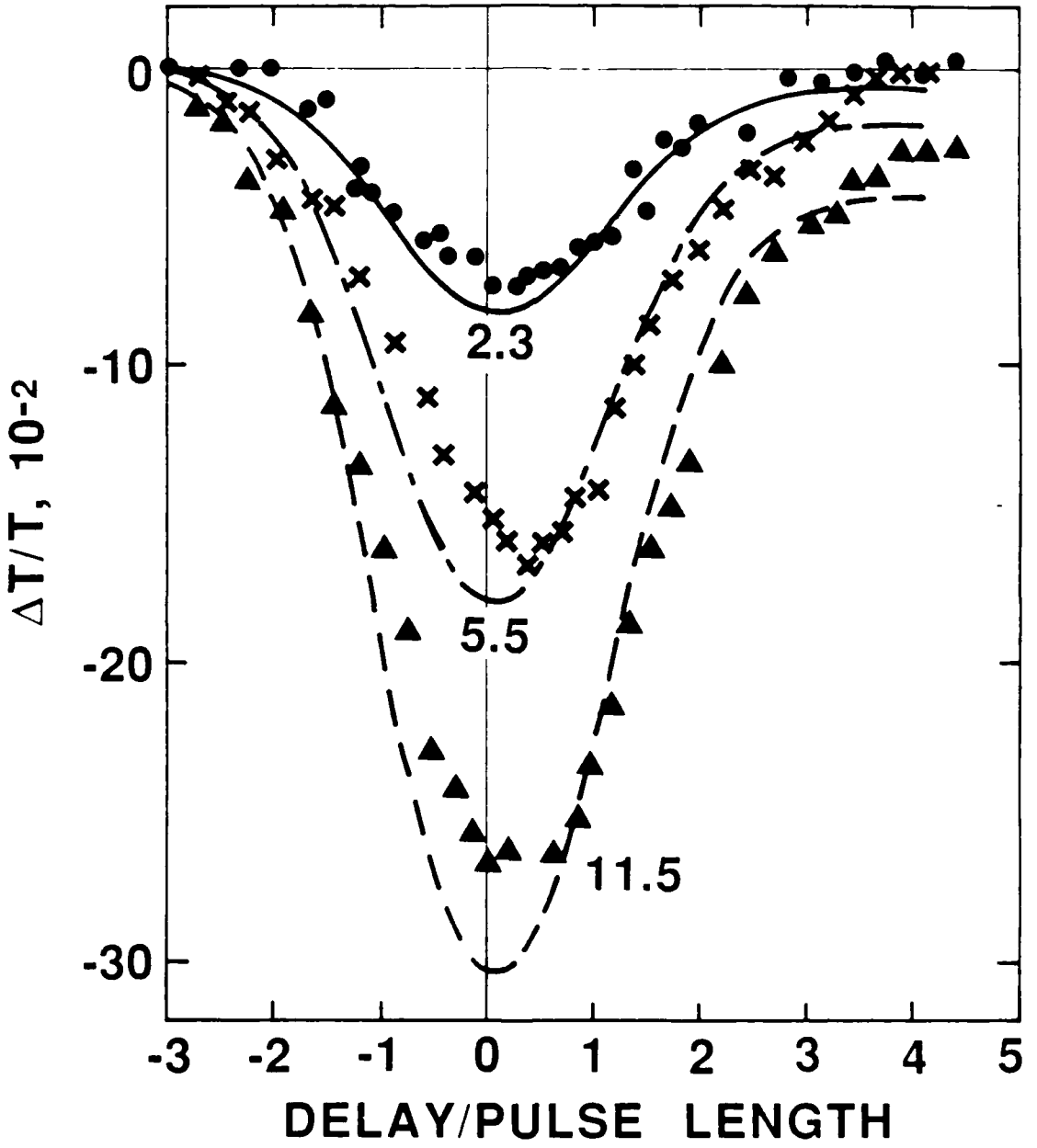
0
-10
-20
-30
ΔT/T, 10-2
2.3
5.5
11.5
-3
-2
-1
0
1
2
3
4
5
DELAY/PULSE LENGTH

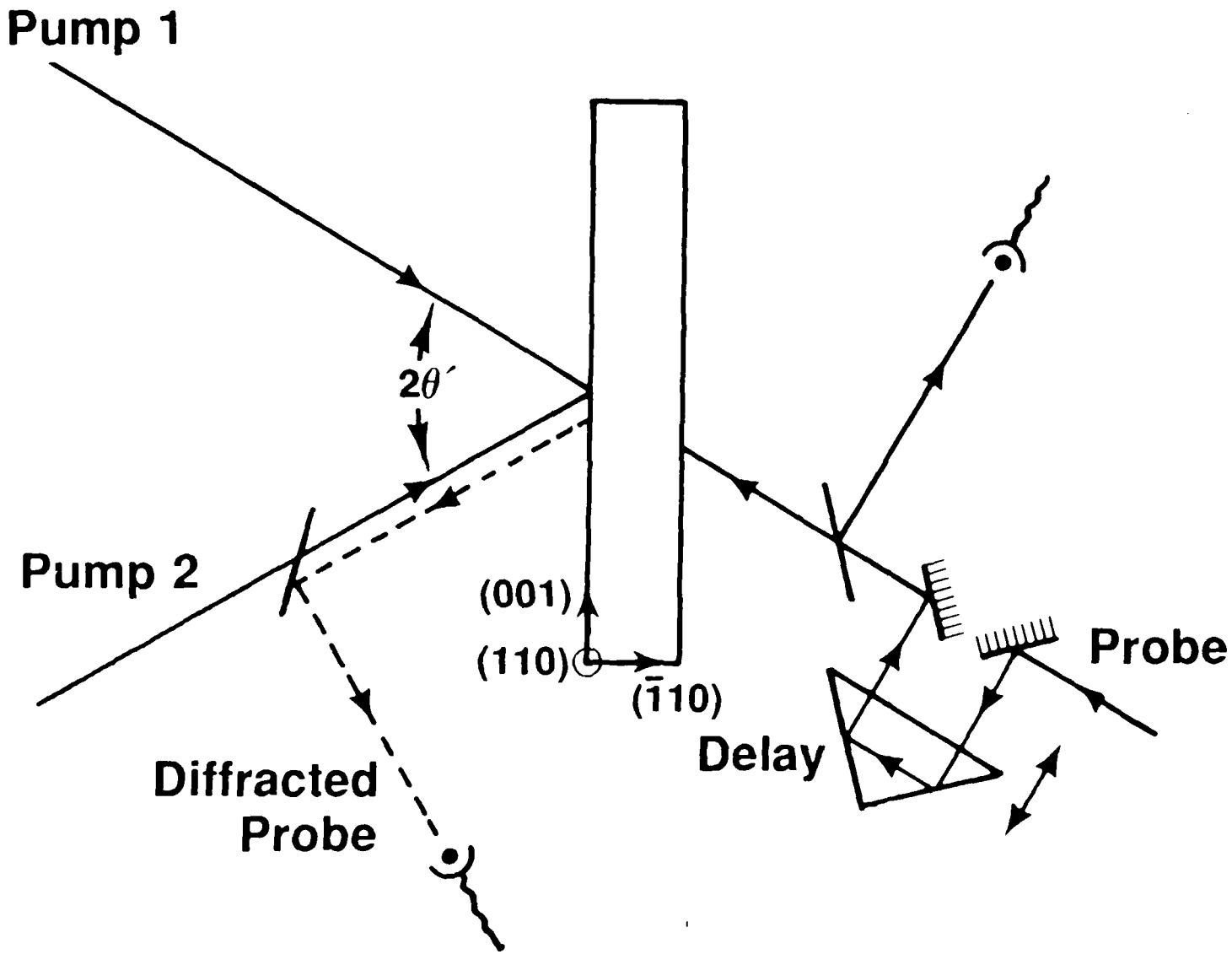
Pump 1
2θ´
Pump 2
(001)
(110)
(1̄10)
Probe
Delay
Diffracted
Probe

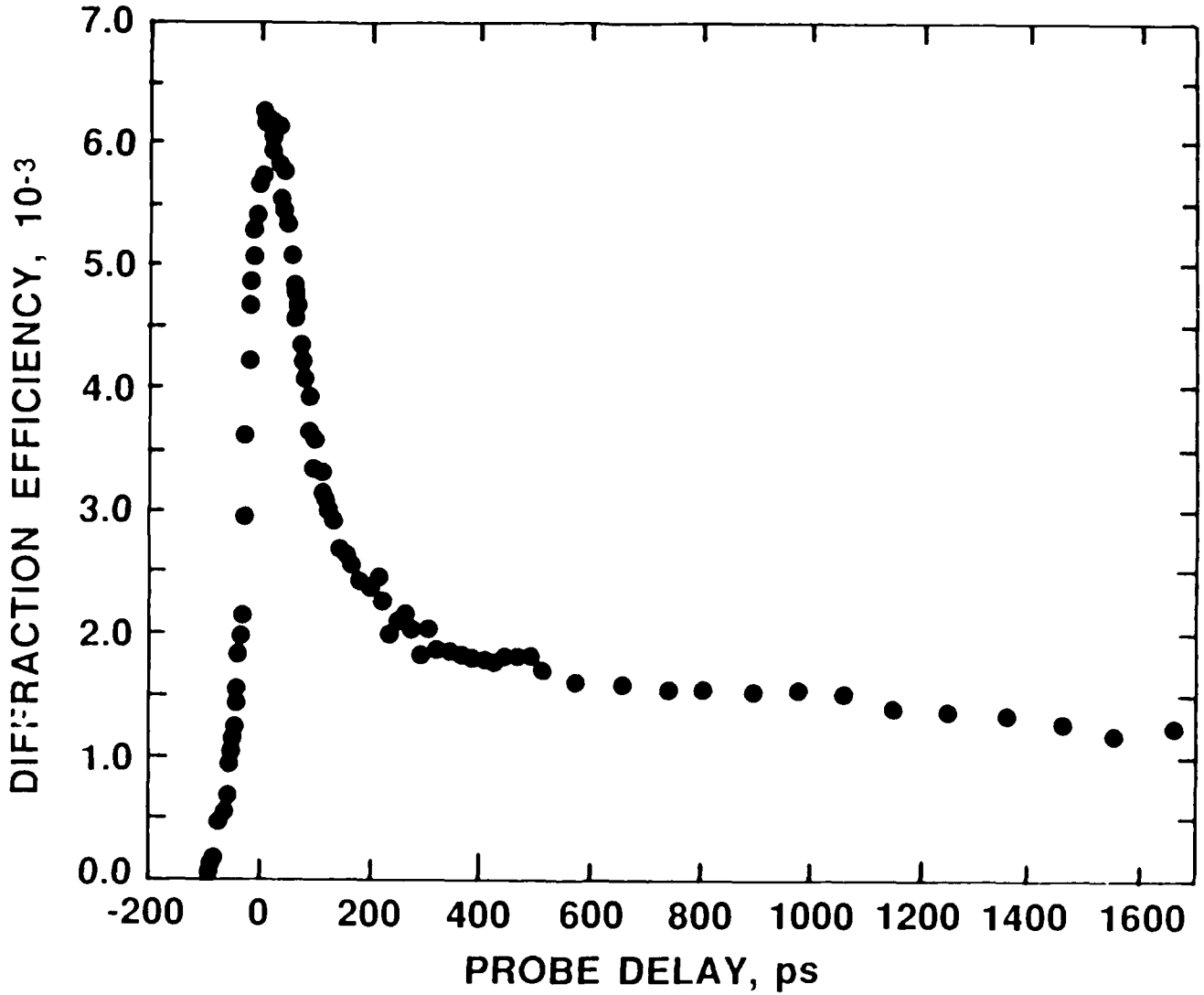
7.0
6.0
5.0
4.0
3.0
2.0
1.0
0.0
DIFFRACTION EFFICIENCY, 10-3
-200
0
200
400
600
800
1000
1200
1400
1600
PROBE DELAY, ps

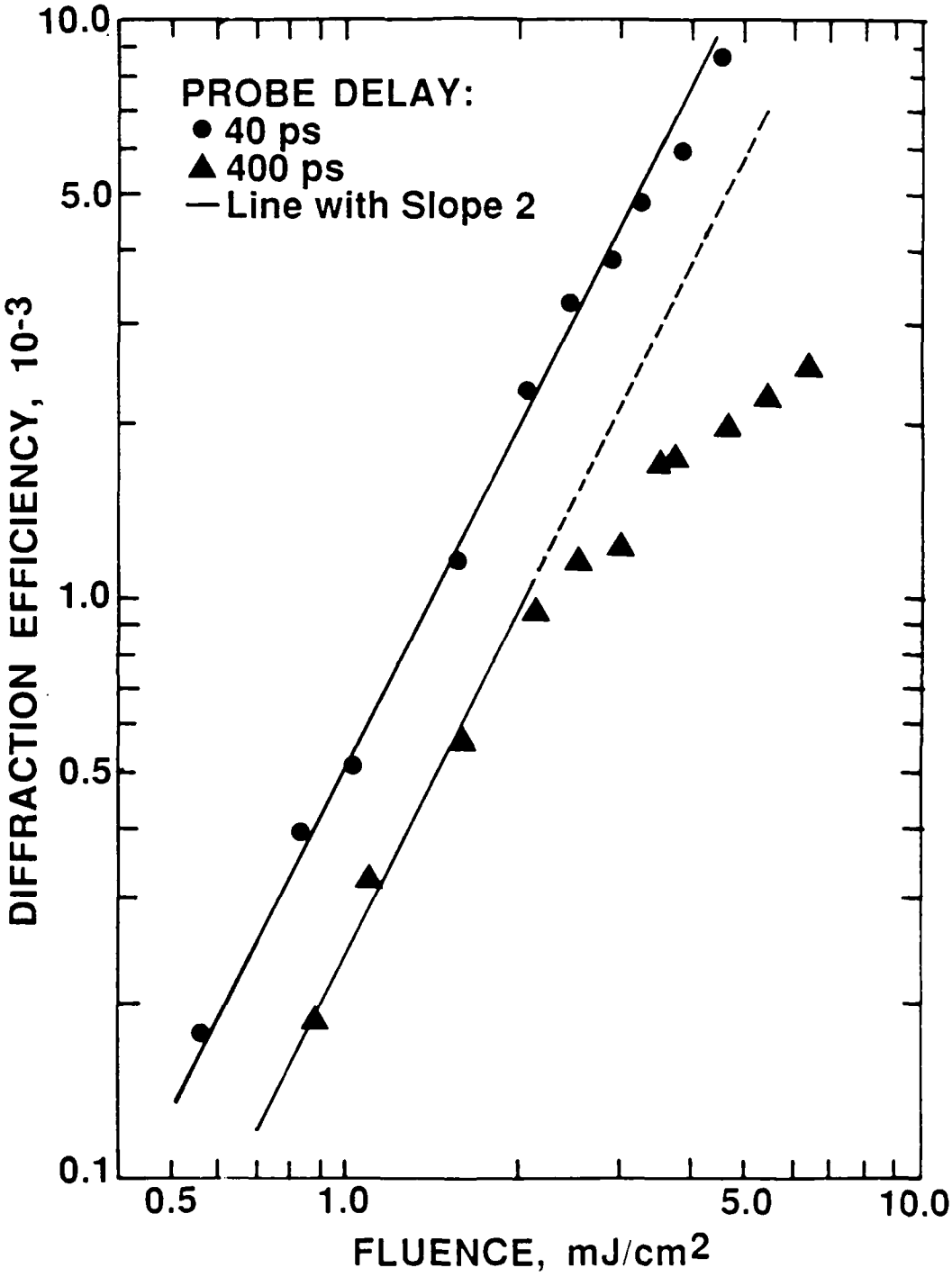
PROBE DELAY:
● 40 ps
▲ 400 ps
— Line with Slope 2
10.0
5.0
1.0
0.5
0.1
DIFFRACTION EFFICIENCY, 10-3
0.5
1.0
5.0
10.0
FLUENCE, mJ/cm2

Appendix J: A Hybridly Mode-Locked CW Laser with Brewster Prisms.

A preprint of a paper published in Optics Communications 60, 79 (1986).

A HYBRIDLY MODE-LOCKED CW DYE LASER WITH BREWSTER PRISMS

Martin D. DAWSON, Thomas F. BOGGESS and Dennis W. GARVEY
Center for Applied Quantum Electronics, North Texas State University, Denton, TX 76203, USA

and

Arthur L. SMIRL
Hughes Research Laboratories, Malibu, CA 90265, USA

Received 2 May 1986; revised manuscript received 8 July 1986

Stable pulses as short as 69 fs duration have been generated by a linear-cavity, synchronously-pumped cw rhodamine 6G dye laser incorporating a pair of Brewster-angled quartz prisms and the saturable absorbers DQOCI and DODCI.

Direct generation of optical pulses having durations below 200 fs has most commonly been achieved with a cw-pumped, colliding-pulse, passively mode-locked (CPM), dye laser [1]. Recent recognition of the role played by self-phase modulation (SPM) and group velocity dispersion (GVD) in the pulse formation process [2,3] has culminated in the generation of 27 fs pulses from such a laser, where a sequence of four Brewster-angle cut quartz prisms was used to introduce adjustable GVD [4]. Synchronously mode-locked cw dye laser systems capable of producing pulses of 200 fs or less have been complicated by either the use of fiber/grating pulse compressors [5–7] or, alternatively, conventional ring [8,9] or antiresonant ring [10,11] cavity arrangements which require either extremely critical positioning of a saturable absorber or external splitting of the pump beam [9] to achieve hybrid CPM. A four prism sequence has recently been incorporated into a synchronously pumped antiresonant ring laser to produce pulses as short as 70 fs [12].

With one published exception [13], simple linear-cavity, hybridly mode-locked, cw dye lasers have been limited to producing pulses longer than 200 fs, typically in the 300–800 fs range [14–17]. We report the generation of pulses with duration as short as 69 fs (full width at half maximum intensity, fwhm) from a linear-cavity hybridly mode-locked, cw dye laser incorporating a pair of Brewster-angle quartz prisms for dispersion compensation. Separate gain and absorber jet-streams helped to prolong the usable life of the absorber dyes (to several weeks) and allowed independent focusing to adjust the relative saturation parameters of the active and passive dyes. The authors of [13] reported the generation of 70 fs pulses in a pellicle-tuned laser that had no deliberate means of dispersion compensation and incorporated a single jet-stream for both dyes. The low loss and high optical quality of the prisms compared to the uncoated pellicle used in [13] is an additional advantage of our system.

The cavity arrangement is shown in fig. 1. A related cavity has produced 33 fs pulses by purely passive mode-locking [4]. The dye laser was pumped at a repetition rate of 82 MHz by frequency doubled pulses from a mode-locked cw Nd:YAG laser (Spectra-Physics Series 3000). The average pump power at 532 nm was 650 mW and the pulse duration was 70 ps as determined by a synchroscan streak camera. The pump beam was coupled into the gain medium (2×10^{-3} M rhodamine 6G in ethylene glycol) by a focusing mirror with a radius of curvature of 5 cm. The folded focusing section around the gain medium consisted of two mirrors, each with a radius of curvature of 7.5 cm, about a vertical jet-stream that was 200 μm thick. A 2.5×10^{-5} M solution of DQOCI, a $3.0 \times$

0 030-401/86/$03.50

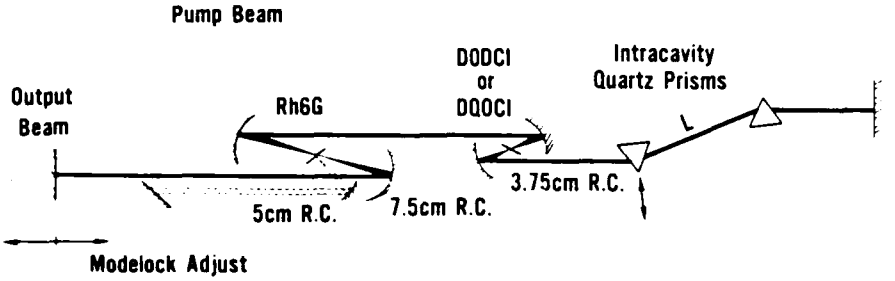

Fig. 1. Laser cavity configuration.

10^{-5} M solution of DODCI, and a mixed solution of 1.8×10^{-5} M DQOCI/1.2×10^{-5} M DODCI in ethylene glycol were tried alternatively in the absorber section. A 100 μm absorber jet-stream was used with focusing mirrors of 3.75 cm radius of curvature. The dyes DQOCI and DODCI have been reported to have upper state lifetimes of 16 ps and 1.15 ns respectively [18]. All mirrors used were nominally 100% reflectively at 632.8 nm with a sufficient bandwidth to allow operation over the gain band of rhodamine 6G, except the output coupler which had a reflectivity of ~90% at 590 nm. The two identical quartz prisms were arranged as shown in fig. 1 and were aligned for minimum deviation and Brewster's-angle incidence at each surface. Each prism was mounted on a translation stage which allowed motion along a line normal to its base, and on tilt and rotation tables.

Fork et al. [19] have shown that terminating a linear-cavity laser with such a two-prism and flat mirror combination is equivalent to incorporating a four-prism sequence into a ring cavity. This configuration allows the introduction of variable GVD of either sign, adjustable through zero, without any net deviation of the beam after traversing the sequence. This geometry can compensate for frequency chirp in the pulses arising from the combined effects of SPM and GVD in the remainder of the cavity. The amount of negative dispersion, which is proportional to the prism separation L, is adjustable to be large enough to compensate for the positive dispersion of the prism material (which may be varied by translating either prism normal to its base) combined with any additional chirp in the pulses. A length L = 250 mm has been calculated to be adequate to compensate for 6.6 mm of quartz at ~600 nm wavelength [19], and the prism sequence was initially set to operate close to these values.

Pulsewidth measurements were performed using non-collinear background-free autocorrelation in a 1 mm KDP crystal. The cross-over length due to the two converging beams has been estimated to be ~100 μm providing temporal resolution well below 100 fs. Spectral information was obtained with an optical multichannel analyzer and vidicon system coupled to a 1/4-meter spectrometer.

With a 2.5×10^{-5} M solution of DQOCI as saturable absorber, pulses as short as 114 fs (fwhm duration, hyperbolic secant squared profile assumed) were obtained when the dye laser cavity length was carefully matched to that of the pump laser. Such pulses were spectrally centered near 585 nm, a wavelength just below the 595 nm absorption peak of DQOCI. The spectral width of greater than 7 nm indicates operation above the Fourier transform limit for a hyperbolic secant squared pulse shape and may imply some residual frequency structure that cannot be compensated for by adjustment of the prism sequence.

Pulses of 96 fs duration (fig. 2, hyperbolic secant squared profile assumed) of similar spectral width, centered at 581 nm, have been obtained using a 3×10^{-5} M solution of DODCI as the saturable absorber in the same cavity arrangement. The laser showed some tendency to be bistable in this case, with small (μm) adjustments of cavity length or slight realignment resulting in the wavelength jumping between 581 nm and 622 nm. However, insertion of an aperture between the second prism and the high reflectivity end mirror, a region of the cavity in which the frequency components are spatially dispersed, allowed suppression of oscillation at one or other of these wavelengths. Minimum pulse-widths and highest output power were

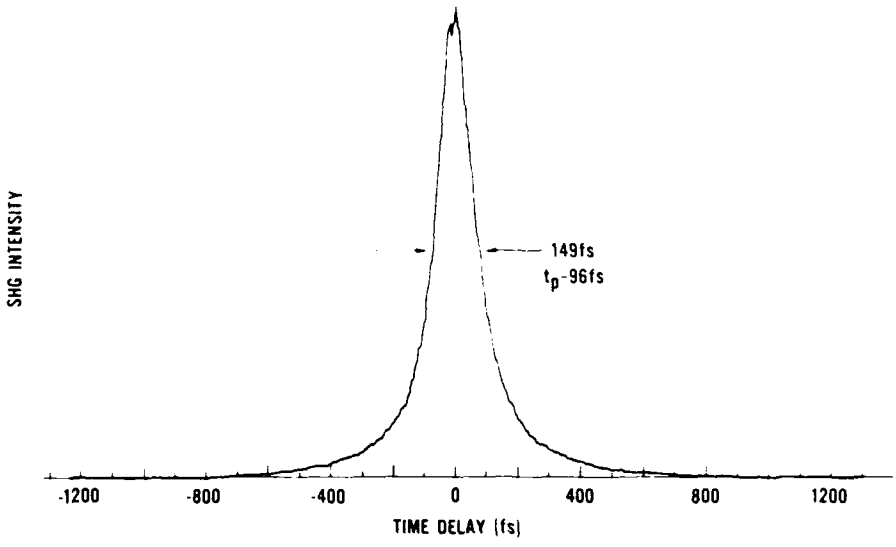

Fig. 2. Autocorrelation trace of 96 fs pulses obtained using DODCI.

obtained at the shorter wavelength. Other authors [20,21] have also reported optimal operation of linear rhodamine 6G/DODCI hybrid lasers near 590 nm, closer to the peak of the gain than for optimal pulse-width performance in the purely passively mode-locked case [1,2]. The high stability of the system when operating at 581 nm is evident from the auto-correlation of fig. 2 which was obtained without a lock-in amplifier or other integrating device (other than the chart recorder itself) over a relatively long (minute) recording time.

Optimal operation of the laser was obtained using a

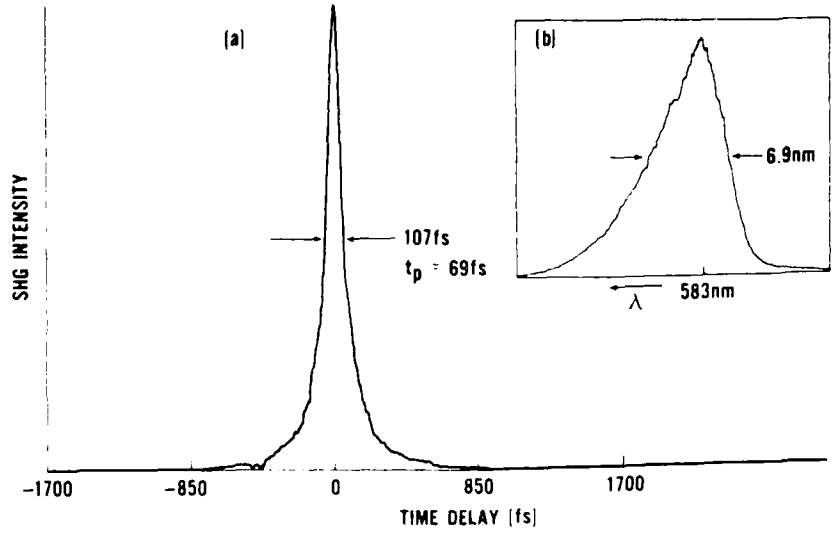

Fig. 3. Autocorrelation trace of 69 fs mode-locked pulses (a) and corresponding integrated laser spectrum (b), obtained using mixed DQOCI/DODCI absorber.

mixed solution of the two saturable absorbers consisting of 1.8×10^{-5} M DQOCI and 1.2×10^{-5} M DODCI. Pulses of duration as short as 69 fs have been obtained with this combination (fig. 3), with no tendency for dual wavelength operation. The time-bandwidth product of $\Delta\nu\Delta t = 0.42$ indicates operation close to the Fourier transform limit ($\Delta\nu\Delta t = 0.315$ for transform-limited hyperbolic secant squared pulses). Many such traces have been recorded on a day-to-day basis with pulsewidths consistently below 85 fs and average power of 55 mW for a 650 mW pump. An examination of the autocorrelation function over a delay of several tens of picoseconds with respect to the main pulse, indicated that the pulses were remarkably free of satellites. Satellite pulses are known to be suppressed in hybridly mode-locked lasers, particularly when a rapid recovery time saturable absorber (such as DQOCI [18]) is used [15].

The effect of the passive dyes was investigated by switching off the absorber jet-stream. The resulting autocorrelation function consisted of a coherence spike on top of a broad base several picoseconds wide at the optimum cavity length. Such behavior is characteristic of synchronously mode-locked dye lasers with insufficient intracavity bandwidth restriction.

The performance of the laser with only a single prism in the cavity, but otherwise unchanged, was observed. At a DQOCI concentration of 2.5×10^{-5} M, a 520 fs pulse was obtained (again assuming a hyperbolic secant squared pulse shape). This duration is more characteristic of linear-cavity hybridly mode-locked cw dye lasers [14–17]. An autocorrelation of such a pulse is shown in fig. 4.

In conclusion, we have demonstrated a linear-cavity, hybridly mode-locked, dye laser capable of producing pulses below 100 fs duration. Its advantages over other designs are principally its simplicity, ease of alignment and non-critical positioning of the saturable absorber jet, combined with its high efficiency and stability. The laser is well-suited for synchronous amplification into the mJ pulse energy regime, and we are currently characterizing such a system.

This research was supported by the U.S. Office of Naval Research, The Robert A. Welch Foundation, and the North Texas State University Faculty Research Fund. The authors wish to acknowledge useful discussions with Dr. J.-C. Diels.

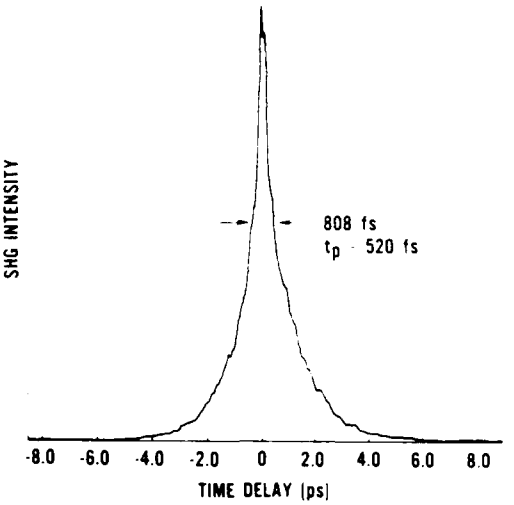

Fig. 4. Autocorrelation trace of 520 fs pulse obtained with DQOCI at 605 nm with a single prism in the cavity.

References

[1] R.L. Fork, B.I. Greene and C.V. Shank, Phys. Lett. 38 (1981) 671.
[2] J.-C. Diels, J.J. Fontaine, I.C. McMichael, B. Wilhelmi, W. Dietel and D. Kuhlke, Sov. J. Quantum Electron. 13 (1983) 1562.
[3] O.E. Martinez, J.P. Gordon and R.L. Fork, Ultrafast Phenomena IV, eds. D.H. Auston and K.B. Eisenthal, (Springer-Verlag, New York, 1984) p. 7.
[4] J.A. Valdmanis, R.L. Fork and J.P. Gordon, Optics Lett. 10 (1985) 131.
[5] A.M. Johnson and W.M. Simpson, IEEE J. Quantum Electron. 22 (1986) 133.
[6] S.L. Palfrey and D. Grischkowsky, Optics Lett. 10 (1985) 562.
[7] J.D. Kafka and T. Baer, Proc. SPIE 533 (1985) 38.
[8] A.M. Johnson and W.M. Simpson, Optics Lett. 8 (1983) 554.
[9] M.C. Nuss, R. Leonhardt and W. Zinth, Optics Lett. 10 (1985) 16.
[10] H. Vanherzeele, R. Torti and J.-C. Diels, Appl. Optics 23 (1984) 4182.
[11] T. Norris, T. Sizer, II and G. Lourou, J. Opt. Soc. Am. B 2 (1985) 613.
[12] T. Norris, I.N. Duling, M. Pessot, T. Sizer II, J. Dawes and G. Mourou, Paper TuE4, Conf. on Lasers and electro-optics (May 1985), Technical Digest.
[13] G. Mourou and T. Sizer II, Optics Comm. 41 (1982) 47.

[14] G.W. Fehrenbach, K.J. Gruntz and R.G. Ulbrich, Appl. Phys. Lett. 33 (1978) 159.
[15] D. Kuhlke, U. Herpers and D. von der Linde, Appl. Phys. B 38 (1985) 233.
[16] Y. Ishida, K. Naganuma and T. Yajima, IEEE J. Quantum Electron. QE-21 (1985) 69.
[17] J.P. Ryan, L.S. Goldberg and D.J. Bradley, Optics Comm. 27 (1978) 12F.
[18] W. Sibbett, J.R. Taylor and D. Welford, IEEE J. Quantum Electron. QE-14 (1981) 500.
[19] R.L. Fork, O.E. Martinez and J.P. Gordon, Optics Lett. 9 (1984) 150.
[20] Y. Ishida, T. Yajima and K. Naganuma, Jpn. J. Appl. Phys. 19 (1980) L717.
[21] B. Couillaud, V. Fossati-Bellani and G. Mitchell, Proc. SPIE 533 (1985) 46.

Appendix K: Generation of 55-fs Pulses and Variable Spectral Windowing in a Linear-Cavity Synchronously Pumped cw Dye Laser.

A reprint of a paper published in Ultrafast Phenomena V, G.R. Fleming and A.E. Siegman, Eds., (Springer-Verlag, New York, 1986) pp 5-7.

ULTRAFAST PHENOMENA V, (SPRINGER-VERLAG, NY, 1986)

Generation of 55-fs Pulses and Variable Spectral Windowing in a Linear-Cavity Synchronously Pumped cw Dye Laser

M.D. Dawson[1], *T.F. Boggess*[1], *D.W. Garvey*[1], *and A.L. Smirl*[2]

[1]Center for Applied Quantum Electronics, North Texas State University, Denton, TX 76203, USA

[2]Hughes Research Laboratories, 3011 Malibu Canyon Road, Malibu, CA 90265, USA

Direct generation of optical pulses with duration below 100 fs from cw dye lasers has almost exclusively been limited to the spectral region 605-630 nm.[1-4] Typically, conventional ring[1] or antiresonant ring[2,3] cavity arrangements designed to utilize the colliding pulse mode-locking (CPM) effect,[1] where counterpropagating pulses meet in a saturable absorber jet-stream, are also required.

We describe the generation of pulses as short as 55 fs at 675 nm and 69 fs at 583 nm from a linear-cavity synchronously pumped, hybridly mode-locked cw dye laser incorporating Brewster prisms, which does not require the CPM technique. In addition, we have demonstrated variable spectral windowing of the spatially dispersed frequency components occurring within the intracavity prism sequence in this laser.

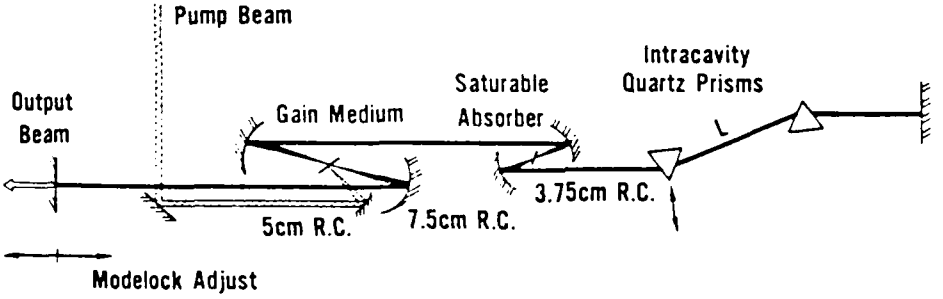

Fig. 1 Laser cavity configuration

The laser oscillator is shown in Fig. 1. A related cavity has produced 33-fs pulses by purely passive mode-locking.[4] The laser was pumped by 650 mW average power, 70-ps pulses from a frequency-doubled cw mode-locked Nd:YAG laser. The dual-jet linear resonator was terminated by a two-Brewster-prism and plane mirror arrangement used for adjustment of intracavity dispersion.[4] High reflectivity cavity mirrors with single stack coatings, having their reflectivity centered at 632.8 nm were used throughout, except for the output coupler which was 95% reflecting at 632.8 nm. Pulsewidth measurements were performed by both collinear type I and non-collinear background-free autocorrelation techniques.

Two different dye combinations yielded femtosecond pulses from this laser, provided the cavity length was carefully matched to that of the pump. Using Sulforhodamine 101 as gain medium (1.8×10^{-3}M in ethylene glycol) and a 5×10^{-4}M solution of DQTCI[5,6] as saturable absorber, stable

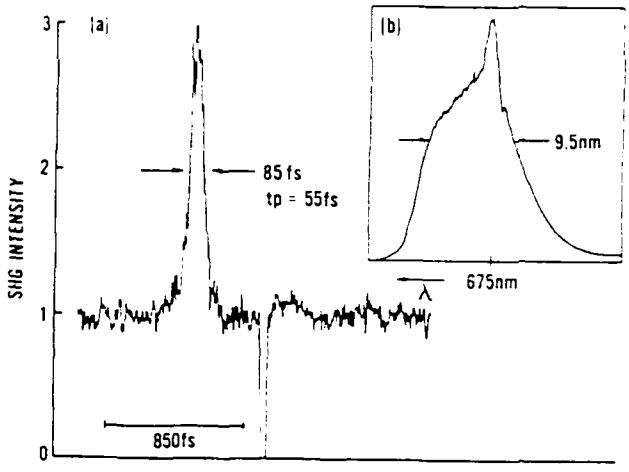

Fig. 2 Collinear type I autocorrelation at 675 nm

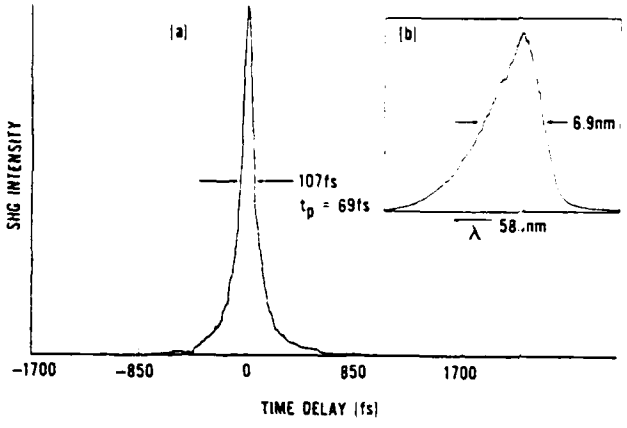

Fig. 3 Background-free autocorrelation at 583 nm

pulses as short as 55 fs were obtained (Fig. 2, sech^2 pulse shape assumed) with time-averaged output powers ~35 mW. The pulses were spectrally centered near 675 nm with a bandwidth of 9.5 nm, giving a time-bandwidth product $\Delta\nu\Delta t = 0.34$. A 2×10^{-3}M solution of Rhodamine 6G and a mixed 1.8×10^{-5}M DQOCI/1.2×10^{-5}M DODCI saturable absorber solution yielded pulses as short as 69 fs (Fig. 3) with output power of 55 mW. These pulses were spectrally centered near 583 nm with a bandwidth of 6.9 nm, which also implies operation close to the transform limit.

Inclusion of a simple variable aperture between the second prism and the end mirror, a region of the cavity in which the frequency components are spatially dispersed, allowed adjustment of the intracavity laser spectral width (in direct analogy to the extracavity spectral windowing techniques developed by Thurston et al.[7]). This simple expedient allowed the output pulsewidth to be directly controlled in the range up to 500 fs (Fig. 4) and wavelength tuning of the laser could be achieved by translating the aperture transversely.

In conclusion, we have demonstrated a linear-cavity, hybridly modelocked cw dye laser capable of producing pulses well below 100 fs duration outside the "common" wavelength range for femtosecond generation and in which the laser bandwidth can be directly controlled. Its advantages over other designs are principally its simplicity, ease of alignment and non-

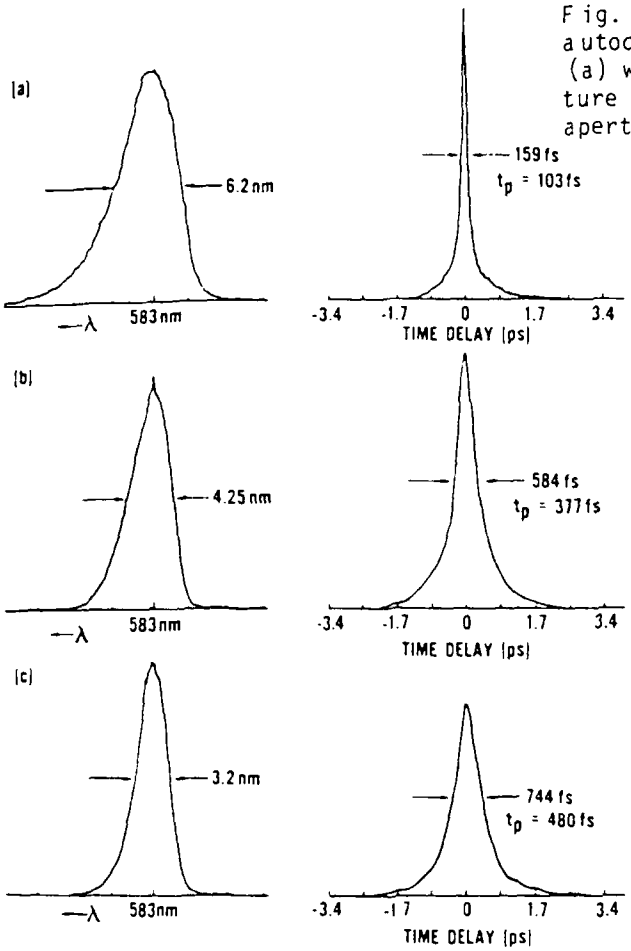

Fig. 4 Spectrum and corresponding autocorrelation for hybrid dye laser (a) without aperture (b) with aperture width 1.1 mm and (c) with aperture width 0.95 mm

critical positioning of the saturable absorber-jet, combined with its high efficiency and stability.

Acknowledgements

This research was supported by the U. S. Office of Naval Research, The Robert A. Welch Foundation and the North Texas State University Faculty Research Fund.

1. R. L. Fork, B. I. Greene and C. V. Shank: Appl. Phys. Lett. 38, 671 (1981).
2. H. Vanherzeele, R. Torti and J.-C. Diels: Appl. Opt. 23, 4182 (1984).
3. T. Norris, T. Sizer, II and G. Mourou: J. Opt. Soc. Am. B 2, 613 (1985).
4. J. A. Valdmanis, R. L. Fork and J. P. Gordon: Opt. Lett. 10, 131 1985).
5. J. R. Taylor: Opt. Commun. 57, 117 (1986).
6. P. M. W. French and J. R. Taylor: IEEE J. Quantum Electron. (to be published).
7. R. N. Thurston, J. P. Heritage, A. M. Weiner and W. J. Tomlinson: IEEE J. Quantum Electron. QE-22, 682 (1986).

Appendix L: Variable Intracavity Spectral Windowing in a Synchronously Pumped Femtosecond cw Dye Laser.

A reprint of a paper published in Optics Letters 11, 721 (1986).

Reprinted from Optics Letters, Vol. 11, page 721, November, 1986.

Variable intracavity spectral windowing in a synchronously pumped femtosecond cw dye laser

Martin D. Dawson, Thomas F. Boggess, and Dennis W. Garvey

Center for Applied Quantum Electronics, North Texas State University, Denton, Texas 76203

Arthur L. Smirl

Hughes Research Laboratories, Malibu, California 90265

Received July 14, 1986; accepted November 18, 1986

An aperture of variable width has been placed within an intracavity prism sequence in a synchronously pumped femtosecond dye laser. This is shown to permit direct control of the output pulse width in the range ~100–500 fsec. Wavelength tunability is achieved by translating the aperture transversely.

In a fiber-and-grating pulse compressor,[1-5] pulses frequency-chirped by propagation in a single-mode optical fiber are compressed by using a grating-pair dispersive delay line. Apodization of the amplitude and the phase of the spatially dispersed spectral components occurring within the grating-pair compressor recently allowed workers[6-9] to manipulate the temporal profile of the compressed picosecond and subpicosecond optical pulses. Using a variety of spectral masks, these authors have demonstrated nearly complete elimination of the energy in the wings of the compressed pulses,[6] synthesis of phase-coherent picosecond optical square pulses,[7] and generation of other temporal pulse shapes. These pulse shapes include pulse doublets and a burst of evenly spaced picosecond pulses.[8,9]

Transversely dispersed spectral components also occur within the Brewster prism sequence introduced to permit adjustment of intracavity group-velocity dispersion (GVD) in femtosecond dye lasers.[10] In a four-prism geometry,[10] typically used in ring cavities, the laser spectrum is angularly dispersed by the first prism in the sequence and is then collimated and transversely dispersed between the two central prisms. An equivalent arrangement can be achieved by terminating a linear cavity laser with two Brewster prisms near the high-reflectivity end mirror.[10] In this case, the collimated dispersed spectral components occur between the second prism and the end mirror (Fig. 1). We recently reported the generation of pulses of as short as 69-fsec duration from a dual-jet, synchronously pumped, and passively mode-locked linear cw dye laser terminated by such a two-prism and plane-mirror arrangement.[11] Here we describe spectral windowing of the intracavity spatially dispersed laser spectrum occurring within the prism sequence in that linear cavity. A variable-width aperture allowed the oscillating laser bandwidth to be varied in a controllable manner, resulting in direct, continuous tunability of the pulse width from below 100 up to 500 fsec. Translation of the aperture transversely to the beam direction provided wavelength tuning of the laser output.

The cavity arrangement used was described in detail in Ref. 11, and we present only an outline of its characteristics here. Briefly (Fig. 1), the laser was pumped by 650-mW average-power, 70-psec pulses from a frequency-doubled mode-locked cw Nd:YAG laser. The pump pulses were coupled into the gain medium (2×10^{-3} *M* Rhodamine 6G in ethylene glycol) by a 5-cm radius-of-curvature focusing mirror. The folded focusing section around the gain-dye jet stream consisted of two mirrors with a radius of curvature of 7.5 cm. The focusing mirrors around the saturable-absorber jet stream had a radius of curvature of 3.75 cm. The two identical quartz prisms were arranged as shown in Fig. 1 and were aligned for minimum deviation and Brewster's angle incidence at each surface. A mixed saturable-absorber solution, con-

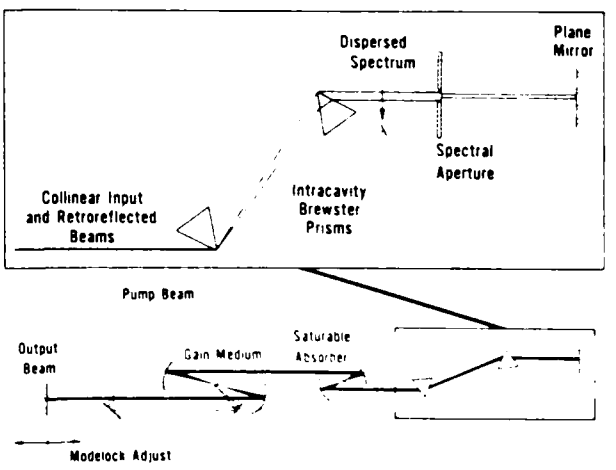

Fig. 1. Laser-cavity configuration with inset showing prism arrangement and position of spectral aperture.

0146-9592/86/110721-03$2.00/0

sisting of 1.8×10^{-5} M DQOCI and 1.2×10^{-5} M DODCI in ethylene glycol, gave pulses as short as 69 fsec spectrally centered at 583 nm. It had previously been determined[11] that, in this cavity arrangement, this absorber mixture resulted in the generation of shorter pulses than those achieved by using either absorber separately. The time-averaged output power was ~60 mW when there was no windowing of the spectrum.

Pulse-width measurements were performed by noncollinear background-free second-harmonic generation in KDP using an autocorrelator that has a scanning display facility. Hyperbolic secant-squared pulse shapes are assumed throughout in deriving the pulse width from the full widths at half-maxima (FWHM's) of the autocorrelation functions. Spectral information was obtained with an optical multichannel analyzer (OMA) and vidicon system coupled to a 0.25-m spectrometer. The overall spectral resolution of the OMA–vidicon system was 0.42 nm.

We first investigated the effect of a spectral aperture on the performance of the laser in purely synchronously mode-locked operation, i.e., with the saturable-absorber jet stream switch off. When no aperture is used, the two-prism sequence shown in Fig. 1 provides an inadequate bandwidth restriction for complete mode locking by synchronous pumping. At the optimum cavity length, the resulting autocorrelation consists of a coherence spike on a broad base that is 2.3 psec in duration [Fig. 2(a)]. The corresponding integrated spectral width of the laser output was 3.1 nm, giving a large time–bandwidth product, $\Delta\nu\Delta t$ = 6.4 (for transform-limited sech^2 pulses, $\Delta\nu\Delta t$ = 0.315). The output power of the laser was 90 mW in this case.

When the aperture was inserted and closed to 0.7 mm, the output power was reduced to 20 mW and the oscillating bandwidth to 1.18 nm (deconvolved from the 1.25-nm measured bandwidth). As can be seen from Fig. 2(b), this cavity configuration then produced more completely mode-locked and considerably shorter (800-fsec) pulses. In related early work on prism-tuned synchronously pumped cw dye lasers, aperturing of the angularly dispersed spectrum was used, in a similar manner to that reported here, to improve the quality of the mode locking.[12,13] By translating the aperture transversely to the laser-beam direction in our laser, it was possible to tune the output between 572 and 600 nm. The corresponding time–bandwidth product of $\Delta\nu\Delta t$ = 0.84 for these pulses indicates some excess bandwidth. An attempt was made to reduce this by further closing of the aperture; however, the loss introduced by the aperture was such as to prevent laser oscillation when the aperture was closed much below 0.7 mm.

With the saturable-absorber jet stream flowing in the cavity and the aperture fully opened, pulses of 100-fsec duration were typically obtained in the manner described in Ref. 11. The autocorrelation of a typical pulse (with a duration of 103 fsec) together with the corresponding integrated laser spectrum is shown in Fig. 3(a). The time–bandwidth product for this pulse is $\Delta\nu\Delta t$ = 0.57, indicative of reasonably well mode-locked operation. The aperture could be closed to 1.4 mm before any effect on the pulse width was observed. Under these conditions, the laser output could be tuned to well beyond 600 nm (~40-nm tunability). An aperture within the four-prism sequence in a passively mode-locked colliding-pulse laser has been used for wavelength tuning in this manner.[14] Figures 3(b) and 3(c) show the result of further reducing the aperture below 1.4 mm to 1.1 and 0.95 mm, respectively. It can be seen that the pulse width broadens from 100 to 500 fsec as the oscillating laser bandwidth is reduced. The time–bandwidth product increases somewhat as the aperture is closed, most likely because the laser operates progressively nearer the threshold. (No readjustment of the prism sequence was performed between these measurements, and the reduction in power as the aperture is closed results in, among other effects, a changing of the frequency chirp imposed by the saturable-absorber jet stream.) The adjustable spectral aperture thus provides a direct means of varying the output pulse width and spectrum in a controllable manner. The output power for the 0.95-mm aperture width was 20 mW at 583 nm; the pulse width was 480 fsec. Under these conditions, translation of the aperture across the beam resulted in some tunability of the laser in the wavelength range 578–586 nm. Further reduction of the aperture width below 0.95 mm resulted in increasingly unstable laser output, and laser oscillation ceased at an aperture width of 0.85 mm.

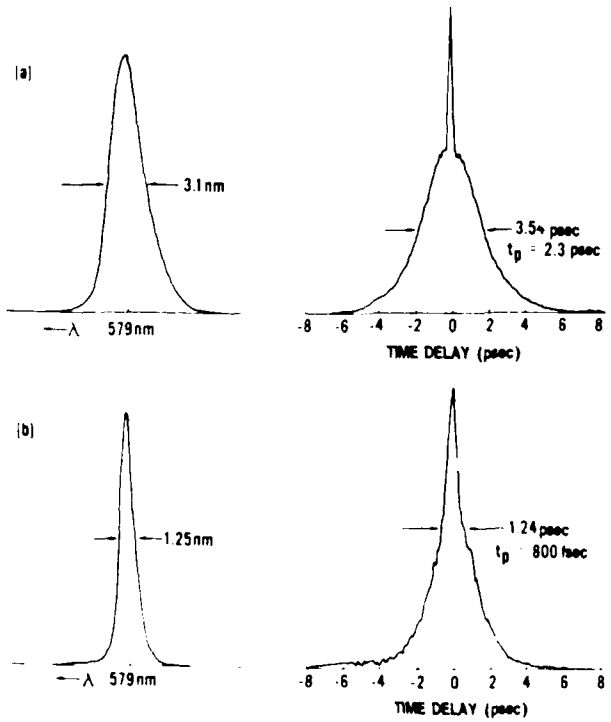

Fig. 2. (a) Spectrum and autocorrelation from purely synchronously mode-locked laser without aperture and (b) spectrum and autocorrelation with aperture width 0.7 mm.

In conclusion, we have reported a demonstration of variable intracavity spectral windowing in a femtosecond mode-locked cw dye laser. Use of a simple vari-

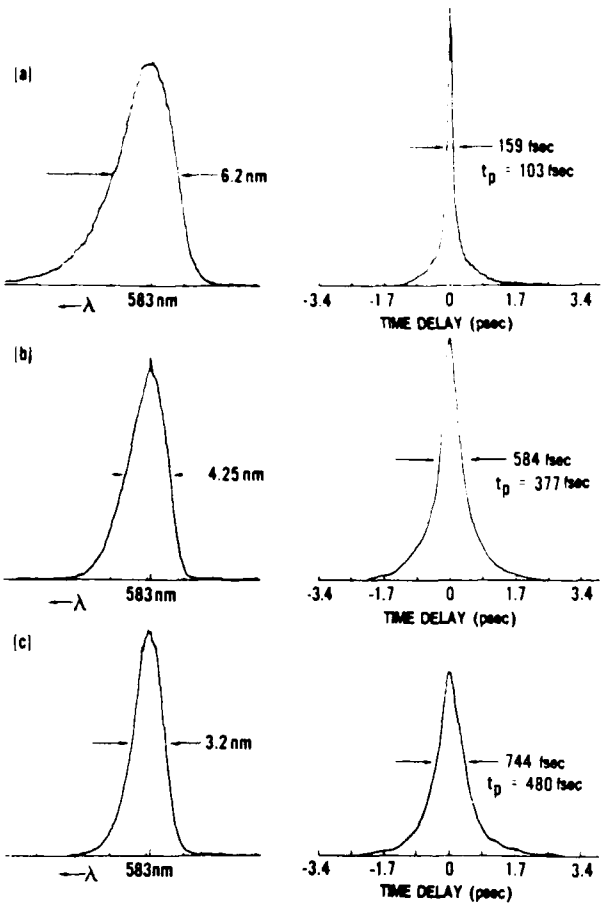

Fig. 3. Spectrum and corresponding autocorrelation for synchronously pumped passively mode-locked dye laser (a) without aperture, (b) with aperture width 1.1 mm, and (c) with aperture width 0.95 mm.

able aperture has permitted the lasing spectrum to be adjusted in a controllable manner, resulting in direct tunability of the output pulse width in the range 100–500 fsec. In addition, translation of the aperture transversely to the beam direction provides some wavelength tunability. Variation of output pulse width from mode-locked lasers incorporating a prism sequence was previously obtained[15] by increasing the negative dispersion introduced by the prism arrangement with respect to that giving optimal short-pulse generation (excess positive GVD leads to increasing instabilities in laser output). The advantage of variable aperturing for pulse-width tunability in hybridly mode-locked systems is that no cavity-length readjustment is required, which is not true for adjustments in the prism sequence. Such pulse-width tunability can be readily applied, for example, to distinguish between intensity-dependent and fluence-dependent nonlinear optical processes.[16] It is also feasible that other low-loss masks could be used to produce additional *intracavity* pulse shaping, provided that the loss introduced were not sufficient to prevent lasing. In addition, it may be possible to improve the spectral resolution in these intracavity windowing experiments by, for example, focusing the input beam through the prism sequence to decrease the spot size of any particular spectral component.[17]

This research was supported by the U.S. Office of Naval Research, The Robert A. Welch Foundation, and the North Texas State University Faculty Research Fund.

References

1. C. V. Shank, R. L. Fork, R. Yen, R. H. Stolen, and W. J. Tomlinson, Appl. Phys. Lett. **40**, 761 (1982).
2. B. Nikolaus and D. Grischkowsky, Appl. Phys. Lett. **43**, 832 (1983).
3. A. M. Johnson, R. H. Stolen, and W. M. Simpson, Appl. Phys. Lett. **44**, 729 (1984).
4. J. D. Kafka, B. H. Kolner, T. Baer, and D. M. Bloom, Opt. Lett. **9**, 505 (1984).
5. A. S. L. Gomes, U. Osterberg, W. Sibbett, and J. R. Taylor, Opt. Commun. **54**, 377 (1985).
6. J. P. Heritage, R. N. Thurston, W. J. Tomlinson, A. M. Weiner, and R. H. Stolen, Appl. Phys. Lett. **47**, 87 (1985).
7. A. M. Weiner, J. P. Heritage, and R. N. Thurston, Opt. Lett. **11**, 153 (1986).
8. J. P. Heritage, A. M. Weiner, and R. N. Thurston, Opt. Lett. **10**, 609 (1985).
9. R. N. Thurston, J. P. Heritage, A. M. Weiner, and W. J. Tomlinson, IEEE J. Quantum Electron. **QE-22**, 682 (1986).
10. R. L. Fork, O. E. Martinez, and J. P. Gordon, Opt. Lett. **9**, 150 (1984).
11. M. D. Dawson, T. F. Boggess, D. W. Garvey, and A. L. Smirl, Opt. Commun. (to be published).
12. R. K. Jain and J. P. Heritage, Appl. Phys. Lett. **32**, 41 (1978).
13. J. P. Heritage and R. K. Jain, Appl. Phys. Lett. **32**, 101 (1978).
14. R. L. Fork, AT&T Bell Laboratories, Holmdel, New Jersey 07733 (personal communication).
15. J. A. Valdmanis and R. L. Fork, IEEE J. Quantum Electron. **QE-22**, 112 (1986).
16. T. F. Boggess, K. Bohnert, K. Mansour, S. C. Moss, I. W. Boyd, and A. L. Smirl, IEEE J. Quantum Electron. **QE-22**, 360 (1986).
17. J. P. Heritage, Bell Communications Research, Nanesink Research and Engineering Center, Red Bank, New Jersey 07701 (personal communication).

Appendix M: Tunable Near-Infrared Picosecond Pulses from a Short-Cavity Dye Laser.

A reprint of a paper published in IEEE Journal of Quantum Electronics QE-22, 2195 (1986).

Tunable Near-Infrared Picosecond Pulses from a Short-Cavity Dye Laser

K. Bohnert
T. F. Boggess
K. Mansour
D. Maxson
A. L. Smirl

Reprinted from: IEEE JOURNAL OF QUANTUM ELECTRONICS, Vol. QE-22, No. 12, DEC. 1986.

Tunable Near-Infrared Picosecond Pulses from a Short-Cavity Dye Laser

K. BOHNERT, THOMAS F. BOGGESS, KAMJOU MANSOUR, DWIGHT MAXSON, AND ARTHUR L. SMIRL

Abstract—**We report on the generation of tunable infrared picosecond pulses by a short-cavity dye laser system consisting of a short cavity, a three-stage amplifier, and a wavelength control unit. The laser emission is temporally, spectrally, and spatially resolved. The conditions for optimum performance are ascertained, and the output characteristics important to experimental applications are determined.**

I. Introduction

NEAR-infrared, tunable, picosecond pulses are of considerable interest for numerous applications in ultrafast spectroscopy. In particular, optical spectroscopy of novel semiconductor materials with bandgaps in the near-infrared spectral region has been a field of growing importance in recent years. A promising method for efficiently generating tunable, picosecond pulses within a wide spectral range is the short-cavity dye laser (SCDL) [1]-[3].

In the past, there have been various reports of the operation of short cavity dye lasers within the visible spectrum [1]-[11]. Early investigations were mainly concerned with the pulse-shortening properties of these systems and were performed with lasers that produced a multimode spectral output [1], [2], [4], [6], [9]. Cox *et al.* [7], [8] demonstrated that tunable, nearly Fourier transform-limited, single-mode, picosecond pulses could be generated with an SCDL. Recently, Kortz *et al.* [10], [11] have achieved total energy conversion efficiencies between 5 and 15 percent by amplifying such pulses.

In spite of these encouraging results, information concerning the reliable operation of short-cavity dye lasers for experimental applications is scarce. Also, few experimental details have been published on the effects of the various system parameters such as cavity lifetime, dye concentration, or pump power on the laser emission, and to our knowledge, there have been no reports on the performance of short-cavity dye lasers operating in the infrared.

In this paper, we report a detailed investigation of an SCDL system [12], primarily using the near-infrared dye LDS 821. The laser system consisted of a short cavity, a longitudinally pumped three-stage amplifier, and a wavelength control unit. The laser emission was analyzed temporally, spectrally, and spatially as a function of the pump level, the cavity length (i.e., the cavity lifetime), and the dye concentration. Further experiments included the determination of the energy conversion efficiency and of the amplitude and wavelength stabilities. From these measurements, the conditions for optimized performance were ascertained and the output parameters important to experimental applications were determined. In addition to LDS 821, the laser also was tested with rhodamine 590 (RH 590) in order to examine its performance in a different spectral region and to demonstrate its spectral versatility.

Manuscript received April 18, 1986; revised July 3, 1986. This work was supported in part by the U.S. Office of Naval Research, the Robert A. Welch Foundation, and the North Texas State University Faculty Research Fund.

K. Bohnert, T. F. Boggess, K. Mansour, and D. Maxson are with the Department of Physics, Center for Applied Quantum Electronics, North Texas State University, Denton, TX 76203.

A. L. Smirl is with the Hughes Research Laboratories, Malibu, CA 90265.

IEEE Log Number 8610726.

II. Experimental Configuration and Procedure

The experimental apparatus (consisting of the pump source, the SCDL system, and the characterization instrumentation) is shown in Fig. 1. The pump source was an actively and passively mode-locked Nd:YAG laser (Quantel YG 402). This system provided excellent energy stability (~ 5 percent shot-to-shot integrated over the entire pulse train), a key factor in stable SCDL operation. From the emitted pulse train, a single pulse was selected by a photodiode-triggered pulse slicer. The selected pulse, after amplification and frequency doubling to 532 nm, had an energy of ~ 1 mJ and a temporal width of 32 ± 4 ps (full width at half maximum, FWHM) [13]. The remaining, nonconverted 1.064 μm pulse was rejected. The pulse repetition rate was chosen as either 1 or 5 Hz.

The heart of any single-mode short-cavity dye laser system is a Fabry-Perot resonator. The resonator mirror spacing is typically adjusted in a range (of a few microns) where only a single longitudinal mode is allowed to lase within the emission spectrum of the dye; the entire cavity volume is filled by an appropriate dye solution. The wavelength is then tuned by changing the cavity length. Since the resonator emission typically is only a few nanojoules, most experimental applications require additional amplification. Also, to prevent a drift of the emission wavelength, a control circuit is necessary to stabilize the cavity length and to compensate for mechanical relaxations.

In our experiments, the cavity was formed by two identical broad-band dielectric-coated mirrors with reflectivities greater than 90 percent over the emission band of LDS 821 and reflectivities between 80 and 90 percent for the RH 590 emission band. The transmission at the pump beam wavelength was approximately 80 percent. The res-

0018-9197/86/1200-2195$01.00

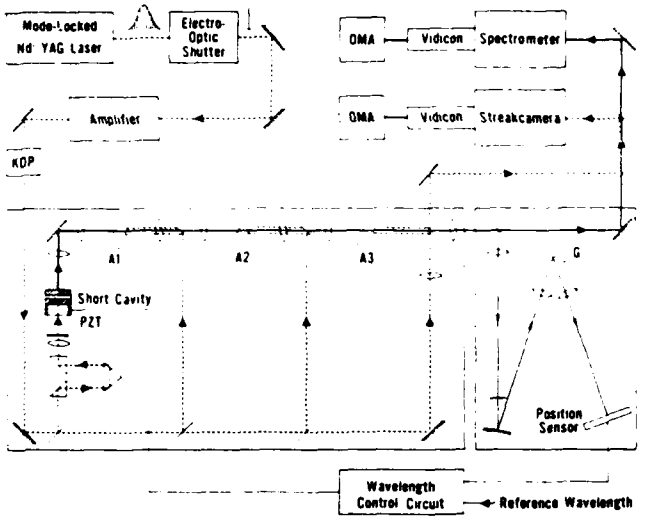

Fig. 1. Experimental setup. PZT: piezoelectric translator, $A1$–$A3$: amplifier stages, G: reflection grating.

onator length was coarsely adjusted with micrometer screws; the fine adjustment and wavelength tuning were achieved with a piezoelectric translator. The actual magnitudes of the resonator length were determined by interferometric methods. For our pulse repetition rates and small cavity volumes, only a small dye flow rate (typically a few milliliters per hour) was required. Consequently, a simple closed-cycle gravity pump was used for dye circulation; a single dye filling could be used for several days. The cavity was longitudinally pumped by a residual reflection of the incoming pump beam from an antireflection coated mirror substrate. The pump power was controlled further by neutral density filters. Finally, a lens focused the pump beam into the cavity; it was adjusted to maximize the SCDL output pulse energy.

Approximately 3, 10, and 87 percent of the incoming pump beam longitudinally pumped the first ($A1$), second ($A2$), and third ($A3$) cells, respectively, of a three-stage amplifier. The amplifier system was designed to operate in the saturated regime in order to minimize amplified spontaneous emission (ASE). This required a good spatial overlap of pump and SCDL beams, as well as an appropriate choice of the size of the pumped dye volumes. The proper temporal synchronization of pump and SCDL pulses was achieved by a movable prism in the path of the cavity pump beam and/or by moving the amplifier cells. The longitudinal pumping geometry chosen here yields better uniformity of the beam profile than side-pumping geometries while maintaining excellent efficiencies. The disadvantage is that dichroic mirrors are required, which make the system more expensive and cause losses for both pump and amplified pulses. For details on the amplifier design, see [11].

The cavity mirror spacing, i.e., the emission wavelength, was stabilized by an optoelectronic feedback loop similar to the one described in [10]. A small fraction of the emitted SCDL pulse was fed into a wavelength detector, which consisted of an 1800 grooves/mm grating and a silicon position sensor. The wavelength-dependent signal from the position sensor was electronically compared to a reference voltage, i.e., a reference wavelength. A deviation of the laser wavelength, i.e., of the position sensor signal, from the reference value generated an appropriate corrector voltage. This voltage was applied to the piezoelectric translator to readjust the cavity length such that agreement of actual and reference wavelength were again achieved. The feedback loop was designed to keep the wavelength fluctuations small compared to the laser line width, which typically is on the order of 2–4 Å. This requires a stabilization of the cavity mirror spacing with a precision of roughly 1–2 nm.

A streak camera and a double 0.25 m spectrometer were used to temporally and spectrally analyze the emitted pulses. In both cases, the signals were recorded by vidicons connected to multichannel analyzers. The overall temporal and spectral resolutions were 2.5 ps and 1.2 Å, respectively. In addition to the SCDL pulses, a small fraction of the 532 nm pump pulses was directed to the streak camera to serve as a reference for the determination of the expected pulse-shortening properties of the SCDL. The relative time differences and the jitter between pump and SCDL pulses were also examined with this arrangement. The spatial beam profiles were determined by placing one of the vidicons directly into the beam path. The pulse energies were measured with a calibrated energy detector.

III. Results and Discussion

The amplified SCDL emission was analyzed as a function of the pump power, cavity length, and dye concentration. The spectral, temporal, and spatial pulse profiles, the energy conversion efficiency, the amplitude and wavelength stabilities, as well as the width of the tuning range were investigated in detail. The majority of these experiments were performed using the near infrared dye LDS 821. In order to compare the infrared performance to the emission characteristics in the visible, the laser was operated with RH 590 as well. Since with the latter dye a wider range of dye concentrations could be obtained, it also was used to investigate the concentration dependence of the laser emission. In the following, we first describe the infrared performance of the SCDL.

In a first set of measurements, the SCDL pulses were analyzed temporally and resolved spectrally, while the cavity pump power was varied between the lasing threshold and 50 times this value. The LDS 821 concentrations were 3.5×10^{-2} mole/l in the cavity and 4×10^{-4} mole/l in the amplifier cells. The solvent was methanol. The cavity length was adjusted to 17 μm, and the laser line was tuned close to the emission maximum of the dye at 820 nm. Under these conditions, two additional modes were lasing at the edges of the tuning range. These modes, however, were between one and two orders of magnitude less in energy than the central mode.

At the highest pump levels, the time-resolved SCDL pulses consisted of a main peak with a width of 13 ± 3

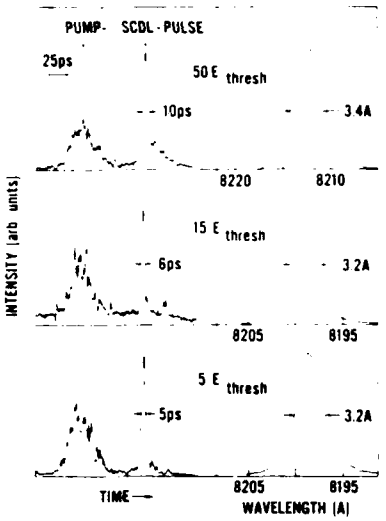

Fig. 2. Temporally and spectrally resolved SCDL pulses and temporally resolved pump pulses for various pump powers (in units of the lasing threshold E_{thresh}).

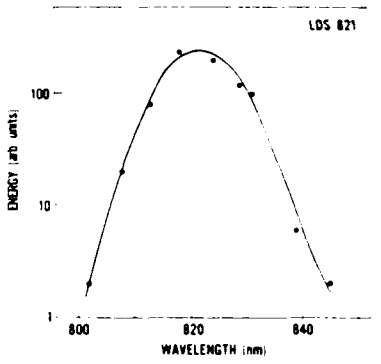

Fig. 3. Output energy per mode as a function of wavelength.

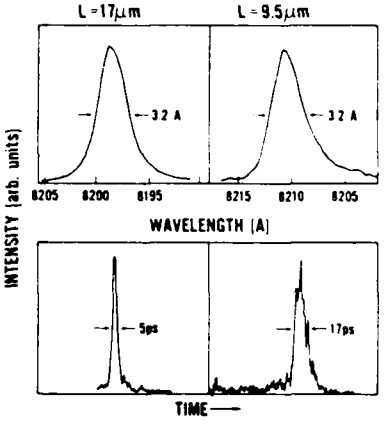

Fig. 4. Temporally and spectrally resolved SCDL pulses for cavity lengths of 17 and 9.5 μm. The pump power was approximately five times the lasing threshold.

ps (FWHM) and a smaller trailing secondary feature. As the pump power was decreased, the tail first evolved into a single spike and, eventually, completely disappeared. Simultaneously, the main peak narrowed to a width of 7.5 ± 2.5 ps (FWHM). This value corresponds to a factor of four reduction compared to the pump pulses and is approximately one order of magnitude longer than the cavity lifetime. This behavior is illustrated in Fig. 2 for pump levels between 5 and 50 times threshold. Note that the pulse widths shown were among the shortest observed for each corresponding pump level.

In contrast to the temporal envelope of the pulses, the spectra varied only weakly with pump power. Although the resolution of the spectrometer did not permit the detection of detailed structure within the laser line, the results indicate a symmetric, Gaussian-like spectral profile at all pump powers above a few times the threshold value. With decreasing pump level, the spectral width decreased slightly from 4 ± 0.5 Å at 50 times the lasing threshold to 3.4 ± 0.4 Å at five times threshold. The average time-bandwidth product $\Delta t \Delta \nu$ was a factor of 2.5 above the Fourier transform limit. The latter pump level produced the most satisfying temporal and spectral pulse shapes and amplitude stability. Closer to threshold, stronger amplitude fluctuations were observed. The usable tuning range under these conditions extended from 805 to 840 nm as shown in Fig. 3.

The jitter between the pump and amplified SCDL pulses was determined by our streak camera measurements to be less than ~1.5 ps for a cavity spacing of 17 μm and a pump level five times threshold. Moreover, the experimentally measured time differences between pump and amplified SCDL pulses were nearly constant for pump powers between 15 and 50 times the lasing threshold. A reduction of the excitation level from 15 to 5 times threshold, however, introduced an additional relative time delay of 4–5 ps. The absolute time delays between pump and SCDL pulses were always considerably less than the pump pulse width. We emphasize that, for this reason, our results cannot be described by the giant pulse model originally developed to account for laser pulse evolution in Q-switched lasers [14] or by direct application of the theoretical analysis of picosecond SCDL developed by Duncanson and Struve [15] since these divide the temporal evolution of the laser pulse into four separate time periods: pumping, amplification, lasing, and decay. Our observations of secondary pulses and a decrease in the time delays between pump and SCDL pulses with increasing pump level are in qualitative agreement with the simple rate equation approach presented by Scott *et al.* (see [8, Fig. 4]). The latter model, however, predicts much larger delay changes than those experimentally observed. Our observations are, in this regard, similar to those reported by Scott *et al.* [8] for SCDL operation in the visible.

In a second set of experiments, the amplified SCDL emission was analyzed at various cavity lengths L. Results for 17 and 9.5 μm are compared in Fig. 4. In both cases, the pump level was a few times the lasing threshold. The dye concentrations were identical. Decreasing the cavity length increased the lasing threshold as well as the temporal pulse width. The spectral width also increased slightly. The absolute pump power for L = 9.5 μm was three times the value for L = 17 μm. The average

temporal widths differed by roughly a factor of two. The relative magnitude of the broad-band spontaneous emission from the cavity gradually increased as the cavity mirror spacing was reduced to values below 10 μm. Simultaneously, the short-cavity emission also became more divergent. An increase of the pump power and the introduction of a diaphragm into the beam path behind the cavity reduced the relative magnitude of the spontaneous emission and narrowed the spectral width of the laser line. At cavity lengths less than 5 μm, lasing was no longer observed.

In a further step, we determined the gain in the individual amplifier stages and the overall energy conversion efficiency. The cavity length was 17 μm. The dye concentrations were as given above. The cavity was pumped at 15 times the lasing threshold. For a total pump pulse energy of 1 mJ, we found preliminary amplification factors for the stages $A1$, $A2$, and $A3$ of 60, 20, and 5, respectively, yielding a total gain of 6×10^3. The decreasing gain values from stage 1 to stage 3 indicate an increasing gain saturation. The overall energy conversion efficiency under these conditions was 0.6 percent. The contribution of amplified spontaneous emission to the total output energy was on the order of a few percent. Although no serious efforts were made to optimize the amplifier dye concentrations for maximum amplification, we believe that this relatively small energy conversion efficiency can be mainly attributed to the lower efficiency of infrared dyes compared to dyes for the visible.

Another favorable characteristic of the SCDL is its amplitude stability. When optimized to produce stable temporal and spectral pulse profiles, we found that the energies of 40 percent (90 percent) of the pulses were within 10 percent (25 percent) of their average value. This has to be compared to the stability of the pump source. Approximately 70 percent of the pump pulses were within 10 percent of their average.

A determination of the wavelength stability showed that the optoelectronic feedback loop kept the laser line at the desired position with an accuracy of $\sim \pm 1.5$ Å. This value may be improved by optimizing the imaging optics of the stabilization unit. Within an observation period of 30 min, no detectable long-term drift of the wavelength was observed. Such a drift could be produced, e.g., by mechanical or electronic instabilities of the feedback system itself.

Fig. 5 shows the spatially resolved SCDL beam in the near field as recorded on an optical multichannel analyzer. Fig. 5(a) is a horizontal scan with integration over the vertical dimension. Fig. 5(b) shows a scan through the beam center with a 250 (75) μm resolution on the vertical (horizontal) dimension. The beam profile was found to be essentially Gaussian, although there were some small higher frequency (compared to the spot size) spatial fluctuations. The small energy associated with these fluctuations is diffracted well into the wings of the spatial profile in the far field and is easily filtered.

Replacing LDS 821 by RH 590 did not introduce any

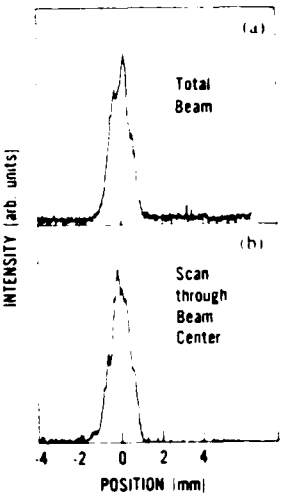

Fig. 5. Vidicon recording of the spatial beam profile in the near field of slightly focused beam. (a) scan integrated in vertical direction, (b) scan through beam center.

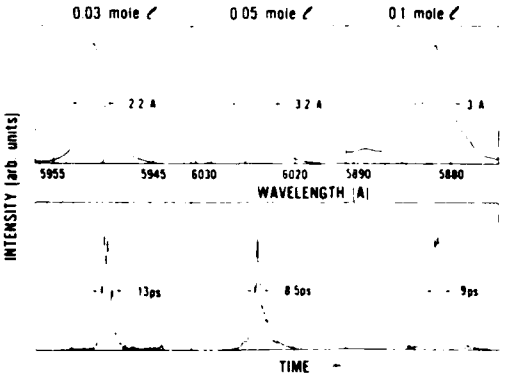

Fig. 6. Temporally and spectrally resolved SCDL pulses for various dye concentrations in the short cavity at pump levels a few times the lasing threshold.

significant changes in the system performance. In spite of the somewhat lower cavity finesse in the spectral region of RH 590, for comparable experimental conditions, similar temporal and spectral pulse profiles were observed. Temporally and spectrally resolved pulses of various RH590 concentrations are shown in Fig. 6. The pump levels were again a few times the lasing threshold. The cavity length was 10 μm. We found that the dye concentration could be varied over a relatively wide range without dramatic effects on the SCDL output. The best results regarding pulse width, spectral width, and amplitude stability were obtained at relatively low concentrations of 3×10^{-2} mole/l. At concentrations above 10^{-1} mole/l, the emission became less stable, and the spectra often exhibited two or more individual spikes. For cavity lengths shorter than 10 μm, dye concentrations closer to 10^{-1} mole/l seemed to yield better results. Throughout the laser operation with RH 590, a Kiton red solution (4×10^{-4} mole/l) was used in the amplifier stages. An accurate measurement of the energy conversion efficiency for the RH590/Kiton red combination could not be made since

TABLE I
SCDL INFRARED PERFORMANCE

Dye	LDS 821
Concentrations	3.5×10^{-2} mole/l (cavity) 4×10^{-4} mole (amplifier cells)
Solvent	methanol
Cavity lengths	17 μm, 9.5 μm
Pump power	5x threshold

	Input	Output	
		L = 17 μm	L = 9.5 μm
Wavelength	532 nm	805 – 840 nm (tunable)	805 – 840 nm (tunable)
Temporal width (FWHM)	32 ± 4ps	7.5 ± 2.5ps	15 ± 4ps
Spectral width (FWHM)	0.6 Å	3.4 ± 0.4 Å	4.0 ± 1.0 Å
Energy pulse	1 ± 0.15 mJ	5 ± 1.2μJ	~ 3μJ
ASE	–	10%	
Temporal jitter	–	± 1.5ps	
Wavelength stability	–	± 1.5 Å	± 1.5 Å
Free spectral range	–	15 nm	27 nm

the dichroic mirrors were not optimized for this dye. Based on the present results, we estimate that a finally attainable efficiency of about five percent can be expected for pump levels near threshold.

IV. CONCLUSION

The measurements described above demonstrate that an SCDL system allows the generation of tunable, infrared, picosecond pulses with good stability. The significant performance characteristics are summarized in Table I. For the given design and for operation in the infrared with the dye LDS 821, the best performance regarding temporal and spectral pulse shapes, output energy (per mode), and output stability was achieved for cavity lengths around 15 μm, dye concentrations of $\sim 3 \times 10^{-2}$ mole/l, and pump powers of roughly five times the threshold for lasing. Since under these conditions the mode spacing is slightly less than the width of the tuning range, additional spectral dispersion of the laser emission by a grating or prism (or the use of suitable spectral filters) may be necessary for some experimental applications. For true single-mode operation in the near infrared, the cavity length must be reduced to 7–8 μm. These conditions still produced satisfying results. The pulses, however, were longer, less stable, and the relative magnitude of amplified spontaneous emission was enhanced. Improvements in this regard can be expected by optimizing the cavity mirror reflectivities and by selecting a more appropriate dye solvent that permits a wider solubility range for LDS 821. The energy conversion efficiency is, compared to operation in the visible, relatively low. Even so, the output energy is sufficient for experimental applications. Moreover, the pump power can be easily increased above the level used in the present experiments.

Our investigations also demonstrate that, with the same set of cavity mirrors, similar performance (at an improved energy conversion efficiency) can be obtained in the visible. The SCDL thus represents an effective and relatively simple method for the conversion of fixed-wavelength, single-picosecond pulses into tunable picosecond pulses over an extended spectral range. Simultaneously, a considerable pulse width reduction can be achieved.

REFERENCES

[1] B. Fan and T. K. Gustafson, "Narrow-band picosecond pulses from an ultrashort-cavity dye laser," *Appl. Phys. Lett.*, vol. 28, pp. 202–204, 1976.

[2] H. Salzmann and H. Strohwald, "Single picosecond dye laser pulses by resonator transients," *Phys. Lett.*, vol. 57A, pp. 41–42, 1976.

[3] A. J. Cox, G. W. Scott, and L. D. Talley, "Tunable blue picosecond pulses from a dye laser," *Appl. Phys. Lett.*, vol. 31, pp. 389–391, 1977.

[4] J. A. Buck and Z. A. Yasa, "Dual frequency subnanosecond pulses from a millimeter-cavity dye laser," *IEEE J. Quantum Electron.*, vol. QE-13, pp. 935–936, 1977.

[5] A. J. Cox, D. E. Damschen, C. D. Merritt, G. W. Scott, and L. D. Talley, "Evidence for nearly transform-limited pulses from a short cavity dye laser," in *Picosecond Phenomena*, C. V. Shank, E. P. Ippen, and S. L. Shapiro, Eds. Berlin: Springer-Verlag, 1978, pp. 63–66.

[6] F. Aussenegg and A. Leitner, "A short resonator dye laser pumped by a traveling wave N_2-laser," *Opt. Commun.*, vol. 32, pp. 121–122, 1980.

[7] A. J. Cox, C. D. Merritt, and G. W. Scott, "Single mode, piezoelectrically tuned, picosecond short-cavity dye laser," *Appl. Phys. Lett.*, vol. 40, pp. 664–666, 1982.

[8] G. W. Scott, J. H. Clark, M. A. Tolbert, S. P. Webb, A. J. Cox, and G. Renz, "Simultaneous determination of the spectral and temporal properties of tunable, single, picosecond pulses from a short-cavity dye laser," *IEEE J. Quantum Electron.*, vol. QE-19, pp. 544–550, 1983.

[9] P. H. Chiu, S. Hsu, S. John, C. Box, and H.-S. Kwok, "A cascade pumped picosecond dye laser system," *IEEE J. Quantum Electron.*, vol. QE-20, pp. 652–658, June 1984.

[10] H. P. Kortz, P. Pax, and R. Aubert, "Generation of high energy tunable picosecond pulses," in *Ultrashort Pulse Spectroscopy and Applications*, M. J. Soileau, Ed., *Proc. SPIE*, vol. 533, pp. 32–37, 1985.

[11] H. P. Kortz, A. J. Cox, G. W. Scott, D. M. Guthals, H. Nathel, S. W. Yeh, S. P. Webb, and J. H. Clark, "Amplification of tunable picosecond pulses from a single-mode, short cavity dye laser," *IEEE J. Quantum Electron.*, vol. QE-21, pp. 1795–1798, Nov. 1985.

[12] The experiments were performed with a Quantel prototype short-cavity dye laser, which was improved by a home-made wavelength control unit.

[13] Throughout this paper, the ± error bars for the pulse durations and bandwidths represent the standard deviation for typicaly 10–20 laser shots.

[14] W. G. Wagner and B. A. Lengyel, "Evolution of a giant pulse in a laser," *J. Appl. Phys.*, vol. 34, pp. 2040–2046, 1963.

[15] J. A. Duncanson and W. S. Struve, "The picosecond ultrashort cavity dye laser: Giant pulse analogy and active erbium model," *IEEE J. Quantum Electron.*, vol. QE-17, pp. 3800–3820, 1981.

Appendix N: Femtosecond Pulse Generation in the Red/Deep Red Spectral Region.

A reprint of a paper published in IEEE Journal of Quantum Electronics QE-23, 290 (1987).

J-QE/23/3/12562

Femtosecond Pulse Generation in the Red/Deep Red Spectral Region

M. D. Dawson
T. F. Boggess
D. W. Garvey
A. L. Smirl

Reprinted from: IEEE JOURNAL OF QUANTUM ELECTRONICS, Vol. QE-23, No. 3, MAR. 1987.

Femtosecond Pulse Generation in the Red/Deep Red Spectral Region

MARTIN D. DAWSON, THOMAS F. BOGGESS, DENNIS W. GARVEY, AND ARTHUR L. SMIRL

Abstract—**Optical pulses as short as 55 fs in duration have been generated near 675 nm in a synchronously pumped, hybridly mode-locked, sulforhodamine 101 dye laser. Hybrid mode locking of rhodamine B in the same cavity arrangement yielded 187 fs pulses at 650 nm.**

LASER systems capable of generating femtosecond optical pulses include synchronously pumped hybridly mode-locked [1], [2] and, more commonly, passively mode-locked [3], [4] CW dye lasers. Although a variety of novel gain/saturable absorber dye combinations have recently been identified for use in these systems [5]–[10], direct production of sub-100 fs pulses has thus far almost exclusively been limited to the spectral region around 615 nm, primarily using rhodamine 6G and the saturable absorber DODCI [1]–[4]. Typically, the generation of pulses of this duration also requires the use of conventional ring [3] or antiresonant ring [1], [2] cavity arrangements designed to utilize the colliding pulse mode-locking (CPM) effect where counterpropagating pulses meet in the saturable absorber dye jet stream.

We have lately reported obtaining 69 fs pulses centered at 583 nm from a linear cavity synchronously pumped, hybridly mode-locked, rhodamine 6G dye laser [11]. In addition, pulses down to 65 fs have been achieved near 850 nm [12] using the gain/saturable absorber dye combination of Styryl 9 and IR 140, with which subpicosecond pulse generation had previously been demonstrated [10]. These are the only published reports of directly generated sub-100 fs pulses from dye lasers outside the "common" 605–630 nm wavelength range [13]. We describe here a further extension, producing 55 fs pulses around 675 nm by hybrid synchronous mode locking of a sulforhodamine 101 (SR 101) dye laser that does not require the CPM technique. To our knowledge, these are the shortest pulses yet reported from a synchronously pumped CW dye laser without the use of extracavity fiber-and-grating pulse compression. Hybrid mode locking of rhodamine B (RhB) in the same cavity arrangement yielded 187 fs pulses at 650 nm.

The dual jet laser cavity was described in detail previously [11], and only an outline of its characteristics is presented here. Briefly, the laser was pumped at 82 MHz by 650 mW average power, 70 ps pulses from a frequency-doubled mode-locked CW Nd:YAG laser (Spectra-Physics Series 3000). The pump beam was coupled into the gain medium (a 1.8×10^{-3} M solution of SR 101 or a 2×10^{-3} M solution of RhB in ethylene glycol) by a 5 cm radius of curvature focusing mirror. Except for the output coupler, single-stack dielectric coatings, highly reflecting at 632.8 nm and having bandwidth of greater than 100 nm, were used for all cavity mirrors. The pair of cavity mirrors about the gain dye jet stream had radius of curvature 7.5 cm, while those about the saturable absorber jet stream had 3.75 cm radius of curvature. A plane output coupler, 94 percent reflecting at 650 nm, 90 percent reflecting at 675 nm, terminated the linear laser cavity at the end nearest the gain section. The high-reflectivity end of the cavity, nearest the absorber section, was terminated by two Brewster prisms followed by a retroreflecting plane mirror, an arrangement that allows continuous adjustment of the intracavity dispersion [4]. The laser pulse thus double passes the prism pair at the high-reflectivity end of the cavity, with the result that the different spectral components are collinear throughout the remainder of the cavity and at the laser output.

Pulsewidth measurements were performed by both standard collinear type I and noncollinear background-free second-harmonic generation autocorrelation in a 1 mm KDP crystal. Hyperbolic secant-squared pulse shapes were assumed throughout in deriving the pulsewidths from the full width at half maxima of the intensity autocorrelation functions. Although not entirely appropriate for the data in Fig. 3 where the pulse exhibits large wings, this pulse shape provides a useful comparison to other systems of this type, for which it is commonly assumed. It also represents a more cautious estimate of the pulsewidth in Fig. 3 than that which would come from assuming an exponential-type pulse shape. The autocorrelator had a scanning display facility that enabled straightforward optimization of dye laser performance. Hard copies were, however, taken not from a stored image of the scanning display, but directly onto a slow pen recorder while the delay in one arm of the autocorrelator was varied using a motor-driven micrometer. No lock-in amplifier or other integrating device (other than the chart recorder itself) was used over the relatively long (minute) recording time, which accounts for the quite poor signal-to-noise characteristics of the autocorrelation in Fig. 1. Spectral information was recorded using an optical multichannel analyzer and vidicon system coupled to a $\frac{1}{4}$ m spectrometer.

Manuscript received July 22, 1986. This work was supported by the U.S. Office of Naval Research, the Robert A. Welch Foundation, and the NTSU Faculty Research Fund.

M. D. Dawson, T. F. Boggess, and D. W. Garvey are with the Center for Applied Quantum Electronics, Department of Physics, North Texas State University, Denton, TX 76203.

A. L. Smirl is with the Hughes Research Laboratories, Malibu, CA 90265.

IEEE Log Number 8612562.

0018-9197/87/0300-0290$01.00 © 1987 IEEE

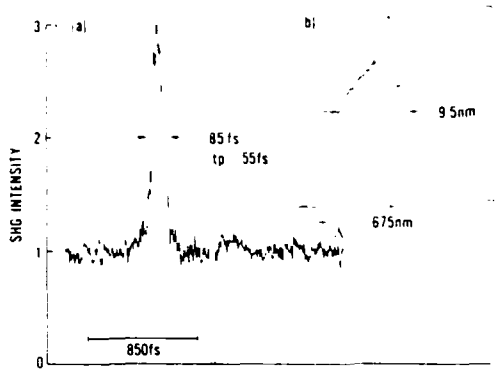

Fig. 1. Collinear type I autocorrelation (a) and corresponding integrated laser spectrum (b) of 55 fs pulses obtained using SR 101 and DQTCI.

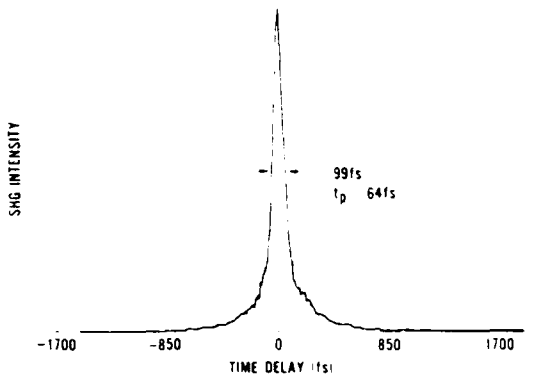

Fig. 2. Background-free autocorrelation of typical 64 fs pulses obtained using SR 101 and DQTCI which more clearly shows the pulse shape.

Optimal performance of the SR 101 laser was obtained using the dye 1,3′ Diethyl 4,2′ quinolylthiacarbocyanine iodide (DQTCI) as a saturable absorber. This dye has a peak extinction coefficient of $11 \times 10^4\ M^{-1} \cdot cm^{-1}$ at 628 nm in a 3:1 ethylene glycol:ethanol solution [7]. It has been identified as a versatile saturable absorber for use in flashlamp-pumped [14], [15] and CW-pumped [7], [8], passively mode-locked dye laser systems in the wavelength range 620–690 nm. The authors are not familiar with any reports of strong photoisomer generation with this dye under lasing conditions. Although the absorption maximum of the SR 101 gain dye (in ethanolic solution) occurs at 576 nm, typically requiring an energy transfer mixture with rhodamine 6G for optimum power performance using CW argon ion laser pumping [8], [16], efficient direct excitation of the dye can readily be achieved using a frequency-doubled mode-locked Nd:YAG laser. Prior to addition of the saturable absorber dye, 95 mW average power output was obtained at 661 nm with ethylene glycol flowing in the passive section jet stream.

Addition of DQTCI to form a 5×10^{-4} M solution resulted in the generation of stable pulses having duration as short as 55 fs (Fig. 1) and time-averaged output power ~35 mW when the dye laser cavity length was carefully matched (to $< 1\ \mu m$) to that of the pump laser. These pulses were spectrally centered near 675 nm, with a bandwidth of 9.5 nm, giving a time-bandwidth product of $\Delta\nu\Delta t = 0.34$ (note that $\Delta\nu\Delta t = 0.315$ for transform-limited $sech^2$ pulses). A more typical result, taken using the background-free autocorrelation technique, is shown in Fig. 2, indicating a pulse width of 64 fs. Such autocorrelations proved remarkably free of satellites when examined over a delay several tens of picoseconds with respect to the main pulse. Satellite pulses are known to be suppressed in hybridly mode-locked dye lasers [17], as compared to their purely synchronously pumped counterparts. In addition, with the autocorrelator aligned for collinear type I measurements, interferometric autocorrelations [18] of the pulses were displayed by reducing the scanning rate to 6 Hz and suitably decreasing the amplitude of the scan. These autocorrelations showed the necessary 8:1 peak-to-background ratio required for complete mode locking and directly illustrated the highly coherent nature of the pulses.

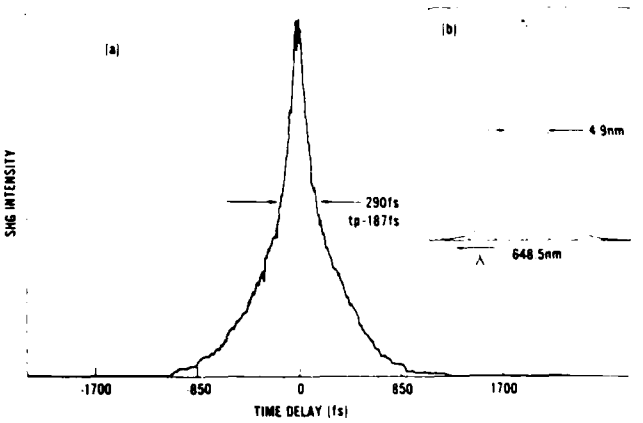

Fig. 3. Background-free autocorrelation (a) and corresponding integrated laser spectrum (b) of 187 fs pulses obtained using RhB and oxazine 720.

Similar performance was achieved when the gain medium was replaced by the dye rhodamine 101. Using a 2.1×10^{-3} M solution of this dye, 90 mW of time-averaged output power was measured, centered at 652 nm, prior to addition of the DQTCI saturable absorber. With the 5×10^{-4} M solution of DQTCI, 59 fs pulses were recorded with average power ~30 mW. These pulses were also spectrally centered near 675 nm, as in the case of SR 101, most likely because this wavelength is close to the long wavelength cutoff of the cavity mirrors.

Considerably longer pulses were obtained when DQTCI was used with RhB as the gain medium. Using a 2×10^{-3} M solution of RhB and a 10^{-4} M solution of DQTCI, the shortest pulses observed were of 320 fs duration, centered at 628 nm. The output power in this case was 25 mW. Improved performance was achieved, however, when DQTCI was replaced by oxazine 720 (perchlorate) as the saturable absorber. This dye has a peak extinction coefficient that has been measured as $9.2 \times 10^4\ M^{-1} \cdot cm^{-1}$ at 627 nm in ethanolic solution [19]. Pulses as short as 187 fs (Fig. 3) were obtained near 649 nm, using an absorber concentration of 3×10^{-4} M, with time-averaged

output power ~30 mW. The large wings on these pulses differ significantly from autocorrelations we have observed with the sulforhodamine 101 and rhodamine 6G [11] systems in this laser cavity. This may arise from the lower gain in the Rh B case, combined with near-resonant saturation of the absorber, leading to reduced spectral broadening and less effective pulse shaping.

In conclusion, femtosecond pulse generation has been obtained from synchronously pumped sulforhodamine 101, rhodamine 101, and rhodamine B dye lasers, hybridly mode-locked with DQTCI and oxazine 720 (perchlorate) saturable absorbers. With the sulforhodamine 101/DQTCI combination, 55 fs pulses were recorded near 675 nm, achieving direct generation of sub-100 fs pulses in the deep red spectral region for the first time. Similar results should be achievable with these dye combinations in either conventional or antiresonant ring synchronously pumped cavity arrangements. This could perhaps lead to some reduction in the wings of the pulses, but at the expense of critical positioning of the absorber jet stream and possible sensitivity of the pulse duration to absorber thickness.

Acknowledgment

We gratefully acknowledge useful conversations with J. R. Taylor and P. M. W. French of Imperial College, London, England, and thank them for making available preprints of their work prior to publication.

References

[1] T. Norris, T. Sizer II, and G. Mourou, "Generation of 85 fsec pulses by synchronous pumping of a colliding-pulse mode-locked dye laser," *J. Opt. Soc. Amer. B*, vol. 2, pp. 613-614, Apr. 1985.

[2] H. Vanherzeele, R. Torti, and J.-C. Diels, "Synchronously pumped dye laser passively mode-locked with an antiresonant ring," *Appl. Opt.*, vol. 23, pp. 4132-4184, Dec. 1984.

[3] R. L. Fork, B. I. Greene, and C. V. Shank, "Generation of pulses shorter than 0.1 psec by colliding pulse modelocking," *Appl. Phys. Lett.*, vol. 38, pp. 671-672, May 1981.

[4] J. A. Valdmanis, R. L. Fork, and J. P. Gordon, "Generation of optical pulses as short as 27 femtoseconds directly from a laser balancing self-phase modulation, group velocity dispersion, saturable absorption, and saturable gain," *Opt. Lett.*, vol. 10, pp. 131-133, Mar. 1985.

[5] P. M. W. French, M. D. Dawson, and J. R. Taylor, "Passive modelocking of a cw dye laser in the yellow spectral region," *Opt. Commun.*, vol. 56, pp. 430-432, Jan. 1986.

[6] P. M. W. French and J. R. Taylor, "Passively mode-locked continuous-wave Rhodamine 110 dye laser," *Opt. Lett.*, vol. 11, pp. 279-281, May 1986.

[7] ——, "The passive modelocking of the continuous wave Rhodamine B dye laser," *Opt. Commun.*, vol. 58, pp. 53-55, May 1986.

[8] ——, "Passive modelocking of an energy transfer continuous wave dye laser," *IEEE J. Quantum Electron.*, vol. QE-22, pp. 1162-1164, Aug. 1986.

[9] K. Smith, N. Langford, W. Sibbett, and J. R. Taylor, "Passive modelocking of a continuous-wave dye laser in the red-near-infrared spectral region," *Opt. Lett.*, vol. 10, pp. 559-561, Nov. 1985.

[10] K. Smith, W. Sibbett, and J. R. Taylor, "Subpicosecond generation via hybrid mode-locking of Styryl 9 in the near-infrared," *Opt. Commun.*, vol. 49, pp. 359-361, Apr. 1984.

[11] M. D. Dawson, T. F. Boggess, D. W. Garvey, and A. L. Smirl, "A hybridly mode-locked cw dye laser with Brewster prisms," *Opt. Commun.*, vol. 60, pp. 79-83, Oct. 1986.

[12] J. Dobler, H. H. Shultz, and W. Zinth, "Generation of femtosecond light pulses in the near infrared around λ = 850 nm," *Opt. Commun.*, vol. 57, pp. 407-409, Apr. 1986.

[13] A preliminary report of our measurements was presented as postdeadline paper WD8 at the Topical Meeting on Ultrafast Phenomena, Snowmass, CO, June 1986: M. D. Dawson, T. F. Boggess, D. W. Garvey, and A. L. Smirl, "Generation of 55 fs pulses and variable spectral windowing in a linear cavity synchronously-pumped cw dye laser." A further dye combination for femtosecond pulse generation was reported as postdeadline paper WD6 at the same meeting: W. H. Knox, "Generation of 70 fs pulses around 800 nm with the dye pair LDS 751 HITC-I in a synchronously pumped linear laser."

[14] E. G. Arthurs, D. J. Bradley, and A. G. Roddie, "Passive modelocking of flashlamp-pumped dye lasers tunable between 580 and 700 nm," *Appl. Phys. Lett.*, vol. 20, pp. 125-127, Feb. 1972.

[15] J. R. Taylor, "Passive modelocking of DCM and Rhodamine 101 flashlamp-pumped dye laser systems," *Opt. Commun.*, vol. 57, pp. 117-120, Feb. 1986.

[16] M. Yamashita, M. Kasamatsu, H. Kashiwagi, and K. Machida, "The selective excitation of lithium isotopes by intracavity nonlinear absorption in a cw dye laser," *Opt. Commun.*, vol. 26, pp. 343-347, Sept. 1978.

[17] D. Kuhlke, U. Herpers, and D. von der Linde, "Characteristics of a hybridly mode-locked cw dye laser," *Appl. Phys. B*, vol. 38, pp. 233-240, 1985.

[18] J.-C. Diels, J. J. Fontaine, I. C. McMichael, and F. Simoni, "Control and measurement of ultrashort pulse shapes (in amplitude and phase) with femtosecond accuracy," *Appl. Opt.*, vol. 24, pp. 1270-1282, May 1985.

[19] W. Rudolph, private communication.

Appendix O: Femtosecond Synchronously Pumped Pyridine Dye Lasers.

A reprint of a paper published in Optics Letters 12, 254 (1987).

Reprinted from Optics Letters, Vol. 12, page 254, April 1987.

Femtosecond synchronously pumped Pyridine dye lasers

Martin D. Dawson and Thomas F. Boggess

Center for Applied Quantum Electronics, North Texas State University, Denton, Texas 76203

Arthur L. Smirl

Hughes Research Laboratories, Malibu, California 90265

Received November 17, 1986; accepted December 30, 1986

Optical pulses as short as 103 fsec at 695 nm and 263 fsec at 733 nm have been generated in synchronously pumped hybrid Pyridine 1 and Pyridine 2 cw dye lasers, respectively, both using the saturable absorber 1,1′-diethyl-2,2′-dicarbocyanine iodide (DDI). These results combine with other data from the same linear cavity to give direct femtosecond generation over the spectral range 560–840 nm.

The majority of laser systems capable of generating femtosecond optical pulses are based either on purely passively mode-locked[1,2] or on hybrid synchronously pumped, passively mode-locked[3–5] cw dye lasers. Until recently, these lasers almost exclusively utilized the dyes Rhodamine 6G and DODCI as the gain medium and the saturable absorber, respectively, which restricted direct femtosecond generation to the 600–635-nm spectral region. However, rapid progress has been made during the past year in extending the wavelength coverage of such systems by using a variety of novel gain/saturable-absorber dye combinations. Femtosecond passive mode locking of cw dye lasers has now been reported at near-infrared,[6] red,[7,8] and yellow[9–11] wavelengths. The last-named kind of laser includes the first sub-100-fsec-pulse passive system operating at 585 nm (Ref. 11) that uses the Rhodamine 110–HICI combination[10] in a colliding-pulse mode-locked ring resonator.[1] Sub-100-fsec pulse generation has also now been achieved at new wavelengths in the synchronously pumped hybrid systems in the near infrared at 850 nm (Ref. 12) and 800 nm (Ref. 13) and at visible wavelengths near 583 nm (Ref. 14) and 675 nm.[15] In this Letter we report the production of femtosecond pulses near 695 and 733 nm with hybrid Pyridine 1 and 2 dye lasers, respectively, both using the saturable absorber 1,1′-diethyl-2,2′-dicarbocyanine iodide (DDI, also known as DDCI). These combine with other results from the same cavity arrangement to yield direct femtosecond generation over the spectral range 560–840 nm.

We used the linear-cavity dye-laser arrangement described in detail previously[14,15] synchronously pumped at 82 MHz by 650-mW average-power 70-psec pulses from a frequency-doubled mode-locked cw Nd:YAG laser (Spectra-Physics Series 3000). The resonator incorporated separate jet streams for the active and passive dyes; the focusing mirror pair around the gain jet had a 7.5-cm radius of curvature, and those about the absorber, a 3.75-cm radius of curvature. The pump beam was coupled into the gain medium by an independent 5-cm radius-of-curvature focusing mirror. A plane output coupler, 90% reflecting at 730 nm, 85% reflecting at 695 nm, terminated the laser cavity at the end nearer the gain section. The high-reflectivity end of the cavity, nearer the absorber section, was terminated by two Brewster prisms followed by a retroreflecting plane mirror, an arrangement permitting continuous adjustment of the intracavity dispersion.[2] Except the output coupler, all cavity mirrors had single-stack high-reflectivity dielectric coatings for 680 nm and a bandwidth of greater than 100 nm. Pulse-width measurements were performed by both standard collinear type I and noncollinear background-free second-harmonic-generation (SHG) autocorrelation in a 1-mm KDP crystal. Hyberbolic secant-squared pulse shapes are assumed throughout in deriving the pulse widths from the full widths at half-maxima of the intensity autocorrelation functions. The autocorrelator had a scanning display facility that permitted straightforward optimization of the dye-laser performance. Hard copies were, however, taken not from a stored image of the scanning display but directly onto a slow pen recorder without the use of a lock-in amplifier, while the delay in one arm of the autocorrelator was varied by using a motor-driven micrometer. Spectral information was recorded by using an optical multichannel analyzer and vidicon system coupled to a 0.25-m spectrometer.

Both the Pyridine 1 and Pyridine 2 dye lasers used 2×10^{-3} *M* solutions of the gain dye in a 15% propylene carbonate/85% ethylene glycol solvent. Before addition of the saturable absorber, with pure ethylene glycol flowing in the passive section jet stream, 150 mW of output power near 695 nm and 100 mW at 715 nm were measured for the two respective gain media. The pulses in this case were long (~2 psec) and incompletely mode locked. This is because, as described previously,[14,16] synchronous pumping alone is inadequate for good mode locking in a cavity such as this, where the bandwidth is not sufficiently limited. Both laser systems produced well-mode-locked femtosecond pulses, however, when the dye DDI was used as the saturable absorber. This dye has a peak extinction coefficient of 24.3×10^4 L mol^{-1} cm^{-1} at 710 nm in an ethanolic solution.[17] It has an upper-state lifetime

0146-9592/87/040254-03$2.00/0

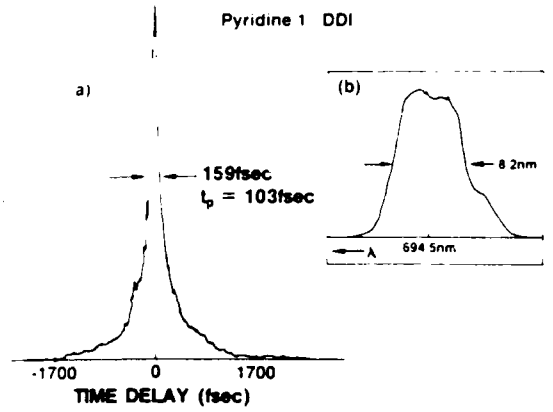

Fig. 1. (a) Background-free autocorrelation and (b) corresponding time-integrated laser spectrum of 103-fsec pulses obtained using Pyridine 1/DDI.

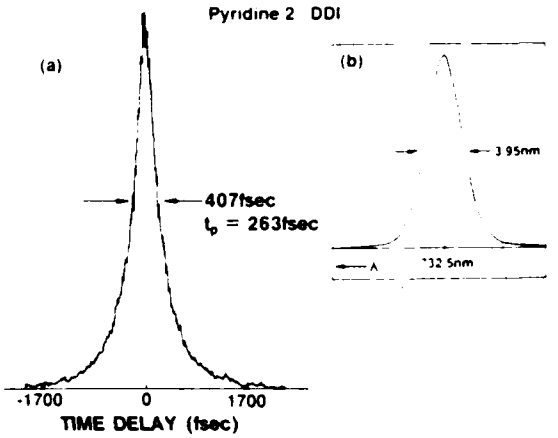

Fig. 2. (a) Background-free autocorrelation and (b) corresponding time-integrated laser spectrum of 263-fsec pulses obtained using Pyridine 2/DDI.

reported to be 14 psec (in methanol)[18] and was previously used in passive mode locking of the ruby laser[18] and in Cresyl Violet[18] and Rhodamine 700[17] flashlamp-pumped dye-laser systems.

For the Pyridine 1 dye laser, addition of DDI to form a 2.5×10^{-5} M solution resulted in the generation of stable pulses having durations as short as 103 fsec (Fig. 1) and time-averaged output power of ~65 mW when the dye-laser cavity length was carefully matched (to <1 μm) to that of the pump laser. These pulses were spectrally centered near 695 nm, with a bandwidth of 8.2 nm. The time–bandwidth product of $\Delta\nu\Delta t = 0.512$ (note that $\Delta\nu\Delta t = 0.315$ for transform-limited sech^2 pulses) implies some small residual frequency structure that cannot be compensated for by adjustment of the prism sequence. The rapid-recovery-time saturable absorber[18] was effective in suppressing the satellite pulse formation common in synchronously pumped dye lasers.

Somewhat longer pulses were obtained with the Pyridine 2 dye-laser system. A 3.0×10^{-5} M DDI solution resulted in the generation of 263-fsec pulses (Fig. 2) spectrally centered at 733 nm with a bandwidth of 3.95 nm. The output power was 35 mW, and the lower gain (originating partly through small leakage from the high-reflectivity mirrors near their long-wavelength cutoff) may account for the reduced spectral broadening and less effective pulse shaping in this case. Small (~20-nm) tunability was achieved in both systems, at the expense of increased pulse duration, by translating a slit across the dispersed fluorescence spectrum occurring between the second prism and the high-reflectivity cavity end mirror. The technique was described previously[16] for wavelength tuning and bandwidth control in this laser cavity.

Figure 3 illustrates additional wavelength coverage achieved with the same hybrid oscillator arrangement, following a suitable change of dyes and cavity mirrors. By using the high-reflectivity optics of Ref. 14 and an output coupler 95% reflecting at 590 nm, a Rhodamine 110 (4.1×10^{-3} M in ethylene glycol) dye laser was mode locked using the saturable absorber DASBTI.[9,10] A 10^{-4} M absorber solution resulted in the generation

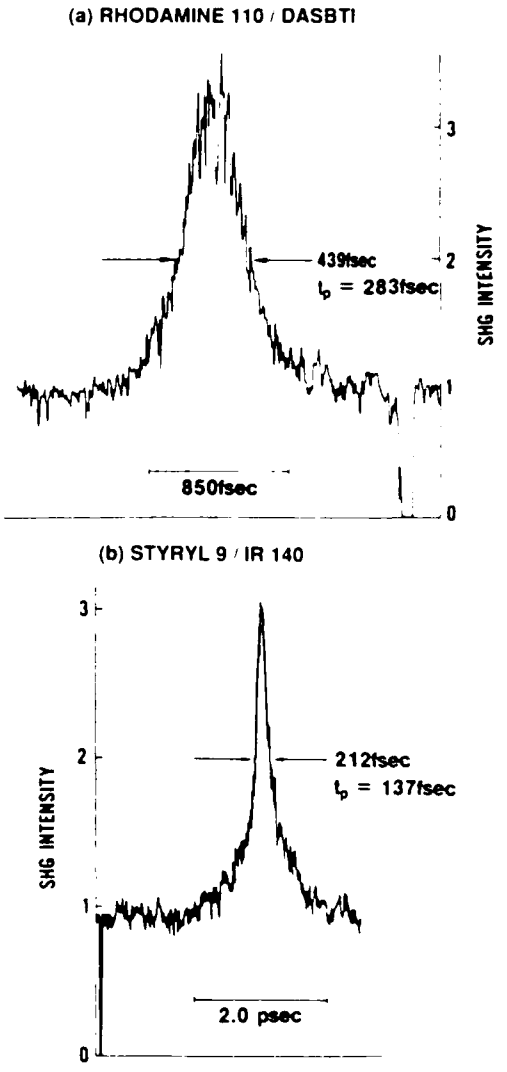

Fig. 3. Collinear Type I autocorrelation obtained with (a) Rhodamine 110/DASBTI at 560 nm and (b) Styryl 9/IR 140 at 825 nm.

Table 1. Femtosecond Hybrid cw Dye Lasers

Gain Dye	Saturable Absorber	Wavelength (nm)	Pulse Width (fsec)	Reference
Rhodamine 110	DASBTI	560	280	This work
Rhodamine 6G	DODCI, DQOCI	583	69	14
Rhodamine 6G	DODCI	622	<150	3, 4, 5, 14
Rhodamine B	Oxazine 720 or/DTDCI	650	190	15
Sulforhodamine 101	DQTCI	675	55	15
Pyridine 1	DDI	695	103	This work
Pyridine 2	DDI or DOTCI	733	263	This work
Styryl 8	HITCI	800	70	13, this work
Styryl 9	IR 140	840	65	12, this work

of 283-fsec pulses near 560 nm, with average output power ~25 mW [Fig. 3(a)]. Shorter pulses have been achieved with a Rhodamine 110 dye laser when passively mode locked by the dye HICI,[10,11] which may be a more effective saturable absorber for this wavelength region.

Other authors have reported generating 70-fsec pulses at 800 nm in the Styryl 8/HITCI hybrid system[13] and 65 fsec near 850 nm in the Styryl 9/IR 140 system[12] with which subpicosecond-pulse generation had previously been demonstrated.[19] We have also mode locked these dye combinations in our cavity setup. Figure 3(b) shows a 137-fsec pulse obtained at 825 nm with a 1.5×10^{-3} *M* Styryl 9 solution (15% propylene carbonate, 85% ethylene glycol solvent) and a 1.1×10^{-4} *M* solution of IR 140 (also predissolved in propylene carbonate). The output power was 40 mW, tunable over 800–840 nm. Similar power and pulse-width performance was achieved near 800 nm using the Styryl 8–HITCI combination. A 1-mm $LiIO_3$ SHG crystal was used for these autocorrelations; the output coupler was 90% reflecting at 850 nm and all other cavity mirrors highly reflecting at 800–940 nm.

Table 1 represents a summary of the results. We have achieved femtosecond generation near 695 and 733 nm using Pyridine 1 and Pyridine 2 dye lasers, respectively, hybridly mode locked by DDI. This combines with other results from the same cavity arrangement to yield direct femtosecond coverage of the wavelength range 560–840 nm. Further extension to ~1-μm wavelength is anticipated if the dyes Styryl 13 and Styryl 14 (Ref. 20) become commercially available, as suitable saturable absorbers have been identified for these systems.

This research was supported by the U.S. Office of Naval Research, The Robert A. Welch Foundation, and the North Texas State University Faculty Research Fund. Useful conversations with J. R. Taylor and P. M. W. French of Imperial College, London, are gratefully acknowledged.

Note added in proof: After the manuscript of this Letter was submitted, the shortest pulse generated with Pyridine 2/DDI was improved to 170 fsec.

References

1. R. L. Fork, B. I. Greene, and C. V. Shank, Appl. Phys. Lett. **38**, 671 (1981).
2. J. A. Valdmanis, R. L. Fork, and J. P. Gordon, Opt. Lett. **10**, 131 (1985).
3. T. Norris, T. Sizer II, and G. Mourou, J. Opt. Soc. Am. B **2**, 613 (1985).
4. H. Vanherzeele, R. Torti, and J.-C. Diels, Appl. Opt. **23**, 4182 (1984).
5. M. C. Nuss, R. Leonhardt, and W. Zinth, Opt. Lett. **10**, 16 (1985).
6. K. Smith, N. Langford, W. Sibbett, and J. R. Taylor, Opt. Lett. **10**, 559 (1985).
7. P. M. W. French and J. R. Taylor, Opt. Commun. **58**, 53 (1986).
8. P. M. W. French and J. R. Taylor, IEEE J. Quantum Electron. **QE-22**, 1162 (1986).
9. P. M. W. French, M. D. Dawson, and J. R. Taylor, Opt. Commun. **56**, 430 (1986)
10. P. M. W. French and J. R. Taylor, Opt. Lett. **11**, 279 (1986).
11. P. M. W. French and J. R. Taylor, "The passively mode-locked and dispersion compensated Rhodamine 110 dye laser," Opt. Commun. (to be published).
12. J. Dobler, H. H. Shultz, and W. Zinth, Opt. Commun. **57**, 407 (1986).
13. W. H. Knox, in *Digest of Topical Meeting on Ultrafast Phenomena* (Optical Society of America, Washington, D.C., 1986), postdeadline paper WD-6.
14. M. D. Dawson, T. F. Boggess, D. W. Garvey, and A. L. Smirl, Opt. Commun. **60**, 79 (1986).
15. M. D. Dawson, T. F. Boggess, D. W. Garvey, and A. L. Smirl, "Femtosecond pulse generation in the red/deep red spectral region," IEEE J. Quantum Electron. Lett. (to be published).
16. M. D. Dawson, T. F. Boggess, D. W. Garvey, and A. L. Smirl, Opt. Lett. **11**, 721 (1986).
17. W. Sibbett and J. R. Taylor, IEEE J. Quantum Electron. **QE-20**, 108 (1984).
18. D. J. Bradley in *Ultrashort Light Pulses*, S. L. Shapiro, ed., Vol. 18 of Topics in Applied Physics (Springer-Verlag, Berlin, 1977), p. 19.
19. K. Smith, W. Sibbett, and J. R. Taylor, Opt. Commun. **49**, 359 (1984).
20. K. Kato, Opt. Lett. **9**, 544 (1984).

Appendix P: Picosecond and Femtosecond Pulse Generation near 1000 nm from a Frequency-Doubled Nd:YAG-Pumped cw Dye Laser.

A reprint of a paper published in Optics Letters 12, 590 (1987).

Reprinted from Optics Letters, Vol. 12, page 590, August 1987.

Picosecond and femtosecond pulse generation near 1000 nm from a frequency-doubled Nd:YAG-pumped cw dye laser

Martin D. Dawson, Thomas F. Boggess, and Arthur L. Smirl*

Center for Applied Quantum Electronics, Department of Physics, North Texas State University, Denton, Texas 76203

Received April 15, 1987; accepted May 21, 1987

We report efficient synchronous mode locking of a 532-nm pumped cw dye laser tunable from 840 to 1030 nm, using a styryl compound as the gain medium. Hybrid synchronously pumped, passive mode locking of the laser using the saturable absorber DaQTeC generated 230-fsec pulses near 975 nm.

Highly efficient picosecond pulse generation has been reported in the 675–930-nm spectral region by synchronous pumping of styryl and pyridine dye lasers using green-wavelength pump-laser radiation.[1] Kato[2] recently introduced two new styryl derivatives—dyes Styryl 13 (S13) and Styryl 14 (S14)—which lased to beyond 1000 nm under cw Ar-ion laser excitation. We report synchronous mode locking of an S14-based dye-laser medium, permitting generation of picosecond pulses to 1030 nm when pumped by a frequency-doubled mode-locked cw Nd:YAG laser. This is believed to be the first report of green-pumped synchronously mode-locked cw dye-laser operation beyond 1 μm. Identification of suitable polymethine cyanine dye saturable absorbers has permitted hybrid synchronously pumped, passive mode locking of the dye laser. Femtosecond pulses were produced in this manner in previously uncovered spectral regions near 975 and 900 nm.

The gain dye exhibited a rather broad absorption band, with a measured peak extinction coefficient (ϵ_{max}) $\sim 4 \times 10^4\ M^{-1}\ cm^{-1}$ at 610 nm in a 3:1 ethylene glycol:propylene carbonate solvent. Synchroscan streak-camera measurements indicated a fluorescence lifetime of ~250 psec in propylene carbonate.[3] The short lifetime of this dye essentially precludes the possibility of obtaining stable ultrashort pulse generation by cw-pumped passive mode locking alone. This follows from literature on the theory of slow-saturable-absorber mode locking in quasi-continuous dye-laser systems.[4,5] In order to satisfy the criterion that the relaxation time of the amplifying medium be of the order of the cavity round-trip time,[4,5] a cavity most likely impractically short for a jet-stream dye laser would be required. Synchronous pumping of the laser by a mode-locked pump source is therefore necessary.

For synchronous mode locking, we used the gain section and pump focusing mirror arrangement from the dye-laser system reported previously.[6-8] The linear cavity setup was completed by a plane output coupler at one end and a plane high-reflectivity mirror at the other. Either one or two dispersive Brewster prisms and an adjustable aperture were placed in the cavity near the high-reflectivity end mirror to provide frequency tuning and bandwidth restriction, in the manner of Ref. 9. All cavity mirrors, except the output coupler, had coatings highly reflecting from 800 to 1100 nm. Pulse-width measurements were performed by standard noncollinear background-free second-harmonic-generation (SHG) autocorrelation in a 1-mm $LiIO_3$ crystal. Hyperbolic secant-squared pulse shapes are assumed throughout in deriving the pulse widths from the full widths at half-maxima of the intensity autocorrelation functions. The autocorrelator had a scanning display facility, permitting straightforward optimization of the dye-laser performance. Spectral information was obtained by using an optical multichannel analyzer and vidicon system coupled to a 0.25-m spectrometer.

A $1.5 \times 10^{-3}\ M$ solution of the gain dye in a 15% propylene carbonate/85% ethylene glycol solvent was employed. With ~950 mW of 532-nm (Spectra-Physics Series 3000 Nd:YAG laser) pump power, composed of 70-psec pulses at 82 MHz, the laser was tuned over 840–990 and 940–1030 nm by using output couplers 90% reflecting at 900 and 1000 nm, respectively (Fig. 1). The maximum time-averaged output power from the dye laser was ~70 mW near 910 nm. Pulses in the range 1.5 to 2.0 psec were obtained across the tuning curve (Fig. 2). The corresponding spectral widths, typically 1.2 to 1.35 nm, do, however, indicate some excess bandwidth, assuming $sech^2$ pulse shapes (an additional dispersing prism in the cavity would have limited the spectrum more). Little degradation of the dye was observed in almost two months of day-to-day synchronously pumped operation.

Nuclear-magnetic-resonance spectroscopy identifies, in addition to S14, a considerable Styryl 9 (S9) related impurity in the gain dye samples.[10] This is presumably responsible for the short-wavelength laser action and limited long-wavelength tunability, compared with Kato's data.[2] The tuning indicates, however, that an S14:S9 mixture may be usefully employed to cover the same spectral region as S13.[2] S13 is unlikely to become available because its synthesis involves use of β-naphthylamine,[10] which is strictly regulated as a carcinogen.

Hybrid synchronously pumped, passive mode lock-

0146-9592/87/080590-03$2.00/0

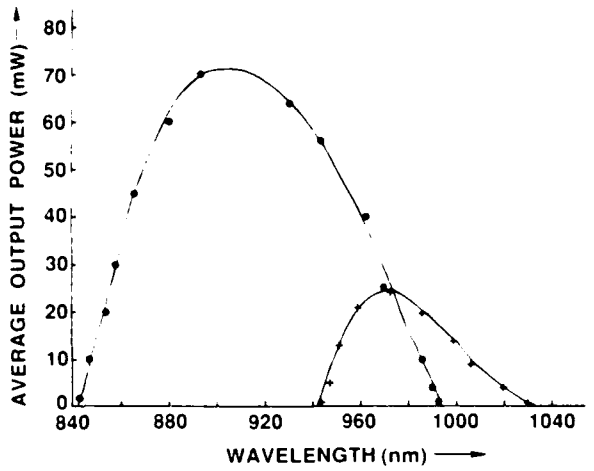

Fig. 1. Synchronously mode-locked cw dye-laser tuning curve for output couplers 90% reflecting at 900 nm (●) and 1000 nm (+), respectively.

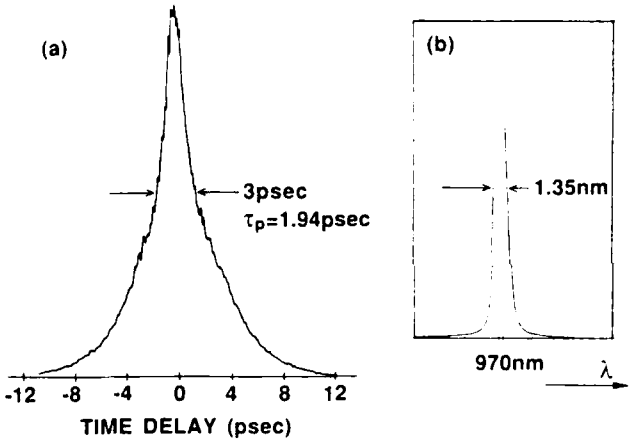

Fig. 2. (a) Background-free autocorrelation and (b) corresponding time-integrated spectrum of synchronously mode-locked pulses at 970 nm.

ing utilizes saturable absorption in addition to synchronous mode locking and is capable of producing subpicosecond pulses. To achieve this, we used the full-cavity arrangement described in detail previously,[6-8] with which 55–280-fsec pulses have been generated over the range 560–840 nm (Ref. 8) when pumped by a frequency-doubled mode-locked cw Nd:YAG laser. Briefly, the linear cavity dye laser incorporated, in addition to the gain section described earlier, a separate jet stream for the saturable-absorber dye. The output coupler, 90% reflecting at 900 nm (83% reflecting at 975 nm), terminated the cavity at the end nearer the gain section. The high-reflectivity end of the cavity, nearer the absorber section, was terminated by two Brewster prisms followed by a retroreflecting plane mirror, in an arrangement permitting continuous adjustment of the intracavity dispersion.[11] All high-reflectivity mirrors had the same coating as those in the gain section.

Optimum results were obtained using 1,1′-diethyl-13-acetoxy-2,2′-quinotetracarbocyanine iodide as a saturable absorber, which we abbreviate as DaQTeC, consistent with previous notation for a related dye.[12] This dye[13] and its perchlorate salt were employed previously to generate high-power (~1 MW peak), tens-of-nanosecond pulses beyond 1 μm under Q-switched ruby-laser excitation.[14,15] The structural formula of the dye and its absorption profile in a 3:1 ethylene glycol:propylene carbonate solution are shown in Fig. 3. The peak extinction coefficient (ϵ_{max}) was measured to be $9.5 \times 10^4\ M^{-1}\ cm^{-1}$ at 928 nm.

Before the addition of the saturable absorber, 65-mW output power was measured at 930 nm, using a fresh sample of the gain dye and with ethylene glycol flowing in the passive section jet stream. An output power of ~40 mW had been previously measured for this gain dye sample when the laser was prism tuned to 975 nm, under synchronous pumping only, without the intracavity aperture. Addition of DaQTeC to form a $6 \times 10^{-5}\ M$ solution resulted in the generation of stable pulses having duration as short as 228 fsec at 974 nm (Fig. 4) when the dye-laser cavity length was matched (to <1 μm) to that of the pump laser. The time-averaged output power was ~15 mW. The corresponding spectral bandwidth of 4.45 nm implies a time–bandwidth product $\Delta\nu\Delta t = 0.32$, i.e., the pulses are effectively transform limited (note that $\Delta\nu\Delta t = 0.315$ for bandwidth-limited sech^2 pulses). Adjusting the absorber concentration in the range $6–4 \times 10^{-5}\ M$ permitted pulses below 350 fsec to be generated from 974 to 965 nm. Examination of the SHG autocorrelation function over a delay of greater than 40 psec with respect to the main pulse and monitoring the laser output by using a fast-photodiode/oscilloscope combination showed no evidence of either satellite or multiple pulse formation.

Additional wavelength coverage was obtained by using the absorber 1,1′-diethyl-4,4′-quinotricarbocyanine iodide[13] ($\epsilon_{max} = 11 \times 10^4\ M^{-1}\ cm^{-1}$ at 933 nm in 3:1 ethylene glycol:propylene carbonate). This dye has

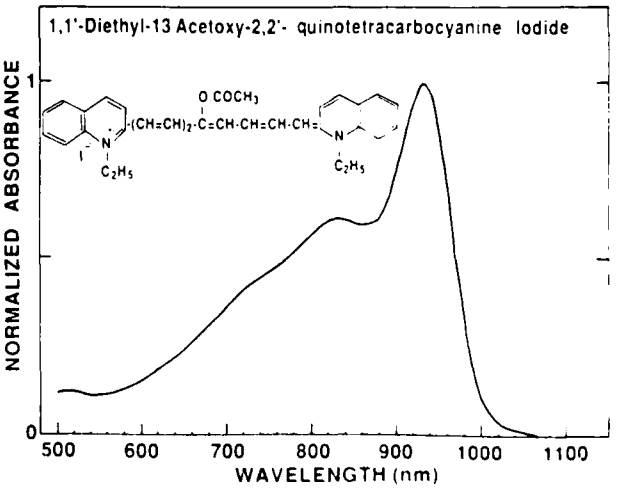

Fig. 3. Asorption profile and structural formula for the saturable-absorber dye DaQTeC.

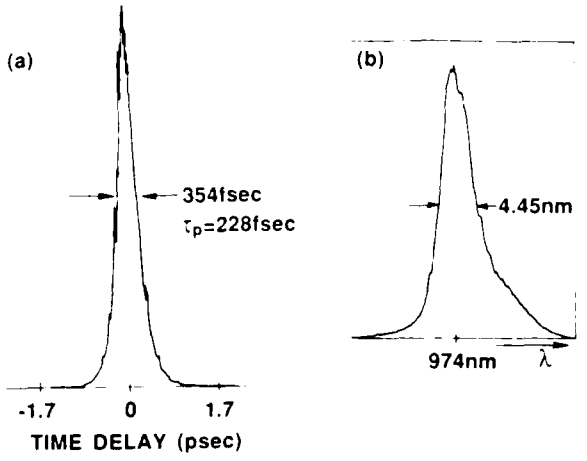

Fig. 4. (a) Background-free autocorrelation and (b) corresponding time-integrated spectrum of 228-fsec pulses near 974 nm obtained from a hybrid dye laser using DaQTeC as a saturable absorber.

also been shown to exhibit laser action beyond 1 μm under ruby-laser pumping.[14,15] Before the addition of the absorber dye to the passive section jet stream, the laser's operating wavelength was 930 nm; this dye pushed the laser to shorter wavelengths. Adjusting the absorber concentration in the range $7\text{–}3 \times 10^{-5}$ *M* allowed pulses of 265 to 350 fsec to be generated from 897 to 905 nm. These pulses did, however, exhibit slight evidence of a coherence spike, in marked contrast to those near 975 nm. It should be pointed out, in addition, that both absorbers were observed to degrade significantly after several days in solution. Nevertheless, this is a more than adequate period for almost all experiments, and the small dye concentrations required, together with their relative low cost, ensures their usefulness.

In conclusion, we have demonstrated 532-nm pumped synchronous mode locking of a cw dye laser to 1030 nm and extended to ~975 nm the utility of hybrid mode locking as a simple means of generating femtosecond pulses. These pulses should provide immediate application in, for example, investigations of the photorefractive effect in GaAs on a picosecond and subpicosecond time scale,[16] since they are at wavelengths longer than the band-gap absorption edge. For the same reason, the systems may find application as simple sources for electro-optic sampling of voltage waveforms in integrated circuits.[17,18] The pulses retain the time-jitter characteristics of synchronously mode-locked cw dye-laser systems,[19] however, which will somewhat limit the temporal resolution obtainable.

This research was supported by the U.S. Office of Naval Research and the Robert A. Welch Foundation. Provision of the gain dye samples by, and useful conversations with, L. Knaak, Exciton Chemical Company, and G. Mourou and P. Bado, University of Rochester, are gratefully acknowledged.

*Permanent address, Hughes Research Laboratories, 3011 Malibu Canyon Road, Malibu, California 90265.

References

1. P. Bado, C. Dupuy, K. R. Wilson, R. Boggy, J. Bowen, and S. Westra, Opt. Commun. **46**, 241 (1983).
2. K. Kato, Opt. Lett. **9**, 544 (1984).
3. K. Smith, University of St. Andrews, Scotland (personal communication).
4. G. H. C. New, Opt. Commun. **6**, 188 (1972).
5. G. H. C. New, K. E. Orkney, and M. J. W. Nock, Opt Quantum Electron. **8**, 425 (1976).
6. M. D. Dawson, T. F. Boggess, D. W. Garvey, and A. L. Smirl, Opt. Commun. **60**, 79 (1986).
7. M. D. Dawson, T. F. Boggess, D. W. Garvey, and A. L. Smirl, IEEE J. Quantum Electron. Lett. **QE-23**, 290 (1987).
8. M. D. Dawson, T. F. Boggess, and A. L. Smirl, Opt. Lett. **12**, 254 (1987).
9. R. K. Jain and J. P. Heritage, Appl. Phys. Lett. **32**, 11 (1978).
10. L. Knaak, Exciton Chemical Company, Dayton, Ohio 45431 (personal communication).
11. J. A. Valdmanis, R. L. Fork, and J. P. Gordon, Opt. Lett. **10**, 131 (1985).
12. M. Leduc and C. Weisbuch, Opt. Commun. **26**, 78 (1978).
13. Absorber dyes purchased from Gallard-Schlesinger Chemical Manufacturing Corporation, Carle Place, New York 11514.
14. H. Lotem, Opt. Commun. **9**, 346 (1973).
15. Y. Miyazoe and M. Maeda, Opto-Electron. **2**, 227 (1970).
16. G. C. Valley, A. L. Smirl, M. B. Klein, K. Bohnert, and T. F. Boggess, Opt. Lett. **11**, 647 (1986).
17. B. H. Kolner and D. M. Bloom, IEEE J. Quantum Electron. **QE-22**, 79 (1986).
18. J. A. Valdmanis and G. Mourou, IEEE J. Quantum Electron. **QE-22**, 69 (1986).
19. P. G. May, W. Sibbett, K. Smith, J. R. Taylor, and J. P. Willson, Opt. Commun. **42**, 285 (1982).

Appendix Q: Cavity Length Detuning Effects and Stabilization of a Synchronously-Pumped Femtosecond Linear Dye Laser.

A preprint of a paper to be published in Opt. Lett., 1988.

Submitted to Optics Letters

CAVITY LENGTH DETUNING EFFECTS AND STABILIZATION OF A SYNCHRONOUSLY-PUMPED FEMTOSECOND LINEAR DYE LASER

Martin D. Dawson and Dwight Maxson
Center for Applied Quantum Electronics
North Texas State University
Denton, Texas 76203

Thomas F. Boggess and Arthur L. Smirl
Hughes Research Laboratories
Malibu, California 90265

Abstract

We report on the cavity length detuning characteristics of a synchronously-pumped femtosecond linear-resonator cw dye laser. The severe cavity matching requirement (to within 0.2 μm) for optimum short pulse generation is addressed by an active cavity-length stabilization scheme based on second harmonic generation. This allows pulses ~100 fsec in duration to be maintained for periods of several hours.

Much interest has recently been shown in the generation of femtosecond pulses using synchronously-pumped, passively mode-locked cw dye lasers.[1-9] Such systems offer some advantages over their continuously-pumped, passively mode-locked[10] counterparts. These include higher efficiency and the possibility of using a frequency-doubled cw mode-locked Nd:YAG laser[1] as pump source. Also, direct synchronization to an external r.f. source via the pump laser mode-locker driver allows synchronous amplification of the pulses[1] and synchronous pumping of a conventional tunable picosecond laser in parallel.[2] In addition, synchronous pumping has allowed a wider variety of gain dyes to be used in femtosecond lasers, particularly the styryl[3-6] and pyridine[3] dyes for efficient extended near-infrared operation.

Several cavity designs[1-9] and pumping schemes[2] for femtosecond synchronously-pumped dye lasers have been demonstrated. In particular, the dual-jet, dispersion-compensated, linear cavity arrangement[3,4,6,9] offers ease of alignment and non-critical positioning of the saturable absorber jet-stream on a micron scale. The purpose of this letter is to describe an investigation of what is believed by many to be the principal disadvantage of synchronously-pumped femtosecond lasers. That is, we study the high sensitivity of the pulse duration and characteristics of such a system to sub-micron detuning of the cavity length. We have developed an active cavity length stabilization scheme, of general applicability in such systems, that allows pulses ~100 fsec in duration to be maintained for periods of several hours against critical length variations.

The laser setup has been described in detail elsewhere.[3,4,9] For the measurements reported here, we used the gain-saturable absorber dye combination of Sulforhodamine 101 and DQTCI, which has previously been shown to generate pulses as short as 55 fsec near 675 nm in this cavity arrangement.[9] For present purposes, it suffices to mention that the linear cavity incorporated separate jet-streams for the gain and saturable absorber dyes. The output coupler, 90% reflecting at 675 nm, terminated the cavity at the end nearer the gain section. Intracavity dispersion compensation was obtained by using a Brewster-prism-pair and retroreflecting plane mirror arrangement to terminate the high reflectivity end of the cavity, nearer the absorber section. All highly reflecting mirrors had single-stack dielectric coatings for 632.8 nm, with a bandwidth of

greater than 100 nm. Pulsewidth measurements were performed by noncollinear background-free second-harmonic-generation (SHG) autocorrelation in a 1-mm KDP crystal. Pulse profiles are assumed throughout to be hyperbolic secant-squared. Spectral data was obtained using an optical multichannel analyzer and vidicon system coupled to a 0.25-m spectrometer. The overall spectral resolution was ~0.4 nm.

Using $2x10^{-3}$ M and $4x10^{-4}$ M solutions in ethylene glycol of the gain and saturable absorber dyes, respectively, typical autocorrelations and spectra at the optimum cavity length (labeled $\Delta x=0$ μm) were as shown in Fig. 1(b). (The value $\Delta x=0$ μm is not meant to necessarily imply absolute matching of the physical lengths of the pump and dye laser cavities.) Pulse durations of 85 fsec with time-averaged power ~65 mW were obtained using 750 mW of frequency-doubled cw mode-locked Nd:YAG (Spectra Physics Series 3000) laser pump power, consisting of 70 psec pulses at 82 MHz. The time-bandwidth product $\Delta\nu\Delta t=0.32$ implies that the pulses are effectively transform-limited. (Note that $\Delta\nu\Delta t=0.315$ for bandwidth-limited $sech^2$ pulses.)

The data in Fig. 1 illustrate the effect of a systematic variation of the cavity length, about $\Delta x=0$ μm, on the corresponding autocorrelations and spectra. Related studies have been performed for conventional synchronously-pumped systems,[11-13] and the qualitative behavior is similar, indicating the strong role played by synchronous pumping in the pulse formation process. This has a number of implications regarding interpretation of various aspects of the detuning behavior, which will be discussed later. The progression from Fig. 1(a) to 1(e) corresponds to increasing the cavity length. A piezoelectric (PZT) stack (Photon Control Type MGS15), which was magnetically coupled to a precision translation stage on which the dye laser output coupler was mounted, was used to adjust the cavity length. The piezoelectric stack gave 16.7 μm of travel when activated by only 150 volts, with a setting sensitivity of better than 0.04 μm.[14] The position readings in Fig. 1 were directly confirmed by independent manual adjustments of cavity length using a differential micrometer.

The features of Fig. 1 may be summarized as follows. At Δx near +5 μm, the autocorrelations show a coherence spike on a broad base, indicating incomplete mode-locking. In

purely synchronously-pumped systems, such behavior at positive cavity displacements has been explained[11-13] in terms of the pulse seeing high and relatively flat gain at increasing delay with respect to the pump pulse. This introduces pulse-broadening and random substructure. As the cavity length is decreased towards $\Delta x=0$ μm, the autocorrelation function narrows sharply and the spectral width increases. Decreasing the cavity length by ~0.2 μm beyond $\Delta x=0$ μm results in high instabilities followed by an abrupt collapse (evident in Fig. 2; see later) of the autocorrelation to the form shown in Fig. 1(a). Similar, though less critical, behavior in purely synchronously pumped systems has been related[11-13] to the reduced gain seen by the dye pulse as the cavity is shortened and the pulse moves towards the initial instant where laser threshold occurs. Here, this is compounded by a reduction in the absorber saturation.

Cavity length changes of 0.1-0.2 μm cause observable changes in the scanning display of the autocorrelation function near $\Delta x=0$ μm, in agreement with previous reports.[2,5,8] (The long ~450 psec pump pulses used in Ref. 7 may partly account for the relaxed 40 μm matching requirement observed in that particular case.) This severe matching condition vividly illustrates the need for active cavity length stabilization. Without it, many mechanisms, including thermal drift, mechanical relaxation of mounts, atmospheric pressure and temperature changes, etc., act to detune the pulses from their optimum length over periods of several minutes (or longer), depending on exact operating conditions. A useful summary of these effects may be found in Ref. 15.

In Fig. 1(a)-(e), we observe a shift in the spectral peak of less than 0.5 nm. This is in marked contrast to the ~15 nm shift reported by Chesnoy and Fini[8] for a 1 μm change of cavity length in their antiresonant ring system. The small spectral shift observed here may be due, at least in part, to operation near the long-wavelength cut-off of the high reflectivity cavity mirrors restricting spectral movement. Nevertheless, a stabilization scheme based on large, monotonic spectral shifts, such as that suggested in Ref. 8, appears not to be useful in our case and is less generally applicable than the one demonstrated here.

Figure 2 shows the variation of SHG intensity with cavity length, in the vicinity of $\Delta x=0$. The length decreases from positive to negative detuning values. These data were obtained by

focusing a small fraction of the output beam into a 1 mm KDP crystal independent of the autocorrelator setup. The cavity length was scanned by applying a 10 Hz triangular waveform to the PZT stack. A photomultiplier tube (PMT) detected the second harmonic, and the output of the PMT was observed on a storage oscilloscope. The rising edge of the triangular waveform results in the mirror image of Fig. 2; this response is not displayed for reasons of clarity. This figure illustrates that the SHG intensity is a sensitive indicator of the cavity length detuning, and this forms the basis of our feedback arrangement. Figure 2 has several noteworthy features. The high sensitivity of the detuning characteristic and the assymmetric behavior about $\Delta x=0$, are clearly evident. Also, the shortest pulse ($\Delta x=0$) occurs at the point of maximum SHG intensity. The trends of increased detuning sensitivity, and of the shortest pulse occurring nearer the point of maximum SHG,[11] with increased intracavity bandwidth for purely synchronous mode-locking have been previously identified.[11] (In the case of strong frequency selection by an intracavity etalon, the shortest pulse occurs for a distinct (several μm) negative detuning from the point of maximum SHG.[11,16])

The abrupt "collapse" of the SHG intensity for slight negative detuning means that long-term stabilization of the very shortest pulses produced by the system is difficult. Periodic modulation of the cavity length to determine the point of maximum SHG was felt to be neither practicable, because of the sensitivity of the detuning characteristic, nor desirable, because of the pulse width modulation which would be introduced. Instead, we chose to set the operating point of the system at a small (0.5 to 0.7 μm) positive detuning. (Evidently, this was also necessary in the feedback scheme described in Ref. 8.) Stable pulses such as those displayed in Fig. 1(c), with pulsewidths ~125 fsec, were then typically obtained. Operating on the slope of the SHG characteristic allows fluctuations in the SHG signal about the set point to be fed as an error signal directly to the PZT stack.

The feedback electronics had the following characteristics. A two-component feedback error signal was generated: one had a fast response (up to 300 Hz) and one a slow response (~1/30 Hz). The fast response was dynamically constrained to follow only limited excursions in the

SHG intensity. This allowed for a fast correction to the cavity length, but precluded the feedback system being put out of lock by an occasional large fluctuation occurring on a timescale faster than the feedback response. The frequency response of the fast error signal, the magnitude of the SHG excursions that it could follow, and the positive cavity length detuning point at which the feedback loop was set to operate, were all adjustable. These factors could then be optimized for particular laser operating conditions. Further details of the feedback electronics will be published elsewhere.[17]

With the feedback system operational, pulses such as those in Fig. 1(c) can be maintained for periods of several hours. Figure 3 illustrates the stabilizing effect of the feedback system on the SHG intensity over an ~3 minute time segment. In Fig. 3(a), with the feedback loop operating, fluctuations in SHG intensity (and thus also fluctuations in the scanning autocorrelator display) are limited to ±10%. This corresponds to a pulse train amplitude stability of within ±5%. The remaining excursions are most likely the result of fluctuations in the pump laser power[18] occurring on a timescale faster than the feedback response (integrated by the 0.35 sec full scale response of the x-y recorder). An electronic feedback system to control the pump laser intensity can greatly reduce this noise[18] and is currently being incorporated into our system. The fluctuations shown in Fig. 3(b) which are corrected by the feedback loop, are most likely caused by air currents or some mechanical effects on the cavity components. The possibility that the feedback loop will adjust the cavity length in response to pump power fluctuations (and not cavity length detuning effects) and, thus, modulate the pulsewidth, is minimized by deliberately limiting the frequency and amplitude response of the fast feedback error signal and by choosing the slow feedback error signal to have a time constant longer than that of typical pump power fluctuations.[18] Indeed, no induced pulsewidth fluctuations were evident on the scanning (30 Hz) autocorrelator display. In any case, present theoretical models of laser systems of this type predicts inherent statistical variations of the pulse duration.[19]

In conclusion, we have presented a study of the cavity length detuning characteristics of a synchronously-pumped femtosecond linear laser. The high sensitivity of the pulse characteristics to slight (<0.2 μm) cavity length detuning dictates that an active feedback scheme be employed

AD-A191 926 NONLINEAR OPTICAL PROPERTIES AND SUBPICOSECOND DYNAMICS 3/3
OF EXCITONS AND E..(U) ARMY LAB COMMAND WATERTOWN MA
MATERIAL TECHNOLOGY LAB T F BOGGESS ET AL. DEC 87
UNCLASSIFIED MAC-REF-F4767 AFOSR-TR-88-0012 F/G 20/12 NL

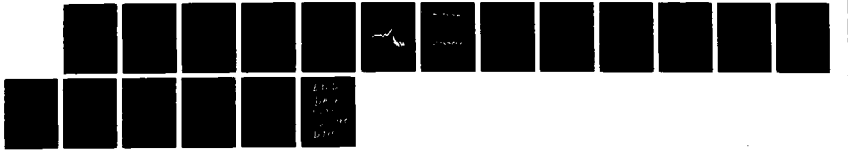

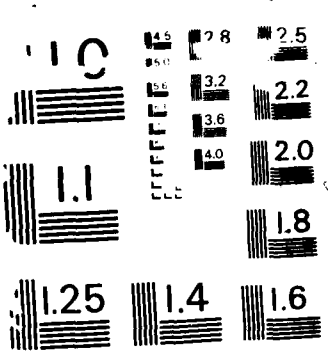

term stabilization. We achieved long-term pulsewidth stability and pulse train amplitude fluctuations within ±5% by deriving the feedback error signal directly from the SHG intensity of a fraction of the dye laser output. With the laser optimized to produce pulses as short as 55 fsec[9] and feedback stabilization of the pump laser, we expect to be able to maintain pulses well below 100 fsec with this setup, over several hours. This stabilization technique should be generally applicable to other gain-saturable absorber dye combinations demonstrated to produce femtosecond pulses over the range 560-975 nm with this cavity arrangement.[3,4]

Acknowledgements

This research was supported by the U.S. Office of Naval Research and The Robert A. Welch Foundation.

References

1. J. D. Kafka, T. Sizer, I. N. Duling, C. W. Gabel, and G. Mourou, IEEE J. Quantum Electron. QE-19, 506 (1983).
2. M. C. Nuss, R. Leonhardt, and W. Zinth, Opt. Lett. 10, 16 (1985).
3. M. D. Dawson, T. F. Boggess, and A. L. Smirl, Opt. Lett. 12, 254 (1987).
4. M. D. Dawson, T. F. Boggess, and A. L. Smirl, Opt. Lett. 12, 590 (1987).
5. J. Dobler, H. H. Schulz, and W. Zinth, Opt. Commun. 57, 407 (1986).
6. W. H. Knox, in Digest of Topical Meeting on Ultrafast Phenomena (Optical Society of America, Washington, DC, 1986), post deadline paper WD-6.
7. H. Vanherzeele, R. Torti, and J.-C. Diels, Appl. Opt. 23, 4182 (1984).
8. J. Chesnoy and L. Fini, Opt.Lett. 11, 635 (1986).
9. M. D. Dawson, T. F. Boggess, D. W. Garvey, and A. L. Smirl, IEEE J. Quantum Electron. Lett. QE-23, 290 (1987).
10. R. L. Fork, B. I. Greene, and C. V. Shank, Appl. Phys. Lett. 38, 671 (1981).
11. C. P. Auschnitt, R. K. Jain, and J. P. Heritage, IEEE J. Quantum Electron. QE-15, 912 (1979).
12. S. L. Shapiro, R. R. Cavanagh, and J. C. Stephenson, Opt. Lett. 6, 470 (1981).
13. P. G. May, W. Sibbett, K. Smith, J. R. Taylor, and J. P. Willson, Opt. Commun. 42, 285 (1982).
14. Photon Control Ltd., Cambridge, U.K., manufacturer's data sheet.
15. N. Frigo, C. Hemenway, and H. Mahr, Appl. Phys. Lett. 37, 981 (1980).
16. S. R. Rotman, C. Roxlo, D. Bebelaar, T. K. Lee, and M. M. Salour, Appl. Phys. B 28, 319 (1982).
17. D. Maxson, M. D. Dawson, and A. L. Smirl, "Active Cavity Length Stabilizer for a Synchronously-Pumped Femtosecond cw Dye Laser," to be submitted to Rev. Sci. Inst.
18. T. M. Baer and D. D. Smith, in Ultrafast Phenomena IV, D. H. Auston and K. B. Eisenthal, eds., Vol. 33 of Series in Chemical Physics (Springer-Verlag, Berlin, 1984), p. 96.
19. D. Kuhlke, U. Herpers, and D. von der Linde, Appl. Phys. B 38, 233 (1985).

Figure Captions

Figure 1. Background-free SHG autocorrelations and corresponding time-integrated spectra as a function of cavity mismatch.

Figure 2. SHG intensity versus cavity length detuning around $\Delta x=0$ (from an oscillograph).

Figure 3. SHG intensity versus time (a) with, and (b) without, feedback loop. The beam was temporarily blocked near 150 sec to show the zero level in each case.

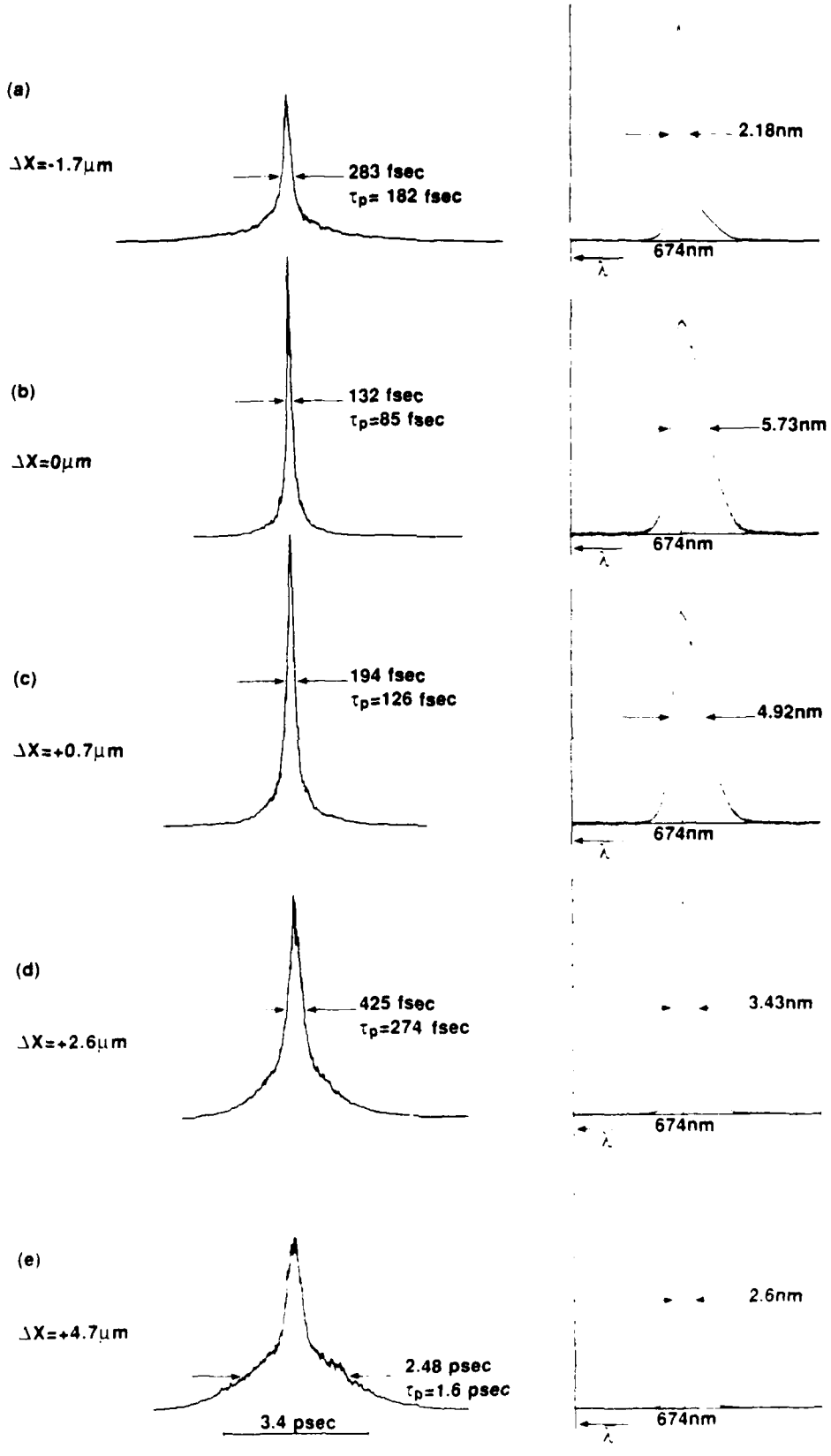
(a)
ΔX=-1.7μm
283 fsec
τp= 182 fsec
2.18nm
674nm
λ
(b)
ΔX=0μm
132 fsec
τp=85 fsec
5.73nm
674nm
λ
(c)
ΔX=+0.7μm
194 fsec
τp=126 fsec
4.92nm
674nm
λ
(d)
ΔX=+2.6μm
425 fsec
τp=274 fsec
3.43nm
674nm
λ
(e)
ΔX=+4.7μm
2.48 psec
τp=1.6 psec
3.4 psec
2.6nm
674nm
λ

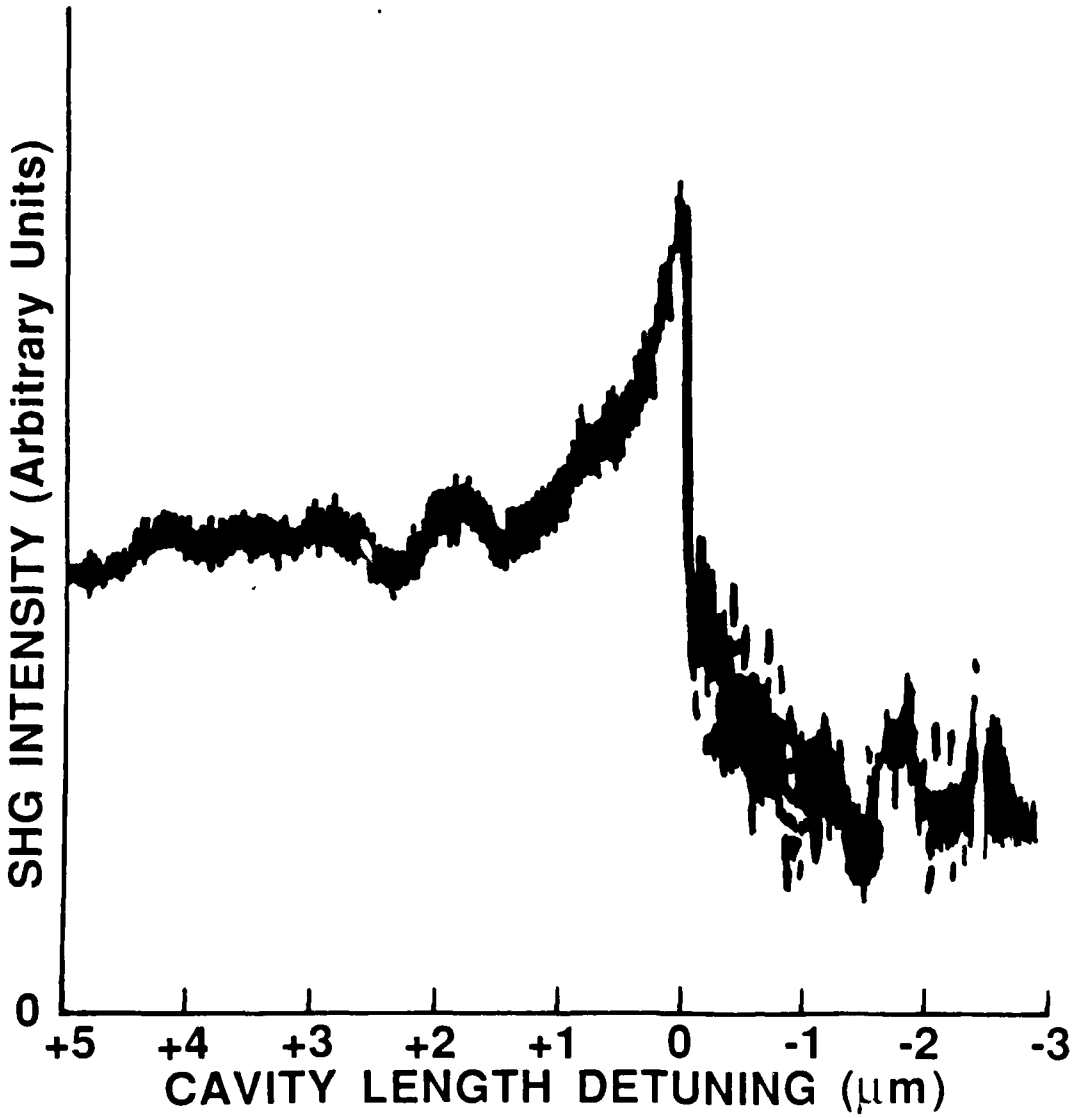
SHG INTENSITY (Arbitrary Units)
0
+5
+4
+3
+2
+1
0
-1
-2
-3
CAVITY LENGTH DETUNING (μm)

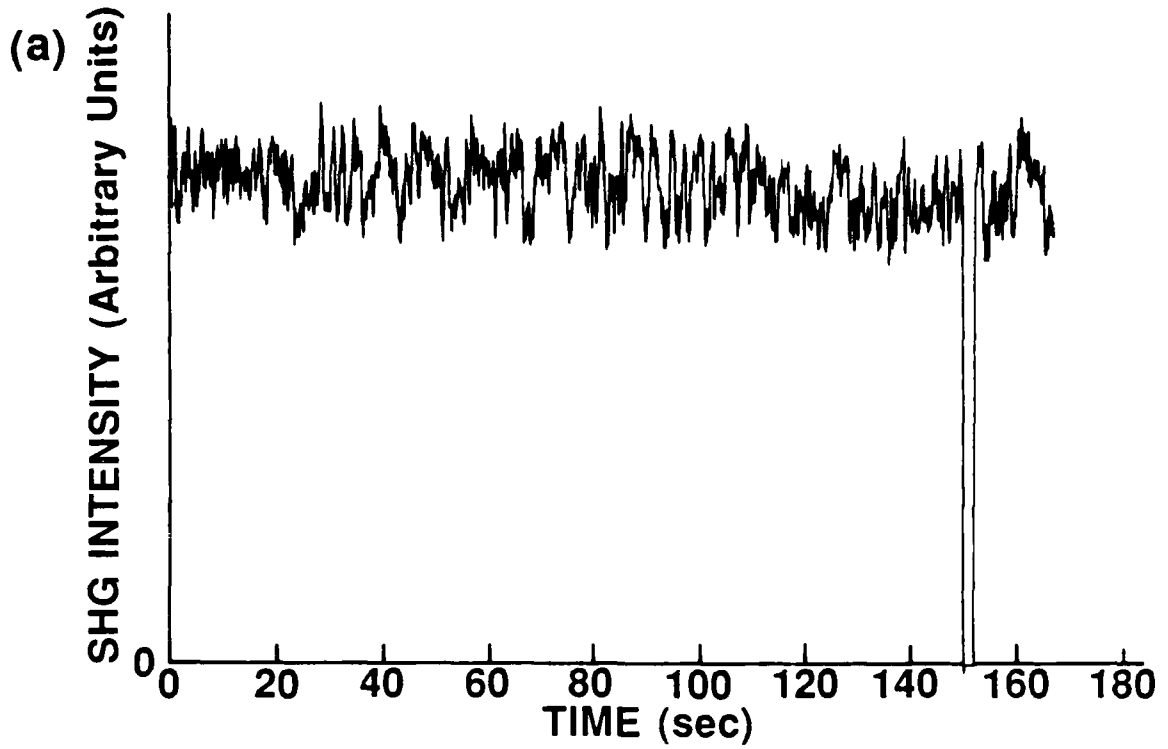
(a)
SHG INTENSITY (Arbitrary Units)
0
0
20
40
60
80
100
120
140
160
180
TIME (sec)

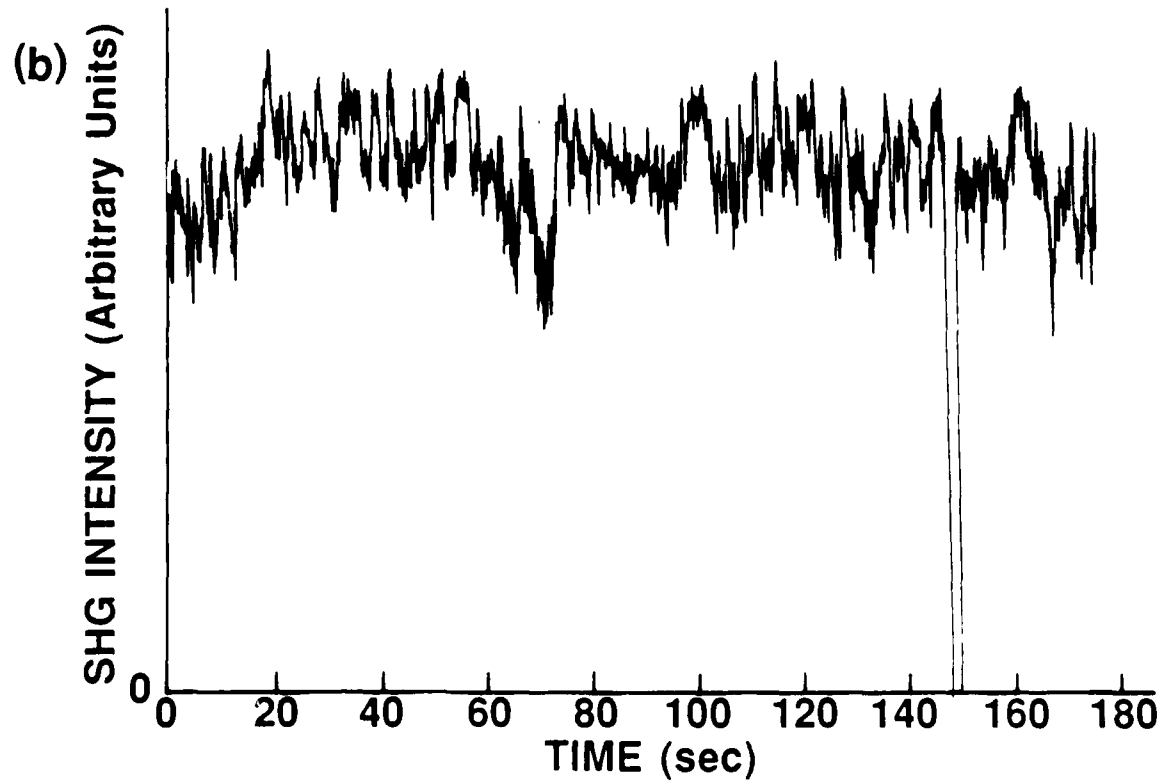
(b)
SHG INTENSITY (Arbitrary Units)
0
0
20
40
60
80
100
120
140
160
180
TIME (sec)

Appendix R: Photoreflectance of GaAs Doping Superlattices.

A reprint of a paper published in Superlattices and Microstructures 2, 513 (1986).

PHOTOREFLECTANCE OF GaAs DOPING SUPERLATTICES

X.C. Shen,* H. Shen,** P. Parayanthal,* and F.H. Pollak**
Physics Department, Brooklyn College of CUNY
BROOKLYN, N.Y. 11210 USA

and

J.N. Schulman, Arthur L. Smirl, R.A. McFarlane, and Irnee D'Haenens
Hughes Research Laboratories
Malibu, CA 90265 USA

We have performed room-temperature photoreflectance measurements on two GaAs doping superlattices having considerably different built-in potentials (1.2 eV and 85 meV). The first sample exhibits Franz-Keldysh oscillations, the period of the oscillations corresponding to the large built-in dc field. A second dc pump beam has been used to change the electron-hole concentration and hence the built-in field. The spectrum of the second sample displays a number of features corresponding to quantized electron and hole states. There is qualitative agreement between experiment and theoretical calculation based on a two-band tight binding model. In both samples the dependence of the amplitude of the photoreflectance signal on pump chopping frequency yields the minority carrier lifetime.

Semiconductors with a periodic doping profile of n- and p-doped layers, possibly separated by undoped (intrinsic, i) regions (n i p-i superstructures), exhibit interesting properties not found in either bulk crystals or compositional superlattices.[1,2] These n-i-p-i structures have an "indirect gap" in real-space, long electron-hole recombination lifetimes because of the spatial separation of the carriers, and a two-dimensional subband structure for the electrons and holes that can be tailored independently for each carrier type. Even though there have been considerable optical studies on these semiconductor structures, most of the investigations have dealt with the near band gap and below band gap regions.[1-3] Recently, work on the above band gap optical properties has also been reported.[4] The quantization of the electron states has been observed in resonance Raman scattering[5] and photoreflectance.[4] Investigators, however, have not reported on the quantization of the holes.

It has been demonstrated recently that electromodulation (electroreflectance and photoreflectance) is a powerful method for studying quantum effects in compositional superlattices and quantum wells.[6,7] Electromodulation produces such sharp structures that, even at room temperatures, all the confined interband quantum transitions can be observed. The electromodulation spectra of these microstructural geometries can be fit by a derivative functional form (DFF),[4,7,8] thus making it possible to accurately determine the quantum energies, broadening parameters, etc. In addition, electromodulation yields information about the nature of the internal electric fields in these structures. Photoreflectance (PR), specifically, is a contactless mode of electromodulation in which the electric field is modulated by the photoinjection of electron hole pairs via a chopped pump beam.[4,6,7]

In this paper we report room temperature measurements on two GaAs n-i p i superlattices having considerably different built in potentials, i.e., 1.2 eV and 85 meV. In the 1.2 eV sample the spectrum is caused by Franz Keldysh (FK) oscillations,[9] the period being related to the large built in dc field.[10] We used a second dc pump beam to change the electron-hole concentration and hence the built in field. This variation in turn resulted in a change in the FK oscillations, enabling us to gain information about the nature of the built in field. In the second (85 meV) sample we observed a number of features in the spectrum both below and above the band gap of GaAs. The spectrum was fit by a DFF procedure, and we performed a theoretical calculation of the

*Permanent address: Shanghai Institute of Technical Physics, Academia Sinica, Shanghai, China
**Also at Physics Dept., Graduate School and University Center, City University of New York, New York, N.Y. 10036
*Present address: AT&T Bell Telephone Laboratories, Murry Hill, N.J. 07974

0749 6036/86/060513 + 05 $02.00/0

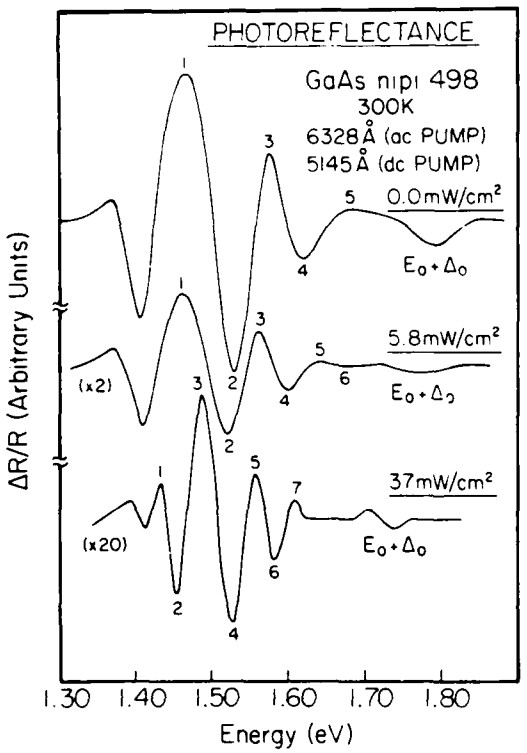

Fig. 1. Photoreflectance spectra at 300K of GaAs n-i-p-i 498 for dc pump power densities of 0, 5.8, and 37 mW/cm^2.

energy levels and intensities using a two band tight-binding model[11] with material parameters deduced from the growth conditions.

There is general agreement between experiment and theory. In both samples the dependence of the amplitude of the PR signal on the pump chopping frequency (Ω_m) yields the minority carrier lifetime. In the former sample we observed a significant decrease in the minority carrier lifetime with increased dc pump power because of the change in spatial separation of the carriers. Thus, the PR investigation yielded important information about the doping superlattices.

The n-i-p-i superlattices used in this experiment were fabricated by molecular beam epitaxy at Hughes Research Laboratories. Sample n-i-p-i 498 consists of 21 n (6.5×10^{17}cm^{-3}) and p (2.5×10^{17}cm^{-3}) layers with n- and p layer thicknesses of 800 Å (d_n) and 1400 Å (d_p). The second sample, n-i-p-i 497, has nominal $n = 7\times10^{17}$cm^{-3} and $p = 5\times10^{17}$cm^{-3} with $d_n = d_p = 233$ Å. The values of the built-in potential, ($2V_n$), have been deduced from the growth parameters with n-i-p-i 498 having $2V_n = 1.2$ eV, and n-i-p-i 497 having $2V_n = 85$ meV, using Eq. (11) of Ref. 2. The PR technique has been described in the literature.[6,9,10] The probe beam was from a Photon Technology International[12] 1/4-meter monochromator. The ac pump beam was the 6328-Å line of a 1-mW He-Ne laser; the power density was about 1.5 mW/cm^2. The chopping frequency was in the 1.5 to 4000 Hz range. In addition, investigations were carried out on n-i-p-i 498 with a dc pump beam (5145-Å line of an Ar-ion laser).

Plotted in Fig. 1 are the 300K PR spectra of sample n-i-p-i 498, using 6328 Å as the ac pump, with dc pump (5145 Å) power densities of (a) 0.0, (b) 5.8 mW/cm^2 and (c) 37 mW/cm^2. For n-i-p-i 498 there is a very large built-in potential (1.2 eV) and hence the PR features are FK oscillations of the fundamental gap, E_o. The numbered peaks correspond to these electro-optical features. The structure denoted $E_o + \Delta_o$ corresponds to the spin-orbit split component of E_o. According to FK theory in the literature, the period of FK oscillations is related to the amplitude of the modulating electric field[9]. It should be pointed out that these theories are based on modulation from flat-band and do not take into account the presence of large built-in dc fields. It can be shown that if the dc built-in field is considerably larger than the ac field, the period of the FK oscillations is a measure of the former field, not the latter.[10] This appears to be the case for n-i-p-i 498, since it has such a large $2V_n$; i.e., built-in potential. From the period of the oscillations in Fig. 1(a) we deduce a field of 1.2×10^5 V/cm. This value agrees quite well with the value of the average built-in field:

$$2V_n/[(d_n+d_p)/2] = 1.1\times10^5 \text{ V/cm}.$$

The dc pump beam creates electron-hole pairs, reducing the value of $2V_n$ and thus the built-in field. This effect is evident in Figs. 1(b) and 1(c). From the FK oscillations in Fig. 1(c) (37 mW/cm^2 at 5145 Å) we deduce a built-in field of 0.5×10^5 V/cm, a significant decrease in relation to the case of zero dc pump power.

The dotted line in Fig. 2 shows the 300K PR spectrum of sample n-i-p-i 497 in the 1.30-to-1.55-eV range using 6328 Å as the ac pump at $\Omega_m = 150$ Hz. Experimental conditions were in the "low-field regime"; i.e., lineshape independent of ac pump beam intensity.

It has been proposed that electromodulation spectra from superlattices and quantum wells can be fit by a derivative functional form:[4,7,8,9]

$$\frac{\Delta R}{R} = \mathrm{Re}\left[\sum_{j=1}^{p} C_j e^{i\theta_j}\left(E - E_{g,j} + i\Gamma_j\right)^{k_j}\right] \quad (1)$$

where E is the photon energy, p is the number of spectral features to be fit, and C_j, θ_j, $E_{g,j}$, and Γ_j are the amplitude, phase, energy, and broadening parameters of the j^{th} structure. The parameter k_j represents the type of critical

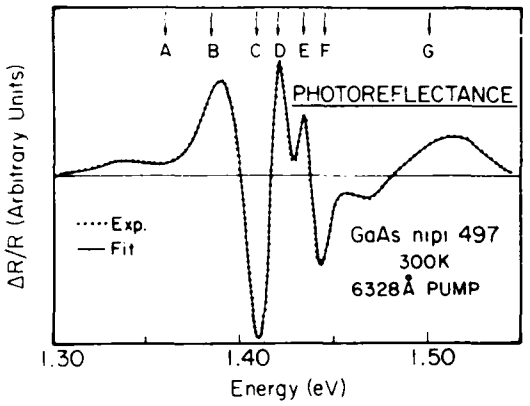

Fig. 2. Experimental photoreflectance spectrum at 300K (dotted line) of GaAS n-i-p-i 497. The solid line is a least-squares fit to Eq. (1) for $k_j = 1$.

point and order of the derivative. For example, $k_j = 1$ is the first derivative of a two-dimensional critical point, $k_j = 3$ corresponds to the third-derivative of a two-dimensional critical point, etc.

The solid line in Fig. 2 is a least-squares fit of the experimental data to Eq. (1) with $p = 7$ and $k_j = 1$ (for $j = 1$ to 7). The energies obtained are indicated by arrows at the top of the figure and are listed in Table I, along with the corresponding k_j. We find the fit for $k_j = 3$ is indistinguishable from the former fit, but that it yields somewhat different energies and broadening parameters. These are also given in Table I. Thus, at present, we cannot make a definitive statement about the order of the derivative[4,8] to fit the PR spectra of n-i-p-i structures.

We have performed a theoretical calculation of the quantized energy levels and transition intensities using a two-band tight-binding model[11] with material parameters cited above. Listed in Table I are the energies of the most intense transitions (based on matrix element and density of states) in the region of the various spectral features. The notation nmH(0) or nmH(π) denotes a transition from the n^{th} conduction subband to the m^{th} valence band of heavy-hole (H) character at the minizone center (0) or edge (π), respectively. We have found that transitions involving light-hole valence bands have considerably less amplitude than heavy-hole features and thus they have been neglected. Also we have neglected a number of weak heavy-hole transitions. For example, if we examine the energy region in the vicinity of the D feature there is a theoretical 33H(0) transition at 1.419 eV but it is weaker than 17H(0) or 25H(π) (see Table I) and therefore has not been included.

Unfortunately, theoretical calculation using the growth parameters does not give a unique assignment to the experimental data. We have also performed the calculation using other values of n, p, d_n, and d_p such that $2V_n$ is kept constant at 85 meV. It is also possible to make a correspondence between theory and experiment, but not necessarily with the same transitions. Thus, for other material parameters (keeping $2V_n$

Table I. Experimental energies and broadening parameters ( ) for the various photoreflectance features from a fit to Eq. (1) for $k_j = 1$ and 3. Also listed are the theoretical energies and corresponding transitions.

Spectral Feature	Experiment				Theory	
	Energy[a] (eV)	[a] (meV)	Energy[b] (ev)	[b] (meV)	Energy (eV)	Transition
A	1.360	21	1.350	74	1.369	13H(0)
B	1.385	20	1.386	27	1.381	22H(0)
C	1.408	12	1.414	23	1.408 1.408	16H( ) 24H(0)
D	1.420	6	1.419	17	1.417 1.421	17H(0) 25H( )
E	1.434	4	1.432	13	1.433	26H(0)
F	1.444	3	1.443	16	1.445	35H(0)
G	1.500	20	1.507	34	1.491	55H( )

(a) obtained with $k_j = 1$ in Eq. (1) (b) obtained with $k_j = 3$ in Eq. (1)

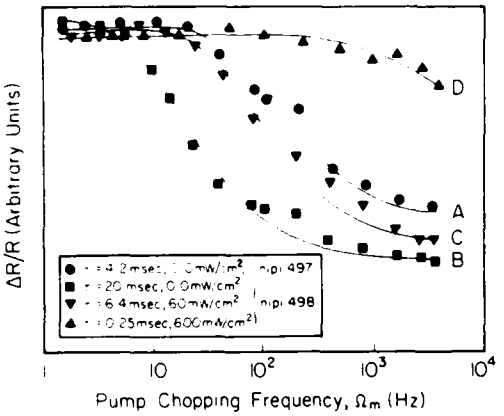

Fig. 3. Photoreflectance intensity as a function of ac pump chopping frequency for GaAs n-i-p-i 497 (curve A) and 498. For n-i-p-i 498 the dependence on dc pump (5145 Å) power densities of 0 (curve B), 60 mW/cm² (curve C), and 600 mW/cm² (curve D) is shown. The respective time constants, τ, are ilndicated.

constant) there are also fairly strong theoretical transitions in the energy range of the various experimental features, but they do not necessarily correspond to the same transitions. For example, in other calculations the theoretical energies around the D feature (1.420 eV) are not 17H(0) or 25H(π).

The PR of InP n-i-p-i structures at 300K and 80K has been reported in Ref. 4. The lineshapes have been fit by an expression based on a Lorentzian oscillator model originally developed for the electroreflectance of excitons. This corresponds to $k_j = 2$ in Eq. (1). In interpreting their data the above-referenced authors considered only the quantization of the electron subbands and not the valence (and spin-orbit split) states. We found that the valence band quantization is an important consideration for our case.

The optical transition selection rules between confined valence and conduction band states are similar to those for a Type II superlattice, in which the electrons and holes are spatially separated [13]. Thus n-m must be even at the minizone center, while n-m must be odd at the minizone edge. These selection rules do not hold for unconfined states. Since miniband dispersion was not considered in Ref. 4 these authors report contributions to the PR spectra from all miniband transitions.

We have also investigated the dependence of the amplitude of the PR signal on the chopping frequency, Ω_m. Shown in Fig. 3 are some experimental results (solid points) for samples n-i-p-i 497 and 498. Curve A is the frequency dependence of n-i-p-i 497 (no dc pump). From an exponential fit to the data points (solid line) we extract a time constant, τ, of 4.2 msec. For sample n-i-p-i 498 we have investigated the effects of the intensity of the dc pump on the lifetime. Curves B, C, and D correspond to power densities of 0, 60, and 600 mW/cm², respectively. The corresponding τ are listed in the figure. Increasing the dc pump power decreases the recombination lifetime, since the built-in potential is decreased and hence there is less separation of carriers.

In conclusion, we have measured the room temperature PR spectra from two GaAs doping superlattices with substantially different built-in potentials. The large-potential sample exhibits FK oscillations, the period being related to the dc built-in field rather than the ac modulation field. A second dc pump beam was used to reduce the built-in potential. In the second sample PR structures are observed which are caused by transitions between quantized electron and hole states. A correspondence between experiment and theory can be made, although not uniquely. The dependence of the PR on pump chopping frequency is a measure of the recombination lifetime.

Acknowledgement - The Brooklyn College group wishes to thank IBM Shared University Research (SUR) program and the New York State Foundation for Science and Technology as part of its Centers for Advanced Technology Program for support of this research. One of the authors (ALS) wishes to acknowledge partial support by the Office of Naval Research, the Air Force Office of Scientific Research and The Robert A. Welch Foundation.

References

[1] K. Ploog and G.H. Dohler, Advances in Physics 32, 285 (1983).
[2] H. Dohler, Superlattices and Microstructures 1, 279 (1985).
[3] G.H. Dohler, H. Kunzel, and K. Ploog, Physical Review B 25, 2616 (1982); G.H. Dohler and P. Ruden, Physcial Review B 33, 5932 (1984).
[4] M. Gal, J.S. Yuan, J.M. Viner, P.C. Taylor and G.B. Stringfellow, Physical Review B 33, 4410 (1986).
[6] G. Fasol, P. Ruden, and K. Ploog, Journal of Physics C 17, 1395 (1984) and references therein.
[6] O.J. Glembocki, B.V. Shanabrook, N. Bottka, W.T. Beard and J. Comas, Applied Physics therein.
[7] P. Parayanthal, H. Shen, F.H. Pollak, O.J. Glembocki, B.V. Shanabrook and W.T. Beard, Applied Physics Letters 48, 1261 (1986).
[8] B.V. Shanabrook, O.J. Glembocki and W.T. Beard, submitted to Physical Review. B.V. Shanbrook and O.J. Glembocki, this conference.

[9]D E. Aspnes in Handbook on Semiconductors, Vol. 2, ed. by T S Moss (North Holland, N.Y., 1980) p. 109 and references therein.
[10]R Bhattacharya, H Shen, P. Parayanthal, F H. Pollak, T. Coutts and H. Aharoni, to be published in Solar Cells.
[11]J N. Schulman, in Proceedings of the Symposium on Layered Structures and Epitaxy, 1985 Fall Meeting of the Materials Research Society, Vol. 56 of Materials Research Society Symposium Proceedings.
[12]Photon Technology International, Princeton, N.J, 08542.
[13]P. Voisin, G. Bastard, and M. Voos, Physical Review B 29, 935 (1984).

Appendix S: Observation of Symmetery Forbidden Transitions in the Room Temperature Photoreflectance Spectrum of a GaAs/GaAlAs Multiple Quantum Well.

A reprint of a paper published in Solid State Communications 59, 557 (1986).

Solid State Communications, Vol. 59, No. 8, pp. 557–560, 1986.
Printed in Great Britain.

0038-1098/86 $3.00 + .00
Pergamon Journals Ltd.

OBSERVATION OF SYMMETERY FORBIDDEN TRANSITIONS IN THE ROOM TEMPERATURE PHOTOREFLECTANCE SPECTRUM OF A GaAs GaAlAs MULTIPLE QUANTUM WELL

H. Shen*, P. Parayanthal and F.H. Pollak*

Physics Department, Brooklyn College of the City University of New York, Brooklyn, N.Y. 11210, USA

and

A.L. Smirl, J.N. Schulman, R.A. McFarlane and I. D'Haenens

Hughes Research Laboratory, Malibu, CA 90265, USA

(*Received* 13 *March* 1986 *J. Tauc*)

We have measured the room temperature photoreflectance spectrum from a 100A/150A GaAs/GaAlAs multiple quantum well (MQW) ($x \approx 0.17$). The entire spectrum from the MQW has been fit by a third-derivative functional form lineshape expression. In addition to all the allowed quantum transitions we have clearly observed features from several symmetry forbidden transitions. There also appears to be evidence for unconfined transitions, i.e. energies above the band gap of the GaAlAs barrier layer. There is good agreement between the experimentally determined energies of the various features and a theoretical calculation.

ELECTROMODULATION (electroreflectance and photoreflectance) is rapidly becoming an extremely powerful tool to study microstructural geometries (superlattices, quantum wells and heterojunctions) in semiconductors [1–8]. This method is useful since it yields sharp structure (related to the third-derivative of the optical constants) even at room temperature, has a well-defined lineshape [8] (Aspnes third-derivative functional form [9]) that can be used to accurately fit the spectra and is a function of a surface (interfacial) electric fields.

The enhanced sensitivity and well-defined lineshape of electromodulation makes it a very important method to study weak features in the optical properties of these structures. For example, recent works indicate additional structure in the absorption coefficient due to the appearance of new critical points arising from a mixing of the light and heavy hole character of the valence subbands [10–13]. Photoreflectance (PR) is particularly useful since it is a contactless mode of electromodulation [1, 5, 9]. In PR the optical constants of the material are modulated by the photo-injection of electron-hole pairs by a secondary (pump) light source [1, 5, 9].

In this note we report a room temperature PR study of a GaAs/GaAlAs multiple quantum well (MQW) in which, for the first time, forbidden transitions have been clearly observed at 300K. We have detected three symmetry forbidden features from the MQW in addition to all the allowed quantum transitions. Also, there are features in the spectrum which may be due to transitions involving unconfined states [14]. Glembocki *et al.* have recently reported the temperature dependence of PR in GaAs/GaAlAs multiple quantum wells [6]. Although they clearly observe forbidden features at low temperatures (149 and 125 K) their room temperature spectrum reveals only two very weak structures which correspond to the forbidden transitions.

The sample used in this study was a 100A/150A GaAs/GaAlAs MQW ($x \approx 0.17$) grown by molecular beam epitaxy at the Hughes Research Laboratory. The PR technique has been described in the literature [1, 5, 9]. The pump beam was a 1 milliwatt He–Ne laser (6328A), the power density on the sample being about 100 microwatts cm^{-2}. For the probe beam we employed a Photon Technology International [15] 1/4 meter monochromater with *f*-matched Xenon arc source. All measurements were made in the "low-field" limit, i.e. the lineshape was independent of pump power density.

Shown by the dotted line of Fig. 1 is the experimental PR spectrum. It has been demonstrated that the electromodulation spectra from superlattices and quantum wells [8] can be fit by the Aspnes third-derivative functional form (TDFF) [9]:

$$\frac{\Delta R}{R} = \mathrm{Re}\left[\sum_{j=1}^{p} C_j e^{i\theta_j}(E - E_{g,j} + i\Gamma_j)^{-m_j}\right], \qquad (1)$$

where p is the number of spectral features to be fit, C_j,

*Also at Physics Department, Graduate School and University Center, City University of New York, New York, N.Y. 10036, USA.

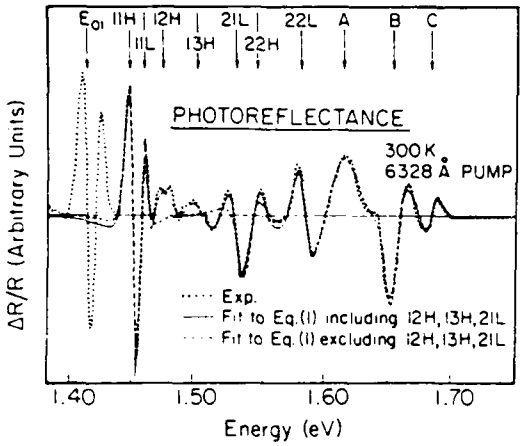

Fig. 1. Shown by the dotted line is the experimental room temperature photoreflectance spectrum. The solid line is a least squares fit to equation (1) of the spectrum from the multiply quantum well including the $12H$, $13H$ and $21L$ features while the dashed line is the fit to equation (1) excluding these forbidden transitions.

θ_j, E_{gj}, and Γ_j are the amplitudes, phases, energies and broadening parameters respectively of the j-th structure and m_j denotes critical point type.

The solid line in Fig. 1 shows a least-squares fit of equation (1) to the experimental data originating from the MQW (we have not fit E_{01} and will return to this point later) for $p = 10$ (i.e., ten spectral features). The energies of the various features are given by arrows at the top of the figure. The E_{01} structure at 1.415 ± 0.002 eV corresponds to the band gap of GaAs and originates from the GaAs substrate. Similar observations of E_{01} have been reported by other authors [2, 5, 8] on superlattice or quantum well systems.

The structure B is related to the direct band gap of the GaAlAs barrier layers. However, because of quantum effects it occurs at a somewhat higher energy, the energy difference being a function of the well and barrier parameters. The observation of this feature in electromodulation [3, 5, 8] is important since it is an indirect measure of the barrier height. The notation nmH or nmL for several of the peaks represents transitions between the n-th conduction subband and the m-th valence subband of heavy hole (H) or light hole (L) character. Allowed transitions have $m = n$ while for symmetry forbidden transitions $m \neq n$. The features A, B and C will be discussed in more detail below. The energies and broadening parameters of the various features from the MQW are listed in Table 1. We find that the E_{01} structure could not be fit to equation (1) since it apparently exhibits Franz–Keldysh oscillations. However, an accurate value for the energy of E_{01} can be obtained from a three-point fit [9].

In order to demonstrate that the forbidden features $12H$, $13H$ and $21L$ are indeed real we have attempted a fit of equation (1) to the experimental data by excluding these transitions (i.e., $p = 7$). This is shown by the dashed line in Fig. 1. The fit which includes the forbidden transitions (solid line) is clearly better than the dashed line, particularly for the resolved peaks $12H$ and $13H$. By adding $21L$, which is not clearly resolved from

Table 1. Energies and broadening parameters (Γ) for the various quantum well transitions from a fit of equation (1) to the experimental data. Also listed are theoretical values for the various transitions using E_{01} (1.415 ± 0.002 eV) as the energy gap of the quantum wells.

Spectral Features	Experiment		Theory*†	
	Energy (eV)	Γ (meV)	Energy (eV)	Transition
$11H$	1.448 ± 0.002	8 ± 1	1.449	$11H$
$11L$	1.456 ± 0.002	7 ± 2	1.461	$11L$
$12H$	1.470 ± 0.010	25 ± 5	1.471	$12H$
$13H$	1.498 ± 0.005	19 ± 5	1.503	$13H$
$21L$	1.529 ± 0.005	10 ± 2	1.531	$21L$
$22H$	1.545 ± 0.005	10 ± 2	1.541	$22H$
$22L$	1.580 ± 0.003	13 ± 2	1.581	$22L$
A	1.614 ± 0.005	30 ± 5	1.602	$24H$
			1.618–1.632	$33H$
B	1.653 ± 0.003	13 ± 2	1.650–1.673	$35H$
C	1.682 ± 0.003	11 ± 2	1.654–1.680	$33L$
			1.678–1.640	$43H$

*$m_e^* = 0.0665$, $m_{lh}^* = 0.094$, $m_{hh}^* = 0.34$ and $Q = 0.60$ from [18].
†Using a well width of 99.1 A (35 layer of thickness 2.83 A per layer).

$22H$, we have substantially improved the fit to the amplitude in the region of the allowed features $22H$ and $22L$. This result demonstrates that there are features at the positions of these three forbidden transitions.

In order to verify the origins of the structures from the quantum wells in Fig. 1, we have performed a calculation based on the two-band tight-binding model [16]. We have employed the energy of E_{01} for the energy gap of the quantum well layers. The structure B cannot be interpreted as the energy gap of the barrier layers, however. Calculations show that the barrier gap is not directly observable as an optical transition. The quantum effect due to the finite layer widths raises the energy of the lowest allowed transition above the barrier transition to slightly higher than the barrier band gap. We find the $35H$ transition is the first unconfined to unconfined feature. The tight-binding model indicates it should be strong and easily observable. A good fit is achieved for the various transitions (including B) using a barrier height of 1.634 eV ($x \approx 0.17$) [17] and a well width (W) of 99.1 A (35 layers of 2.83 A per layer). This value of W is in good agreement with the growth conditions. The various theoretical energies and corresponding transitions also are listed in Table 1. For several of the transitions we give a range of energies due to the dispersion along the direction of the minizone corresponding to the growth axis.

As can be seen from Table 1, there is very good agreement between the experimentally determined energies of the various quantum transitions and the theoretical values, thus verifying the origins of the different allowed and forbidden features. The forbidden features $12H$, $13H$ and $21L$ have recently been reported in the low temperature photoluminescence excitation spectra [13] of quantum wells GaAs/GaAlAs ($x \approx 0.30$) quantum wells having dimensions similar to our sample. With respect to broadening parameters [14] finds the relation $\Gamma = C_0 hm$ meV, C_0 being an adjustable parameter equal to the linewidth of the $11L$ transitions. As can be seen from Table 1 our room temperature broadening parameters do not follow this relationship. The relative intensities of our observed transitions (except for A, B and C) appear to be in good agreement with those of [14]. For example, we also find $21L$ and $22H$ to have about the same magnitude.

The origins of the A and C features are not clear at this point. The former could be due to either the forbidden $24H$ transition (1.598–1.595 eV from Table 1) or possibly the $33H$ transition (1.610–1.624 eV). This latter transition is from a confined hole state to an unconfined conduction level. The C peak at 1.682 eV could be attributed to a $33L$ transition (both states being unbound), a $43H$ transition, or possibly a Franz–Keldysh oscillation of the B feature. These spectral features are under further investigation.

In conclusion we have investigated the room temperature PR spectrum of a GaAs/GaAlAs superlattice. In addition to the allowed transitions we have clearly observed, for the first time at room temperature, three features corresponding to forbidden transitions. The fit to the Aspnes TDFF has allowed us to accurately determine the energies and broadening parameters for all the transitions. For the energies there is very good agreement between experiment and theory based on a two band tight-binding model. There are three features which may be related to transition involving unconfined states.

Acknowledgements – Three of the authors (H.S., P.P. and F.H.P.) acknowledge the partial support of the IBM Shared University Research (SUR) program and the New York State Foundation for Science and Technology as a part of its Centers for Advanced Technology program and A.L. Smirl wishes to acknowledge the support of the Office of Naval Research and the Robert A. Welch Foundation.

REFERENCES

1. See, for example, F.H. Pollak, in *Proceedings of the Society of Photo-Optical Instrumentation Engineers* (SPIE, Bellingham, 1981) **276**, 142 (1981) and references cited therein.
2. E.E. Mendez, L.L. Chang, G. Landgren, R. Ludeke, L. Esaki & F.H. Pollak, *Phys. Rev. Lett.* **46**, 1230 (1981).
3. M. Erman, J.B. Theeten, P. Frijlink, S. Gaillard, F.J. Hia & C. Alibert, *J. Appl. Phys.* **56**, 3241 (1984).
4. C. Alibert, S. Gaillard, J.A. Brum, G. Bastard, P. Frijlink & M. Erman, *Solid State Commun.* **53**, 457 (1985).
5. O.J. Glembocki, B.V. Shanabrook, N. Bottka, W.T. Beard & J. Comas, *Appl. Phys. Letts.* **46**, 970 (1985); *Proceedings of Society of Photo-Optical Instrumentation Engineers* (SPIE, Bellingham, 1985) **524**, 86 (1985).
6. O.J. Glembocki, B.V. Shanabrook & W.T. Beard, to be published in the *Proceedings of the 2nd Int. Conf. (Yamada) on Modulated Semiconductor Structures*, Kyoto, (1985).
7. T.P. Pearsall, F.H. Pollak, J.C. Bean & R. Hull, *Phys. Rev.* **B33**, 6821 (1986).
8. H. Shen, P. Parayanthal, F.H. Pollak, M. Tomkiewicz, T.J. Drummond & J.N. Schulman, to *Appl. Phys. Letts.* **48**, 653 (1986).
9. See, for example, D.E. Aspnes in *Handbook on Semiconductors, Vol. 2*, p. 109, (Edited by T.S. Moss), North Holland, N.Y., (1980) and references cited therein.
10. R.C. Miller, D.A. Kleinman, O. Munteanu & W.T. Tsang, *Appl. Phys. Lett.* **39**, 1 (1981).
11. G.D. Sanders & Y.C. Chang, *Phys. Rev.* **B31**, 6892 (1985).
12. Y.C. Chang, & G.D. Sanders, *Phys. Rev.* **B32**, 5521 (1985).
13. R.C. Miller, A.C. Gossard, G.D. Sanders, Y.C. Change & J.N. Schulman, *Phys. Rev.* **B32**, 8452 (1985).

14. J.N. Schulman & Y.C. Chang, *Phys. Rev.* **B31** 2056 (1985).
15. Photon Technology International, Princeton, N.J. 08542.
16. J.N. Schulman & Y.C. Chang, *Appl. Phys. Letts.* **46**, 571 (1985).
17. J.L. Aubel, U.K. Reddy, S. Sundaram, W.T. Beard & J. Comas, *J. Appl. Phys.* **58**, 495 (1985).
18. R.C. Miller & D.A. Kleinman, *J. Luminescence* **30**, 520 (1985).

END

DATE

FILMED

6-1988

DTIC